Scuola Internazionale Superiore di Studi Avanzati - Trieste

DYNAMICS IN EXTREME ENVIRONMENTS: GALACTIC NUCLEI

Alessandro Alberto Trani

SUPERVISORS:
Michela Mapelli
Alessandro Bressan

20 October 2017

SISSA - Via Bonomea 265 - 34136 TRIESTE - ITALY

A mio nonno Alfonso, che mi ha trasmesso la curiosità
e l'amore per la conoscenza

ABSTRACT

In this Thesis, I tackle several open issues regarding the Galactic center (GC) and other galactic nuclei (GNs).

First, I describe a novel scenario for the formation of the so-called circumnuclear ring (CNR), a clumpy torus of molecular gas which orbits at ~2 pc from the supermassive black hole (SMBH) in the GC. Using smoothed-particle hydrodynamics (SPH) simulations, I show that the infall of a molecular cloud and its subsequent tidal disruption can form a clumpy ring whose properties match those of the CNR.

An analogous tidal disruption episode has been proposed to explain the origin of the clockwise (CW) disk, the nearly-Keplerian disk of young (~3 Myr old) stars orbiting the SMBH in the GC. However, only 20-50% of the observed young stars lie in the CW disk, suggesting that some kind of perturbation had partially disrupted the disk in the past and produced the outliers.

I investigate whether the source of such perturbation can be the CNR, by means of combined direct N-body and SPH simulations. I find that the CNR is not efficient in affecting the stellar disk on timescale consistent with the age of the young stars. On the other hand, I describe how gas in the inner cavity of the CNR could have played a substantial role in shaping the CW disk.

The presence of gaseous rings is not a peculiarity of our Galaxy, but seems to be a rather common feature in GNs. Motivated by this, I performed the first systematic study on the formation of circumnuclear gas in GNs other than the GC. I simulate the infall of molecular clouds towards the center of several different GNs. All simulated GNs are modeled as a SMBH plus a nuclear star cluster (NSC), for which I considered a wide range of masses. I find that the morphology of circumnuclear gas can show distinct features depending on whether the gas settles inside or outside the SMBH influence radius. This suggests that the formation of CNR-like structures occurs only in the nuclear regions dominated by the gravity of the NSC.

Finally, I investigated the origin of G2, a faint dusty object that has been observed to orbit the SMBH in the GC with a pericentre of only 133 AU. Recent work indicates that G2 might be a starless planet brought into highly-eccentric orbit by some kind of mechanism. I investigate how the SMBH tidal field can strip planets from nearby stars, by means of high-accuracy few-body simulations and analytic models. I find that the orbit of planets escaped from the closest stars to the SMBH can match that of G2, except for its inclination. Future detection of stars with similar orbital plane as G2 in the central $1''$ of the GC will be able to further support this scenario.

PUBLICATIONS

Mapelli, M. and A. A. Trani (2016). "Modelling the formation of the circumnuclear ring in the Galactic centre". In: *A&A* 585, A161, A161. DOI: 10.1051/0004-6361/201527195. arXiv: 1510.05259.

Trani, A. A., M. Mapelli, and A. Bressan (2014). "The impact of metallicity-dependent mass-loss versus dynamical heating on the early evolution of star clusters". In: *MNRAS* 445, pp. 1967–1976. DOI: 10.1093/mnras/stu1898. arXiv: 1409.3006.

Trani, A. A. et al. (2016a). "Dynamics of Tidally Captured Planets in the Galactic Center". In: *ApJ* 831, 61, p. 61. DOI: 10.3847/0004-637X/831/1/61.

Trani, A. A. et al. (2016b). "The Influence of Dense Gas Rings on the Dynamics of a Stellar Disk in the Galactic Center". In: *ApJ* 818, 29, p. 29. DOI: 10.3847/0004-637X/818/1/29. arXiv: 1512.02682.

IN SUBMISSION

Trani, A. A. et al. (2017). "Circumnuclear rings and disks as indicators of supermassive black hole presence". In:

PROCEEDINGS

Mapelli, M., A. A. Trani, and A. Bressan (2014). "The Impact of Metallicity and Dynamics on the Evolution of Young Star Clusters". In: pp. 137–140. arXiv: 1402.0669 [astro-ph.GA].

Trani, A. A. et al. (2016). "Dynamics of tidally captured planets in the Galactic Center ". In: *Mem. Soc. Astron. Italiana* 87, p. 705. arXiv: 1608.07230.

CONTENTS

ACRONYMS

GN Galactic nucleus

AGN active galactic nucleus

SMBH supermassive black hole

GC Galactic center

CNR circumnuclear ring

CW clockwise

NSC nuclear star cluster

SPH smoothed-particle hydrodynamics

SC star cluster

1 INTRODUCTION

Galactic nuclei (GN) are among the most complex ecosystems in the Universe, where large concentrations of gas and dust, newborn star clusters and old stellar populations can coexist in a relatively small (~100 pc) environment. A supermassive black hole (SMBH) might lurk in their center, dominating the gravitational potential of the central parsecs. The SMBH may even manifest itself by accreting matter and turning the GN into an active galactic nucleus (AGN), one of the most luminous sources of the Universe. Unraveling the phenomena occurring in GNs is crucial to gain insights into several astrophysical conundrums, such as SMBH growth, galaxy evolution, the formation of AGNs and nuclear starbursts. A schematic representation of the main processes occurring in GNs is given in Figure 1.1.

Why galactic nuclei?

Due to its proximity to Earth, the Galactic center (GC) is the most well studied GN. The GC is nowadays the only case in which we can resolve individual stars inside the sphere of influence of the SMBH, wherein the gravity of the SMBH dominates the one of the galaxy. Indeed, near-infrared observations of the GC indicate that the velocity dispersion σ of stars in the inner parsec becomes Keplerian, i.e. decreases as $\sigma(r) \propto r^{-1/2}$, where r is the distance from a compact radio source known as Sgr A*. Thanks to precise astrometric measurements it is now known beyond any doubt that Sgr A* is in fact a SMBH of $4.3 \times 10^6\,M_\odot$, which lies at the bottom of the potential the Milky Way at 8.3 kpc from the Sun (Gillessen et al. 2017). More details about GNs and particularly about the GC environment are presented in Chapter 2 of this Thesis.

The Galactic center: the closest GN

Over the past decade, the GC has been subject of countless observations which exposed several intriguing puzzles. The first apparent inconsistency is the presence of young (3-6 Myr old) stars in innermost 0.1 pc, where the gravity of the SMBH should disrupt nearby molecular clouds and prevent star formation. Many theories have been proposed to explain the presence of the young stars, either using migration scenarios or unconventional mechanisms of *in situ* star formation. The most accepted scenario is the infall and disruption of a molecular cloud, which settles down into a disk around the SMBH, fragments and form stars. This scenario is corroborated by the fact that a fraction (~20%, Yelda et al. (2014)) of the young stars lie in a disk around the SMBH, named clockwise (CW) disk (Figure 1.2). However, this scenario fails to explain the stars which do not lie in the disk. A possible explanation is that the CW disk is the remnant of a more massive and extended stellar disk, which underwent disrup-

The young stars puzzle

tion after its formation. Disruption could have been caused by gravitational perturbations that induced precession on the stellar orbits, displacing stars from the disk.

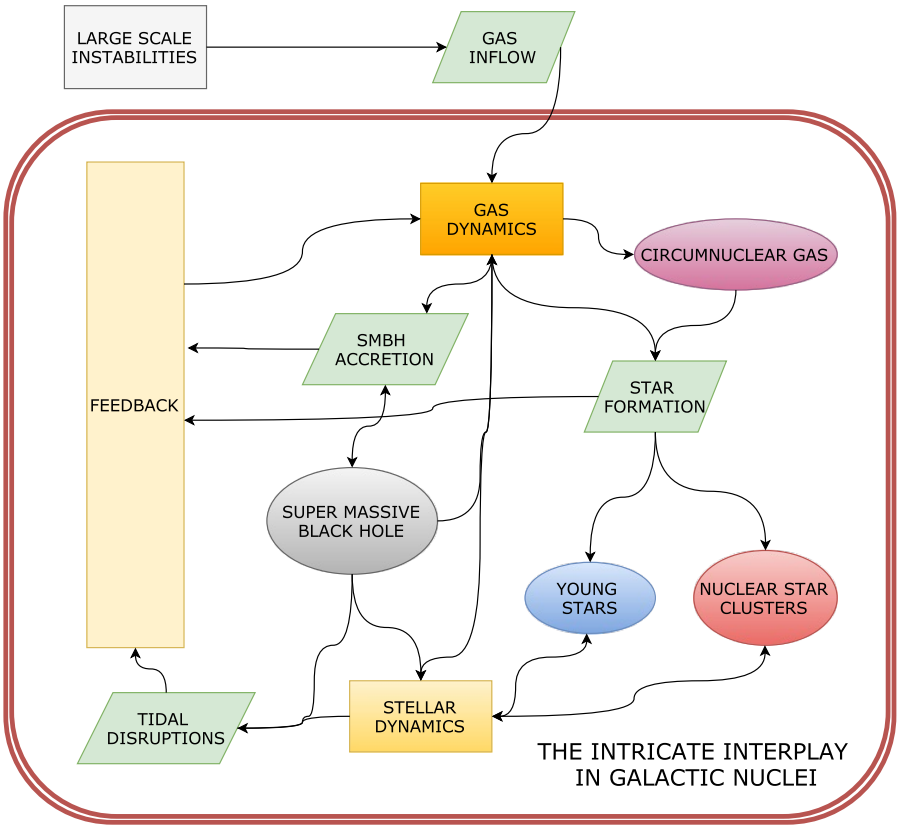

Figure 1.1: Scheme of the main processes and phenomena occurring in GNs. In this Thesis I will focus on stellar and gas dynamics and star formation.

The circumnuclear ring (CNR), a ring of molecular gas orbiting at ~1.5 pc from the SMBH, has been often invoked as the source of such perturbations. Few numerical studies so far investigated the role of the CNR in shaping the properties of the CW disk. This is mostly due to numerical issues. In fact, modeling the CNR requires the employment of hydrodynamic codes which lack the accuracy to properly follow orbital dynamics around a SMBH. On the other hand, direct N-body codes can follow the stellar orbits with great accuracy, but lack the hydrodynamical treatment of gas. To overcome this limit and investigate the perturbations exerted on the stellar disk by the CNR, I have ran multi-physics simulations that combined both gas and stellar physics into a single simulation. In this way, I achieved high-accuracy to model the stellar orbits and self-consistent hydrodynamics treatment to model the gaseous CNR.

As a first step, I investigated the formation of the CNR by means of smoothed-particle hydrodynamics (SPH) simulations. I modeled the infall of giant molecular clouds towards the GC, and their subse-

quent disruption caused by the strong tidal field of the central parsec. In this way, I found that a molecular cloud disruption episode can produce a ring of gas with properties similar to those of the CNR. This scenario is supported by the observation of streamers (Liu et al. 2012) in the GC that seems to feed the CNR, a feature also present in the simulations. This work is presented in Chapter 3.

Then, I coupled the SPH simulation with a direct N-body code which I used to follow the evolution of a nearly-Keplerian disk of stars around the SMBH. Thanks to this novel approach, I found that the CNR is not efficient in affecting the stellar disk on a timescale shorter than its age. Therefore, some additional mechanism is needed to displace stars from the original stellar disk. On the other hand, I found that the gas in the inner cavity of the CNR plays a crucial role in the evolution of the stellar disk, inducing precession of the orbits and significantly affecting the stellar disk inclination. This effect, combined with mutual gravitational interactions of disk stars, might have contributed to the CW disk disruption in the past. More details are found in Chapter 4.

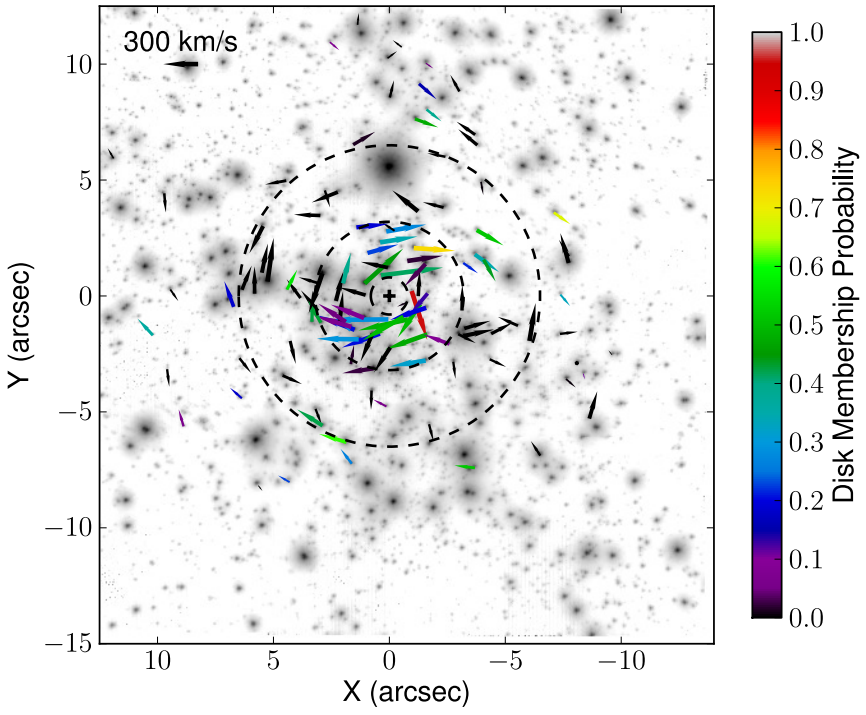

Figure 1.2: Velocity vectors of 116 young stars stars. Sgr A* is marked as a cross in the center. The arrows are color-coded according to their disk membership probability. From Fig. 11 of Yelda et al. (2014).

It is not straightforward to predict the result of similar episodes in nearby GNs. In general, kinematics and morphology of circumnuclear gas is affected by the gravitational potential of the GN. In turn,

the shape of the gravitational well is determined by the properties of the SMBH and the nuclear star cluster (NSC). Understanding the impact of different components of GNs on circumnuclear gas is particularly important given the recent advancements in high resolution interferometry, which enable the use of molecular gas kinematics to measure the dynamical mass of SMBHs (Yoon 2017; Davis et al. 2017). This method for measuring the SMBH mass suffers from systematic errors that arise from the spatial and velocity structure of circumnuclear gas. However, there has been no detailed investigation of these systematic uncertainties using self-consistent hydrodynamical simulations. In addition, circumnuclear gas can be star forming, so that its properties affect the distribution of stars close to the SMBH (e.g. the CW disk of the Milky Way or the stellar rings in M31) . Knowing how the specific properties of GNs affect the stellar distribution in the inner parsecs of nearby GNs is crucial to interpret data from forthcoming facilities (e.g. 30 m-class telescopes, Do et al. 2014; Gullieuszik et al. 2014).

Formation and evolution of circumnuclear rings

To this purpose, I have performed the first systematic study on the formation of circumnuclear disks/rings in GNs with properties different from those of the GC, by means of smoothed particle hydrodynamics simulations. I found that the relative masses of the SMBH and the NSC have a deep impact not only on the kinematics but also on the morphology of circumnuclear gas. In the simulations, extended gaseous disks form only inside the sphere of influence of the SMBH, where the gravity of the SMBH dominates over that of the NSC. In contrast, compact gaseous rings form only outside the sphere of influence of the SMBH. This result holds for a variety of SMBH to NSC mass ratios, and it is in agreement with the properties of the Milky Way's CNR, which orbits just outside the SMBH sphere of influence. I suggest that the morphology of circumnuclear gas can be used as a probe for SMBH presence: with some *caveats*, the inner radius of circumnuclear rings can be used to infer an upper limit to the SMBH sphere of influence.

Furthermore, I show that the distribution of newborn stars can be quite different from that of circumnuclear gas. Depending on the molecular cloud initial orbit, stars decouple from the gaseous stream in which they are born. Afterwards, gaseous streams tend to circularize, while stars retain their orbital properties at birth. This results in highly-eccentric stellar orbits and an external, circularized ring of gas. A full discussion can be found in Chapter 5.

One of the most intriguing puzzles in the GC regards the so-called cloud G2, a faint dusty object that has been observed to orbit Sgr A* on an extremely eccentric orbit. Since the fist detection in 2011 G2 has been subject of much attention: was it going to be disrupted by the SMBH and flare up the GC? The quiet survival of the source after its 200 AU pericenter passage in 2014 sparkled even more de-

The misterious G2 cloud

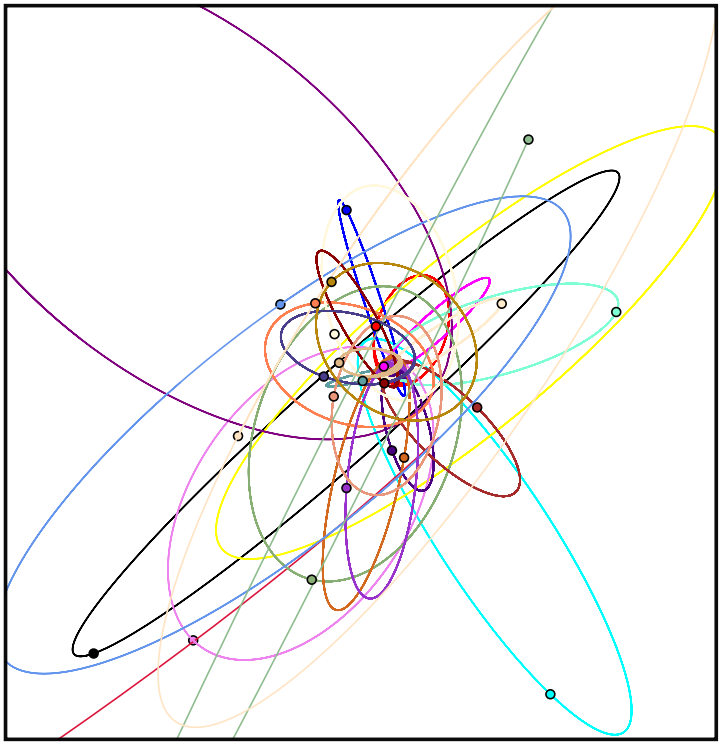

Figure 1.3: Reconstruction of the S-stars orbit and their current position. Rendered using orbital data from Gillessen et al. (2009a).

bate about its nature. The observational features of G2 are different than any other star in the region and are open to many interpretations. Interestingly, G2 might have a protoplanetary origin: its observational signatures are compatible with a photoevaporating planetary embryo, being disrupted by the SMBH tidal field (Mapelli and Ripamonti 2015). However, this scenario requires that planets are stripped from their parent star and brought into highly-eccentric orbit around the SMBH. A mechanism to produce this kind of orbits can be tidal capture: the gravitational potential of the SMBH might strip planets from their parent star, bringing them into highly eccentric orbits.

Few studies have investigated in detail the dynamics of planets close to SMBHs, and none examined the tidal stripping of planetary systems. Therefore, I performed high-accuracy simulations to model the tidal capture of planets orbiting around stars in the CW disk and around the S-stars (Figure 1.3), the ~30 closest stars to the SMBH. I also developed an analytic model based on the restricted three-body problem to predict the orbital properties of planets after capture by the SMBH.

In this way, I showed that planets escaped from stars in the CW disk remain in the disk and cannot reproduce the orbital properties of G2. On the other hand, planets escaped form the ~30 closest stars to the SMBH can match eccentricity and semimajor axis of G2, but not its orbital orientation. Nonetheless, more stars close to the SMBH

are expected to be detected in the near future with the new GRAVITY interferometric instrument at VLT. Therefore, the future detection of stars with same orbital orientation will prove crucial to further support this scenario. More complete results are discussed in Chapter 6.

1.1 THESIS OUTLINE

In this Thesis, I tackle major issues related to the GC and GNs from a theoretical and numerical perspective. Chapter 2 introduces the main properties of GNs, with particular attention to the GC. In this Chapter I also present the main issues that will be covered in subsequent chapters.

In Chapter 3 I describe the mechanism by which the CNR may have formed in the GC. Using hydrodynamical simulations, I show that the infall of a molecular cloud can lead to the formation of a clumpy gas ring orbiting the SMBH, whose properties match the CNR in the GC. This Chapter is based on Mapelli and Trani (2016).

Chapter 4 deals with the formation and evolution of the young stars observed in the innermost 0.1 pc of the GC. First I describe the novel numerical methods I have employed to simulate the interaction between stars and gas close to the SMBH. Then I discuss the physical processes that drive the evolution of the young stars in the GC, explaining how this can help us to shed light on the past history of the GC. The Chapter is based on Trani et al. (2016b).

Chapter 5 is dedicated to the formation and evolution of circumnuclear gas rings/disks in GNs. Here I generalize the mechanism described in Chapter 3 to GNs with properties different from those of the GC. I illustrate how the morphology of circumnuclear gas can be used to infer an upper limit on the mass of SMBHs. This Chapter is based on (Trani et al. 2017, to be submitted).

In Chapter 6 I discuss the dynamics of planets in the GC by means of regularized, high-accuracy simulations and analytic models. I describe how the interaction with the SMBH could produce an object with orbital properties of the cloud G2. The Chapter is based on Trani et al. (2016a).

Chapter 7 summarizes the main results of this Thesis, and discusses possible future developments of the subject.

In addition, I included an Appendix A in which I discuss the evolution of young massive star clusters, extreme environments where the interaction between stellar evolution and stellar dynamics drives the long-term evolution of the cluster. This Appendix is based on Trani, Mapelli, and Bressan (2014).

2 THE ENVIRONMENT OF GALACTIC NUCLEI

GNs are unique environments located at the bottom of the potential well of galaxies. Arguably, the most outstanding feature of GNs is the presence of a SMBH. The interaction of SMBHs with its environment is far from understood and it is of central importance to several fields, from galaxy formation to general relativity.

It is now generally accepted that SMBH and galaxies co-evolve by regulating each others growth. Evidences come from the correlation between the SMBH mass and properties of the host galaxy. The most studied scaling relations are the M_{SMBH}-M_{bulge} (or M_{SMBH}-L_{bulge}) and the M_{SMBH}-σ, which link the SMBH mass with the mass (or luminosity) and the velocity dispersion of the host spheroid (either elliptical galaxy or bulge in spiral galaxy), respectively.

The M_{SMBH}-M_{bulge} relation has been widely considered to be near-linear (Dressler and Richstone 1988; Kormendy and Richstone 1995; Magorrian et al. 1998; Sigurdsson and Rees 1997; Ferrarese and Ford 2005; Graham 2008; van den Bosch et al. 2012; McConnell and Ma 2013; Rusli et al. 2013), at least for $M_{SMBH} \gtrsim 2 \times 10^6\, M_\odot$ (Jiang et al. 2011; Mathur et al. 2012; Reines, Greene, and Geha 2013; Jiang et al. 2013). However, there is currently a strong debate on whether the M_{SMBH}-M_{bulge} relation takes a bend at the low-mass end and whether it varies in function of the galaxy morphology. In particular, Graham and Scott (2013, 2015) and Savorgnan et al. (2016) find that for early-type (E and S0) galaxies the M_{SMBH}-M_{bulge} is near-linear, while it becomes steeper for late-type galaxies (Figure 2.1). Savorgnan et al. (2016) interpret this as the result of two different scenarios driving the black-hole growth in early and late type galaxies: gas-poor ("dry") mergers in the fist case and gas-rich ("wet") mergers in the latter. In wet merger, gas accretion would make the SMBH grow quadratically (or cubically) relative to the host spheroid, whereas in dry mergers the SMBH and the bulge would grow at the same pace. Savorgnan et al. (2016) and Graham and Scott (2015) also find a superlinear M_{SMBH}-M_{bulge} relation for spheroids with a centrally depleted core (i.e. with a central stellar deficit of stars), for which they give a similar interpretation.

In contrast, Kormendy and Ho (2013) distinguish between bulges, indistinguishable from elliptical galaxies, and "pseudobulges", which are flatter and more disk-like[1]. Kormendy and Ho (2013) argue that

1 There can be significant overlap in the properties of classical bulges and pseudobulges so the classification between the two is done by looking at multiple indicators, as each individual criterion has a non-negligible failure rate (Kormendy 2016; Fisher and Drory 2016).

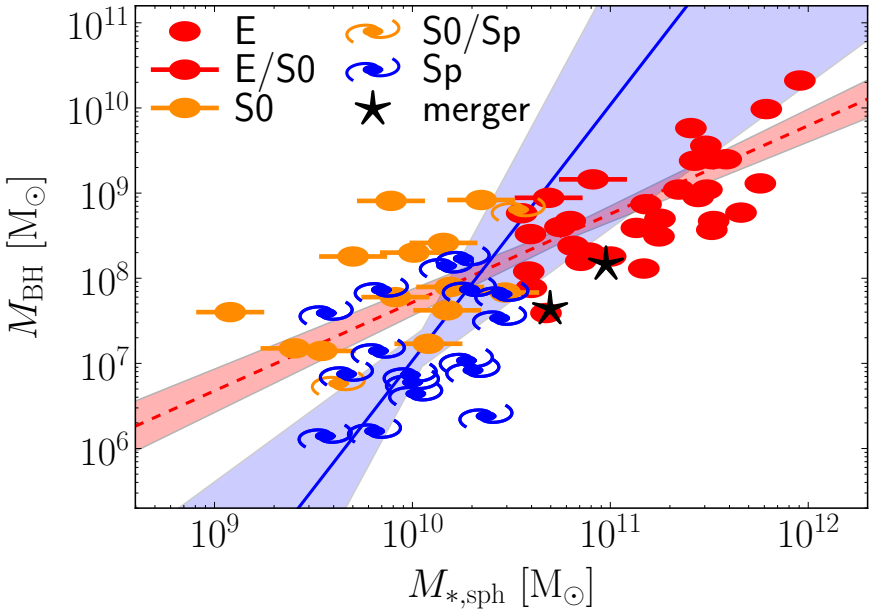

Figure 2.1: Left: black hole mass vs spheroid stellar mass. The bulges of early-type galaxies follow $M_{SMBH} \propto M_{bulge}^{1.04\pm0.10}$, a near-linear relation consistent with a dry-merging formation scenario. The bulges of late-type galaxies follow $M_{BH} \propto M_{bulge}^{2-3}$, indicating that gas-rich processes feed the black hole more efficiently than the host bulge grows in stellar mass. From Fig. 5 of Savorgnan et al. (2016).

pseudobulges grow from secular evolution of disk galaxies, in contrary to bulges, which are thought to form through galaxy mergers (Brooks and Christensen 2016). Furthermore Kormendy, Bender, and Cornell (2011) reported that SMBHs correlate little or not at all with pseudobulges (but see also Savorgnan et al. 2016, which do not confirm this result). For this reason, Kormendy and Ho (2013) omit pseudobulges from their analysis and find a linear M_{SMBH}-M_{bulge} relation. More information on this controversial topic can be found in Graham (2016) and Kormendy (2016).

On top of this, recent work has shown that the dynamical SMBH mass estimates are heavily biased and sample only the densest galaxies, due to the observational constraint that the SMBH sphere of influence must be resolved (see paragraphs below, Bernardi et al. 2007; van den Bosch et al. 2015; Shankar et al. 2016; Shankar, Bernardi, and Sheth 2017). This leads to strong bias in the M_{SMBH}-M_{bulge} relation. In particular, Shankar et al. (2016) find that the M_{SMBH}-M_{bulge} relation is mostly a consequence of the M_{SMBH}-σ relation, which is less affected by such bias.

Although there is still little agreement on the precise details of the scaling relations between galaxies and SMBHs, broad correlations do

exist, suggesting that SMBH and galaxy growth may be directly (or indirectly) linked. The key to better understand how SMBH and galaxies coexist is to obtain an as much as complete and unbiased sample of SMBH mass measurements.

The most reliable way to estimate SMBHs mass is the so-called dynamical method, i.e. to use the kinematics of stars and gas in close proximity to the SMBH. Within the sphere of influence of the SMBH, defined as the region in which the gravity of the SMBH dominates over that of the surrounding material, the dynamics becomes Keplerian. The observation of Keplerian rotation or velocity dispersion is therefore an almost[2] unambiguous proof of the presence of a SMBH.

This method requires that the SMBH sphere of influence is spatially resolved, which is typically much smaller than $1''$ even for nearby galaxies. So far, only ≈ 90 galaxies have their SMBH reliably measured via dynamical modeling (Savorgnan et al. 2016; Graham 2016). Most of the galaxies are ellipticals or S0, which explains the difficulty of distinguishing trends among different galaxy morphology. Only space-borne telescopes (such as the Hubble Space Telescope), 8-10m telescopes assisted by adaptive optics (Keck and VLT) and radio facilities (ALMA) currently have the angular resolution to probe the SMBH sphere of influence in few nearby GNs. The situation will change with the advent of 30-meter telescopes, which will be able to observe Milky Way mass SMBHs out the distance of the Virgo Cluster (Do et al. 2014; Gullieuszik et al. 2014).

Up to recent years, dynamical measurements of SMBH have relied primarily on stellar kinematics (Dressler and Richstone 1988; Kormendy 1988; van der Marel and van den Bosch 1998; Cappellari et al. 2002; Gebhardt et al. 2003; Valluri et al. 2005; McConnell et al. 2011; van den Bosch et al. 2012; Rusli et al. 2013), ionized gas kinematics (Ferrarese, Ford, and Jaffe 1996; Macchetto et al. 1997; van der Marel and van den Bosch 1998; Cappellari et al. 2002; Sarzi et al. 2001; Ho et al. 2002; Neumayer et al. 2007; de Francesco, Capetti, and Marconi 2008; Walsh et al. 2013) and, in rare cases, kinematics of nuclear megamasers (Miyoshi et al. 1995; Greenhill, Moran, and Herrnstein 1997; Moran, Greenhill, and Herrnstein 1999; Lo 2005; Kuo et al. 2011; van den Bosch et al. 2016).

Each method has different strength and weaknesses. Stellar kinematics measurements, obtained from optical/near infrared observations, have the advantage that stars are ubiquitous and their motion is affected only by gravitational force. However, observations require both high spatial resolution and high spectral signal-to-noise ratio, and they are severely affected by dust obscuration. In addition, the

2 In many cases, the estimated dark mass is confined into a radius which is too large to rule out alternative explanations, such a cluster of stellar remnants. In the Milky Way case, the dark mass has such a density that any hypothetical dark cluster would have evaporated via dynamical interactions in few million years, much less than the age of the Galaxy (Maoz 1998).

modeling of the observables is theoretically challenging due to the unknown stellar orbital distribution, and often requires assumptions to be made. As a consequence, this method has been mostly applied to early-type galaxies.

Ionized gas kinematics is probed through emission lines at optical/near infrared wavelengths from the small nuclear disks hosted in many galaxies. The challenge for this method is the modeling the non-gravitational forces (e.g. shocks, turbulence, outflows) which are often superimposed on the rotational motion of ionized gas around the SMBH.

Water megamasers arise when X-ray AGN emission excites H_2O vapors in the accretion disk. Megamasers allow for accurate measurement of the mass of SMBHs but seem to be very rare, with a detection fraction of few percents over all the object searched so far.

Recently, kinematics of circumnuclear molecular gas is emerging as a promising method to infer the SMBH masses (Davis et al. 2013; Onishi et al. 2015; Barth et al. 2016a,b; Onishi et al. 2017; Davis et al. 2017). Molecular gas is considerably less affected by non-gravitational forces than ionized gas and thus it is a better tracer of the gravitational potential. Furthermore, molecular gas observations are unaffected by dust. This method has been enabled thanks to the high angular and velocity resolution of the Atacama Large Millimetre/sub-millimetre Array (ALMA).

On the other hand, circumnuclear gas exhibits a complex morphology and kinematics, with clumpy streamers, warped rings and/or disks that deviate from axisymmetry and circular motion. How the complex spatial and velocity structure of circumnuclear gas forms and evolves remains poorly understood. This uncertainty limits the use of molecular gas dynamics to infer the dynamical mass of SMBHs (Davis 2014; Yoon 2017).

In Chapter 5 I lay the basis to clarify these uncertainties by investigating the formation of gaseous circumnuclear ring/disks in GNs. In particular, I simulate the disruption of molecular cloud in the tidal potential of GNs by means of SPH simulations and study how the properties of circumnuclear gas are affected by those of the GN. One crucial finding is that the presence of a NSC has a strong impact on the properties of circumnuclear gas.

In fact, beside SMBHs, GNs host another class of unique objects: NSCs, compact stellar systems with masses ranging from $10^6\,M_\odot$ to $10^8\,M_\odot$ and half-light radii of $\sim$5 pc (Böker et al. 2002, 2004). Comparable in size to globular clusters but generally more massive, NSCs rank among the densest stellar systems of the Universe.

Most NSCs consists of multiple stellar populations (Rossa et al. 2006; Walcher et al. 2006; Seth et al. 2006; Georgiev et al. 2009; Carson et al. 2015; Mason et al. 2015). While they all have an old stellar component with age $>$1 Gyr, some NSCs show also young stellar popula-

tions with age less than 100 Myr (Siegel et al. 2007; Montero-Castaño, Herrnstein, and Ho 2009). The stellar metallicity of NSCs is varied, ranging from sub-solar (Walcher et al. 2006) to super-solar (Sarzi et al. 2005), and shows significant scatter in individual NSCs (Monaco et al. 2009). In some cases, NSCs exhibit a larger spread in metallicity than their host galaxy (Paudel, Lisker, and Kuntschner 2011).

The fraction of GNs that harbor a NSC, called nucleation fraction, depends on the host-galaxy type and luminosity. The nucleation fraction is 75% for Scd-Sm spirals (Böker et al. 2002; Georgiev and Böker 2014), 55% Sa-Sc spirals (Carollo, Stiavelli, and Mack 1998) and 66% in early-type (S0 and E) galaxies with magnitude $\mathcal{M}_B > -20.5$ (Côté et al. 2006; Turner et al. 2012; den Brok et al. 2014), while early-type galaxies with magnitude $\mathcal{M}_B < -20.5$ lack a NSC.

To date, there has been little agreement on the link between NSCs and SMBHs. In 2006, Ferrarese et al. (2006), Wehner and Harris (2006) and Rossa et al. (2006) independently found a correlation between NSC mass M_{NSC} and host spheroid velocity dispersion σ which was surprisingly similar to the well known M_{SMBH}-σ relation. In particular, Ferrarese et al. (2006) found the M_{NSC}-σ relation to be parallel to the M_{SMBH}-σ relation, with a slope of 4.41 ± 0.43 (middle panel of Figure 2.2). More importantly, Ferrarese et al. (2006) derived a linear relation between the masses of the central massive object M_{CMO} (either a SMBH or a NSC) and their host galaxy: $M_{CMO} \simeq 1.8^{+3.4}_{-1.2} \times 10^{-3} M_{gal}$ (right-hand panel of Figure 2.2).

These findings imply a tight relation between SMBHs and NSCs, suggesting that a single mechanism might be responsible for the growth and formation of both objects. In this picture, NSC and SMBH would reside at the low and high-mass end of the same M_{CMO}-M_{gal} relation, respectively, and may coexist in few cases of the intermediate regime.

This relation has been interpreted by Nayakshin, Wilkinson, and King (2009) as a result of competitive growth of NSCs and SMBHs from the same gas reservoir. They argue that in small spheroids, the shorter crossing timescale makes gas injected by a merger event virialize faster, slowing its infall towards the center. Therefore, star formation would occur before significant SMBH accretion and thus favor the formation of a NSC. An alternative explanation was proposed by Antonini et al. (2012; see also Antonini 2013; Arca-Sedda, Capuzzo-Dolcetta, and Spera 2016), who modeled the formation of NSCs by the infall and merger of globular clusters (see below for more details about this formation mechanism). In massive galaxies, the timescale for a globular cluster to reach the center is much longer than one Hubble time. Moreover, the presence of a central SMBH with mass $>10^8\,M_\odot$ would disrupt the clusters before they could reach the GN, explaining the lack of NSCs in the most massive early-type galaxies. Alternatively, Bekki and Graham (2010) find that the lack of NSCs in

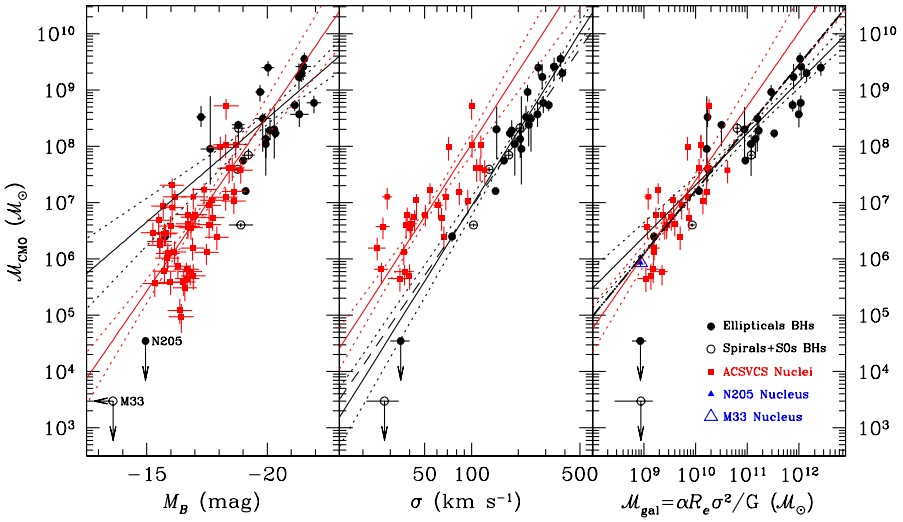

Figure 2.2: Left-hand panel: mass of the central massive object (either SMBH or NSC) plotted against absolute blue magnitude of the host galaxy (or bulge for spiral galaxies). NSCs from the Virgo Cluster Survey are shown as red squares. The SMBHs in early-type and spiral galaxies are shown as filled and open circles respectively. Middle panel: central massive object mass as a function of velocity dispersion of the host galaxy within the effective radius R_{hl}. The dashed line is the best fit M_{SMBH}-σ relation of Tremaine et al. (2002). Right-hand panel: central massive object mass plotted against galaxy mass, defined as $M_{gal} \propto R_{hl}^2/G$ with $\alpha = 5$. The dashed line is the fit obtained for the combined NSCs +SMBHs sample. In all panels, the solid red and black lines show the best fits to the nuclei and early-type SMBH samples respectively, with 1σ confidence levels shown by the dotted lines. From Fig. 2 of Ferrarese et al. (2006).

massive ellipticals can be the consequence of the mergers of galaxies hosting a SMBH seed. Bekki and Graham (2010) show that, during a merger, the inspiral of a SMBH seed binary dynamically heats the NSC, lowering its central stellar density and making it susceptible to tidal disruption.

However, more recent findings seem to question the existence of a common scaling relation for SMBHs and NSCs. Balcells, Graham, and Peletier (2007) found a non-linear relation between the central massive object and the bulge mass for a sample of S0–Sbc galaxies, in contrast to the linear relation of Ferrarese et al. (2006). Graham (2012) reanalyzed the Ferrarese et al. (2006) data including a larger sample of low-luminosity galaxies, and derived a shallower $M_{NSC} \propto \sigma^{1.57\pm0.24}$. Graham (2012) argued that the previous $\propto\sigma^5$ relation was biased by the sample selection of luminous spheroids. Similar conclusion were reached by Leigh, Böker, and Knigge (2012) and Scott and Graham (2013) (see Figure 2.3). In particular, Scott and Graham (2013) notice

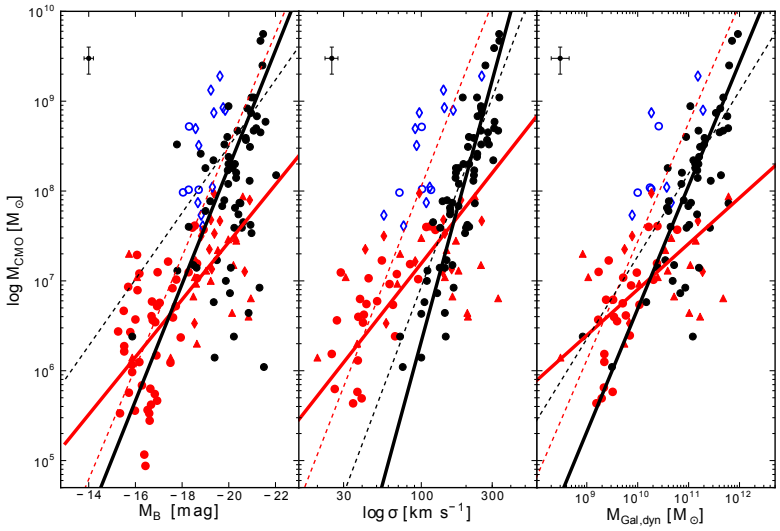

Figure 2.3: M_{NSC} and M_{SMBH} versus galaxy magnitude $\mathcal{M}_B$ (left-hand panel), velocity dispersion σ (middle panel) and dynamical mass M_{gal} (right-hand panel). Black dots indicate SMBHs, red symbols indicate NSCs and open blue symbols show those objects identified as nuclear disks. For the NSCs and nuclear disks the symbol indicates the sample each datapoint was drawn from: circles for Ferrarese et al. (2006), diamonds for Balcells, Graham, and Peletier (2007) and triangles for Graham and Spitler (2009). The thick black and red lines indicate the best-fitting linear relations for the SMBH sample and the NSC sample respectively. The thin dashed lines indicate the corresponding best-fitting relations from Ferrarese et al. (2006). A representative error bar is shown in the upper left corner of each panel. From Fig. 1 of Scott, Graham, and Schombert (2013).

that mass of NSCs is not a constant fraction of the host total mass, but it decreases in more massive galaxies.

On top of this, NSCs and SMBHs are observed to coexist in many GNs, and the ratio of M_{SMBH} to M_{NSC} varies widely above and below 1 (Seth et al. 2008b; Graham and Spitler 2009; Kormendy et al. 2009; Kormendy and Ho 2013; Georgiev and Böker 2014; Georgiev et al. 2016). Neumayer and Walcher (2012) point out that the apparent segregation of NSCs in low-mass galaxies and SMBHs in high-mass galaxies could arise from observational reasons: at high galaxy masses, the NSC mass has large uncertainties due to NSC being poorly resolved, while in less massive galaxies the error bars on SMBH measurements are typically very large and NSC masses are well measured.

Furthermore, the relation between SMBHs and NSCs might differ depending on the host galaxy morphology. Building on the idea that dwarf ellipticals are defunct late-type galaxies that lost some of

their baryons (Kormendy 1985), Kormendy and Ho (2013) notice that the correlation between SMBHs and NSCs becomes tighter if they omit dwarf ellipticals from the analysis. They find that the ratio of $M_{SMBH} + M_{NSC}$ over the galaxy mass shows less scatter than the mass ratios of M_{SMBH} and M_{NSC} individually, suggesting that their growth might be related.

Besides, Scott and Graham (2013), Erwin and Gadotti (2012) and Zasov and Cherepashchuk (2013) note that the M_{NSC} correlates better with the host galaxy total stellar mass, while M_{SMBH} correlates better with the host spheroid. This would naturally mislead any analysis based on samples overly populated with ellipticals, like those of Ferrarese et al. (2006) and Wehner and Harris (2006). Based on this, they conclude that different physical processes regulate NSC and SMBH growth.

A deviation in the M_{NSC}-M_{gal} relation among different galaxy types was reported also by Georgiev et al. (2016). Specifically they found that NSCs in early-type galaxies become progressively more massive with increasing total galaxy mass, compared to NSCs in late-type galaxies. However, Georgiev et al. (2016) are not able to discriminate whether this feature is caused by measurement biases or evolutionary differences. Nevertheless, they find for galaxies that host both SMBH and NSC a relation $M_{SMBH} + M_{NSC}$-M_{gal} consistent with the M_{SMBH}-M_{bulge} in early type galaxies (McConnell and Ma 2013; Savorgnan et al. 2016). Georgiev et al. (2016) conclude that this is probably suggesting a similar physical mechanisms driving the growth of both objects.

In brief, the lack of understanding about the formation and growth of either objects, the observational biases and the scarce agreement on the subject makes difficult to properly assess the relation between SMBHs and NSCs.

In fact, much uncertainty still exists about the formation of NSCs. Two main mechanisms have been proposed: the migration of stellar clusters towards the nucleus and *in situ* continuous star formation. In the first scenario, star clusters (either globular or young) fall by dynamical friction onto the GN and buildup a NSC (Tremaine, Ostriker, and Spitzer 1975; Capuzzo-Dolcetta 1993; Bekki et al. 2004; Capuzzo-Dolcetta and Miocchi 2008a,b; Agarwal and Milosavljević 2011; Antonini et al. 2012; Antonini 2013; Gnedin, Ostriker, and Tremaine 2014; Perets and Mastrobuono-Battisti 2014; Arca-Sedda and Capuzzo-Dolcetta 2014; Aharon and Perets 2015). The migration scenario is supported by the detection of star clusters on the way to fall and merge at the center of their host galaxy (Andersen et al. 2008; Kornei and McCrady 2009; Nguyen et al. 2014). In addition, a deficit of globular clusters has been observed in the inner region of several dwarf ellipticals, suggesting that the cluster orbit already decayed onto the center by dynamical friction (Lotz et al. 2001; Lotz, Miller, and Ferguson 2004).

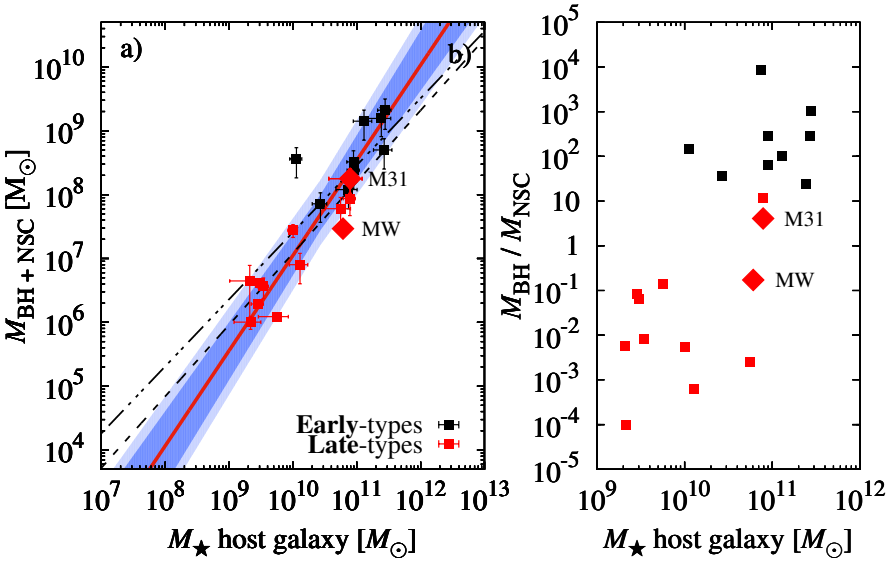

Figure 2.4: Sum of the mass of NSC with SMBH (left-hand panel) and their mass ratio against host galaxy stellar mass (right-hand panel). The different symbol types indicate late- and early-type galaxies, as indicated in the legend. The fit through the data in the left-hand panel is shown with solid line and the shaded region indicates the uncertainty of the fit values and the rms of the data. For reference, dashed line is the McConnell and Ma (2013) $\log_{10} M_{SMBH} \propto 1.05 \pm 0.11 \log_{10} M_{bulge}$ relation and dash-dotted line is the $\log_{10} M_{NSC} \propto 1.001^{+0.054}_{-0.067} \log_{10} M$ relation for late-type galaxies obtained by Georgiev et al. (2016). From Fig. 7 of Georgiev et al. (2016).

The migration scenario is able to reproduce well the density, shapes and scaling relation of NSCs with the host galaxy mass, and even rotation (e.g. Trippe et al. 2008; Seth et al. 2008a; Schödel, Merritt, and Eckart 2009; Seth et al. 2010). Notwithstanding, Hartmann et al. (2011) pointed out that the second-order kinematic moment ($v_{rms} = \sqrt{v^2 + \sigma^2}$ where v is the observed mean stellar velocity and σ is the mean stellar velocity dispersion) produced by the globular cluster merger scenario is too centrally peaked when compared to observations (although this might not be true for Milky Way's NSC, e.g. see Feldmeier et al. 2014; Tsatsi et al. 2017).

To solve this issue, Hartmann et al. (2011) has proposed that at least 50% of the mass of NSCs is build up with *in situ* star formation (Milosavljević 2004; Li, Haiman, and Mac Low 2007; Emsellem and van de Ven 2008; Pflamm-Altenburg and Kroupa 2009; Hartmann et al. 2011; Aharon and Perets 2015; Antonini, Barausse, and Silk 2015; Guillard, Emsellem, and Renaud 2016; Biernacki, Teyssier, and Bleuler 2017). On the other hand, *in situ* star formation scenarios face the issue of funneling enough gas to form a NSC. Several mechanisms have been proposed to counter this issue: magneto-rotational

instability (Milosavljević 2004), gas cloud mergers (Bekki 2007) and bar instabilities (Shlosman, Frank, and Begelman 1989).

Finally, recent observational data do not seem to exclude either scenario (Turner et al. 2012; Georgiev et al. 2016). From the analysis 31 NSCs in early type galaxies, Turner et al. (2012) conclude that the low-mass galaxies grow NSCs mainly via infall of star clusters through dynamical friction, while for higher mass galaxies gas accretion is likely to dominate, with intermediate-mass galaxies displaying signatures of both formation channels. Georgiev et al. (2016) have come to similar conclusion, suggesting that either mechanism could explain the size of NSCs in late type galaxies.

2.1 THE GALACTIC CENTER

2.1.1 *The supermassive black hole*

The Milky Way is the only known galaxy to hosting a SMBH beyond any reasonable doubt. Early infrared observations already suggested the presence of a compact, dark mass in the GC (e.g. Sanders and Lowinger 1972). However, only later high-spatial-resolution measurements could rule out alternative explanations beside a SMBH, such as a dense star cluster of compact remnants. The definitive evidence in favor of the SMBH hypothesis came from the measurement of the orbit of the so-called S2 star, in Keplerian motion about the central dark mass with a period of only 15 yr (Schödel et al. 2002). The S2 star was later confirmed as the brightest member of a whole star cluster orbiting about the SMBH (see Section 2.1.4.2). From the continuous monitoring of these stars, Gillessen et al. (2017) recently estimated the SMBH mass and distance to be $4.28 \pm 0.10|_{stat} \pm 0.21|_{sys} \times 10^6\,M_\odot$ and $8.32 \pm 0.07|_{stat} \pm 0.14|_{sys}$ kpc.

The SMBH of Milky Way coincides with a compact radio source named Sgr A*, discovered in 1974 by Balick and Brown (1974). More recent observations show that Sgr A* emits an approximately steady flux of $\sim 10^{36}\,erg/s$ in radio to submillimeter band (Falcke et al. 1998; Miyazaki, Tsutsumi, and Tsuboi 2004; Marrone et al. 2006; Yusef-Zadeh et al. 2006a). The radio flux is consistent with synchrotron emission from relativistic electrons.

In addition, Sgr A* coincides with a steady, faint emission in the x-ray, which suggests that the SMBH is in a radiatively inefficient accretion phase (Baganoff et al. 2003; Xu et al. 2006). On top of the steady radio and x-ray emission, there is a variable emission over all the wavelengths, particularly in near-infrared and x-ray (Yusef-Zadeh et al. 2006b; Marrone et al. 2008). The most energetic variable emissions are flares that occur few times per day and can last few hours. The origin of the variable emission is still under debate (see Genzel, Eisenhauer, and Gillessen 2010 for a review).

2.1.2 *The nuclear star cluster*

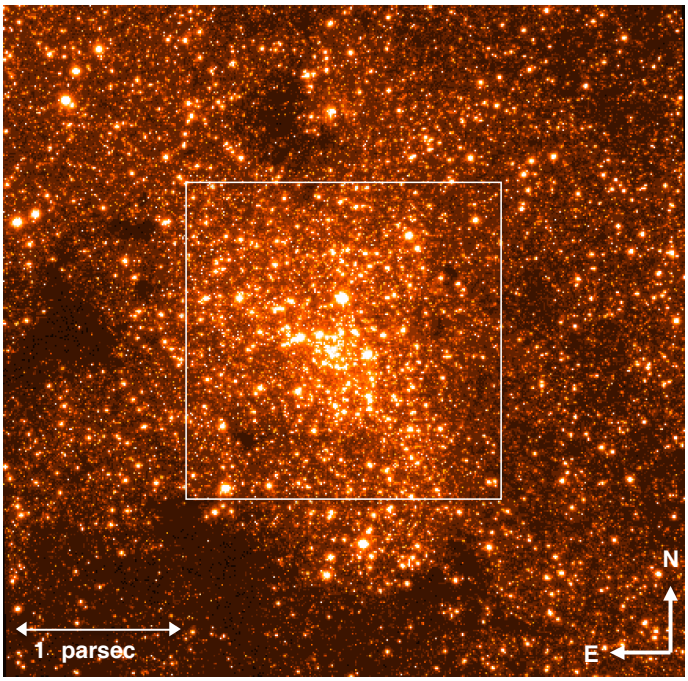

Figure 2.5: Wide-field mosaic of the Galactic NSC using H and K_s-band data obtained with the S27 camera ($0''.027$ pixel scale) of NACO/VLT. The field-of-view is $1'.50 \times 1'.50$. From Fig. 5 of Gallego-Cano et al. (2017).

The NSC of the Milky Way is currently the only NSC in which we can resolve individual stars and study their dynamical properties. However, the GC is not detectable in the visible band due to dust extinction, which also attenuates the infrared fluxes.

In their pioneering near-infrared observation of the GC, Becklin and Neugebauer (1968) detected an extended source of radiation of about $5' - 10'$ ($\approx$12-24 pc at GC distance) size, centered on the radio source Sagittarius A. The source was similar in shape and luminosity to the observed nucleus of M31, suggesting that it was arising from a heavily obscured, unresolved stellar population. Even so, it took 6 more years to rule out other models and recognize that the Galaxy hosted a massive NSC at its center (Oort 1974).

Later on, higher-resolution observations were able to resolve the brightest stars using speckle imaging from ground based facilities (Eckart et al. 1993, 1995; Genzel et al. 1996; Ghez et al. 1998, 2000; Philipp et al. 1999; Mezger et al. 1999; Launhardt, Zylka, and Mezger 2002). The stellar density distribution was found to be isothermal, scaling as $\rho(r) \propto r^{-2}$, with a flat core of radius 0.3-0.5 pc and density $\sim 4 \times 10^7$-$10^8\, M_\odot\, pc^{-3}$ (Genzel et al. 1996). Using data from IRAS and

COBE satellites, Launhardt, Zylka, and Mezger (2002) estimated a total mass of $\sim 3 \times 10^7\,M_\odot$.

However, observation of the central parsec of the NSC were still limited by crowding, due to its extreme stellar density. In particular, was not clear if the NSC had a cusped or cored density profile. A power-law cusp was expected in presence of a SMBH: Fokker-Plank calculation indicated that two-body relaxation would drive stars into an equilibrium configuration, characterized by a power-law $\rho(r) \propto r^{-\gamma}$ density distribution in the gravitational well of the SMBH (Bahcall and Wolf 1976). For a star cluster with equal-mass stars, the expected power-law exponent is $\gamma = 7/4 = 1.75$.

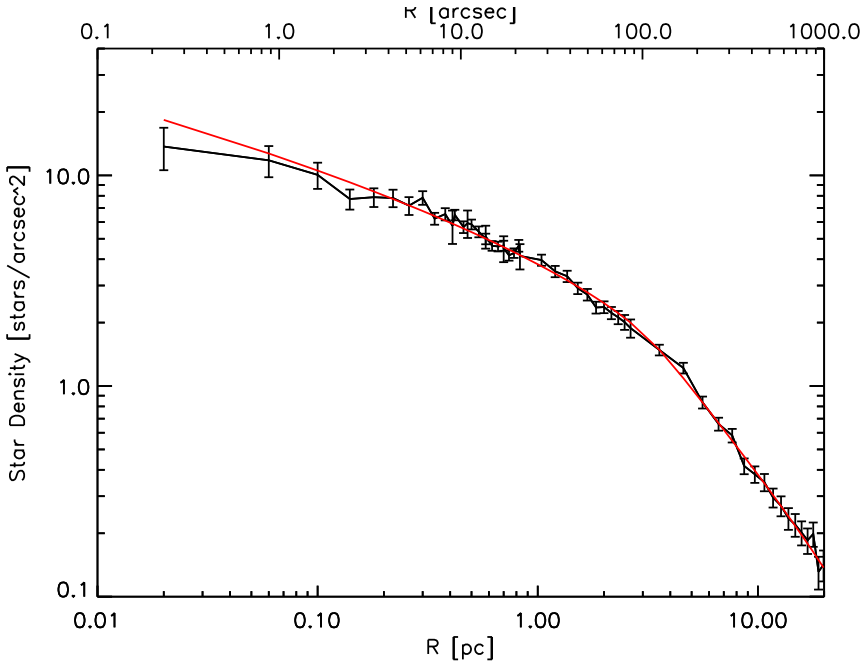

Figure 2.6: Nuker model fit (red line) to the surface density profile of the Galactic NSC for magnitude $17.5 \leqslant K_s \leqslant 18.5$ corrected for the contamination by pre-main sequence stars in the region $0''.8$-$12''.5$. From Fig. 13 of Gallego-Cano et al. (2017).

Only the first adaptive-optics-assisted observations of the NSC revealed the presence of a cusp around Sgr A*. Genzel et al. (2003a) analyzed near-infrared adaptive optics imaging data of the central $1''10''$ from the NACO instrument at ESO/VLT and found that the density distribution was best fitted by a broken power-law

$$\rho(r) = \rho_0 \left(\frac{r}{r_0}\right)^{-\gamma} \tag{2.1}$$

with $\rho_0 = 1.2 \times 10^6\,M_\odot\,pc^{-3}$, $r_0 = 0.4\,pc$ and $\gamma = 1.4 \pm 0.1$ and 2.0 ± 0.1 for $r < r_0$ and $r > r_0$, respectively.

This presence of a cusp is confirmed by more recent observations (Schödel et al. 2007; Graham and Spitler 2009; Schödel, Merritt, and

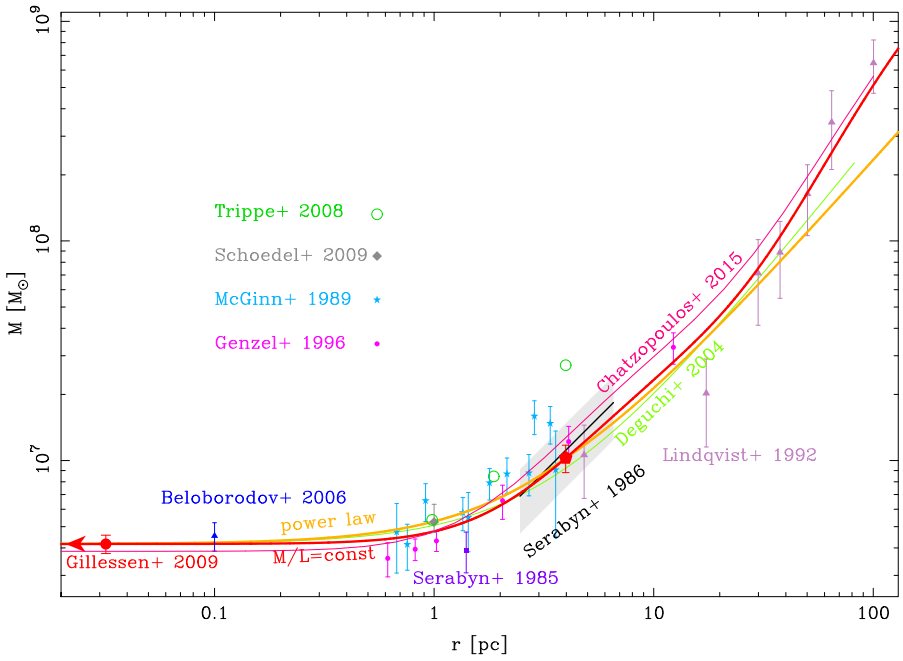

Figure 2.7: Cumulative mass profile of the GC. The main measurement of Fritz et al. (2016) is the red pentagon at 4 pc, through which the profiles for the power-law (red) or constant M/L (yellow) case pass. The value obtained from S-stars orbit is at 0.002 pc (Gillessen et al. 2009a). Other measurements come from S-stars orbit modeling (Beloborodov et al. 2006, blue triangle), Jeans modeling of stellar kinematic data (Genzel et al. 1996; Trippe et al. 2008; Schödel, Merritt, and Eckart 2009, pink dots, open green circles, gray diamond), velocity curves of gas molecular lines (Serabyn and Lacy 1985; Serabyn et al. 1986, violet square, black line with light gray area), Jeans modeling of of integrated spectra (Lindqvist et al. 1992; McGinn et al. 1989; Deguchi et al. 2004, light violet triangles, green stars, light green line). From Fig. 19 of Fritz et al. (2016).

Eckart 2009; Yusef-Zadeh, Bushouse, and Wardle 2012; Schödel et al. 2014; Chatzopoulos et al. 2015; Fritz et al. 2016; Gallego-Cano et al. 2017; Schödel et al. 2017). In the latest work, Gallego-Cano et al. (2017) combined data from VISTA-VV survey and HST Wide Field Camera 3 with new high-angular-resolution images from NACO at VLT (see Figure 2.5). Their best fit for the density profile of the NSC is a 3D Nuker model[3] defined as

$$\rho(r) = \rho_b(r_b) 2^{(\beta-\gamma)/\alpha} \left(\frac{r}{r_b}\right)^{-\gamma} \left[1 + \left(\frac{r}{r_b}\right)^{\alpha}\right]^{(\gamma-\beta)/\alpha} \tag{2.2}$$

with $\alpha = 1$, $r_b = 3.0 \pm 0.4$ pc, $\gamma = 1.29 \pm 0.02$ and $\beta = 2.1 \pm 0.1$. Figure 2.6 shows the Nuker profile fit to the stellar density. It is worth to

3 The Nuker profile is a generalization of the broken power-law introduced by (Lauer et al. 1995). γ and β are the inner and outer power-law exponents, respectively. r_b is the break radius, while α is the sharpness of the transition. Small values of α yield a smooth transition, while for $\alpha \to +\infty$ it reduces to a broken power-law.

note that Gallego-Cano et al. (2017) probe the old (> 1 Gyr), low-mass stellar component, which is expected to be dynamically relaxed. The cumulative mass distribution of the GC, including the contribution from the SMBH and from the bulge is shown in Figure 2.7.

The old stellar component is thought to make up most the mass of the Galactic NSC. Pfuhl et al. (2011) estimate that 80% of the Galactic NSC stellar mass formed > 5 Gyr ago and that star formation continued reaching a minimum 1 Gyr ago, increasing again only in the last 200-300 Myr (see also Blum et al. 2003; Do et al. 2015; Feldmeier et al. 2014; Feldmeier-Krause et al. 2017). Even younger population (~5 Myr old) is present in the inner parsec of the GC.

2.1.3 *The circumnuclear ring*

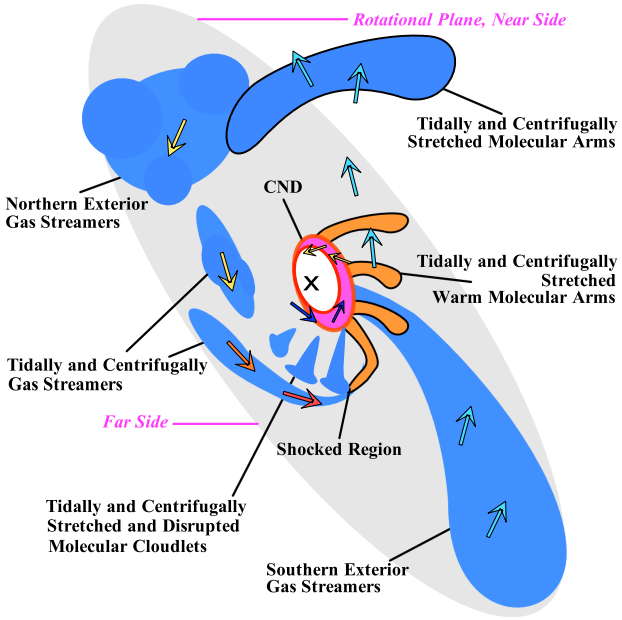

Figure 2.8: Schematic model of the CNR and its streamers. Shapes without heavily outlined boundaries represent gas structures approaching the SMBH; shapes bounded by black lines represent gas structures receding from the SMBH. The magenta shape bounded by red lines represents the hot CNR around the SMBH. Arrows indicate the velocity field. The blue and the orange color of shapes represent cooler and warmer gas temperatures, respectively. From Fig. 7 of (Liu et al. 2012)

Radio observations in the early 1980s indicated the presence of torus of gas and dust in the central parsecs of the GC (Becklin, Gatley, and Werner 1982). Since then, the CNR has been studied extensively in the radio and infrared band (Serabyn et al. 1986; Wright et al. 2001; Christopher et al. 2005; Oka et al. 2011; Liu et al. 2012, 2013; Mills et al. 2013; Smith and Wardle 2014; Harada et al. 2015; Takekawa, Oka, and

Tanaka 2017; Mills, Togi, and Kaufman 2017; Sandqvist et al. 2017; Nguyen et al. 2017).

The CNR has a line of sight inclination of 67° and a sharp inner radius of ~1.5 pc. Its outer edge is more uncertain and depends on the emission lines used to trace it. The CNR is generally considered as composed of a 2 pc torus that extends up 3-4 pc and a 7 pc extension towards negative Galactic longitude (Oka et al. 2011; Takekawa, Oka, and Tanaka 2017). The thickness of the ring increases from ~0.4 pc at the inner edge (Jackson et al. 1993) to ~2 pc in the outer parts (Vollmer and Duschl 2001). Estimates of the CNR mass vary between 10^4 $M_\odot$ from dust thermal emission, and 10^6 $M_\odot$ from molecular gas tracers, although recent works seem to converge on the former value (Etxaluze et al. 2011; Requena-Torres et al. 2012; Mills, Togi, and Kaufman 2017).

The CNR has an asymmetrical, inhomogeneous structure with dense 10^5-10^6 cm^{-3} clumps of 10-10^3 $M_\odot$, and it shows some gaps along the ring. The CNR shows steep velocity gradients because of the rapid (110 $km\,s^{-1}$) rotation about Sgr A*, also due to the presence of several streamers that connect with the CNR (see Figure 2.8).

Whether the CNR is a transient or a long-lived feature is debated. While the densest clumps seems to be marginally above the Roche density limit, the bulk of the material seems highly-turbulent and not self-gravitating (Requena-Torres et al. 2012). On the other hand, the physical properties of the gas are severely uncertain, and it has been suggested that the CNR might be star forming, either now (Yusef-Zadeh et al. 2013, 2015b) or in the future (Oka et al. 2011).

Furthermore, the CNR appears to be in contact with nearby molecular and ionized gas clouds (Oka et al. 2011; Liu et al. 2012; Takekawa, Oka, and Tanaka 2017). Figure 2.8 shows a schematic model of the CNR and the streamers which appear to feed it by infalling from outer radius. In turn, the CNR might be feeding gas towards the central parsec (Liu et al. 2012).

Regardless of its fate, there is strong evidence that the CNR originated from the infall and disruption of a molecular cloud (Wardle and Yusef-Zadeh 2008; Mapelli and Trani 2016). In Chapter 3 I present smoothed particle hydrodynamics simulations of molecular-cloud disruption events. In these simulations, a disrupting molecular cloud forms a ring connected by several external streamers, which eventually settle down and fuel the ring. This picture is similar to what observed in the GC and even in nearby GNs (Müller Sánchez et al. 2009; López-Gonzaga et al. 2014; García-Burillo et al. 2016; Espada et al. 2017). In Chapter 5 I generalize this mechanism to GNs with properties (i.e. SMBH and NSC masses) different from those of the CNR.

2.1.4 *The young stars*

Early spectroscopic and photometric observations suggested the presence of young stars among the old stars in the central parsec of the GC (Treffers et al. 1976; Storey and Allen 1983; Rieke, Rieke, and Paul 1989; Allen, Hyland, and Hillier 1990). Hundreds of these stars have been now identified as Wolf-Rayet and O/B stars (Genzel et al. 2003a; Krabbe et al. 1991, 1995; Blum, Sellgren, and Depoy 1995; Blum, Depoy, and Sellgren 1995; Ghez et al. 2003; Schödel et al. 2003; Eisenhauer et al. 2005; Paumard et al. 2006a; Bartko et al. 2009; Do et al. 2013; Feldmeier-Krause et al. 2015). The Wolf-Rayet stars dominate the far infrared luminosity of the central parsec, generate an intense background of ultraviolet radiation and are expected to be losing 10^{-5}-$10^{-4}\,M_{\odot}\,yr^{-1}$ due to heavy winds.

Orbital parameters for about ~150 stars are known from proper motion and radial velocity measurements in the near-infrared band. This has allowed to identify two kinematically distinct ensembles of stars: the CW disk and the S-Star cluster.

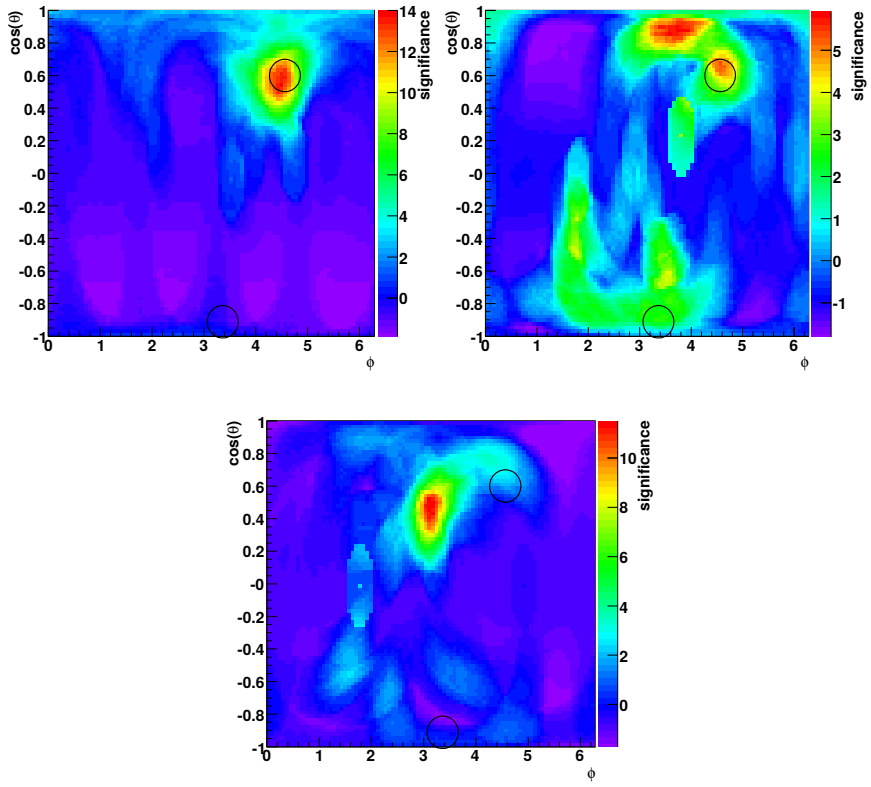

Figure 2.9: Cylindrical equal area projections of the distributions of significance for three radial bins: 32 stars with projected distances in the bin 0.032 pc-0.14 pc (0″.8-3″.5, upper left panel), 30 stars in the bin 0.14 pc-0.28 pc (3″.5-7″, upper right panel) and 28 stars in the bin 0.28 pc-0.48 pc (7″-12″, lower panel). From Fig. 11 of Bartko et al. (2009).

2.1.4.1 *The clockwise disk*

A fraction of the young stars lie in a near-Keplerian disk, called CW disk from the motion that it shows when projected on the plane of the sky (Genzel et al. 2003b; Levin and Beloborodov 2003; Paumard et al. 2006a,b; Lu et al. 2009; Bartko et al. 2009; Yelda et al. 2014). The disk is mostly composed of Wolf-Rayet/O-stars, whose spectral features constrain the age of the disk to 4-8 Myr. The disk extends down to 0.03 pc from Sgr A*. The exact properties of the disk, such as the number of disk stars and the radius of the outer edge, are subject of debate.

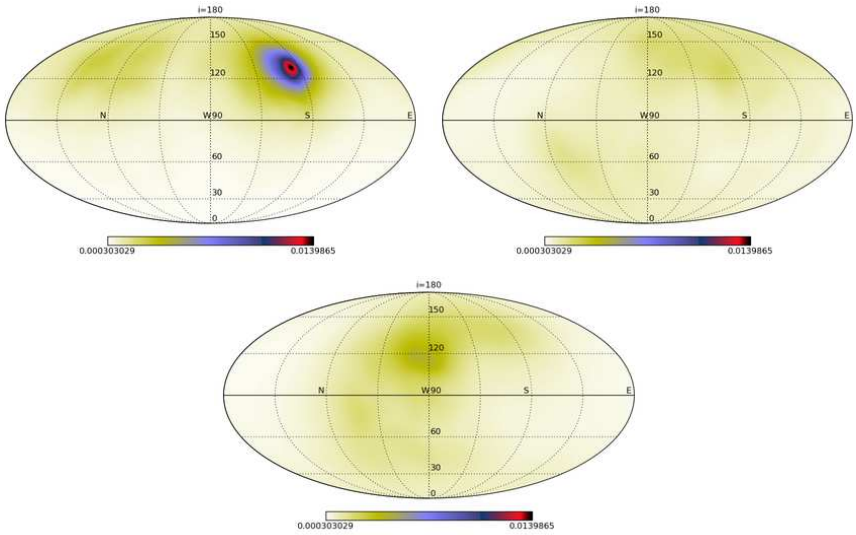

Figure 2.10: Density of angular momentum vectors for stars in the three separate radial bins: 0.032 pc-0.128 pc (0″.8-3″2, upper left panel), 0.128 pc-0.26 pc (3″.2-6″.5, upper right panel), and 0.26 pc-0.532 pc (6″.5-13″.3, upper right panel). From Fig. 14 of Yelda et al. (2014).

Bartko et al. (2009) analyzed the orbit of 90 Wolf-Rayet/O stars between projected radii of $0.032\,\mathrm{pc} - 0.48\,\mathrm{pc}$ from Sgr A*, using the adaptive-optics-assisted near-infrared imager NACO and the integral field spectrograph SINFONI on the ESO/VLT. Bartko et al. (2009) suggest that 55% of the young stars belong to the disk, which would extend up to 0.5 pc and is warped or tilted, since the orientation of its normal axis changes by 60° from the inner edge to the outer edge. In addition, Bartko et al. (2009) find that the CW disk is mildly eccentric, with a mean eccentricity of $e = 0.36 \pm 0.06$. However, Bartko et al. (2009) suggest that 20% of the stars are part of a second, counterclockwise disk, which is almost ortogonal to the CW disk.

Figure 2.9 shows the significance map of sky distributions for three radial intervals in projected distance to Sgr A*, computed from the sky map of the density of reconstructed angular momentum direc-

tions of the observed stars[4]. The excess density at $(\phi, \theta) = (256°, 54°), (262°, 48°)$ and $(179°, 62°)$ corresponds to the CW disk in the inner, middle and outer radial bin, respectively. The disk gets warped with increasing radius. Not only, the middle radial bin shows an counterclockwise excess density, interpreted as a second disk with opposite angular momentum with respect to the CW disk.

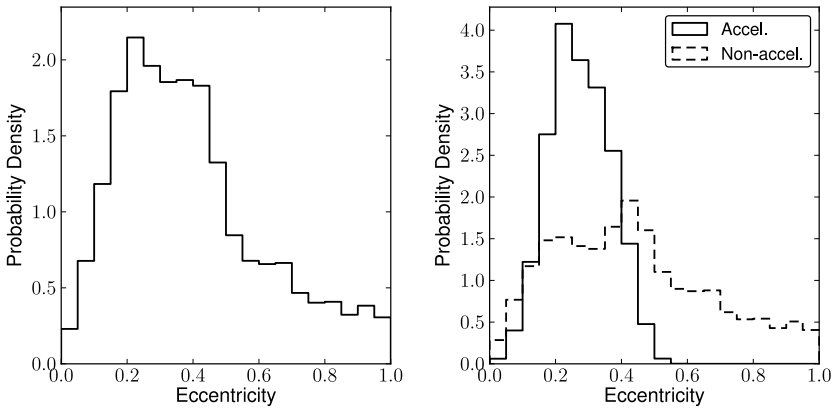

Figure 2.11: Left panel: eccentricity distribution of the CW disk. Only stars within the full width at half-maximum of the density of angular momentum vector distribution (e.g. Figure 2.10) are included, thereby weighting the distributions by disk membership probability. Right panel: eccentricity distributions shown separately for likely disk members with acceleration detections (solid) and without (dashed). From Fig. 12 of Yelda et al. (2014).

Although the presence of a secondary, counterclockwise disk has been long speculated (Genzel et al. 2003b; Paumard et al. 2006a; Bartko et al. 2009), more recent observations by Yelda et al. (2014) find no evince of a second disk. Yelda et al. (2014) analyzed the orbit of 116 stars between projected radii 0.032 pc–0.52 pc, using the integral field spectrograph OSIRIS and the Near Infrared Camera on Keck telescopes. Yelda et al. (2014) find that the CW disk extends only up to 0.13 pc and it is neither significantly warped nor tilted.

Figure 2.10 shows the significance map of angular momentum directions, using a similar method to that used by Bartko et al. (2009). The clockwise disk feature at (i,Ω) = (130°, 96°) is prominent in the inner radial bin and shows a decrease in density with radius. No counterclockwise feature is present in any of the radial bins. Moreover, Yelda et al. (2014) estimate that only ~ 20% of the O and Wolf-Rayet stars lie in the CW disk, suggesting that the CW disk is the remnant of a past, larger disk. They also confirm that the CW disk has

4 Computed as $\rho_{sig}(\Phi, \theta) = (\rho(\Phi, \theta) - \langle \rho_{iso} \rangle) / \langle \rho_{iso}^2 \rangle^{1/2}$, where $\rho(\Phi, \theta)$ is the density of angular momentum directions, while $\langle \rho_{iso} \rangle$ and $\langle \rho_{iso}^2 \rangle^{1/2}$ are the mean and root-mean-square angular momentum density of stars with isotropic distribution, respectively.

a unimodal eccentricity distribution (see Figure 2.11), with a mean eccentricity of $e = 0.27 \pm 0.07$.

There has been little agreement on the mass function of the disk stars, although it is likely top-heavy. Using new data from SINFONI observations, Bartko et al. (2010) find that the stellar mass function is extremely top-heavy with a best-fit power law of $dN/dm \propto m^{-0.45\pm0.3}$. However, using a Bayesian parameter estimation method on OSIRIS data, Lu et al. (2013) find a flatter power-law of $dN/dm \propto m^{-1.7\pm0.2}$. Assuming this mass function, Lu et al. (2013) estimate the total mass of the disk to be $1.4 \times 10^4\,M_\odot - 3.7 \times 10^4\,M_\odot$ above $1\,M_\odot$. Using the same approach of Lu et al. (2013), Do et al. (2013) estimate the disk surface-density profile as $\Sigma(r) \propto r^{-0.93\pm0.09}$. It is important to note that current spectroscopic studies are limited down to $\sim 10\,M_\odot$, and better sensitivity (down to $1\,M_\odot$) is necessary to completely compare the Galactic center mass function with local star-forming regions (Do et al. 2013).

	IRS 16SW	IRS 16NE	IRS E60
a [$R_\odot$]	70.7 ± 2.3	$2575 \pm 105^\dagger$	22.6 ± 3
e	0.088 ± 0.023	0.32 ± 0.01	≈ 0
i	$70°$	$-^\ddagger$	$70° \pm 10°$
P [d]	19.45	224.09 ± 0.09	2.276
M_{tot}	[$M_\odot$]	100	~ 100
q	1	$-^\ddagger$	30 ± 10
Notes	Contact binary	–	Contact binary

Table 2.1: Physical and orbital properties of the three known binaries in the CW disk. a: binary semimajor axis in $R_\odot$; e: eccentricity; i: line-of-sight inclination; P: orbital period in days; M_{tot}: binary total mass in $M_\odot$; q: primary-to-secondary mass ratio.
†: projected separation $a \sin i$
‡: inclination and mass ratio not known

Finally, long-term spectroscopic and photometric surveys of CW disk stars reveled the presence of binaries. To date, three members of the CW disk are confirmed binaries, and few other binary candidates exist (Pfuhl et al. 2014). Table 2.1 shows the main properties of the confirmed binaries in the CW disk. (Pfuhl et al. 2014) estimate a spectroscopic binary fraction in the GC of $f_{SB} = 0.30^{+0.34}_{-0.21}$, broadly consistent with the massive binary fraction observed in dense young clusters.

2.1.4.2 *The S-star cluster*

The ensemble of stars in the inner ~ 0.04 pc ($1''$) of the GC is called the S-star cluster (Schödel et al. 2002, 2003; Ghez et al. 2003; Genzel et al.

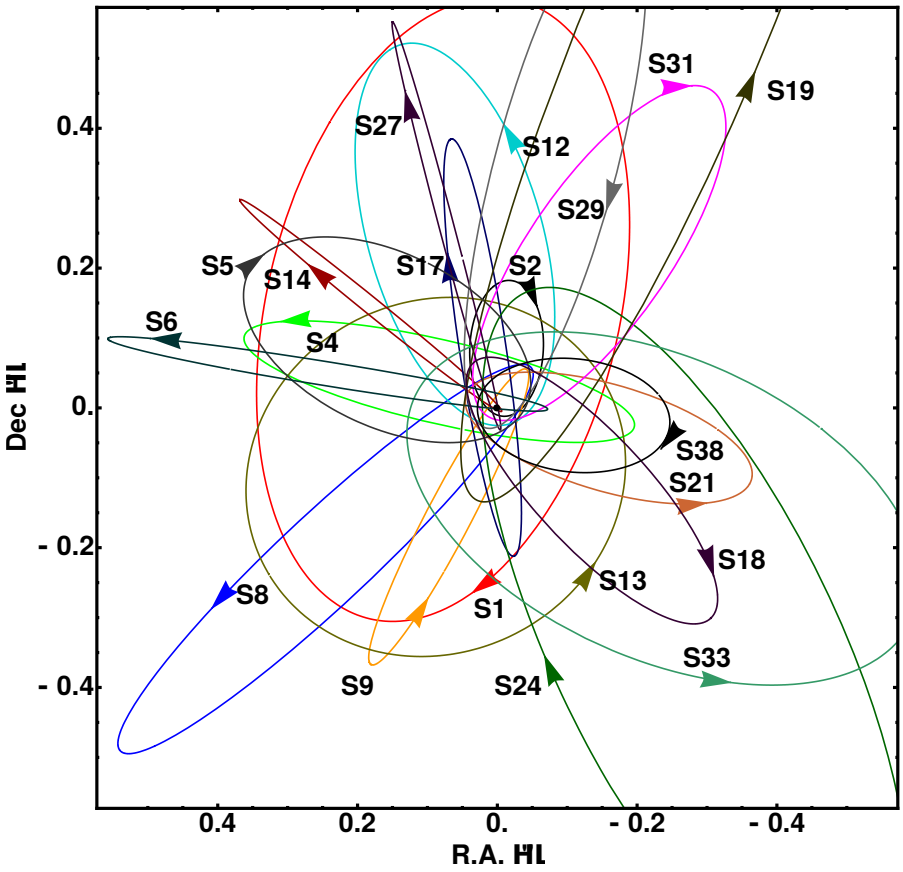

Figure 2.12: The stellar orbits of 27 S-stars in the central arcsecond. In this illustrative figure, the coordinate system was chosen such that Sgr A* is at rest. From Fig. 16 of Gillessen et al. (2009a).

2003b; Eisenhauer et al. 2005; Gillessen et al. 2009a; Boehle et al. 2016; Gillessen et al. 2017). The latest analysis of near-infrared observations by Gillessen et al. (2017) indicates that the S-star cluster is composed of at least 32 stars. The spectral features of the S-stars reveal that 22 are B-type, 8 are late-type, while the spectral type is unknown for the remaining 2. The orbits of the S-stars is known with accuracy and provide the strongest constrain to the mass and distance of the central SMBH (Gillessen et al. 2009a).

Figure 2.12 shows a reconstruction of the orbits of 27 S-stars, in the rest frame of the SMBH. Contrary to the stars of the CW disk, the orbits of the S-stars are highly eccentric and randomly oriented. Figure 2.13 shows the angular momentum directions of the 32 S-stars plus 8 stars identified as members of the CW disk. Note that late-type star S111 has actually an hyperbolic orbit, i.e. it is unbound with respect to the SMBH. The eccentricity of both early and late type stars follows a thermal distribution $n(e) \propto e$, shown in Figure 2.14.

The brightest member of the cluster, named S2, is monitored since 1992 at the ESO New Technology Telescope (Schödel et al. 2002; Gillessen et al. 2009b). Multi-epoch spectra analysis of S2 suggests it is a main-

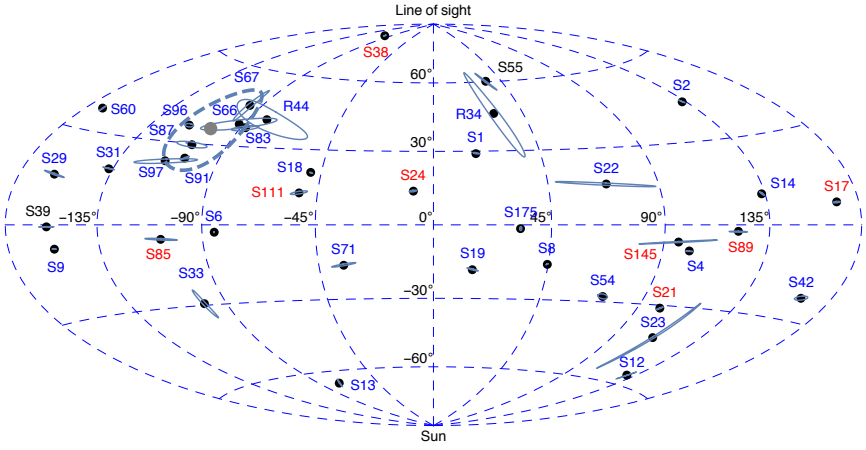

Figure 2.13: Angular momentum directions of those 32 S-stars and 8 stars of the CW disk. The vertical dimension corresponds to the inclination i of the orbit and the horizontal dimension to the longitude of the ascending node Ω. A star in a face-on, clockwise orbit relative to the line of sight would be located at the top of the graph, while a star with an edge-on seen orbit would be located on the equator of the plot. The error ellipses correspond to the statistical 1-σ fit errors. The stars S66, S67, S83, S87, S91, S96, S97 and R44 are members of the CW disk (Bartko et al. 2009; Yelda et al. 2014) at ($\Omega = 104°$, $i = 126°$) marked by the thick grey dot and the dashed line, indicating a disk thickness of 16°. The orbits of the other stars are oriented randomly. The color of the labels indicates the stellar type (blue for early-type stars, red for late-type stars). From Fig. 12 of Gillessen et al. (2017).

sequence dwarf B0-2.5 V star with a zero age main-sequence mass of $19.5\,M_\odot$ (Martins et al. 2008a). The age of the S-stars is poorly constrained, ranging from 6 Myr to 400 Myr, compatible with main sequence B-type stars lifetimes (Eisenhauer et al. 2005).

2.1.4.3 *The paradox of youth*

The origin of the young stars is puzzling: the tidal shear from the SMBH disrupts nearby self-gravitating body with a density lower than the Roche number density

$$n_{RL} = \frac{3\,r^{-3}}{2\pi m_\mu} M_{SMBH} \tag{2.3}$$

where M_{SMBH} is the SMBH mass and r is the distance from the SMBH. For $M_{SMBH} = 4.3 \times 10^6\,M_\odot$ and $r = 0.1$-$1\,pc$ Equation 2.3 yields a Roche density of 10^8-$10^{12}\,cm^{-3}$, which is much higher than the typical molecular cloud density of 10^2-$10^4\,cm^{-3}$. Consequently, the SMBH of the GC is expected to disrupt any nearby molecular clouds, preventing star formation.

One mechanism to explain the presence of young stars in the inner parsec of the GC is stellar migration, in which stars are born at far-

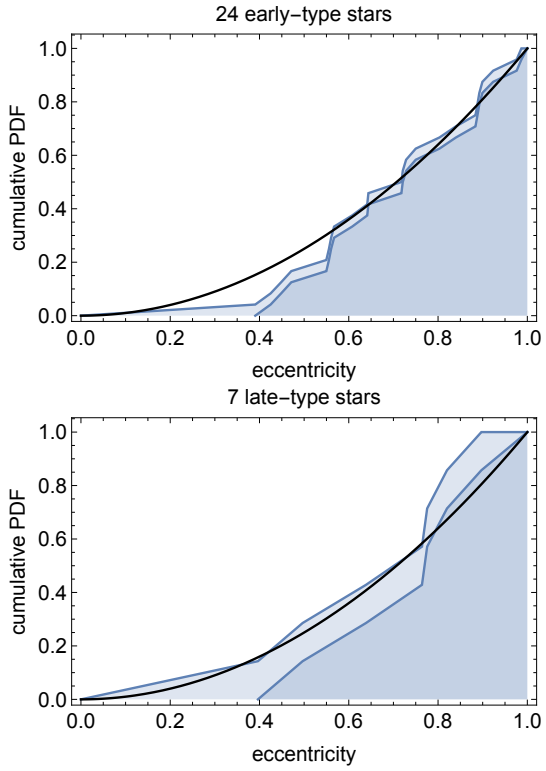

Figure 2.14: Cumulative probability density function for the eccentricities of the stars for 30 S-stars. Left: The sample of 22 early-type stars, after exclusion of the eight stars which are identified as members of the CW disk. The two curves correspond to the two ways to plot a cumulative pdf, with values ranging either from 0 to $(N-1)/N$ or from $1/N$ to 1. The distribution is compatible with $n(e) \propto e$ (black line). Right: The same for the 8 late-type stars, excluding S111 which has a hyperbolic orbit, i.e. $e > 1$. From Fig. 13 of Gillessen et al. (2017).

ther radius and quickly move to the center. However, all the proposed migration scenarios have difficulties in reproducing a fast-enough migration, consistent with the age of the young stars (see Mapelli and Gualandris 2016, for a recent review).

Although the tidal forces of the SMBH prevent the gravitational collapse of molecular clouds, star formation can still occur in a gaseous disk around the SMBH. Indeed, Toomre (1964) showed that a rotating disc of density ρ is gravitationally unstable when the Q parameter

$$Q = \frac{\Omega^2}{2\pi G\rho} \tag{2.4}$$

is smaller than ≈ 1, where Ω is the disk angular velocity. If $Q \ll 1$, a self-gravitating disk of gas is subject to fragmentation and begins to collapse. This star formation mechanism has been investigated extensively in the context of the fragmentation of accretion disks in active galactic nuclei (Poliachenko and Shukhman 1977; Kolykhalov and Syunyaev 1980; Shlosman and Begelman 1987; Sanders 1998; Collin

and Zahn 1999; Gammie 2001; Levin and Beloborodov 2003; Goodman 2003; Milosavljević 2004; Nayakshin and Cuadra 2005; Nayakshin, Cuadra, and Springel 2007; Collin and Zahn 2008).

Several works have proposed that the CW disk originated from the disruption of a molecular cloud, which settled in a disk around Sgr A*, fragmented and formed stars (Bonnell and Rice 2008; Mapelli et al. 2008; Hobbs and Nayakshin 2009; Alig et al. 2011; Mapelli et al. 2012; Lucas et al. 2013). Figure 2.15 shows the density map from an hydrodynamical simulation of an infalling molecular cloud forming a stellar disk around a SMBH. The simulation will be presented in Chapter 5.

This scenario can reproduce the observational features of the CW disk, but it fails to explain the majority (~80%) of the young stars, which do not lie in the disk. One possible explanation is that the CW disk is the remnant of a more extended and massive disk which got partially disrupted after its formation. In this case, precession effects must have acted on the disk after its formation, dismembering it in less then 3-5 Myr.

The CNR is often invoked as the source of such precession effects (Šubr, Schovancová, and Kroupa 2009; Haas, Šubr, and Kroupa 2011; Haas, Šubr, and Vokrouhlický 2011). The CNR might induce precession on the orbital elements of disk stars, randomizing the orbits and eventually disrupting the disk. The effect of an axisymmetric perturbing potential on a Keplerian orbit is well known, and can be analyzed in the framework of so-called Kozai-Lidov mechanism, which has many applications in orbital dynamics (Kozai 1962; Lidov 1962).

The characteristic timescale for the Kozai-Lidov mechanism is

$$T_{KL} = T \frac{M_{SMBH}}{M_{CNR}} \left(\frac{R_{CNR}}{a}\right)^3 \sqrt{1-e^2} \tag{2.5}$$

where a is the semimajor axis of a perturbed star, M_{CNR} and R_{CNR} are the mass and radius of the CNR, M_{SMBH} is the SMBH mass and T is the star orbital period. The orbit-averaged equations for the evolution of the orbital elements of a star are then (Šubr, Schovancová, and Kroupa 2009)

$$T_{KL}\frac{de}{dt} = \frac{15}{8} e\,(1-e^2)\,\sin 2\omega\,\sin^2 i \tag{2.6}$$

$$T_{KL}\frac{di}{dt} = \frac{15}{8} e^2\,\sin 2\omega\,\sin i\,\cos i \tag{2.7}$$

$$T_{KL}\frac{d\omega}{dt} = \frac{3}{4}\left[2-2e^2+5\sin^2\omega\,\left(e^2-\sin^2 i\right)\right] \tag{2.8}$$

$$T_{KL}\frac{d\Omega}{dt} = -\frac{3}{4}\cos i\,\left(1+4e^2-5e^2\cos^2\omega\right) \tag{2.9}$$

where e is the star eccentricity, ω its argument of pericenter, i is the stellar orbit inclination with respect to the plane of the CNR. A characteristic of the Kozai-Lidov mechanism are periodic oscillations in

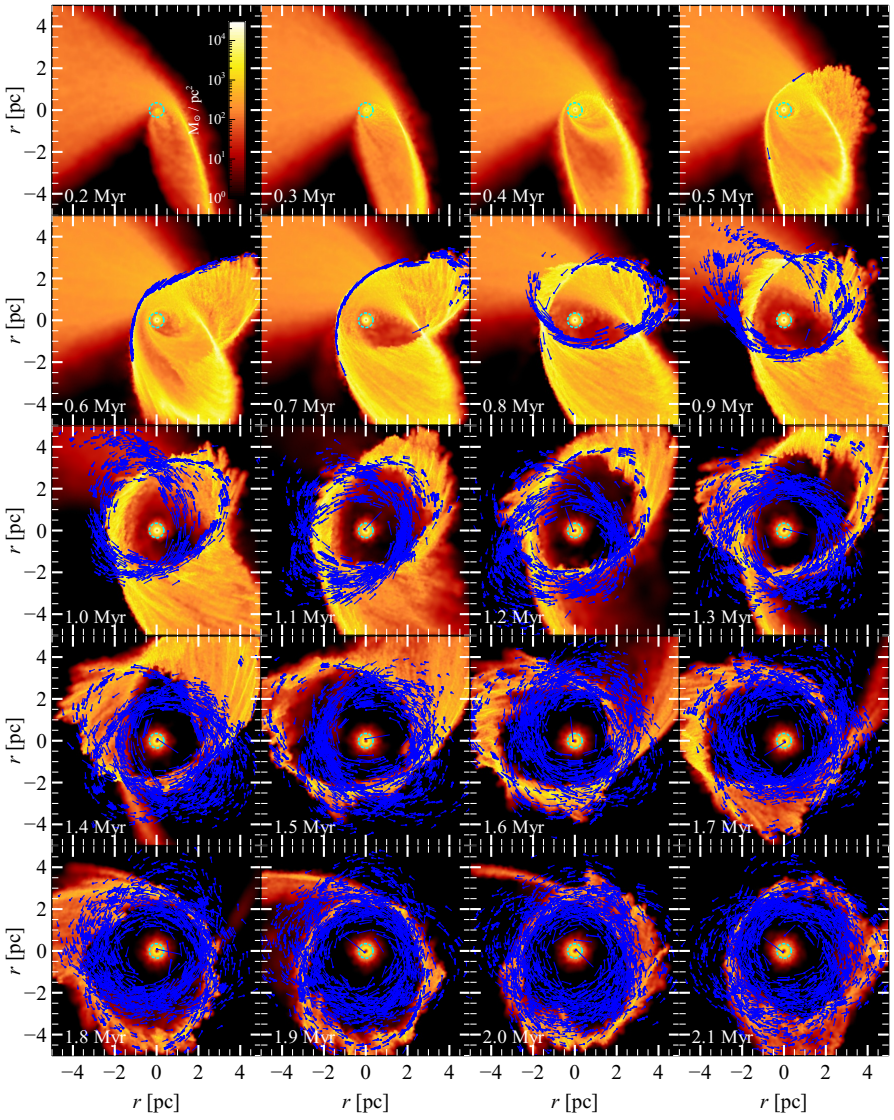

Figure 2.15: Color-coded, density map of gas in as a function of time in a simulation of molecular cloud disruption. From top to bottom, and left to right, the time of the simulation increases by 0.1 Myr in each snapshot. The first snapshot on the top left is taken at 0.2 Myr from the beginning of the simulation. The dotted cyan circle indicates the SMBH radius of influence. The cloud is disrupted by the central potential composed of a SMBH and a NSC, and it settles into a disk. The disk is dense enough to form stars (blue pluses). The blue lines represent the stellar velocity vectors. More details about the simulation can be found in Chapter 5.

inclination and eccentricity, which are a consequence of the conservation of the z-component of the angular momentum $L_z = \sqrt{1-e^2}\cos i$. Note that the Kozai-Lidov mechanism also conserves the energy and consequently the semi-major axis.

In addition, the CW disk is embedded in the cusp of the NSC, which adds another perturbation on the Keplerian motion of the stars. The effect of an extended, spherical distribution of mass is to induce precession of the argument of pericenter ω on the timescale (Merritt et al. 2011)

$$T_{mass} = T\,\frac{M_{SMBH}}{M_{cusp}(<a)}\,\frac{1-\sqrt{1-e^2}}{\sqrt{1-e^2}} \tag{2.10}$$

where $M_{cusp}(<a)$ is the cusp mass enclosed by the star orbit. This kind of precession is also called mass precession and it is prograde, i.e. the pericenter advances along the orbit.

Since T_{KL} is larger than T_{mass} in the case of the CW, ω will precess much faster than in the simple Kozai-Lidov mechanism. This also means that Equations 2.6–2.9 can be averaged over ω, resulting in the cancellation of all right-hand terms except for the $d\Omega dt$ one:

$$T_{KL}\frac{d\Omega}{dt} = -\frac{3}{4}\left(1+\frac{3}{2}e^2\right)\cos i \tag{2.11}$$

In other words, the spherical cusp is expected to damp all Kozai-Lidov oscillations in e and i, leaving only the precession of the longitude of the ascending node Ω.

Another process that can alter the stellar orbits is two body relaxation driven by the mutual gravitational interactions of disk stars. The effect of two body relaxation is to diffuse the orbital energy of stars and randomize the orbits. The two-body relaxation timescale for a stellar cluster is (Spitzer 1987)

$$T_{two-body} = \frac{\langle v^2\rangle^{3/2}}{15.4G^2\langle m\rangle\rho\ln\Lambda} \tag{2.12}$$

where $\langle m\rangle$ is the mean stellar mass, $\langle v^2\rangle$ is the stellar velocity dispersion, ρ is the stellar density, and $\ln\Lambda$ is a numerical coefficient named Coulomb logarithm. The high stellar velocity dispersion due to the SMBH leads to $T_{two-body} \gtrsim 1\,Gyr$ in the case of the CW disk. For this reason, two-body relaxation in the GC has been considered not efficient and it is usually neglected. Only recently, Šubr and Haas (2014) noted that Equation 2.12 is derived from the assumptions of spherical symmetry and random orbital motions, which do not hold for a thin Keplerian disk such as the CW disk. Particularly, if the orbits are coherently oriented in a disk, the local density is enhanced with respect to a random orbital distribution, and the relative velocity between stars is much smaller then their orbital velocity. Šubr and

Haas (2014) find that two-body relaxation can alter eccentricity, inclination and semimajor axis of the stellar orbits on a timescale of few million years and thus can play an important role in the evolution of the CW disk.

While these dynamical process are well studied analytically, their combined effects are still unexplored from the numerical perspective. Previous studies have either assumed a simplified (point-mass) model for the CNR (Haas, Šubr, and Kroupa 2011) or have used low order integrator to follow the evolution of the stellar disk (Mapelli, Gualandris, and Hayfield 2013). In fact, a self-consistent modeling of the CNR requires the employment of hydrodynamic codes which lack the accuracy to proper model orbital dynamics around a SMBH. On the other hand, direct N-body codes can follow the stellar orbits with great accuracy, but lack the hydrodynamical treatment of gas. I have overcome these numerical limits by employing the AMUSE code to combine into the same simulation direct N-body and hydrodynamical codes. In Chapter 4, I present my simulations and discuss the role of the CNR in the evolution of the CW disk.

2.1.5 *Cloud G2*

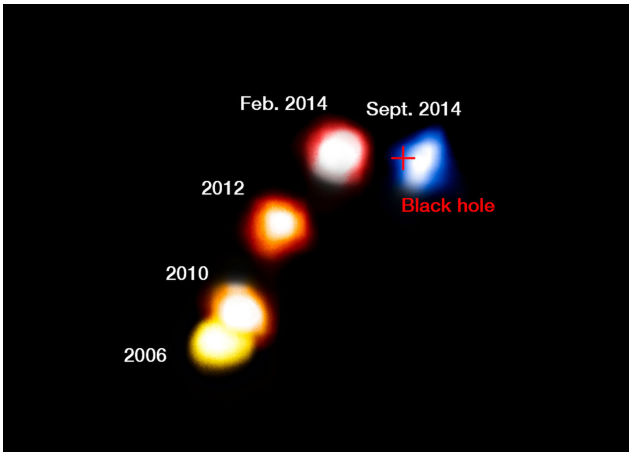

Figure 2.16: This annotated composite image shows the motion of the dusty cloud G2 as it closes in, and then passes, the SMBH at the center of the Milky Way, and remains compact. The blobs have been colorized to show the motion of the cloud, red indicated that the object is receding and blue approaching. The cross marks the position of the supermassive black hole. Credit: ESO/Andreas Eckart

In 2011, Gillessen et al. (2012) discovered a mysterious object approaching Sgr A* on an extremely radial orbit. Named G2 cloud, this object is visible in the L' band and in a few recombination lines (particularly Brγ), but does not show any K-band counterpart, unlike all other stars in the region. The L' continuum emission has total mag-

nitude of ~13.8 and suggests a remarkably low dust temperature of 550 K. The Brγ emission has a luminosity of $\sim 10^{-3} L_{\odot}$ and seems to come from a more extended region than the L' emission. In addition, a tail of gas with lower surface brightness follows G2 on approximately the same orbit, and it appears to be connected to the leading over a large range in position and radial velocity in Brγ. The absence of any K-band emission initially suggested that G2 was a dusty, gas cloud ionized by the UV radiation of nearby massive stars.

	a [pc]	e	i	Ω	ω
G2	0.0384 ± 0.0028	0.983 ± 0.002	$123 \pm 1°$	$65 \pm 3°$	$92 \pm 2°$
G1	0.0144 ± 0.0064	0.860 ± 0.050	$108 \pm 2°$	$69 \pm 5°$	$109 \pm 8°$

Table 2.2: Orbital parameters of G2 and G1. a: semimajor axis in pc; e: eccentricity; i: inclination; Ω: longitude of the ascending node; ω: argument of pericenter.

At the moment of discovery, the G2 cloud was approaching its pericenter at 133 AU from the Sgr A*, equivalent to 1560 Schwarzschild radii of the SMBH (Gillessen et al. 2013a,b; Phifer et al. 2013; Witzel et al. 2014; Plewa et al. 2017). Owing to this, the cloud was expected to be increasingly tidally disrupted, resulting in an enhancement of its L' luminosity and even giving rise to X-ray flares. However, in early 2014 the G2 cloud passed quietly its pericenter and began moving away from Sgr A* with no apparent sign of disruption. In fact, the L' and Brγ luminosity remained constant within uncertainties throughout pre- and post-pericenter-passage evolution (Plewa et al. 2017). This unexpected turn of events raised the debate whether G2 hides a compact source (e.g. a star) that allowed it to survive the tidal shear of the SMBH (Valencia-S. et al. 2015; Shahzamanian et al. 2016; Zajaček et al. 2017; Plewa et al. 2017). Nonetheless, current observational data are compatible with both a compact source enshrouded in dust and a coreless gas cloud. Further observations are required to disentangle between the two models.

Even thought the nature of G2 remains unclear, its orbit is well constrained by observations. Figure 2.16 shows a composite image of the G2 cloud at different epochs, from its earliest detection traced back in 2004 archival images to 2014 observations after its pericenter passage. Latest measurements estimate G2 semimajor axis and eccentricity to $a = 0.042 \pm 0.01$ pc and $e = 0.98 \pm 0.007$, respectively (Pfuhl et al. 2015). Moreover, G2 orbit has an inclination and longitude of ascending node of $(i, \Omega) = (123 \pm 1°, 65 \pm 3°)$, almost coplanar to the CW disk ($i, \Omega = 129 \pm 18°, 98 \pm 18°$).

Pfuhl et al. (2015) reported the existence of another object, named cloud G1, in orbit about Sgr A*. The G1 object, which was first observed by Clénet et al. (2005) and Ghez et al. (2005), shows L' emission but no K-band counterpart much like G2. G1 already passed its pericenter, and its orbit is narrower but less eccentric than the orbit of G2. All the orbital parameters of G1 and G2 are given in Table 2.2. The two orbits are aligned to within $\sim 20°$, and have a similar argument of pericenter. It has been thus speculated that the two objects might share a common origin. In this hypothesis, G1 would be older than G2, so that it is already undergoing tidal circularization (McCourt and Madigan 2016; Madigan, McCourt, and O'Leary 2017).

Countless theories have been proposed to explain the origin of G2: a gas cloud formed by colliding stellar winds (Burkert et al. 2012; Schartmann et al. 2012; Gillessen et al. 2013a; De Colle et al. 2014; Shcherbakov 2014; Calderón et al. 2016) or tidally stripped material (Guillochon et al. 2014), the merger product of a binary (Prodan, Antonini, and Perets 2015), a low-mass star obscured by dust (Ballone et al. 2013; Scott, Graham, and Schombert 2013; Witzel et al. 2014), a star disrupted by a stellar black hole (Miralda-Escudé 2012), and a nova outburst (Meyer and Meyer-Hofmeister 2012).

Although there is not yet direct evidence of planets in the GC (but see Yusef-Zadeh et al. 2015a, 2017 for the observation of protoplanetary disk candidates in the inner 0.1 pc), a protoplanetary origin for the G2 object has been considered by Murray-Clay and Loeb (2012) and Mapelli and Ripamonti (2015). In particular, Mapelli and Ripamonti (2015) demonstrate that a photoevaporating protoplanetary embryo undergoing tidal disruption would have a Brγ luminosity that could match the one of G2. In this hypothesis, the protoplanet could have been stripped from its parent star by the tidal field of the SMBH and brought into a very eccentric orbit. Candidate parent stars can be either in the CW disk (also suggested by the similar orientation of the CW disk and G2), or in the S-star clusters.

This scenario requires that the planet initially bound to a stars is captured by the SMBH and becomes a starless planet. In addition, its orbit about the SMBH must be highly eccentric to match the orbits of G2 and G1. However, few studies have investigated in detail the dynamics of planets in the presence of SMBHs, and none focused on the tidal stripping of planetary systems. For this reason, I investigated the evolution of planets bound to the stars in the CW disk and in the S-stars, by means of high-accuracy, regularized N-body simulations.

I found that starless planets that were initially bound to CW disk stars have mild eccentricities and tend to remain in the CW disk. In contrast, planets initially bound to S-stars are captured by the SMBH on highly eccentric orbits, matching the orbital properties of the G1 and G2 clouds. Moreover, I developed a simple analytic model to pre-

dict the semi-major axis of the planetary orbit after they get captured by the SMBH. In Chapter 6 I present and discuss all my results.

3

MODELING THE FORMATION OF THE CIRCUMNUCLEAR RING IN THE GALACTIC CENTER

3.1 INTRODUCTION

The work presented in this Chapter aims at modeling the formation of the CNR, the dusty gaseous torus that has been observed orbiting in the GC at about 2 pc from Sgr A* (see Section 2.1.3). I simulate the tidal disruption of molecular clouds by strong tidal field in the GC, which arises from the Milky Way's SMBH and NSC (see Section 2.1.1 and 2.1.2). I show that this process can lead to the formation of a clumpy gas ring orbiting the SMBH, whose properties match the CNR in the GC.

In Section 3.2 I describe the numerical techniques and the initial setup of the simulations. In Section 3.3 I present my results, with particular attention for the properties (mass, velocity, radius, inclination) of the rings and for their connection with the orbital properties of the parent molecular cloud. In Section 3.4 I discuss the main implications of these results, while in Section 3.5 I summarize my conclusions.

This Chapter is based on Mapelli and Trani (2016).

3.2 METHODS

For my simulations, I used the N-body/SPH code GASOLINE (Wadsley, Stadel, and Quinn 2004), upgraded with the Read, Hayfield, and Agertz (2010) optimized SPH (OSPH) modifications, to address the SPH limitations outlined, most recently, by Agertz et al. (2007).

Table 3.1 shows a summary of the runs that will be presented in this paper. In all runs, the SMBH is modelled as a sink particle, with initial mass $M_{SMBH} = 3.5 \times 10^6$ $M_\odot$ (Ghez et al. 2003), sink radius $r_{acc} = 5 \times 10^{-3}$ pc and softening radius $\epsilon = 1 \times 10^{-3}$ pc. The SMBH particle is not allowed to move in my simulation, to prevent spurious kicks due to numerical resolution. I add a rigid potential, to account for the stellar cusp surrounding Sgr A* and for the Galactic bulge. The overall density profile of the stellar cusp goes as $\rho(r) = 2.8 \times 10^6\, M_\odot\, pc^{-3}\, (r/0.22\ pc)^{-\gamma}$, where $\gamma = 1.2$ (1.75) for $r < 0.22$ pc ($r > 0.22$ pc), consistent with the values reported in Schödel et al. (2007). The bulge potential is modelled as an Hernquist spheroid (Hernquist 1990) with density $\rho(r) = M_b\, a/[2\pi r\, (r+a)^3]$, where $M_b = 2.9 \times 10^{10} M_\odot$ and $a = 0.7$ kpc.

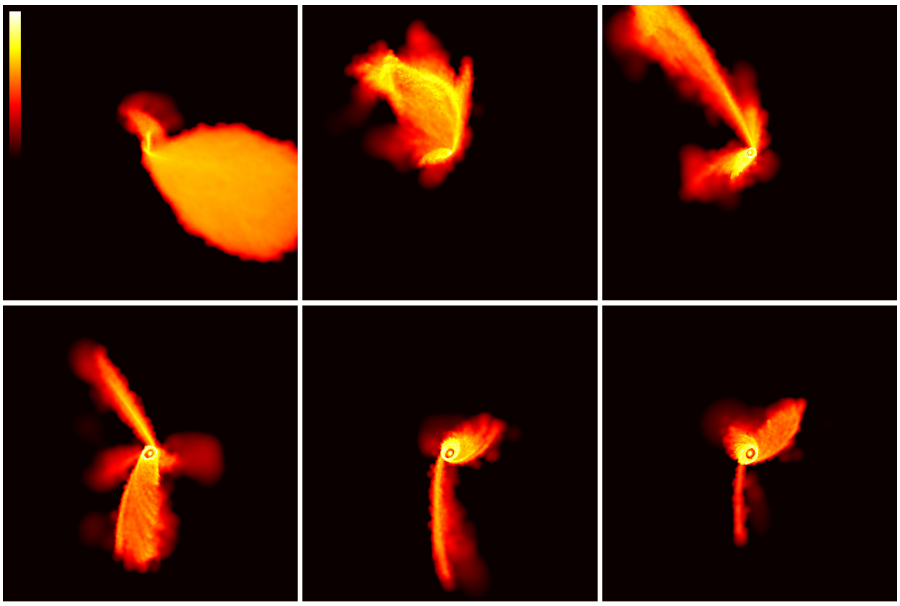

Figure 3.1: Colour-coded density map of gas in run R1, showing the y-z plane of the simulation. The density map is smoothed over the smoothing length of single particles. From top to bottom and from left to right: $t = 1.5, 3.5, 5.5, 7.5, 9.5$ and 10.5×10^5 yr. Each panel measures 50 pc per edge. The color bar ranges from 7×10^{-5} to $70\,M_\odot\,pc^{-3}$.

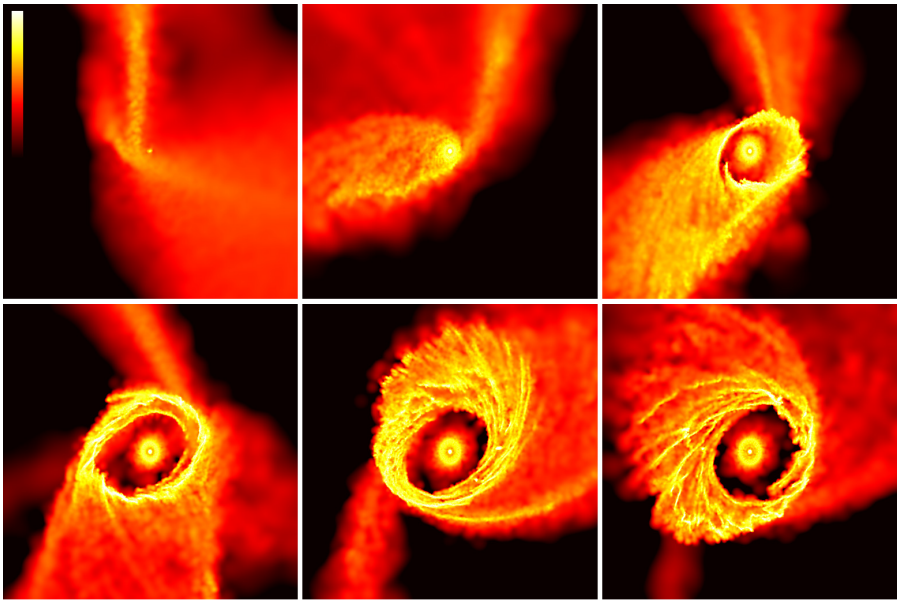

Figure 3.2: Zoom-in view of Fig. 3.1. Each panel measures 6 pc per edge. As in Fig. 3.1, the density map is smoothed over the smoothing length of single particles. From top to bottom and from left to right: $t = 1.5, 3.5, 5.5, 7.5, 9.5$ and 10.5×10^5 yr. Each panel measures 6 pc per edge. The color bar ranges from 0.007 to 223 $M_\odot\,pc^{-3}$.

RUN	MASS [$10^4\,M_\odot$]	v_{in}/v_{esc}	b [pc]	m_{res} [$M_\odot$]
R1	12.7	0.208	26	1.2
R2	4.27	0.208	26	0.4
R3	12.7	0.375	26	1.2
R4	12.7	0.52	8	1.2
R5	12.7	0.52	26	1.2
R6	12.7	0.52	26	0.12

Table 3.1: Initial conditions. Column 1: run name; column 2: total initial cloud mass; column 3: initial orbital velocity of the cloud (v_{in}) with respect to the escape velocity from the SMBH (v_{esc}); column 4: impact parameter of the cloud center of mass with respect to the SMBH (b); column 5: mass of a single gas particle (m_{res}).

I simulate the infall of a molecular cloud towards the SMBH, adopting the same technique as discussed in (Mapelli et al. 2012; Mapelli, Gualandris, and Hayfield 2013). The molecular cloud model is a spherical cloud with homogeneous density and a radius of 15 pc. The cloud is seeded with supersonic turbulent velocities and marginally self-bound (see Hayfield et al. 2011). To simulate interstellar turbulence, the velocity field of the cloud is generated on a grid as a divergence-free Gaussian random field with an imposed power spectrum $P(k)$, varying as k^{-4}. This yields a velocity dispersion $\sigma(l)$, varying as $l^{1/2}$, chosen to agree with the Larson 1981 scaling relations.

The initial distance of the molecular cloud from the SMBH is 26 pc. The stellar mass within 26 pc (i.e. the contribution of the aforementioned rigid potentials) is $\sim 1.3 \times 10^8\ M_\odot$. Thus, the potential well is dominated by the stellar component at the beginning of the simulation. The stellar mass equals the SMBH mass at ~1.6 pc. I investigate different cloud orbits, with impact parameter $b = 8$, 26 pc and initial velocity $v = 0.208$, 0.375 and 0.52 v_{esc}, where $v_{esc} \sim 34$ km s^{-1} is the escape velocity from the SMBH at 26 pc distance. I consider two different cloud masses ($4.3 \times 10^4\ M_\odot$ and $1.28 \times 10^5\ M_\odot$). In addition, I made a test run with a factor of ten better mass and spatial resolution (R6).

I include radiative cooling in all my simulations. The radiative cooling algorithm is the same as that described in Boley (2009) and in Boley et al. (2010). According to this algorithm, the divergence of the flux is $\nabla \cdot F = -(36\pi)^{1/3}\, s^{-1}\, \sigma \left(T^4 - T_{irr}^4\right) (\Delta\tau + 1/\Delta\tau)^{-1}$, where $\sigma = 5.67 \times 10^{-5}$ erg cm^{-2} s^{-1} K^{-4} is the Stefan's constant, T_{irr} is the incident irradiation, $s = (m/\rho)^{1/3}$ and $\Delta\tau = s\,\kappa\,\rho$, for the local opacity κ, particle mass m and density ρ.

D'Alessio, Calvet, and Hartmann (2001) Planck and Rosseland opacities are used, with a 1 μm maximum grain size. Such opacities are

appropriate for temperatures in the range of a few Kelvins up to thousands of Kelvins. In my simulations, the irradiation temperature is $T_{irr} = 100$ K everywhere, to account for the high average temperature of molecular gas in the innermost parsecs (Ao et al. 2013). The only feedback from the SMBH I account for is compressional heating. I neglect any outflows or jet from the SMBH. This is a reasonable assumption for the current activity of Sgr A* (the current bolometric luminosity of the SMBH in the Milky Way is several orders of magnitude lower than the Eddington luminosity, Baganoff et al. 2003).

The mass of the gas particles is $m_{res} = 0.12\,M_\odot$ in run R6, $0.4\,M_\odot$ in run R2 and $1.2\,M_\odot$ in all the other runs. The softening length is 4.6×10^{-4} pc pc in run R6 and 10^{-3} pc pc in all the other runs.

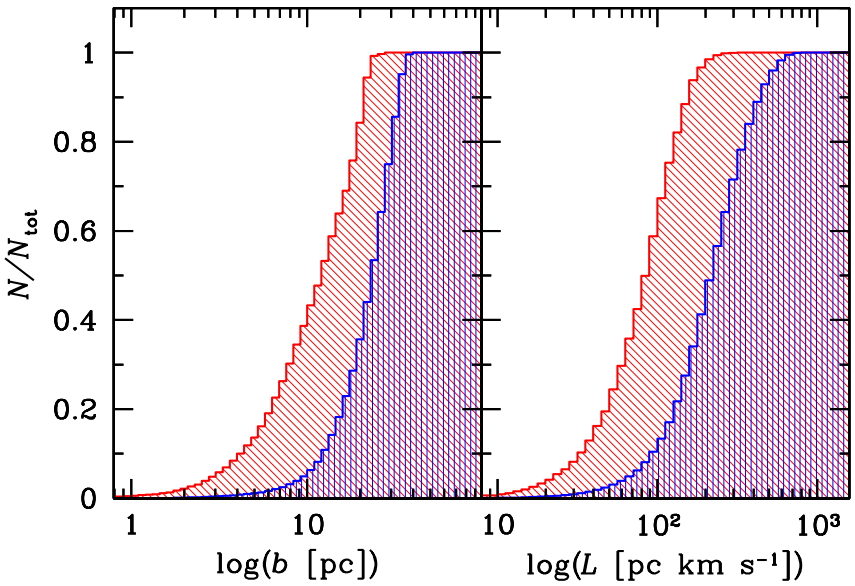

Figure 3.3: Cumulative distribution of impact parameter b (left-hand panel) and specific angular momentum L (right-hand panel) of gas particles in the initial conditions of run R1. Blue vertically-hatched histogram: all gas particles in the simulations. Red diagonally-hatched histogram: gas particles that will become members of the inner ring at time $\leqslant 2.5 \times 10^5$ yr. Both histograms are normalized to the total number of elements in the cumulative distribution (10655 and 107783 particles in the red and blue histogram, respectively).

3.3 RESULTS

Figure 3.1 shows the time evolution of gas in run R1. The cloud is fast disrupted by the SMBH: it is squeezed by tidal forces and becomes a stream of gas in $\lesssim 2.5 \times 10^5$ yr.

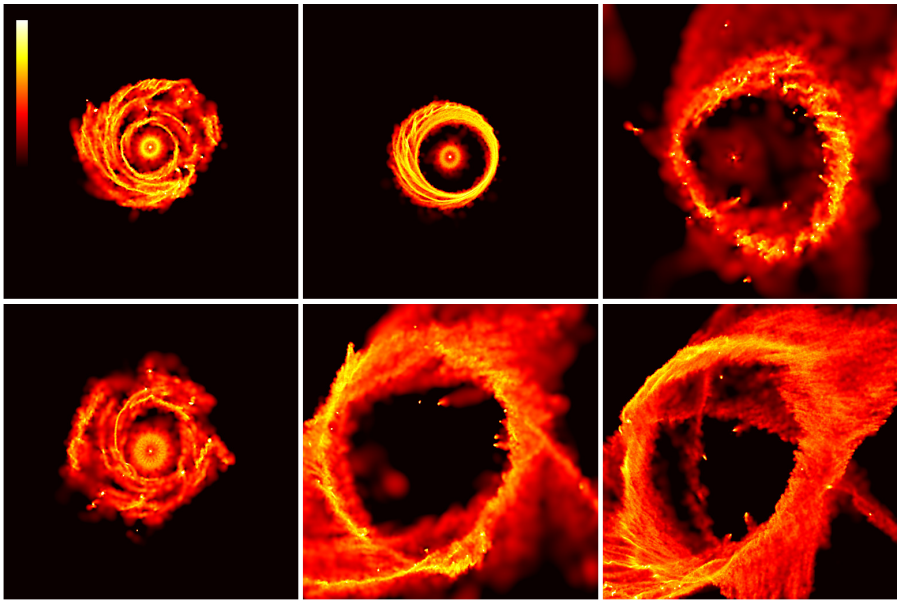

Figure 3.4: Colour-coded density map of gas at $t = 1.5\,\mathrm{Myr}$. The density map is smoothed over the smoothing length of single particles. From top to bottom and from left to right: run R1, R2, R3, R4, R5 and R6. Each panel measures 10 pc per edge. The color bar ranges from 0.007 to $223\,M_\odot\,\mathrm{pc}^{-3}$.

Figure 3.2 is a zoom of Fig. 3.1, in the innermost 6 pc. The first periapsis passage occurs at $1.0 - 2.5 \times 10^5$ yr. The duration of the first periapsis passage is $\sim 1.5 \times 10^5$ yr because the cloud radius is very large with respect to the SMBH and because the cloud is undergoing tidal disruption (hence it is squeezed into a stream). The particles of the disrupted cloud that are trapped by the SMBH during the first periapsis passage form a small disk (hereafter 'inner ring') with outer radius $\lesssim 0.4$ pc around the SMBH. Actually, I name this structure 'inner ring' but it might be considered also an inner disc, since the inner radius of this ring is $\approx 5 \times 10^{-3}$ pc (i.e. the sink radius of the SMBH). Particles inside this radius are likely eaten by the SMBH particle. Moreover, this radius is of the same order of magnitude as the softening length.

At later times ($\gtrsim 3.5 \times 10^5$ yr), a second, larger ring (hereafter 'outer ring') forms, with a radius $\sim$2 pc. The outer ring starts forming during the second periapsis passage and acquires more mass during the next periapsis passages. The outer ring is very clumpy and is connected to the remnant of the disrupted parent cloud by several streamers. Mass from the streamers accretes onto the outer ring. At the end of the simulation, nearly all material from the disrupted cloud settles into the rings.

The formation of two different rings is a consequence of angular momentum and energy differences between gas particles in the initial conditions. The inner ring forms during the first periapsis passage of

the cloud, and originates from a portion of the cloud that is immediately trapped by the SMBH, because of its low angular momentum and impact parameter (see Fig. 3.3). The outer ring forms later (during the next periapsis passages) and originates from material that has higher orbital angular momentum, leading to a larger circularization radius.

Figure 3.4 compares the gas density in different runs (R1, R2, R3, R4, R5, R6) at $t = 1.5$ Myr, when the outer ring has already formed in most runs. Table 3.2 shows the main properties of the rings (final mass, radius, thickness and circular velocity) at the end of the simulation ($t = 2$ Myr). Since the outer ring is a clumpy and irregular structure (sometimes characterized by streamers and spiral structures), the typical radius of the outer ring r_{CNR} listed in Table 3.2 is just an approximate value. From Fig. 3.4 and Table 3.2, it is apparent that the outer radius of the rings depends on the initial orbital velocity and on the impact parameter of the molecular cloud.

If there is no angular momentum transport, I expect the circularization radius to be

$$r_{circ} \sim \frac{b^2 v_{in}^2}{G M_{BH}}, \tag{3.1}$$

where b is the impact parameter, v_{in} the initial orbital velocity of the cloud, G the gravitational constant and M_{BH} the mass of the SMBH. For $M_{BH} = 3.5 \times 10^6$ $M_\odot$, $v_{in} = 0.208\, v_{esc}$ and $b = 26$ pc (as in R1 and R2), equation 3.1 would imply a circularization radius $r_{circ} \sim 2$ pc, consistent with the outer radius of the ring in runs R1 and R2. On the other hand, the outer radius of the ring in my simulations scales approximately as $r_{CNR} \propto v_{in}^{0.8}\, b^{0.5}$ (Fig. 3.5), i.e. a much flatter slope than in equation 3.1. This difference might be explained in the following way. First, the cloud is large with respect to the impact parameter of the centre of mass (the cloud diameter is 30 pc). Thus, the impact parameter is well defined only for the centre of mass of the cloud and for the nearby particles, but is very different from the nominal value for the rest of the cloud (see Fig. 3.3). Similarly, the initial velocity v_{in} provides a good estimate of the circularization radius only for the material that is close to the centre of mass. As a consequence, different regions of the same cloud have very different circularization radii, even in the assumption of angular momentum conservation. Furthermore, while I can reasonably assume angular momentum conservation at the very first periapsis passage, as soon as the disrupted cloud undergoes more periapsis passages there will be important torques between different streams of the cloud, which can significantly transfer angular momentum outwards. In addition, the cloud fragments into sub-clumps, which also lead to angular momentum transfer. If this interpretation is correct, I expect that larger discrepancies with respect to equation 3.1 occur for higher values of v_{in}, because a faster moving cloud undergoes more periapsis pas-

sages before being completely disrupted. This is consistent with the results of my simulations (Fig. 3.5).

N-body simulations are often claimed to be affected by spurious angular momentum dissipation (e.g. Kaufmann, Wheeler, and Bullock 2007). Thus, I checked whether the efficiency of angular momentum transport that I observe in my simulations might be (partially) due to numerical angular momentum dissipation. I find that the total angular momentum is conserved with an error $\lesssim 1\,\%$ in my simulations. In particular, the change of total angular momentum (over a 2-Myr integration time) is ~0.7 %, 0.6 %, 0.3 %, 0.4%, 0.2% and 0.1% in runs R1, R2, R3, R4, R5 and R6, respectively. Remarkably, the total angular momentum does not depend on resolution significantly: deviations from angular momentum conservation are of the order of ~0.2 % and ~0.1 % in run R5 and in (the high-resolution) run R6, respectively. Moreover, the radius of the outer ring is the same in both runs R5 and R6, indicating that angular momentum transport on parsec-scale is not enhanced by some spurious numerical effects. While a 1 % change in angular momentum is non-negligible, the fact that my results do not change with increasing resolution indicates that my main conclusions are fairly robust.

The efficiency of angular momentum transport in my simulations has important consequences for the formation of circumnuclear rings around black holes. In fact, if angular momentum was not transported efficiently during the disruption process (e.g. Wardle and Yusef-Zadeh 2008), a parsec scale ring would not form from the disruption of a molecular cloud, unless the initial angular momentum of the molecular cloud was very small. Moreover, some mechanism is needed (e.g. cloud-cloud collision) that brings the cloud onto a nearly radial orbit. On the other hand, my simulations show that parsec-scale rings can form for a relatively large range of initial orbital angular momenta of the molecular cloud ($L \lesssim 1000$ pc km s^{-1}), thanks to efficient transport of angular momentum. This result is interesting also for the possibility that angular momentum redistribution leads to an inflow of gas toward the SMBH, enhancing the accretion rate (e.g. Carmona-Loaiza et al. 2014).

From Fig. 3.4 and Table 3.2, it is also apparent that a significant inner ring forms only if v_{in} and/or b are sufficiently small (R1, R2 and R4). The mass of the inner ring is generally much smaller than the mass of the outer ring: it reaches a maximum value of $\sim 10-15$ % of the mass of the cloud in run R4 (where $v_{in}/v_{esc} = 0.52$ and $b = 8$ pc) and in runs R1 and R2 (where $v_{in}/v_{esc} = 0.208$ and $b = 26$ pc).

Another interesting feature of the inner ring is that it may have a different inclination (~24° in run R1) with respect to the outer ring (Fig. 3.6). The origin of this misalignment is again connected with the fact that the cloud size is large with respect to the impact parameter of its centre of mass. Portions of the cloud that have initially no or

RUN	M_{CNR}	r_{CNR}	Δr_{CNR}	v_{circ}	M_{in}	r_{in}
R1	11.5×10^4	2.1	1.2	125	1.25×10^4	0.35
R2	3.8×10^4	1.7	0.5	141	0.42×10^4	0.43
R3	12.5×10^4	2.9	0.7	127	0.026×10^4	10^{-4}
R4	10.7×10^4	1.8	1.4	125	2.0×10^4	0.64
R5	10.3×10^4	3.7	0.9	128	–	–
R6	10.3×10^4	3.8	1.1	124	–	–

Table 3.2: Properties of the simulated inner and outer rings at 2 Myr. First column: run name; second column: mass of the outer ring M_{CNR} in $M_\odot$; third column: typical radius of the outer ring r_{CNR} in pc; fourth column: radial extension of the outer ring Δr_{CNR} in pc; fifth column: average circular velocity of the gas rings v_{circ} in $km\,s^{-1}$; sixth column: mass of the inner ring M_{in} in $M_\odot$; seventh column: outer radius of the inner ring r_{in} in pc. The radii of the inner and outer ring were obtained with the TIPSY visualization package, through visual inspection of the density maps.

small impact parameter directly engulf the SMBH, with no or small deviation of their trajectory (see e.g. Wardle and Yusef-Zadeh 2008). In contrasts, the trajectory of a portion of the cloud with large impact parameter is substantially deviated by the SMBH's gravitational focusing. This leads to the formation of different streams with different inclinations. The shocks and torques between different streams do the rest. The cartoon shown in Fig. 3.7 is a simplified visualization of this argument. The contour-plot in the bottom panel of Fig. 3.8 shows the inclination between the angular momentum vectors of gas particles and the total angular momentum vector of the simulated gas, as a function of radius, in runs R1 and R6. From this plot, it is apparent that the inner and the outer ring in run R1 are misaligned by ~24°.

From Fig. 3.6, it is also apparent that the inner ring is slightly warped and tends to align with the outer ring in its outermost parts. This effect is driven by torques between the outer and inner ring, which act on a few dynamical time scales (t_{dyn} ~ 1000 yr for a radius of 0.4 pc).

Finally, Figure 3.8 shows the density (top panels) and temperature (middle panels) of gas as a function of radius at $t = 2$ Myr in run R1 and R6. The density of gas in the main clumps is above the tidal density $\rho_{tid}(r) = [M_{SMBH} + M(r)]/(4\pi/3\,r^3)$, where r is the distance between the gas particle and the SMBH, M_{SMBH} is the SMBH mass and $M(r)$ is the mass of stars within a distance r from the SMBH (Vollmer and Duschl 2001). In run R1, R2 and R4, gas particles populate even the innermost < 0.1 pc around the SMBH. In particular, the left-hand panel of Figure 3.8 shows the existence of a very dense ($> 10^{11}$ cm^{-3}) small gas disk with radius ~0.025 pc, a dense ($> 10^6$ cm^{-3}) gas ring

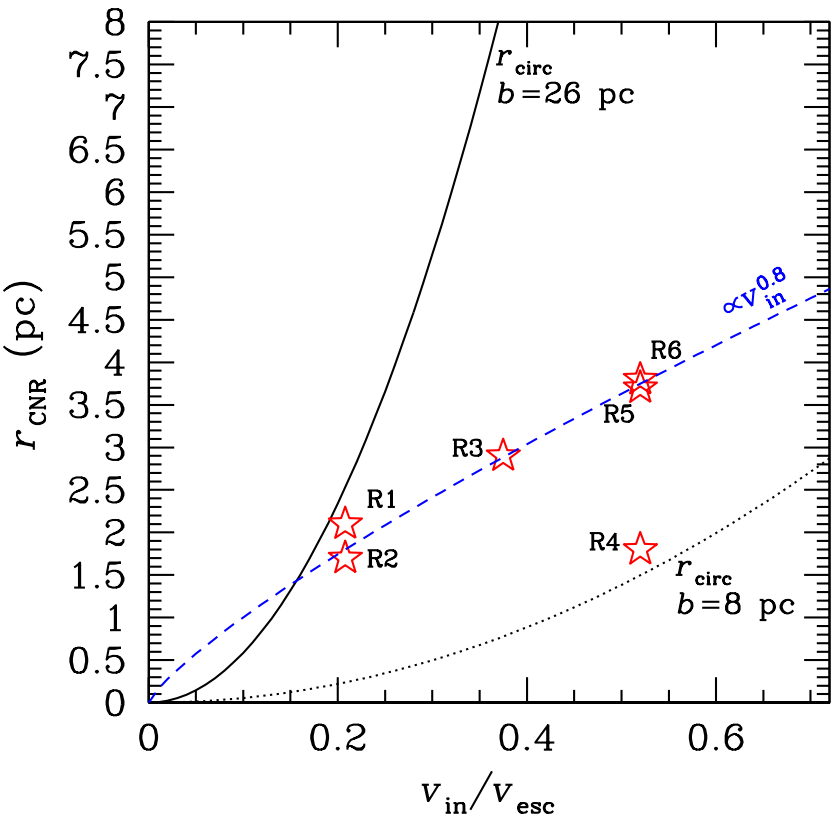

Figure 3.5: Radius of the outer ring (r_{CNR}) as a function of the initial velocity of the cloud (v_{in}) in the six runs listed in Table 3.2 (red stars). The blue dashed line shows the trend of r_{CNR} as a function of v_{in} ($r_{CNR} \propto v_{in}^{0.8}$), as derived from my simulations. The black solid line shows the expected circularization radius (r_{circ}) as a function of v_{in}, assuming angular momentum conservation (equation 3.1), for $b = 26$ pc and $M_{BH} = 3.5 \times 10^6$ $M_\odot$. The black dotted line is the same but for $b = 8$ pc.

(the one I named 'inner ring') with radius $\sim 0.3 - 0.4$ pc, and then a broader ring (the one I named 'outer ring') with radius $\sim 1 - 3$ pc. In the outer ring, several clumps become self-gravitating and start to collapse (i.e. they reach a density much larger than the average disk density). In run R6, R5 and R3, gas particles do not populate the innermost parsec significantly. The right-hand panel of Figure 3.8 shows the existence of a very broad and perturbed ring (the one I named 'outer ring') in run R6, ranging from ~2 pc out to ~8 pc, but with a significant portion of material extending up to ~30 pc. Very dense gas clumps become self-gravitating over the $2 - 30$ pc range, suggesting that the entire ring in run R6 is on the verge of forming stars.

The temperature of most gas particles at the end of my simulations ($t = 2$ Myr) is $\sim 100 - 160$ K, with a maximum temperature of ~1000 K. I recall that gas particles cannot cool below 100 K because I im-

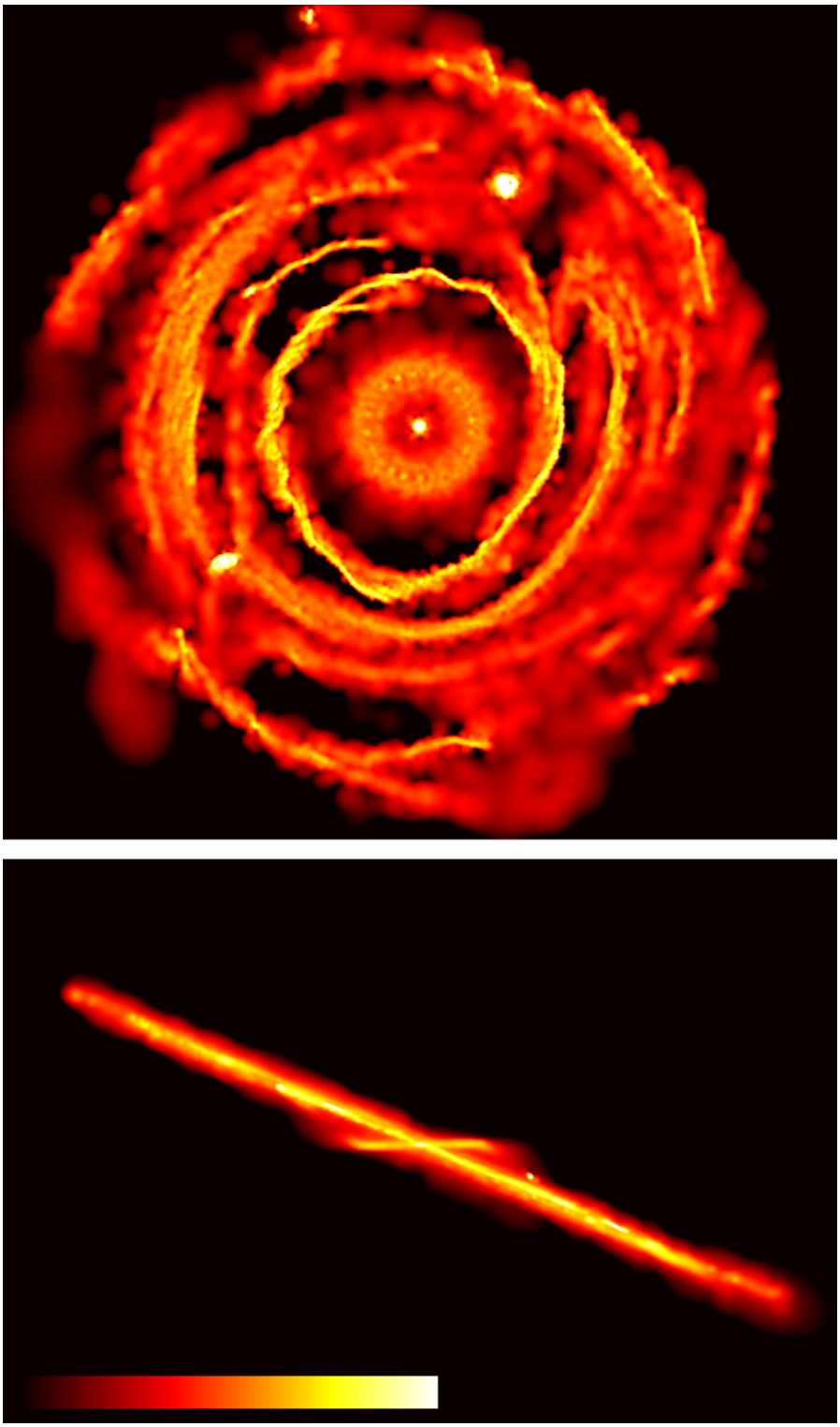

Figure 3.6: Top (bottom): colour-coded density map of gas in run R1 at t = 2 Myr, if the inner ring is projected face-on (edge-on). The density map is smoothed over the smoothing length of single particles. The top (bottom) panel measures 5×5 pc (5×3.4 pc), and the color bar ranges from 0.02 to 700 $M_\odot$ pc^{-3} (from 0.1 to 2230 $M_\odot$ pc^{-3}).

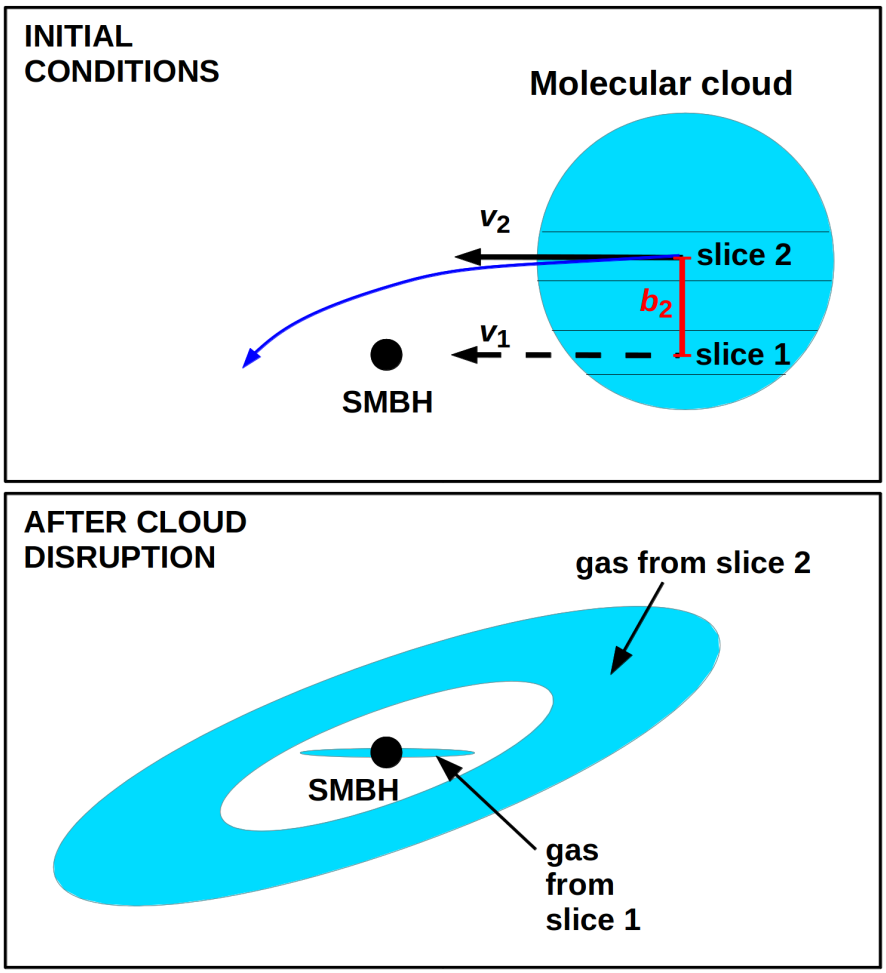

Figure 3.7: Top: cartoon of the initial conditions. The big blue circle and the small black dot represent the molecular cloud and the SMBH, respectively. The dashed black arrow shows the initial velocity ($\mathbf{v}_1$) of a slice of the cloud (named slice 1) with zero impact parameter. The solid black arrow shows the initial velocity ($\mathbf{v}_2$) of a second slice of the cloud (named slice 2) with non-zero impact parameter (b_2, red line). Even if $\mathbf{v}_1$ and $\mathbf{v}_2$ are the same, the trajectory of slice 1 does not change, while the trajectory of slice 2 is deflected because of SMBH's gravitational focusing (blue line). Bottom: cartoon of the evolution of slice 1 and slice 2 after cloud disruption. Slice 1 produces ring 1 (edge-on) around the SMBH, while slice 2 produces ring 2. The (arbitrarily drawn) inclination between the two rings is a consequence of the different initial impact parameter. In this cartoon, I neglect the turbulent motions inside the cloud as well as details connected with cooling, shocks, and angular momentum transfer.

posed a temperature floor. In run R1 (as well as in the other runs with an inner ring, i.e. R2 and R4), the gas temperature rises to ~500 K in the innermost ~0.02 pc, mostly because of SMBH tidal heating[1], then decreases to ~100 K at intermediate radii, and rises again up to ~500 K at ~$1.5-2$ pc, in correspondence to the outer ring (where self-gravitating clumps form). In run R6 (as well as in the other runs without inner ring, i.e. R3 and R5), there is almost no gas at distance $<$ 1 pc. The temperature of most gas is ~100 K, with some hotter clumps in the outer ring (~$3-5$ pc), where self-gravitating clumps form.

3.4 DISCUSSION

3.4.1 *The circumnuclear ring in our Galaxy*

I showed that the disruption of a molecular cloud can produce parsec-scale clumpy rings around a SMBH. Are the properties of such rings consistent with the observations of the CNR in our GC? The mass of the ring ($4\times10^4-1.3\times10^5$ $M_\odot$) is in good agreement with the mass of the CNR, when taking into account the uncertainties on the measurement (Christopher et al. 2005; Liu et al. 2013). Besides, the mass of the CNR is completely determined by the initial mass of the cloud, as most of the cloud mass ends up into a CNR in my simulations. The outer radius ($2-4$ pc) and the rotation speed ($120-140$ km s^{-1}) is also in good agreement with the properties of the CNR. Angular momentum transport enables even clouds with relatively large initial orbital angular momentum ($L \lesssim 1000$ pc km s^{-1}) to produce a CNR with a radius of a few parsecs.

Another interesting feature of my simulations is that the outer ring is a very perturbed and clumpy structure, with several streamers that feed it (e.g. Fig. 3.2). This is reminiscent of the streams that appear to feed the CNR in our Galaxy (e.g. Liu et al. 2012) and in several other nearby galaxies (e.g. NGC1068, Müller Sánchez et al. 2009).

In my simulations, several clumps of gas become self-gravitating and tend to collapse by 2 Myr. The formation of self-gravitating clumps is not a resolution issue, since self-gravitating clumps form even in the high-resolution run R6. The mass of such clumps spans from ~3 $M_\odot$ to 2×10^3 $M_\odot$ in the highest-resolution run R6, and from ~30 $M_\odot$ to 2×10^3 $M_\odot$ in the other runs. While I do not assume any recipes for converting gas to stars in the simulations, it is reasonable to expect that star formation occurs in such clumps. No star formation is observed today in the CNR of our Galaxy, but several studies (e.g. Yusef-Zadeh et al. 2008) indicate that the CNR is on the verge

1 When the tidal forces by the SMBH squeeze and compress the gas cloud in the innermost ~0.05 pc, tidal compressional heating becomes efficient, as discussed in Bonnell and Rice (2008) and Mapelli et al. (2012).

of forming stars. The comparison between star forming clumps in my simulations and in the CNR leads to two possible conclusions: (i) either my simulations indicate that the CNR of the Milky Way is a young structure ($\leqslant 2$ Myr), which did not have enough time to form stars (but star formation will soon take place), (ii) or the formation of stars in the CNR is quenched by some process that is not included in the simulations (e.g. radiative feedback from stars, outflows from the black hole). New simulations including sources of feedback and an accurate treatment of radiative transfer are necessary to address this point.

The main feature of the simulations that does not match the observations of our GC is connected with the distribution of ionized gas. There are no significant structures of ionized gas that match the properties of the minispiral in GC. A possible reason of this difference is numerical: I do not include an accurate treatment for radiative transfer and ionization. Second, I do not include a treatment for outflows and feedback from the SMBH, which can also affect the thermodynamics of gas in the innermost parsec (e.g. Zubovas 2015). These aspects will be included in a forthcoming work, together with a better treatment of chemistry.

Finally, is the existence of an inner gas ring (which forms in runs R1, R2 and R4) in conflict with the observations of the innermost parsec of the Milky Way? The mass of the inner ring in runs R1, R2 and R4 is $4 \times 10^3 - 1.2 \times 10^4$ $M_\odot$ (Table 3.2), and its temperature spans from ~100 K to ~500 K, indicating that the inner ring is composed of warm, but mostly neutral gas. Jackson et al. 1993 found that $\gtrsim 300$ $M_\odot$ of neutral gas lie in the central cavity inside the CNR, but this measurement is quite uncertain and might be an underestimate (see also Goicoechea et al. 2013). The inner ring in the simulations is a factor of $10 - 40$ more massive than this estimate. On the other hand, it might be that a fraction of gas in the inner ring has been converted to stars (see the next section) or that outflows from the SMBH ionized and expelled some of this gas from the central parsec. Thus, I suggest that the origin of the neutral gas observed in the central cavity, within the radius of the CNR, might be connected with the formation of the inner ring in the simulations.

3.4.2 *The young stars in the innermost parsec of the Milky Way*

Several hundred young stars lie in the innermost parsec of our Galaxy (Schödel et al. 2002; Genzel et al. 2003a). About 20 % of them lie in a ring, with outer radius ~0.15 pc, named the clockwise (CW) disk for its orientation when projected in the plane of the sky (Paumard et al. 2006a; Bartko et al. 2009; Lu et al. 2009, 2013; Yelda et al. 2014). The remaining stars share the same properties (e.g. mass function and age) as the members of the CW disk but do not belong to any discs. Recent

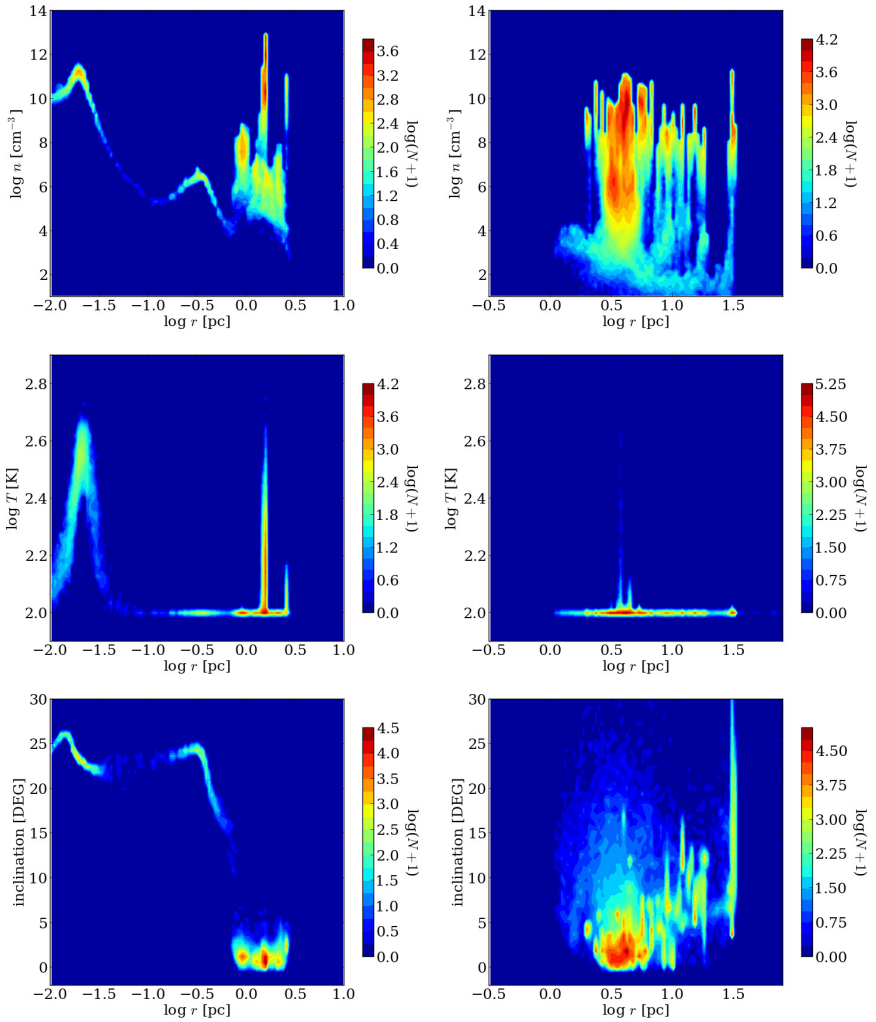

Figure 3.8: Contour-plot of the number density (top panels), temperature (middle panels) and inclination (bottom panels) of gas particles as a function of the distance from the SMBH in runs R1 (left-hand panels) and R6 (right-hand panels) at t = 2 Myr. The inclination is measured with respect to the direction of the total angular momentum vector of the simulated gas at t = 2 Myr. The color-map is in logarithmic scale and represents the number of gas particles (N) per each cell of the contour-plot.

work suggested that the formation of the young stars in the innermost parsec is connected with the disruption of a molecular cloud by the SMBH (Bonnell and Rice 2008; Mapelli et al. 2008; Alig et al. 2011; Mapelli et al. 2012; Lucas et al. 2013; Alig et al. 2013; see Mapelli and Ripamonti 2015 for a review). Furthermore, several studies highlight that the CNR might have played an important role in the dynamical evolution of the CW disk (e.g. Löckmann and Baumgardt 2009; Löckmann, Baumgardt, and Kroupa 2009; Šubr, Schovancová, and Kroupa 2009; Haas, Šubr, and Kroupa 2011; Haas, Šubr, and Vokrouhlický 2011; Šubr and Haas 2012; Ulubay-Siddiki, Gerhard, and Arnaboldi 2009; Mapelli, Gualandris, and Hayfield 2013; Ulubay-Siddiki, Bartko, and Gerhard 2013). Is it possible that the same molecular cloud disruption event leads to the formation of both the CW disk and the CNR?

The simulations presented in this paper show that the same episode of molecular cloud disruption can lead to the formation of two (or more) rings: an inner ring with radius $\sim$0.4 pc (if the cloud orbital velocity and/or impact parameter are sufficiently small) and an outer ring with radius $\sim 2-4$ pc. While fragmentation does not seem to take place in the inner ring (because the tidal shear from the SMBH is too strong), the radius of the inner ring is reminiscent of the size of the cluster of young stars in the GC. The mass of the inner ring in runs R1, R2 and R4 is sufficient to produce the young stars in the GC only for an unrealistically high star formation efficiency ($\sim 50-100$ %). On the other hand, I can speculate that for a smaller impact parameter of the cloud (e.g. the one adopted in Mapelli et al. 2012) and/or for a lower initial orbital velocity of the cloud, the mass of the inner ring might be consistent with the expectations for the formation of the CW disc.

In my simulations, the inner ring is misaligned with respect to the outer ring by $\sim 24^\circ$. I recall that the plane of the observed CNR is nearly perpendicular to the CW disk in our Galaxy, suggesting that, if they formed during the same cloud disruption event, they originated from two nearly perpendicular streams of gas. A cloud-cloud collision might have resulted into the formation of nearly perpendicular streams of gas (e.g. Hobbs and Nayakshin 2009), leading to the formation of both the CW disk and the CNR ring in our Galaxy.

3.5 CONCLUSIONS

I investigated the formation of circumnuclear rings, by means of N-body/SPH simulations of molecular-cloud disruption events. I found that more than one ring can form during the disruption of the same molecular cloud. For sufficiently small values of the initial velocity v_{in} ($v_{in} \lesssim 0.4\ v_{esc}$, if $b = 26$ pc) and/or of the impact parameter b of the cloud ($b \lesssim 10$ pc if $v_{in} > 0.5\ v_{esc}$), the tidal disruption leads to the formation of both an inner ring and an outer ring. The inner ring

forms only if the initial velocity and/or impact parameter are small, it has a radius $\leqslant 0.5$ pc and contains $\approx$ 10 % of the molecular-cloud mass.

The outer ring contains most of the initial molecular cloud mass. The radius of the outer ring depends on the initial velocity and on the impact parameter of the cloud (as $r_{CNR} \propto v_{in}^{0.8}\, b^{0.5}$). I suggest that the inner ring forms from matter with low angular momentum and low impact parameter, which engulfs the SMBH during the first periapsis passage, while the outer ring forms from higher-angular momentum regions of the cloud, that are captured during subsequent periapsis passages. Angular momentum transport is efficient in my simulations, suggesting that parsec-scale rings can form even from relatively high-angular momentum clouds ($L \sim 10^3$ pc km s^{-1}). Because angular momentum is efficiently transferred outwards, and thanks to the torques between different streamers, the inner ring might have a non-negligible inclination with respect to the outer ring ($\sim 20 - 25°$). Furthermore, the inner ring soon becomes warped at the edges, for the interaction with the outer ring. While I cannot completely exclude that spurious numerical dissipation of angular momentum contributes to making angular momentum transport more efficient in my simulations, I find that the error on angular momentum conservation ($\lesssim$ 1 % in 2 Myr) does not depend on the resolution. This suggests that my main conclusions are fairly robust, even if a further study of the dependence of my results on different simulation techniques and cooling algorithms is needed to quantify any spurious numerical issues.

In my simulations, the mass ($4 \times 10^4 - 1.3 \times 10^5$ M$_\odot$), the rotation speed ($120 - 140$ km s^{-1}) and the radius ($2 - 4$ pc) of the outer ring match the observations of the CNR in the Milky Way. During the disruption of the cloud, several streams connect the ring with the outer regions, similar to the streamers observed in our GC (Liu et al. 2012) and in the nucleus of nearby galaxies (e.g. NGC 1068, Müller Sánchez et al. 2009). The simulated rings are very clumpy and are on the verge of forming stars at $t \lesssim 2$ Myr. This indicates that the CNR in our Galaxy is a very young and evolving structure.

The inner ring has a mass of $\sim 4 \times 10^3 - 1.2 \times 10^4$ M$_\odot$, larger than the estimated mass of neutral gas observed in the central cavity ($\gtrsim$ 300 M$_\odot$, Jackson et al. 1993). I argue that the formation of the CW disk and that of the CNR in our Galaxy might be both associated with the disruption of a molecular cloud. It is even possible that the same disruption event gave birth to both the CNR and the progenitor of the CW disc.

4

FORMATION AND EVOLUTION OF THE CLOCKWISE DISK: THE IMPACT OF CIRCUMNUCLEAR DISKS

4.1 INTRODUCTION

In this Chapter, I investigate the precession induced by dense gaseous rings on a Keplerian disk orbiting a SMBH. The gaseous ring is generated self-consistently by simulating the disruption of a turbulence-supported molecular cloud, as in Chapter 3. In this way, I obtain rings that match the main properties of the CNR (Mapelli and Ripamonti 2015). I investigate precession effects by means of a direct-summation N-body code, coupled to the SPH simulation thanks to the AMUSE software environment (Portegies Zwart et al. 2009, 2013; Pelupessy et al. 2013). In particular, I study the dependence of precession upon the angle between the CW disk and a gas ring. I show that the warm gas that lies in the inner cavity might substantially affect the evolution of the young stars in the GC.

First, I describe the methodology I employed for my simulations; in Section 4.3 I present my results. In Section 4.4, I examine in detail the processes driving the evolution of the stellar disk and I discuss the implications of my work for the past evolution of the CW disk. My conclusions are summarized in Section 4.5. The Chapter is based on Trani et al. (2016b).

4.2 METHODS

I make use of the AMUSE software environment (Portegies Zwart et al. 2009, 2013; Pelupessy et al. 2013) to combine different gas and stellar physics in a single simulation. AMUSE is a Python framework that embeds several codes, which are specialized solvers in a single physics domain – stellar evolution, gravitational dynamics, hydrodynamics and radiative transfer. One of the main features of AMUSE is the ability to couple and run different codes in a single simulation. In particular, it enables the gravitational coupling between the particles of different codes through the bridge BRIDGE scheme (Fujii et al. 2007). More details can be find in Appendix B.

4.2.1 *Codes employed*

I use the N-body SPH code GASOLINE (Wadsley, Stadel, and Quinn 2004; Read, Hayfield, and Agertz 2010) to simulate the formation of

RUN	PERTURBER	θ_i	θ_{inner}	NOTES
A	Yes	10	20	–
B	Yes	45	37	–
C	Yes	90	77	–
D	No	–	–	–
A0	Yes	10	20	No outer ring
A1	Yes	10	20	Massless stars

Table 4.1: Main properties of the simulations. Column 1: run name; column 2: presence of a perturber (i.e. a molecular cloud falling towards the SMBH); column 3: initial inclination θ_i between the molecular cloud and the stellar disk; column 4: average inclination θ_{inner} between the stellar disk and the inner ($r \sim 0.2$-0.4 pc) gas ring.

a CNR-like gas ring through the infall and disruption of a molecular gas cloud. The molecular cloud is simulated as in run R1 of Mapelli and Ripamonti (2015), who investigate the formation of circumnuclear disks. In particular, the molecular cloud is modeled as a spherical cloud with a radius of 15 pc and a total mass of $1.3 \times 10^5\,M_\odot$. Each gas particle has a mass of $1.2\,M_\odot$. It has an impact parameter of $b = 26$ pc and an initial velocity of $v_{in} = 0.208 v_{esc}$, where v_{esc} is the escape velocity from the SMBH at 25 pc. The cloud is seeded with supersonic turbulent velocities and marginally self-bound (see Hayfield et al. 2011). The simulations include radiative cooling, using the same prescriptions as used in Mapelli et al. (2012).

GASOLINE uses a kick-drift-kick scheme to integrate the evolution of particles. This scheme is second order accurate in positions and velocities. To achieve higher accuracy in integrating stellar orbits, I calculate the stellar dynamics of a thin stellar disk using the fourth order Hermite N-body code PHIGRAPE and couple this with the time-evolving potential generated by the snapshots of the SPH simulation using a fourth order BRIDGE scheme. The assumption here is that the evolution of the thin stellar disk does not affect the evolution of the gas disk, which is justified by the low mass of the stellar disk compared with the other mass components ($\approx 3\%$).

To achieve higher accuracy in integrating stellar orbits, I calculate the stellar dynamics of a thin stellar disk using the direct N-body code PHIGRAPE (Harfst et al. 2007) and couple this with the time-evolving potential generated by the snapshots of the SPH simulation using a fourth order BRIDGE scheme. The assumption here is that the evolution of the thin stellar disk does not affect the evolution of the gas disk, which is justified by the low mass of the stellar disk compared

with the other mass components ($\approx 3\%$). The mutual interaction between codes occurs in fourth order leapfrog scheme with a fixed interaction timestep. I set an interaction timestep of 50 Myr, which is of the order of few percents of the stars orbital time.

PHIGRAPE uses a fourth order Hermite predictor-corrector scheme to integrate the evolution of the stars. I run PHIGRAPE on GPUs through the SAPPORO library (Gaburov, Harfst, and Portegies Zwart 2009).

I modified both PHIGRAPE and GASOLINE to include the potential of the SMBH and of the stellar cusp. The SMBH in PHIGRAPE is modeled as a point-mass potential with a mass of $M_{SMBH} = 3.5 \times 10^6\, M_\odot$ (Ghez et al. 2003).In GASOLINE, the SMBH is modeled as a sink particle of mass M_{SMBH}, whose position is fixed at the origin in order to avoid spurious effects.

The stellar cusp is modeled as a rigid potential given by a spherical distribution of mass, whose mass density follows the broken-law profile of Schödel et al. (2007):

$$\rho(r) = 2.8 \times 10^6\, M_\odot\, pc^{-3} \left(\frac{r}{r_0}\right)^{-\gamma} \tag{4.1}$$

with $r_0 = 0.22\,pc$, $\gamma = 1.75$ for $r > r_0$ and $\gamma = 1.2$ for $r < r_0$, respectively. We truncate the density profile at $r_{trunc} = 10\,pc$

Acceleration and jerk are computed from

$$a^i = -\frac{\partial\Phi}{\partial r}\frac{x^i}{r} \tag{4.2}$$

$$j^i = -\left[\frac{\partial^2\Phi}{\partial r^2}\frac{v_j x^j}{r}\frac{x^i}{r} + \frac{\partial\Phi}{\partial r}\frac{v^i}{r} - \frac{\partial\Phi}{\partial r}\frac{v_j x^j}{r^2}\frac{x^i}{r}\right] \tag{4.3}$$

while the potential Φ is computed from the density distribution ρ:

$$\Phi(r) = -4\pi G\left[\frac{1}{r}\int_0^r r^2\rho(r)dr + \int_r^\infty r\rho(r)dr\right] \tag{4.4}$$

4.2.2 *Initial conditions*

For the disk of stars I adopt the outcome of run E^1 of Mapelli et al. (2012). In particular, the stellar disk I simulate is composed of 1252

1 This procedure is not completely self-consistent, because I take the initial conditions for the stellar disk from another simulation, instead of forming the young stars and the gas rings in the same simulation. However, integrating the formation of the stars and studying the dynamical influence of gas rings in the same simulation is computationally prohibitive. In fact, run E of Mapelli et al. (2012) has a factor of 30 higher resolution with respect to the simulations that will be discussed in this paper. Such high resolution is necessary to follow the first stages of the fragmentation process with sufficient accuracy, but run E of Mapelli et al. (2012) stalls after $\sim 5 \times 10^5$ yr. In contrast, to investigate the dynamical effects of gas onto the stellar orbits, I can adopt a lower resolution for the gas component, while I need a much higher accuracy in the integration of stellar dynamics (therefore, I use PHIGRAPE).

stars with an initial mass function given by a power-law with index $\alpha = 1.5$ and a lower mass limit of $1.3\,M_\odot$. The total mass of the disk is $4.3 \times 10^3\,M_\odot$, lower than suggested by the most recent observations of the young stars in the central parsec (~5-20 $\times\, 10^3 M_\odot$, according to Lu et al. 2013). However, I prefer to use a set of stellar orbits that formed self-consistently (from the simulation by Mapelli et al. 2012), rather than drawing stellar orbits with Monte Carlo sampling.

The stars have semi-major axis a ranging from 0.1 pc to 0.4 pc and mean eccentricity $\langle e \rangle = 0.3$ (the eccentricity distribution is in excellent agreement with the data reported by Yelda et al. 2014). The apse lines are aligned in a common direction, i.e., the ellipses are mutually aligned. The disk has an initial opening angle of ~7°.

I simulate different inclinations θ_i between the infalling gas cloud and the stellar disk. To do this, I simply rotate the snapshots of the SPH simulation with respect to the plane of the stellar disk. I choose three different inclinations: $\theta_i = 10°$ (run A), 45° (run B), 90° (run C). The secular evolution of the orbital elements of a star in an axisymmetric potential strongly depends on the inclination between the orbital plane and the symmetry axis, I therefore expect different outcomes for different inclinations. To compare my results, I also integrate the evolution of the stellar disk alone, without any infalling molecular gas cloud (run D). Table 4.1 shows a summary of the runs presented in this paper.

I stop the simulations at 3 Myr, because this is the best observational estimate for the age of the young stars in the central parsec (Lu et al. 2013). Furthermore, after this time stellar mass changes and the energy input from supernovae and stellar winds become progressively more important.

4.3 RESULTS

In the first 1 Myr, the gas cloud quickly inspirals towards the SMBH and settles down into a disk. Top (bottom) panel of Figure 4.1 shows the projected density map of the gas ring seen face-on (edge-on) at 1 Myr in run A. The formation of the gas ring is similar to the one described in section 3.1 of Mapelli, Gualandris, and Hayfield (2013). At 0.2 Myr the cloud is completely disrupted into several streamers. At 0.5 Myr the streamers begin to form a ring around the SMBH. The ring is progressively formed as the inspiraling streamers settle down around the SMBH. At 1.2 Myr, each gas streamer has settled down and the gas ring is completely formed. The gas ring is actually composed of two concentric rings. The outer ring is composed of irregular and clumpy gas streamers and has an inner radius of ~1.5 pc. The inner ring is warped and has a radius of ~0.2-0.4 pc, similar to the stellar disk. The inner gas ring has a mass of $\sim 3 \times 10^3\,M_\odot$, while the outer ring has a mass of $\sim 9 \times 10^4\,M_\odot$. In addition, the inner ring is

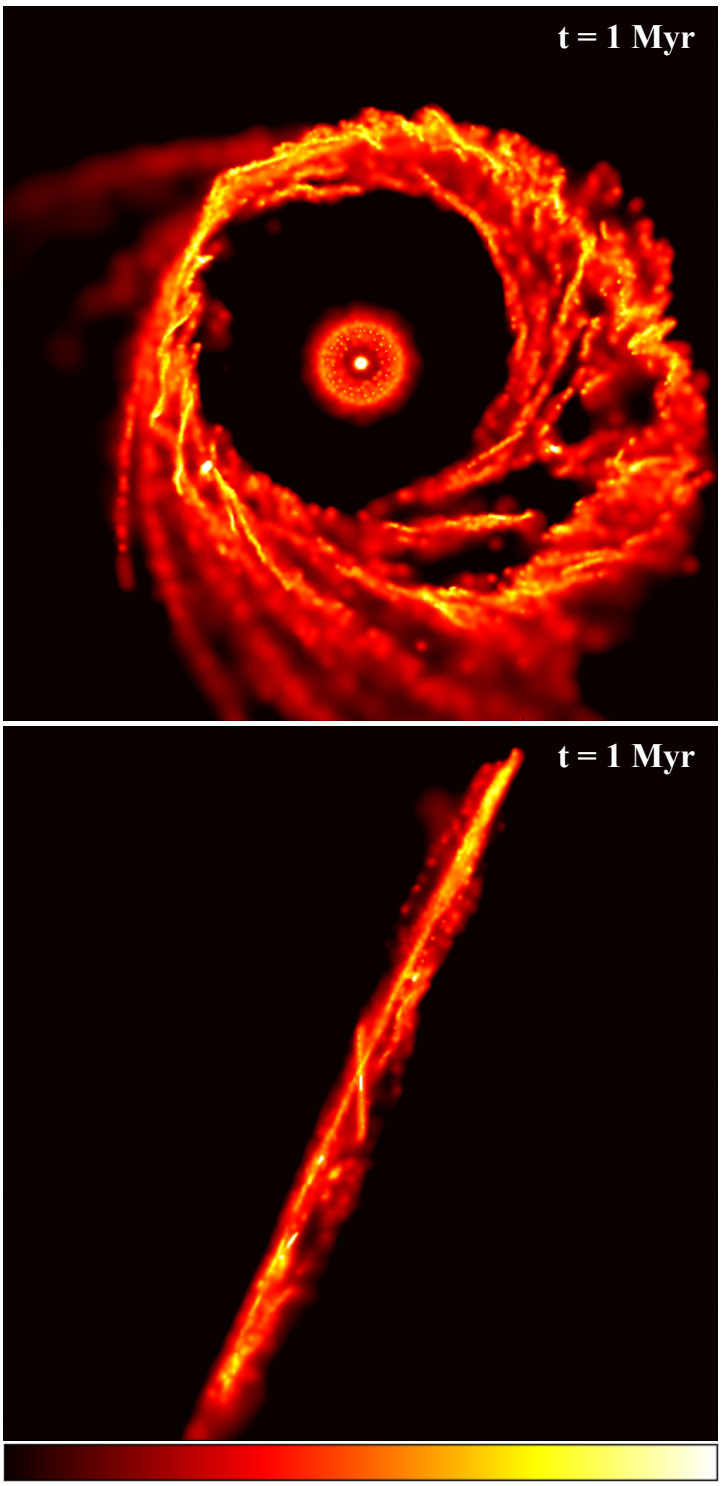

Figure 4.1: Color-coded maps of projected density of gas at 1 Myr in run A. Top panel: gas rings seen face-on. Bottom panel: gas rings seen edge-on. The inner gas ring is inclined by ~24° with respect to the outer one. The top (bottom) panel measures 8 pc (6 pc) per edge. The color bar ranges from 0.04 to 49 $M_\odot$ pc^{-2} (from 0.4 to 119 $M_\odot$ pc^{-2}).

inclined by ~24° with respect to the outer ring, hence the stellar disk and the inner gas ring have a mutual inclination θ_{inner} (see Table 4.1). This misalignment is due to the fact that the inner ring comes from low impact-parameter and low angular-momentum gas, which engulfs the SMBH during the first pericenter passage of the cloud, while the outer ring forms later, during the subsequent pericenter passages of the disrupted cloud (and suffers from gravitational focusing and torques). A detailed explanation is given in Mapelli and Trani (2016).

Once the gas ring has settled, it induces precession on the stellar disk, altering the stellar orbits. The evolution of eccentricity and semi-major axis distributions is similar in each run, both those including the infalling gas cloud (run A, B, C) and those which do not include gas (run D). In particular, after ~1.5 Myr the eccentricity distribution becomes bimodal, showing two peaks at $e \sim 0.15$ and 0.5 (Figure 4.2, top panel).

The semi-major axis distribution does not change significantly through out the simulations (Figure 4.2, bottom panel), indicating that in my model two-body relaxation of orbital energy is inefficient. This result is in agreement with Šubr and Haas (2014), who find that two-body relaxation is inefficient in changing the semi-major axis distribution if $\langle e^2 \rangle^{1/2} \gtrsim 0.3$.

On the other hand, the torques exerted by the gas ring strongly affect the orbital inclinations. In Figure 4.3 I show the inclination distribution at 3 Myr in each run, compared with the initial conditions. In the case of Run A (Figure 4.3, top-left panel), the inclinations of the stars change significantly from the initial one, showing two peaks at ~27° and 50° degrees from the initial disk inclination. This indicates that the whole disk changed its orientation during the simulation.

In run B (Figure 4.3, top-right panel), there is less spread in the inclinations than in run A and the inclination distribution at 3 Myr shows a main peak at ~42°. As in run A, this means that the disk has completely changed its orientation with respect to the initial configuration. In run C the inclination distribution at 3 Myr is peaked at ~12° and shows little spread.

In the case of Run D (Figure 4.3, bottom-right panel), the disk is unperturbed and the inclinations do not change as significantly as in the other runs. At 3 Myr the inclination distribution is broader than the initial one, but the disk has preserved its initial orientation.

In Figure 4.4 I show the evolution of the root mean square inclination $\langle i^2 \rangle^{1/2}$ of the stars. In runs A, B and C, $\langle i^2 \rangle^{1/2}$ begins to increase after 0.75 Myr. In run A $\langle i^2 \rangle^{1/2}$ does not increase above 35°, while in run B it continues to increase. In run C the inclination increases more slowly, while in run D the evolution of $\langle i^2 \rangle^{1/2}$ is negligible compared to the other runs.

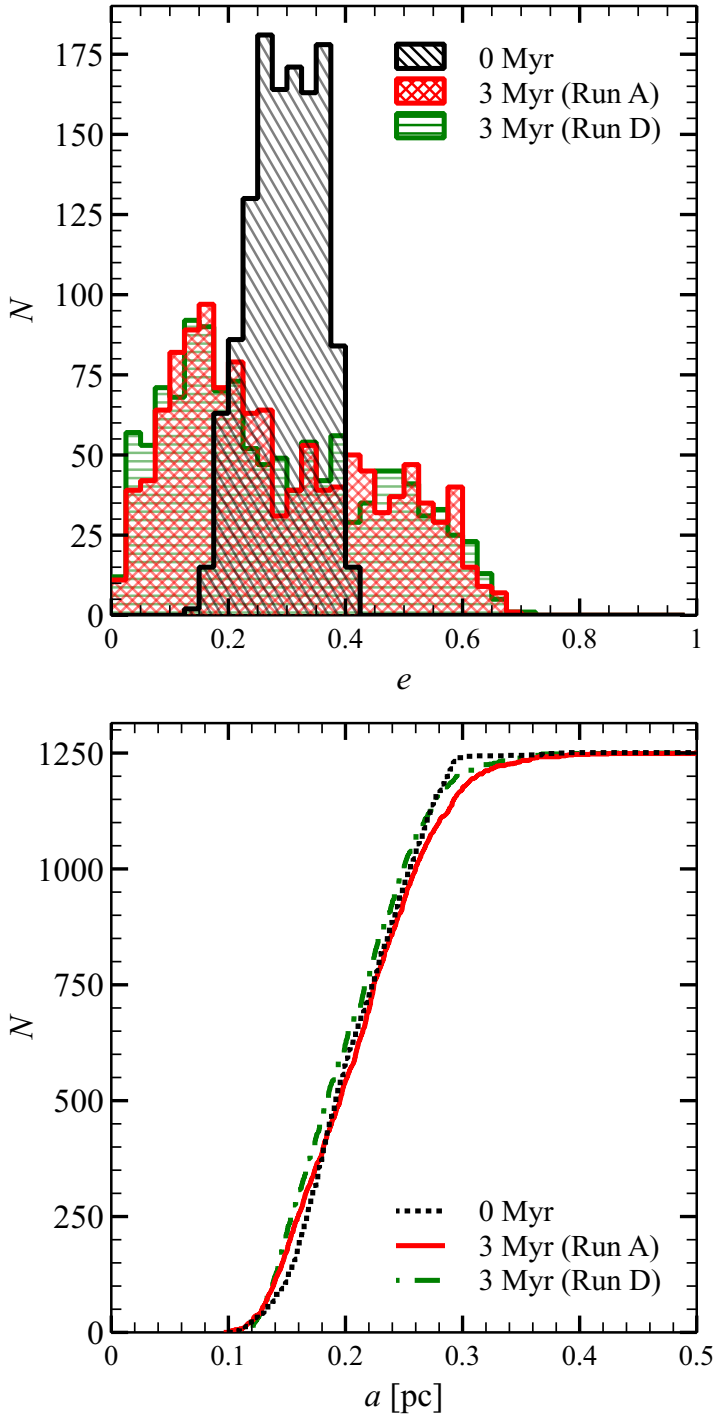

Figure 4.2: Top panel: eccentricity distribution of disk stars. Black hatched histogram: eccentricity distribution at the beginning of the integration. Red cross-hatched area: eccentricity distribution at 3 Myr in run A ($\theta_i = 10°$). Green horizontally-hatched histogram: eccentricity distribution at 3 Myr in run D (no infalling gas cloud). Bottom panel: cumulative distribution of semi-major axis of disk stars. Black dotted line: distribution at the beginning of the integration. Red solid line: run A ($\theta_i = 10°$). Green dot-dashed line: run D (no infalling gas cloud).

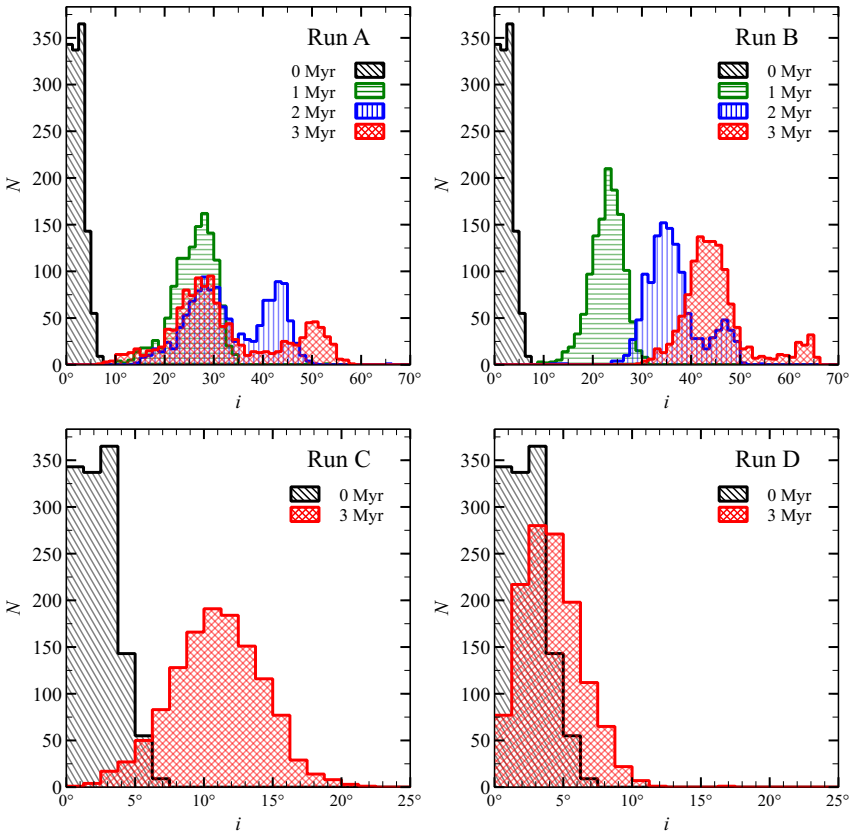

Figure 4.3: Distribution of the inclination of stellar orbits. From top-left to bottom-right: runs A, B, C and D. In all panels, black hatched histogram: distribution at the beginning of the integration; red cross-hatched histogram: distribution at 3 Myr. In the top panels, green horizontally-hatched histogram: distribution at 1 Myr; blue vertically-hatched area: distribution at 2 Myr. In all panels, the inclination is measured with respect to the plane of the stellar disk at 0 Myr.

The large spread in the inclination distribution of runs A and B indicates that the disk loses its coherence. In order to quantify the number of stars that are displaced from the disk, I define the disk membership criterion in a similar way as the one used by Haas, Šubr, and Kroupa (2011). In particular, I assume that a star belongs to the disk if its angular momentum deviates from the mean normalized angular momentum by less than 20°. I recompute the mean normalized angular momentum whenever a star is rejected as a disk member, until the number of disk members does not change anymore.

The number of disk members for different runs as a function of time is shown in Figure 4.5. While the number of disk members remains constant in runs C and D, in the other runs it begins to decrease after 0.75 Myr. In particular, the number of disk members decreases abruptly at ~1 Myr and ~1.25 Myr in runs A and B, respectively. This abrupt change is a consequence of how disk membership is defined,

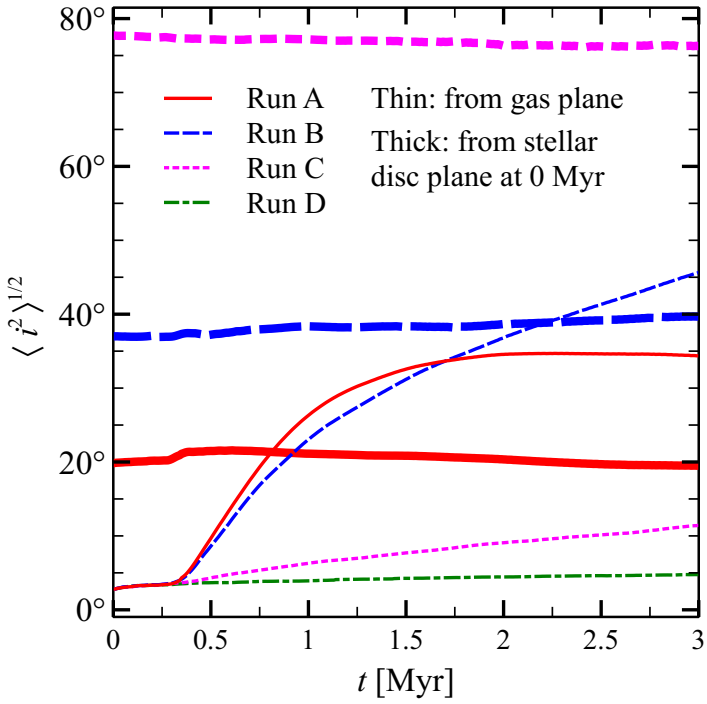

Figure 4.4: Root mean square inclination of the stellar disk as a function of time. Thin lines: inclination measured with respect to the plane of the stellar disk at 0 Myr. Thick lines: inclination measured with respect to the plane of the gas inner ring at 0.5 Myr. Red, solid lines: run A ($\theta_i = 10°$). Blue, dashed lines: run B ($\theta_i = 45°$). Magenta, dotted lines: run C ($\theta_i = 90°$). Green, dot-dashed line: run D (no infalling gas cloud).

indicating that most of the displaced stars cross the 20° threshold approximately at the same time. I find that at 3 Myr the number of disk members decreased by ≈ 30%, 10% in run A and B, respectively.

Figure 4.6 shows the initial position of the stars, with the colors indicating the inclination of the star orbit at 3 Myr in run A. The color gradient indicates that the stars initially on outer orbits reach an higher inclination than the stars on inner orbits.

This trend is confirmed by Figure 4.7, that shows the average inclination as function of semi-major axis for run A, B and C at 3 Myr. In the initial disk the inclinations are of ~7°, regardless of the semi-major axis. At 3 Myr, the average inclination has increased by $30° - 50°$, depending on the run, and the individual inclinations have spread, as shown by the error bars. Moreover, in runs A and B the average inclination is higher for increasing semi-major axis. The origin of these differences between runs is discusses in the next section.

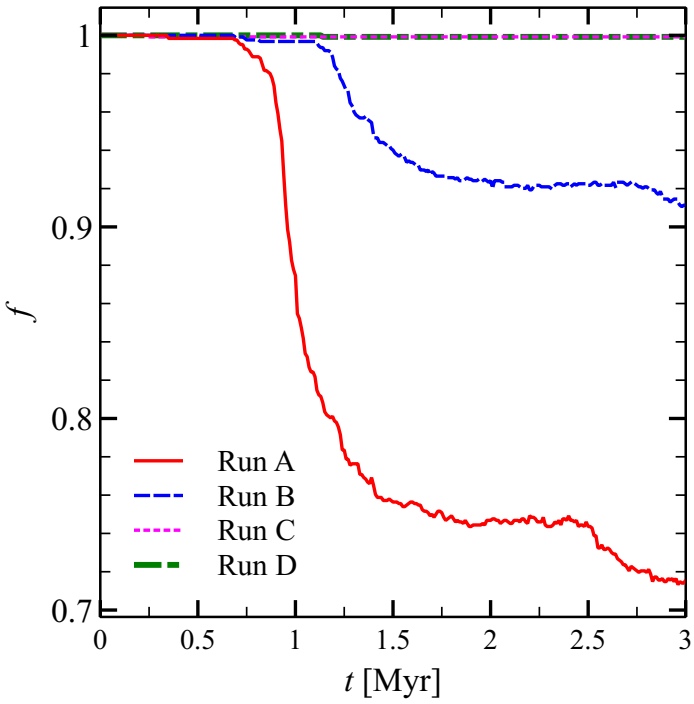

Figure 4.5: Fraction of stars with angular momentum deviating from the total angular momentum of the stellar disk by less than 20° as a function of time. Red, solid line: run A ($\theta_i = 10°$). Blue, dashed line: run B ($\theta_i = 45°$). Magenta, dotted line: run C ($\theta_i = 90°$). Green, dot-dashed line: run D (no infalling gas cloud). The magenta and green lines overlap.

4.4 DISCUSSION

4.4.1 *The importance of the inner gas ring*

In my numerical model, the dynamics of the stellar disk is driven by two processes: two-body relaxation in the stellar disk and precession induced by the external potentials. The external potentials are the analytic cusp, which induces precession of the argument of pericenter and the gas ring. The gas ring is irregular and clumpy, however its potential can consider axisymmetric as a first approximation. Such axisymmetric potential induces precession of the mean orbital elements of a single star on a timescale given by the Kozai-Lidov timescale:

$$T_{KL} = \frac{M_{SMBH}}{M_{CNR}} \frac{R_{CNR}^3}{\sqrt{G M_{SMBH} a^3}} \tag{4.5}$$

where M_{CNR} and R_{CNR} are the mass and radius of the gas ring, G is the gravitational constant and a is the semi-major axis of the star. The equations of motion of the mean orbital elements also depend on eccentricity e and argument of pericenter ω (e.g. see Šubr, Schovancová, and Kroupa 2009).

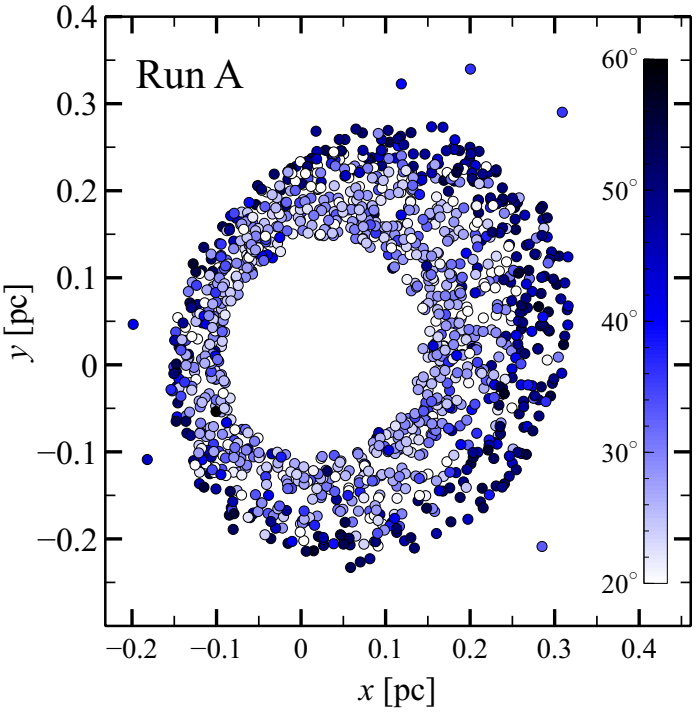

Figure 4.6: Position of disk stars at 0 Myr, projected along the normal to the disk. The circles are colored according to the star inclinations at 3 Myr for run A ($\theta_i = 10°$). The inclinations are measured with respect to the normal to the stellar disk at 0 Myr and range from 20° to 60°.

Since the gas ring is actually composed of two concentric rings, each component induces precession on the stellar disk on a different Kozai-Lidov timescale. The inner ring is less massive than the outer ring by a factor of ~ 30, but has a ~ 5 times smaller radius. Due to the Kozai-Lidov timescale dependence $T_K \propto M_{CNR}^{-1} R_{CNR}^3$, the inner ring induces precession on a shorter timescale than the outer ring. I find $T_K \sim 2$ Myr for the inner ring and $T_K \sim 8$ Myr for the outer ring. Therefore, the precession of stars will be mainly driven by the inner ring, rather than by the outer one.

To check the importance of the outer ring, I run a simulation with the same initial conditions as run A, but removing the gas particles with radius $a > 0.9$ pc from the snapshots of the SPH simulation with $t > 0.5$ Myr. In this way, I remove the outer ring from the simulation without affecting the evolution of the inner ring. In Figure 4.8, I compare the inclination distribution of this run, named A0, with that of run A. The differences between the two runs are negligible, thus the stellar disk is not affected by the outer gas ring, and its evolution is driven mainly by the inner gas ring.

Figure 4.9 shows the time evolution of the density of normal vectors to the stellar orbits in run A. The normal vectors rotate about the angular momentum vector of the inner gas ring (marked with a

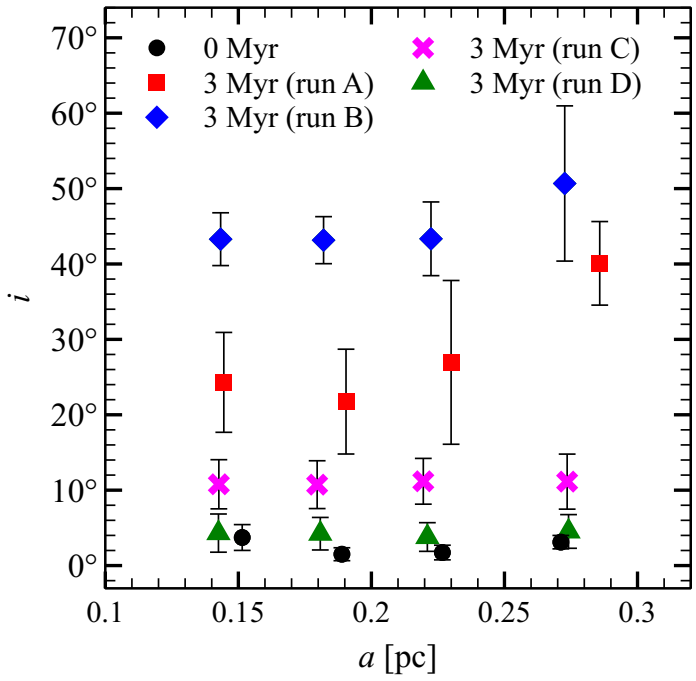

Figure 4.7: Inclination as a function of the semi-major axis binned in four radial bins, so that each bin contains an equal number of stars. Black circles: Inclination at $t = 0\,\mathrm{Myr}$. Red squares: inclination at 3 Myr for run A ($\theta_i = 10°$). Blue diamonds: inclination at 3 Myr for run B ($\theta_i = 45°$). Magenta crosses: inclination at 3 Myr for run C ($\theta_i = 90°$). Green triangles: inclination at 3 Myr for run D (no infalling gas cloud). The inclination is measured with respect to the normal to the stellar disk at 0 Myr. Each point is the average inclination per bin, while the error bars show the standard deviation for each bin.

green cross), losing coherence and forming a spiral-shaped tail. The normal vectors that form the spiral-shaped tail in 4.9 correspond to the secondary peak at 50° in the top-left panel of Figure 4.3. A similar spiral-shaped pattern was found by Löckmann and Baumgardt (2009), who simulated the interaction between two mutually inclined stellar disks (see Fig. 2 of Löckmann and Baumgardt 2009). The formation of the tail is due to the combined effect of two-body relaxation and Ω precession and will be discussed in Section 4.4.2.

In Section 4.3 (Figures 4.3, 4.4 and 4.5), I showed that the inclination distribution changes faster in runs A and B than in run C. The reason is that the precession induced by an axisymmetric potential strongly depends on the angle between the individual stellar orbits and the gas ring. The timescale for precession of the longitude of the ascending node Ω scales as $\cos^{-1}\theta$. In fact, in run C, $\theta_{inner} \simeq 77°$ and the Ω precession is strongly suppressed. As a consequence, the rate of increase of stellar inclinations in run C is much smaller than in run A

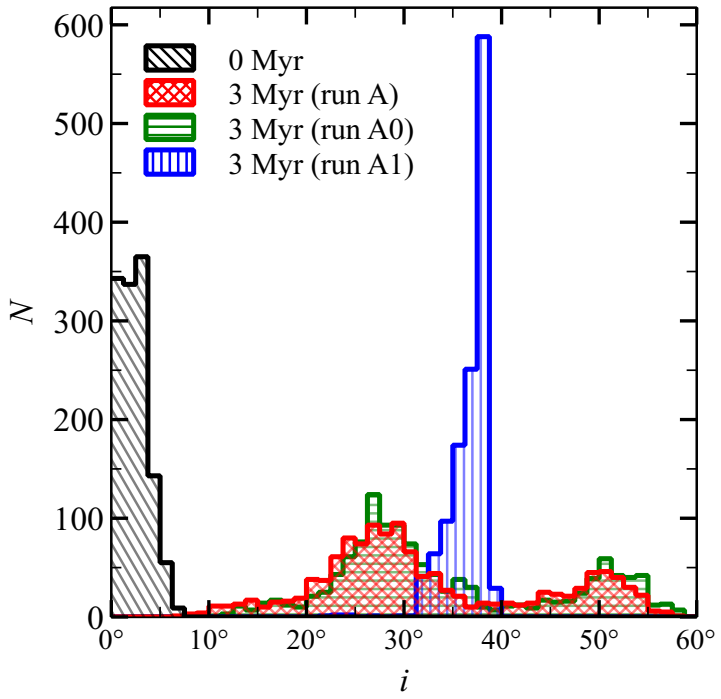

Figure 4.8: Inclination distribution of disk stars. Black, hatched area: 0 Myr. Red, cross-hatched area: run A at 3 Myr ($\theta_i = 10°$). Green, horizontal-hatched area: run A0 at 3 Myr ($\theta_i = 10°$, no outer gas ring). Blue, vertical-hatched area: run A1 at 3 Myr ($\theta_i = 10°$, massless stars). The inclination is measured with respect to the plane of the stellar disk at 0 Myr.

and B, while in run A ($\theta_{inner} \simeq 22°$) is larger than in run B ($\theta_{inner} \simeq 37°$) (Figure 4.4).

However, the increase of stellar inclination in run A halts after 1.5 Myr. This is due the fact that the changes in inclination are related to the changes in the longitude of the ascending node $\Delta\Omega$, which are limited in the range 0-2π. The maximum inclination that can be achieved is $i = 2\,\theta_{inner}$, when $\Delta\Omega = \pi$. Since in run A $\theta_{inner} \simeq 20°$, the inclination does not increase past $i \simeq 40°$. After $\Delta\Omega > \pi$ the inclination should decrease, while in run A it remains approximately constant. This can be due to the fact that these predictions hold in the approximation of a static, axisymmetric potential, while the inner gas ring in my simulations consists of particles that are gravitationally interacting. Two-body relaxation might also play a role in this.

The inner gas ring in the simulations has a density of $10^6\,cm^{-3}$ and a temperature of 100-500 K, indicating that is composed of warm, neutral gas. Jackson et al. (1993) estimated the presence of $\gtrsim 300\,M_\odot$ of dense neutral gas associated to the ionized gas within the cavity of the CNR. This estimate is one order of magnitude smaller than the mass of the inner ring in my simulations, but it is uncertain and only poses a lower limit to the amount of gas present, since it does not ac-

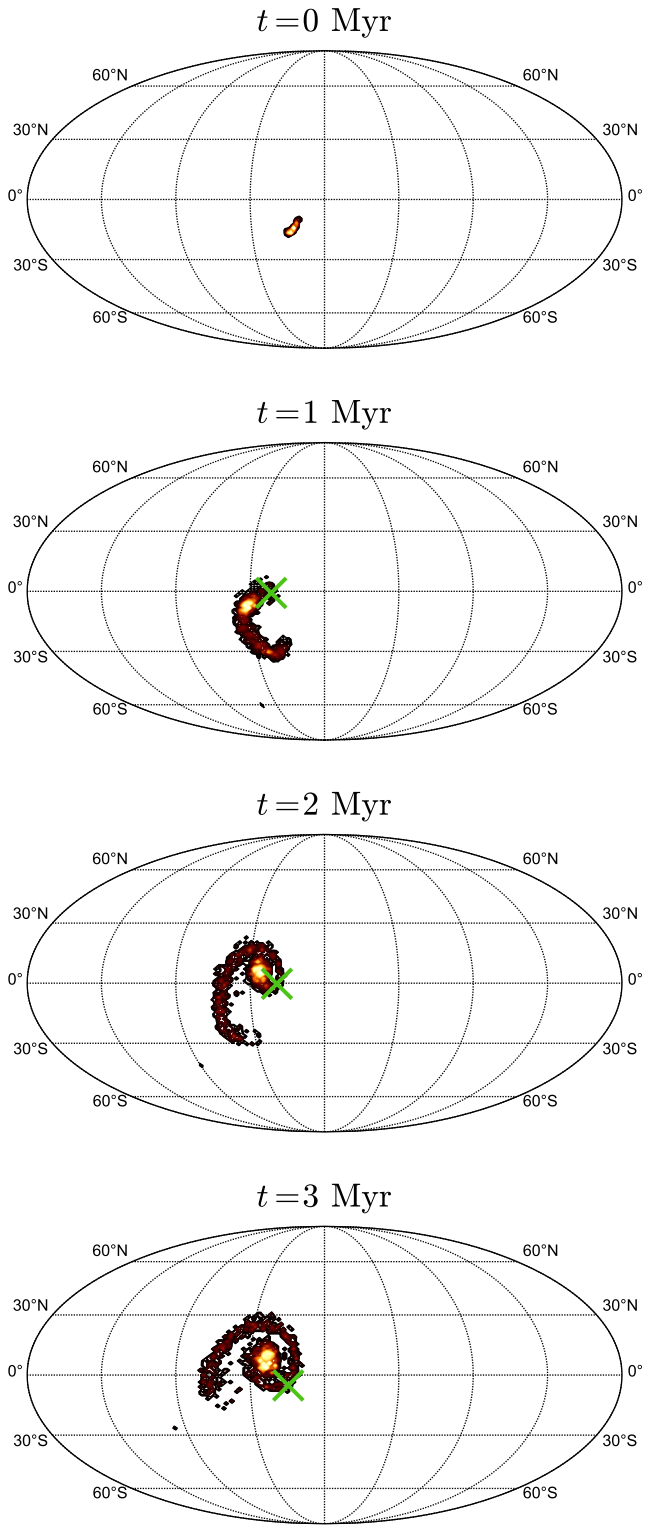

Figure 4.9: Density of normal vectors to the stellar orbits at different times for run A. From top to bottom: $t = 0, 1, 2$ and 3 Myr. The green cross indicates the total angular momentum vector of the inner gas ring (not yet formed at $t = 0$ Myr). Projected using the Mollweide projection.

count for ionized and molecular gas. More recent far-infrared observations suggest that shocks and/or photodissociation dominate the heating of hot molecular gas in central cavity (Goicoechea et al. 2013). Therefore, a more accurate modeling of the central cavity would require a better treatment of ionization and radiative transfer. On the other hand, these results suggest that the kinematics of the CW disk (and of the other young stars) can give us constraints on the gas mass in the central cavity.

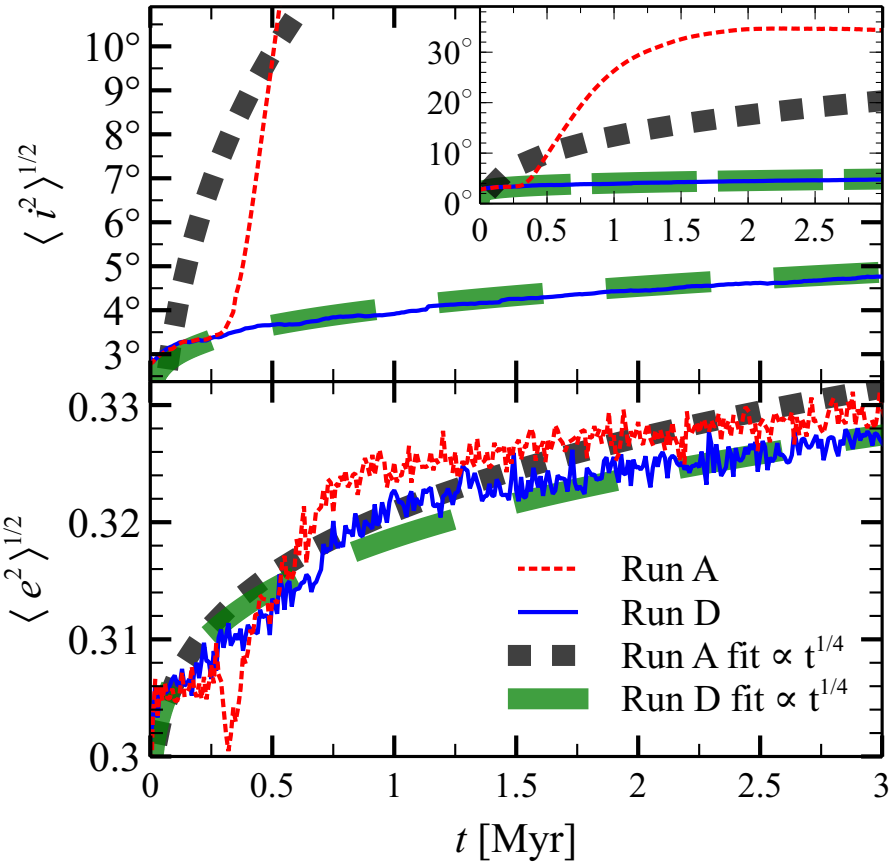

Figure 4.10: Root mean squared inclination (top) and eccentricity (bottom) as a function of time. Thin blue solid line: rms values for run D (no infalling gas cloud). Thin red dotted line: rms values for run A ($\theta_i = 10°$). The thick lines are fit functions $\propto t^{1/4}$, dashed green for run D and dotted black for run A. In the inset: same as the top panel, but zoomed-out to 40°.

4.4.2 *Two-body relaxation*

It has been long demonstrated that the apsidal precession induced by the spherical cusp can suppress Kozai-Lidov cycles (Chang 2009; Löckmann and Baumgardt 2009). Nonetheless, Haas and Šubr (2016) found that oscillations in e and i may still be triggered in an eccentric

disk with aligned apse lines, as in our initial conditions. These oscillations were interpreted by Madigan, Levin, and Hopman (2009) as an eccentric disk instability, which caused the eccentricity distribution to become bimodal. While I do not find evidences of Kozai-Lidov cycles, the inclination and eccentricity distributions evolve throughout my simulations (Figure 4.2, Figure 4.3). The combined effect of two-body relaxation and eccentric disk instability induced by Kozai-Lidov mechanism accounts for changes in eccentricity.

The eccentricity becomes bimodal after 1.5 Myr (Figure 4.2, top panel). This is due to the eccentric disk instability described by Madigan, Levin, and Hopman (2009) and later reinterpreted by Haas and Šubr (2016) as an effect of Kozai-Lidov mechanism between stars of the disk. In fact, I find the same bimodal distribution whether or not I include the gas ring. This result is in agreement with Gualandris, Mapelli, and Perets (2012), who find the same bimodal distribution evolving a similar stellar disk in the potential of a stellar cusp.

While the eccentric disk instability accounts for the bimodality of the eccentricity distribution, two-body relaxation accounts for its overall evolution. According to two-body relaxation theory of thin disks, the root mean square eccentricity and inclination should grow over time as (Stewart and Ida 2000; Šubr and Haas 2014):

$$\langle i^2 \rangle^{1/2} \propto \langle e^2 \rangle^{1/2} \propto t^{1/4} \tag{4.6}$$

Figure 4.10 shows the evolution of $\langle e^2 \rangle^{1/2}$ and $\langle i^2 \rangle^{1/2}$ along with the analytic predictions. It is apparent that the eccentricity evolution is well fit by the analytic predictions for both run A and D. This seems to indicate that the evolution of the eccentricity is predominantly driven by two-body relaxation.

This is not the case for the evolution of inclinations. While the root mean square inclination of run D is consistent with the analytic predictions of two-body relaxation, the fit is inconsistent for run A, B and C. This is due to torques exerted by the gas ring onto the stellar disk. In fact, while the spherical cusp suppresses Kozai-Lidov cycles, it does not hinder the precession of the longitude of the ascending node, measured in the reference frame of the gas ring (Šubr, Schovancová, and Kroupa 2009). Such precession appears as a change in inclination in the reference frame of the stellar disk. This effect is apparent in Figure 4.4, which shows that the root mean square inclination of the stars remains constant if measured from the plane of the inner gas ring.

Moreover, runs A, B and C show higher inclinations at larger radius (Figure 4.7). This is due to the fact that the stars on the outer orbits precess faster than those in the inner ones, as expected from the dependence of precession timescale on the semi-major axis ($T_K \propto a^{-3/2}$, Equation 4.5). This is in agreement with Mapelli, Gualandris, and Hayfield (2013).

Since the stars of the disk have different eccentricity and semi-major axis, they precess at different rates, ultimately causing the disk to dismember. The diffusion of the orbital parameters due to two-body relaxation enhances differential precession, accelerating the dismembering of the disk. To test the importance of two-body relaxation, I run a simulation (named A1) with the same initial conditions as run A, except that I set the stellar masses to zero. In this way I inhibit two-body relaxation, and the evolution of stellar orbits is driven by the external potentials.

The inclination distribution in run A1 at 3 Myr is shown in Figure 4.8. In contrast to run A, the inclinations do not spread and the distribution does not become bimodal. This indicates that the disk changes its orientation without losing coherence and the spiral-shaped tail of normal vectors in Figure 4.9 does not form. Thus, two-body relaxation is a key process in understanding the dismembering of a nearly-Keplerian disk. This result is in agreement with the findings of Haas, Šubr, and Kroupa (2011).

Since the stellar cusp is modeled as a rigid potential, I neglect additional two-body relaxation between cusp and disk stars. Löckmann and Baumgardt (2009) showed that a cusp of stellar remnants enhances the relaxation of angular momentum, increasing orbital eccentricities and disk thickness. However, Löckmann and Baumgardt (2009) find that that relaxation among disk stars dominates over the relaxation between cusp and disk stars. Thus, I expect that a grainy cusp would enhance the disk disruption in my simulations by a negligible amount.

4.5 CONCLUSIONS

I investigate the effect of gas rings on a nearly-Keplerian stellar disk orbiting a SMBH by means of combined SPH and direct N-body simulations. I simulate the formation of a CNR-like gas ring through the infall and disruption of a molecular gas cloud towards the SMBH. In particular, the gas cloud settles down into two concentric rings around the SMBH: the outer ring matches the properties of the CNR in the GC (inner radius $R_{CNR} \sim 1.5\,\mathrm{pc}$, mass $M_{CNR} \sim 10^4\,M_\odot$), while the inner ring is less massive ($\sim 10^3\,M_\odot$) and has an outer radius of $\sim 0.4\,\mathrm{pc}$.

I make use of the AMUSE software to couple the SPH simulation of the infalling gas cloud to a direct N-body code, which I use to integrate the evolution of the stellar disk. The stellar disk has properties similar to the CW disk and was formed self consistently by the infall and collapse of a disrupted molecular cloud. My simulations include the effect of the stellar cusp, modeled as a rigid potential. I simulate different inclinations θ_i between the infalling gas cloud and the stellar disk: $\theta_i = 10°$ (run A), 45° (run B), 90° (run C).

I find that the outer ring is inefficient in affecting the stellar orbits on a timescale of 3 Myr. On the other hand, the inner ring of gas can significantly affect the stellar disk inclination and coherence.

The inner gas ring induces precession of the longitude of the ascending node Ω on the disk stars, which appears as a change of the inclinations in the reference frame of the stellar disk. As a consequence, the disk precesses about the axis of symmetry of the inner gas ring. I do not find precession of eccentricity and inclination with respect to the gas ring, because it is suppressed by the stellar cusp.

I find that the precession of Ω is faster for smaller angles between the stellar disk and the inner gas ring θ_{inner}, as expected from timescale dependence $T_K \propto \cos^{-1}(\theta_{inner})$. After 3 Myr, the stellar disk has changed its orientation by 35°, 45° and 10° in runs A ($\theta_{inner} \simeq 20°$), B ($\theta_{inner} \simeq 37°$) and C ($\theta_{inner} \simeq 77°$), respectively. Since the inclination changes are driven by Ω-precession, the stellar disk inclination cannot increase more than twice the angle between the gas ring and the stellar disk; as a consequence, the stars in run B achieve an higher inclination with respect to run A.

I find that the combined effect of two-body relaxation and Ω-precession can displace stars from the disk. I verified that neither of the two processes can drive the disk dismembering alone. Two-body relaxation introduces a spread in the orbital elements of the individual stars of the disk, inducing differential precession. This differential precession leads to the dismembering of the stellar disk, which loses 30% of the stars in run A ($\theta_{inner} \simeq 20°$) at 3 Myr. In run B ($\theta_{inner} \simeq 37°$), the disk lost only 10% of the stars in 3 Myr, while in run C ($\theta_{inner} \simeq 77°$) Ω-precession is inefficient and the stellar disk remains coherent.

In conclusion, my simulations show that the gas in the innermost 0.5 pc (i.e. the inner cavity) can play a crucial role in the evolution of the stellar orbits in the Galactic center.

5

FORMATION OF CIRCUMNUCLEAR GAS IN GALACTIC NUCLEI: INDICATORS OF SUPERMASSIVE BLACK HOLE PRESENCE

5.1 INTRODUCTION

Circumnuclear gas exhibits a complex morphology and kinematics, with clumpy streamers, warped rings and/or disks that deviate from axisymmetry and circular motion. How the complex spatial and velocity structure of circumnuclear gas forms and evolves remains poorly understood. This uncertainty limits the use of molecular gas dynamics to infer the dynamical mass of SMBHs, a method that is recently emerging thanks to high-resolution (sub-)millimeter interferometry (Davis 2014; Yoon 2017).

In Chapter 3 we have seen that the properties of circumnuclear gas depend on the initial condition of the molecular cloud that gets disrupted in the tidal potential. However, the morphology and kinematics of the gas depends not only on the initial angular momentum (i.e. velocity and impact parameter) of the infalling molecular cloud, but also on the structure of the GN. In particular, the mass of the central SMBH and that of the NSC are expected to dramatically affect the kinematics and morphology of circumnuclear gas.

I present here the first systematic study on the formation of gaseous circumnuclear ring/disks in GNs with properties different from those of the GC. I simulate the infall of a molecular cloud towards the central potential of GNs, composed of a SMBH and the NSC. I run a grid of SPH simulations by varying the mass ratio between the SMBH and the NSC, and study the properties of the resulting distribution of gas and stars formed in the simulations.

In Section 5.2 I describe the methodology I employed for the simulations; in Section 5.3 I present my main results. In Section 5.4, I discuss the impact of the SMBH to NSC mass ratios on circumnuclear gas morphology and its implications for SMBH mass measurement. Finally, the conclusions are presented in Section 5.5. This chapter is based on Trani et al. (2017, to be submitted).

5.2 METHODS

I use the N-body/SPH code GASOLINE2 (Wadsley, Stadel, and Quinn 2004; Read, Hayfield, and Agertz 2010; Wadsley, Keller, and Quinn 2017) to simulate the infall and disruption of a molecular cloud in the central parsecs of GNs.

I consider GNs as composed of a stellar cusp and a central SMBH. The SMBH is a sink particle of mass M_{SMBH} whose position is fixed at the center; in this way I avoid spurious random walk due to numerical effects.

The stellar cusp of the NSC is modeled as a spherical potential and follows a broken power-law density profile:

$$\rho(r) = \rho_0 \left(\frac{r}{r_0}\right)^{-\gamma} \tag{5.1}$$

I use the values given by Schödel et al. (2007) for the cusp of the Milky Way: $\gamma = 1.75$ for $r > r_0$ and $\gamma = 1.2$ for $r < r_0$, where $r_0 = 0.22\,pc$. The cusp is truncated at $r_{trunc} = 10\,pc$ and has a total mass of M_{cusp}. I choose ρ_0 in the following way: first I fix the total mass $M_{tot} = M_{cusp} + M_{SMBH}$ of the GN and the SMBH mass M_{SMBH}. Then I pick ρ_0 so that $M_{cusp} = \int 4\pi\rho(r)r^2 dr = M_{tot} - M_{SMBH}$.

I run two sets of simulations, each with a different value of M_{tot}: 1×10^7 and $5 \times 10^6\,M_\odot$. For each set I run four simulations choosing M_{SMBH} so that $f_{SMBH} = M_{SMBH}/M_{tot} = 0.5, 0.2, 0.1$ and 0.05. This choice lets me explore the parameter space of SMBH and NSC masses while giving at the same time masses consistent with the observations (Seth et al. 2008b; Graham and Spitler 2009; Kornei and McCrady 2009; Kormendy and Ho 2013; Georgiev and Böker 2014; Georgiev et al. 2016).

From the values of the SMBH mass and the NSC cusp profile, I derive the radius of the sphere of influence of the SMBH R_{SOI}. While usually the sphere of influence is defined as the region enclosing a total mass twice that of the SMBH mass, this definition is valid only for an isothermal sphere model of the NSC. Therefore, R_{SOI} is computed numerically from the equation $\Phi_{SMBH} = \Phi_{cusp}$, where Φ_{SMBH} and Φ_{cusp} are the gravitational potential of the SMBH and of the cusp, respectively. Table 5.1 summarizes the main properties of the simulations presented in this paper.

In all simulations, the molecular cloud is modeled as a homogeneous gas sphere of $10^5\,M_\odot$ and 15 pc radius, located at 26 pc from the SMBH. The cloud is seeded with turbulent velocity and marginally self-bound. The velocity field is generated using a grid method (Dubinski, Narayan, and Phillips 1995) from a divergence-free, random Gaussian field with a power spectrum $P(k) = \|\delta v_k\|^2 \propto k^{-4}$. The spectral index -4 reproduces turbulence in agreement with the velocity dispersion relation $\sigma_v \propto l^{0.5}$ observed in molecular clouds (Larson 1981).

The cloud has an impact parameter of $b = 15\,pc$ with respect to the SMBH and an initial velocity of $v_i = 0.2 v_{esc}$, where v_{esc} is the escape velocity of the cloud, taking into account the potential of the SMBH and the NSC. The initial velocity is $v_i = 12$ and $8.1\,km\,s^{-1}$ in the runs with $M_{tot} = 1 \times 10^7$ and $5 \times 10^6\,M_\odot$, respectively. I choose the

RUN	M_{tot}	M_{SMBH}	f_{SMBH}	R_{SOI}	m_{res}
mt1e7_bh5e6	1×10^7	5×10^6	0.5	>10	0.5
mt1e7_bh2e6	1×10^7	2×10^6	0.2	0.90	0.5
mt1e7_bh1e6	1×10^7	1×10^6	0.1	0.35	0.5
mt1e7_bh5e5	1×10^7	5×10^5	0.05	0.15	0.5
mt5e6_bh2.5e6	5×10^6	2.5×10^6	0.5	>10	0.5
mt5e6_bh1e6	5×10^6	1×10^6	0.2	0.90	0.5
mt5e6_bh5e5	5×10^6	5×10^5	0.1	0.35	0.5
mt5e6_bh2.5e5	5×10^6	2.5×10^5	0.05	0.15	0.5
mt1e7_bh5e6_hr	1×10^7	5×10^6	0.5	>10	0.05
mt1e7_bh1e6_hr	1×10^7	1×10^6	0.1	0.35	0.05
mt1e7_bh5e5_hr	1×10^7	5×10^5	0.05	0.15	0.05
mt5e6_bh1e6_hr	5×10^6	5×10^5	0.2	0.35	0.05
mt5e6_bh2.5e5_hr	5×10^6	2.5×10^5	0.05	0.15	0.05

Table 5.1: Main properties of the simulations. Column 1: run name; column 2: mass enclosed in a 10 pc radius M_{tot} in $M_\odot$, composed of the stellar cusp and the SMBH; column 3: mass of the SMBH M_{SMBH} in $M_\odot$; column 4: mass of the SMBH with respect to total mass enclosed f_{SMBH}; column 5: radius of sphere of influence R_{SOI} of the SMBH in pc; m_{res} is the mass resolution of the simulation in $M_\odot$.

coordinate system so that the total velocity vector lies in the x-y plane. The mass of the gas particles is $m_{res} = 0.05\,M_\odot$ in high-resolution runs and $0.5\,M_\odot$ in every other runs. I stop the simulations at 3 Myr.

I model star formation via sink particle creation, implemented following the criteria of Bate, Bonnell, and Price (1995) and Federrath et al. (2010). Specifically, a gas particle is considered a sink candidate if it exceeds a threshold density ρ_{thr}. Neighboring sink candidates within r_{accr} from the densest candidate are then replaced by a sink particle only if they fulfill the following requirements: (i) the divergence of the accelerations is negative (i.e. the flow is accelerating), (ii) the divergence of the velocity is negative (i.e. the flow is converging), (iii) the eigenvalues of the Jacobian of the velocity are negative (i.e. the flow is converging in every direction), (iv) the total thermal energy is less than the total gravitational energy (i.e. they must be thermally subvirial), (v) the total energy is negative (i.e. they must be bound).

In addition, sink particles are allowed to accrete gas particles within r_{accr} if (a) the gas particle is bound to the sink, (b) the specific angular momentum of the particle about the sink is less than required to form a circular orbit at r_{accr}, (c) the gas particle is more tightly bound to the considered sink particle than to other sink particles.

In Gasoline2, the artificial viscosity is implemented as in Monaghan (1997), which proposed a modified version of the classical SPH viscosity (Monaghan 1992) based on an analogy to the Riemann problem. The formulation of Monaghan (1997) treats shocks reflecting the signal speed, i.e. the maximum velocity with which information can be transported between particles. To suppress viscosity away from shocks, I employ the Cullen and Dehnen (2010) viscosity limiter, which uses the total time derivative of the velocity divergence as shock indicator. Unlike previous methods based only on the velocity divergence (e.g. Morris and Monaghan 1997), the Cullen and Dehnen (2010) limiter distinguishes pre-shock from post-shock regions and discriminates much better between converging flows and weak shocks.

I choose $\rho_{thr} = 10^{-17}\,g\,cm^{-3}$, which approximately corresponds to a Toomre Q parameter of 1 at 0.1 pc from the central SMBH. I performed tests to ensure that different values of ρ_{thr} do not impact significantly on the mass function of the formed sink particles. I adopt a gravitational softening length of 10^{-3} pc and 5×10^{-4} pc in runs with $m_{res} = 0.5\,M_\odot$ and $m_{res} = 0.05\,M_\odot$, respectively. I choose a sink radius of $r_{accr} = 2.5 \times 10^{-3}$ pc.

All simulations include radiative cooling algorithm as described in Boley (2009) and Boley et al. (2010). The cooling is calculated from $\nabla\dot{F} = -(36\pi)^{1/3}\,s^{-1}\,\sigma\left(T^4 - T_{irr}^4\right)(\Delta\tau + 1/\Delta\tau) - 1$, where $s = (m/\rho)^{1/3}$ and $\Delta\tau = sk\rho$, for the local opacity k, particle mass m, and density ρ. D'Alessio, Calvet, and Hartmann (2001) opacities are used, with a 1 μm maximum grain size. The irradiation temperature is $T_{irr} = 100\,K$ everywhere.

5.3 RESULTS

5.3.1 *Evolution of molecular gas*

In Figure 5.1 I show the time evolution of the gas cloud in run `mt1e7_bh5e5_hr` ($f_{SMBH} = 0.05$, third and fourth column) and run `mt1e7_bh5e5_hr` ($f_{SMBH} = 0.2$, first and second column). The evolution of gas is very different between the two runs.

In run `mt1e7_bh5e5_hr` the gas cloud is disrupted more rapidly due to the higher total mass ($M_{tot} = 10^7\,M_\odot$). In the first 0.5 Myr the gas is stretched into a nearly-radial streamer, in which high-density clumps are formed. Afterwards, the gas begins to fall back, intersecting the part of the cloud that is still falling towards the center. At 1 Myr the head of the stream is undergoing a third pericenter passage which is slightly off-set form the first. The streamer follows a rosette-like orbit, which causes it to self-interact and lose eccentricity. At ~1.7 Myr the gas cloud has been completely disrupted and a clumpy, eccentric ring becomes definite. The ring shows a large cavity since little gas is captured by the SMBH.

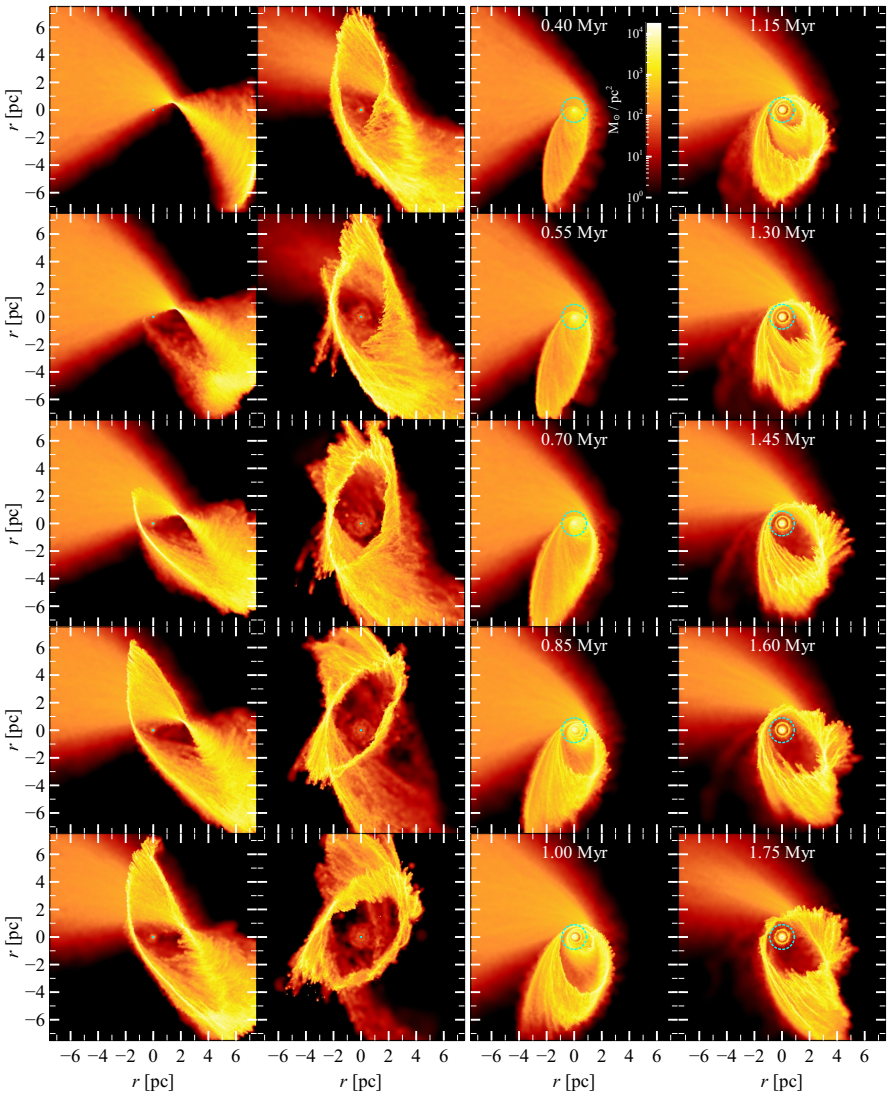

Figure 5.1: Color-coded density map of gas in run `mt1e7_bh5e5_hr` (first and second column) and run `mt5e6_bh5e5_hr` (third and fourth column), projected to the x-y plane of the simulation. From top to bottom and left to right: t = 0.4, 0.55, 0.7, 0.85, 1, 1.15, 1.3, 1.45, 1.6 and 1.75 Myr. The dotted cyan circle indicates the SMBH radius of influence R_{SOI}, which is 0.15 and 0.35 pc in run `mt1e7_bh5e5_hr` and `mt5e6_bh5e5_hr`, respectively.

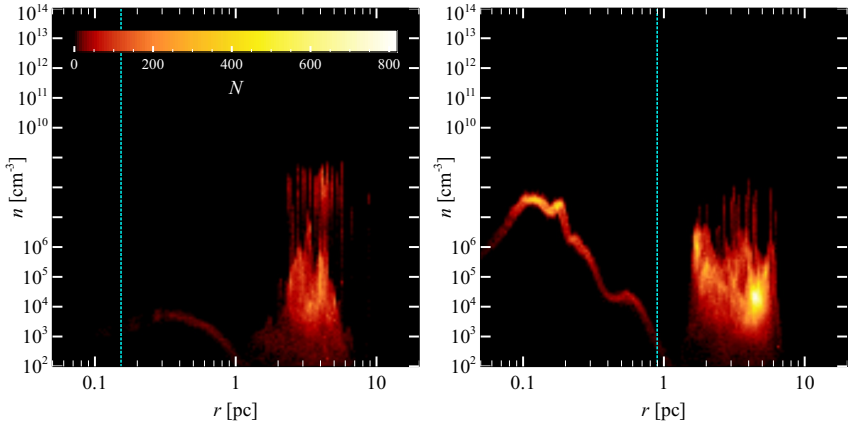

Figure 5.2: Number density of gas as a function of distance from the central SMBH for run `mt1e7_bh5e5_hr` (left-hand panel) and run `mt5e6_bh1e6_hr` (right-hand panel) at 2.5 Myr. The color scale indicates the number of gas particles. The cyan dotted line is the SMBH influence radius R_{SOI}.

Conversely, in run `mt5e6_bh1e6_hr`, the trajectory of the infalling gas is deflected by the SMBH gravity and gas winds up around the SMBH, forming a flattened disk (0.6 Myr). The streamers that compose the disk interact among themselves and with the rest of the cloud that is still falling towards the center. At 1 Myr, there are four distinct structures: a small circular disk of ~0.2 pc radius around the SMBH and three eccentric rings. The eccentricity of the rings increases with their distance from the SMBH and their pericenter is mutually aligned. The two external rings are formed by several streamers. The rings precess because of the cusp potential, so that their pericenter advances along the orbit (in Figure 5.1 it moves clockwise). At 1.4 Myr, the disappearance of the intermediate ring is due to two factors: first, the ring fragments and forms pre-stellar cores, which decouple from the gas (see Section 5.3.2); second, the ring expands radially while accreting material from the cloud, and eventually merges with the external ring. The cloud is completely disrupted at ~1.7 Myr. In the end, the inner ring and the disk have merged into a single disk which remains inside the SMBH sphere of influence.

Figure 5.2 compares the density of gas particles as a function of the distance from the SMBH in run `mt1e7_bh5e5_hr` (left-hand panel) and run `mt5e6_bh1e6_hr` (right-hand panel) at 2.5 Myr. Both simulations exhibit a 10^4-10^5 cm^{-3} dense ring outside R_{SOI} which embeds several higher density (10^7-10^8 cm^{-3}) clumps. However, only in run `mt5e6_bh1e6_hr` a dense disk is present inside R_{SOI}. The disk has a maximum density of ~10^7 cm^{-3} at 0.08-0.2 pc, which decreases outwards up to the disk outer edge at $R_{SOI} = 0.9$ pc.

The disk that forms around the SMBH has increasing eccentricity for increasing semimajor axis, as shown in the left-hand panel of Figure 5.3. This is caused by the broad range of impact parameters

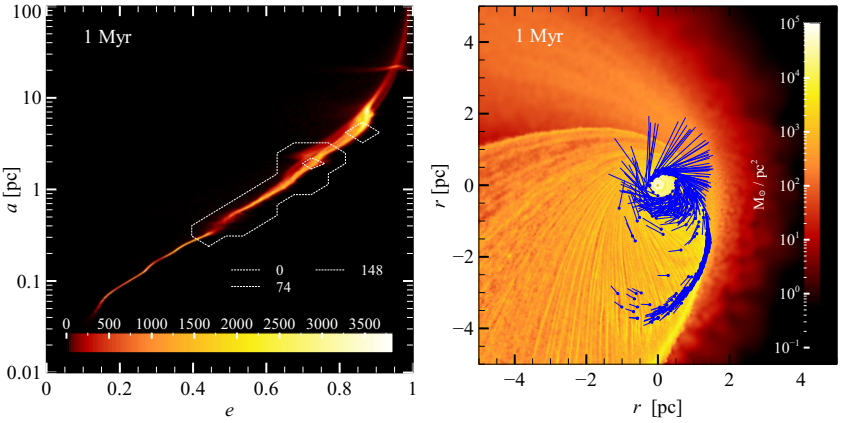

Figure 5.3: Left-hand panel: semimajor axis versus eccentricity for gas particles (color scale) and stars (contour plot) for run `mt1e7_bh5e6_hr` at 100 Myr. The color scale and the contour levels indicate the number of gas and star particles, respectively. Right-hand panel: color-coded, projected density map of gas in the x-y plane for the same run at the same snapshot. The blue pluses mark the stars (i.e. sink particles) formed during the simulation. The small blue segments are aligned along the velocity vector of the sink particles, and corresponds to the distance the particle would cover in 5000 yr.

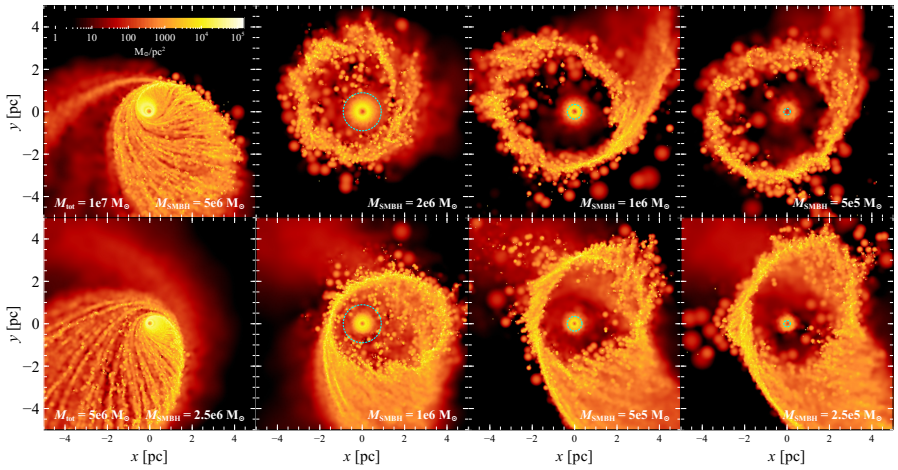

Figure 5.4: Color-coded, projected density map of gas in the x-y plane for the two sets of runs (rows), comprising of four initial setups (columns, see Table 5.1). Each panel corresponds to a different simulation. From top to bottom, each row has $M_{tot} = M_{cusp} + M_{SMBH}$ of 1×10^7 and $5 \times 10^6\,M_\odot$ respectively. From left to right, each column has $f_{SMBH} = M_{SMBH}/M_{tot} = 0.5, 0.2, 0.1$ and 0.05. The dotted cyan circle indicates the SMBH radius of influence R_{SOI}. Top (bottom) row corresponds to a time of 1 Myr (1.5 Myr) from the start of the simulations. Each simulation snapshot in a row is taken at a different times because the gas cloud evolves more slowly in simulations with lower M_{tot}.

of individual gas particles with respect to the SMBH, which results from the large (15 pc) extent of the original cloud. Gas particles with a small impact parameter get captured into tighter, more circular orbits, while gas particles with a large impact parameter settle on larger orbits with higher eccentricity (see also Section 3.3 for a discussion about the effect of initial impact parameters.).

Neighboring streamlines in the disk intersect because of the eccentricity gradient. This gives rise to shocks in the disk (Figure 5.3, right-hand panel). The shocks tend to damp the eccentricity of the disk, although the disk never circularizes completely in any of the simulations.

RUN	r^{in}_{disk}	r^{out}_{disk}	M_{disk}	n_{disk}	r^{in}_{ring}	r^{out}_{ring}
`mt1e7_bh5e6`	0.1	7	7.7×10^4	10^7	–	–
`mt1e7_bh2e6`	0.1	0.9	5800	10^7	1.5	3
`mt1e7_bh1e6`	0.1	0.4	2000	5×10^6	2	4.5
`mt1e7_bh5e5`	0.1	0.3	350	10^5	2	4
`mt5e6_bh2.5e6`	0.1	7	6×10^4	10^7	–	–
`mt5e6_bh1e6`	0.1	0.6	3200	5×10^6	1.5	3.5
`mt5e6_bh5e5`	0.1	0.4	1400	0.35	1.5	3
`mt5e6_bh2.5e5`	0.1	0.3	370	0.15	2	4

Table 5.2: Main outcomes of the simulations. Column 1: run name; column 2: inner radius of the central disk in pc; column 3: outer radius of the central disk in pc; column 4: mass of the central disk in $M_\odot$; column 5: average density of the inner disk in cm^{-3}; inner radius of the ring in pc; column 6 outer radius of the ring in pc.

Figure 5.4 shows the projected density map of the whole grid of simulations at different snapshots. The total mass M_{tot} of the GN decreases from top to bottom, while the mass ratio between the mass of GN and the SMBH f_{SMBH} decreases from left to right. The morphology of circumnuclear gas shows a clear trend with f_{SMBH}. At $f_{SMBH} = 0.5$, the whole cloud gets flattened into an eccentric, extended disk around the SMBH. As the mass of the SMBH becomes lower with respect to that of the NSC ($f_{SMBH} \leqslant 0.2$), the gas gets squeezed into a compact ring outside the sphere of influence of the SMBH. A disk of material captured by the SMBH potential resides within the cavity of the ring.

Table 5.2 summarizes the properties of the disk and the inner ring after the complete disruption of the cloud. While the entire cloud becomes part of the disk for the runs with $f_{SMBH} = 0.5$, only a small fraction of the gas gets captured into the inner disk at smaller f_{SMBH}. Also the size of the disk decreases for decreasing f_{SMBH}. In particular, in runs with $f_{SMBH} = 0.2$ and 0.1 the inner disk resides inside the

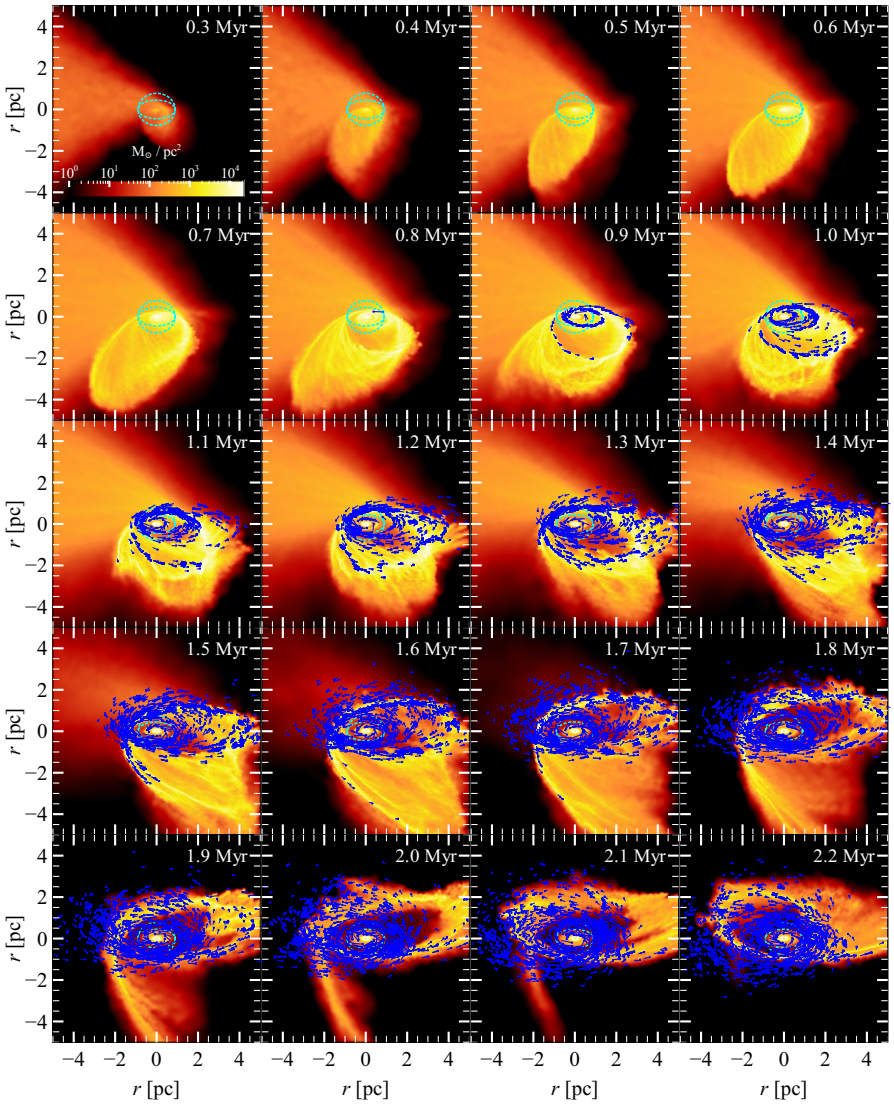

Figure 5.5: Color-coded, density map of gas in run `mt5e6_bh1e6_hr` as a function of time, projected to a view angle inclined by 30° with respect of the x-y plane of the simulation. From top to bottom, and left to right, the time of the simulation increases by 0.1 Myr in each snapshot. The first snapshot on the top left is taken at 0.2 Myr from the beginning of the simulation. The blue pluses mark the stars (i.e. sink particles) formed during the simulation. The small blue segments are aligned along the velocity vector of the sink particles, and corresponds to the distance the particle would cover in 5000 yr. The small and large dotted cyan ellipsis indicate the SMBH radius of influence along the y and z axis, respectively.

sphere of influence of the SMBH, while in the runs with $f_{SMBH} = 0.05$ it extends up to $2R_{SOI}$ (right-hand column of Figure 5.4). The disk inner edge is 0.1 pc in every simulation, which is likely due to the sink radius of the SMBH.

5.3.2 *Formation and dynamical evolution of stars*

In all simulations, the gas fragments and forms stars (or pre-stellar cores) in orbit around the central potential. In general, once the stars are formed, they decouple from the parent gas and take a different dynamical evolution. The effects are more dramatic in simulations with high f_{SMBH}.

In Figure 5.5 I show the time evolution of gas and stars in run `mt5e6_bh1e6_hr`. Stars begin to form in the dense, eccentric gaseous rings that appear during the disruption of the cloud. At this stage, the rings are still accreting gas and are rapidly evolving due to shear and viscous forces, which do not affect the stars. Consequently, the stars keep the orbital properties of the gas at the time of their formation. Stars formed at 0.9 Myr in the middle ring keep orbiting close to the SMBH even after their parent gas ring merges into the external ring at 1.2 Myr.

This is apparent from Figure 5.6, which compares the eccentricity and semimajor axis distributions of gas and stars in run `mt5e6_bh1e6_hr` at different times. The high density spot at 20 pc corresponds to the bulk of the cloud, which has not been disrupted yet at 0.9 Myr . The middle ring of Figure 5.5 corresponds to the density increase at ~1 pc in Figure 5.6. At this time, the eccentricity and semimajor axis of gas and star particles coincide. As the gas evolves, the inner disk at 0.05-0.2 pc circularizes and the middle ring moves to larger radius and higher eccentricity. On the other hand, the distribution of stars follows a different evolution: at 1.5 Myr, the stars have retained the semimajor axis at their formation time and moved towards lower eccentricity.

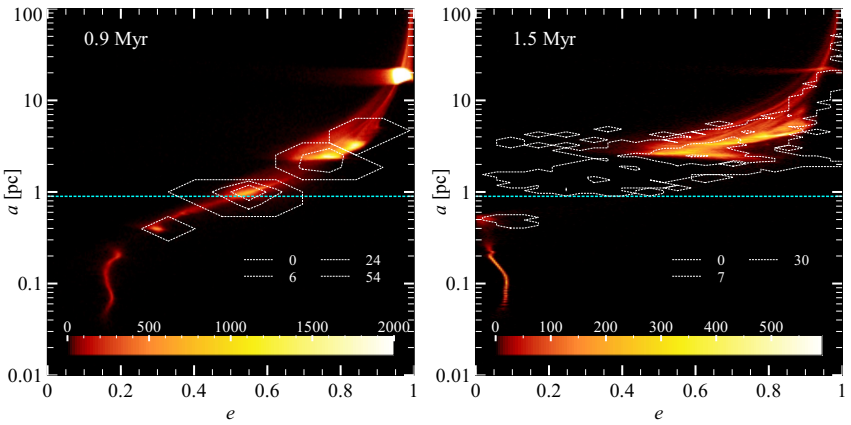

Figure 5.6: Semimajor axis versus eccentricity for gas particles (color scale) and stars (contour plot) for run `mt5e6_bh1e6_hr` at two different times. Left-hand panel: 0.9 Myr. Right-hand column: 1.5 Myr. The color scale and the contour levels indicate the number of gas and star particles, respectively. The dotted cyan line indicates the SMBH radius of influence R_{SOI}.

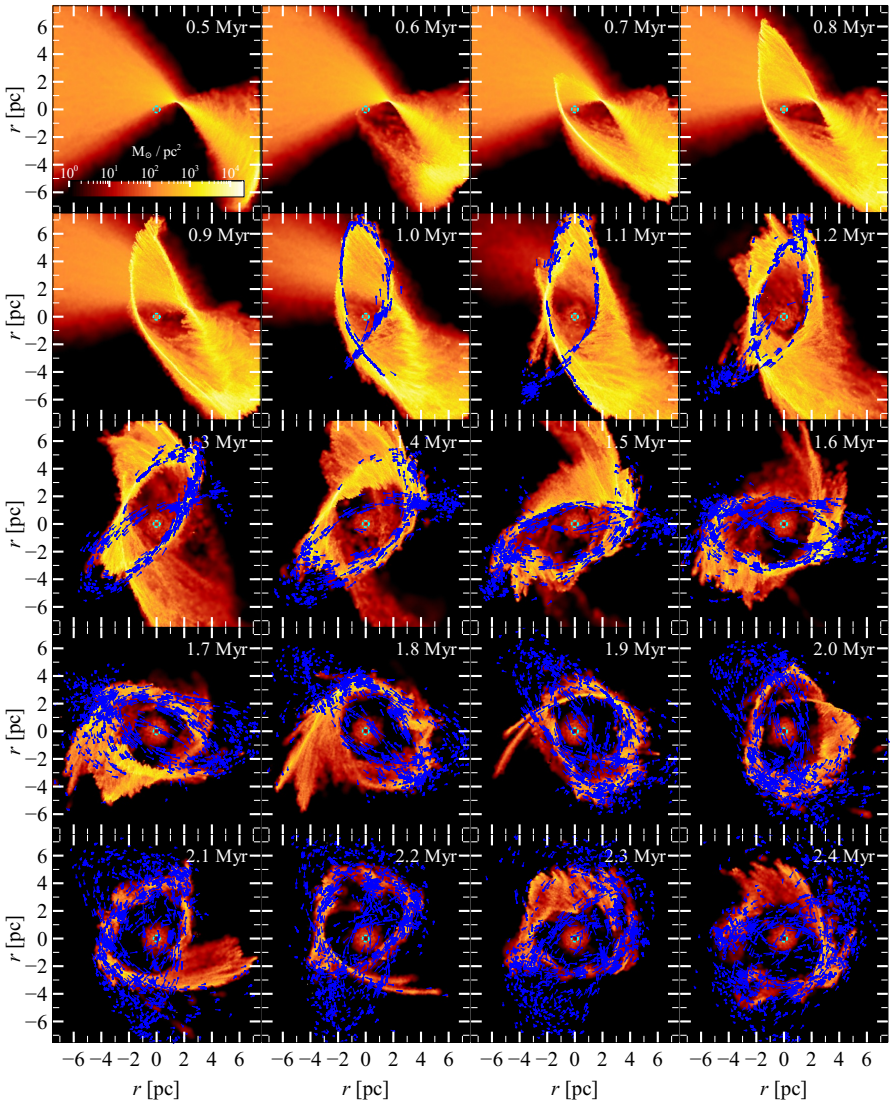

Figure 5.7: Color-coded, density map of gas in run `mt5e6_bh1e6_hr` as a function of time projected to x-y plane. From top to bottom, and left to right, the time of the simulation increases by 0.1 Myr in each snapshot. The first snapshot on the top left is taken at 0.2 Myr from the beginning of the simulation. The blue pluses mark the stars (i.e. sink particles) formed during the simulation. The small blue segments are aligned along the velocity vector of the sink particles, and corresponds to the distance the particle would cover in 5000 yr. The cyan dotted circle indicates the SMBH radius of influence R_{SOI}.

Figure 5.7 shows the evolution of gas and stars in run `mt1e7_bh5e5_hr`. Stars form in the near-radial, high-density streamer during its second pericenter passage. Afterwards, the gas streamer self-interacts and undergoes circularization, whereas the stars remain on eccentric orbits. Stars form also after the part of the gas has circularized, so that the final configuration consists in a semi-circularized

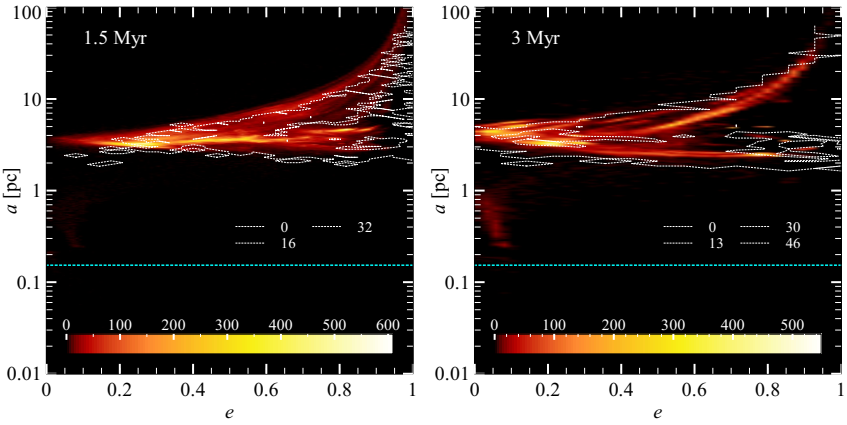

Figure 5.8: Top panels: semimajor axis versus eccentricity for gas particles (color scale) and stars (contour plot) for run `mt1e7_bh5e5_hr` at two different times. Bottom panels: pericenter distance versus eccentricity. Left-hand column: 1.5 Myr. Right-hand column: 3 Myr. The color scale and the contour levels indicate the number of gas and star particles, respectively. The dotted cyan line indicates the SMBH radius of influence R_{SOI}.

gaseous ring and stars with broad range of eccentricity (Figure 5.8, right-hand panel).

5.4 DISCUSSION

The simulations show that the evolution of gas changes drastically depending on the relative masses of SMBH and NSC. The mass ratio between SMBH and NSC determines the radius of the SMBH sphere of influence R_{SOI} (see fifth column of Table 5.1), the region in which the dynamics becomes Keplerian. The simulations indicate that gas inside or close to R_{SOI} exhibits a disk morphology, whereas gas settling further out likely forms an eccentric, clumpy ring with characteristics similar to the CNR in the GC.

This is due to the way the tidal potential compresses and shapes the cloud as it gets disrupted. Gas captured in the SMBH sphere of influence tends to wind up around the SMBH, following eccentric Keplerian orbits. In this case, the gas undergoes circularization through shocks between intersecting disk streamlines. Star formation occurs in the densest streamers, and stars remain embedded into the gaseous disk (right-hand panel of Figure 5.3) A peculiar feature of this formation mechanism is that the eccentricity of the disk increases from inside out (left-hand panel of Figure 5.3) and the apsis lines are mutually aligned.

On the other hand, gas that falls into the potential well of the NSC without reaching R_{SOI} is stretched into a nearly-radial streamer. This occurs because the gravitational acceleration exerted by the NSC scales as $r^{1-\gamma}$, where γ is the density power-law index. Since γ ranges

from 1.2 to 1.75, the acceleration induced by the NSC increases very slowly with r and is not able to strongly alter the orbit of the streamers. In this case, circularization is induced by the streamers self-interactions as they follow a rosette-like orbit. Stars formed in the densest gas quickly decouple from the parent streamers since they are not subject to shocks and viscous forces. As a consequence, stars remain into eccentric orbits while the gas streamers form a clumpy, mildly eccentric ring (or annulus).

This mechanism can naturally explain why the CNR in the GC presents an inner cavity and does not extend below 1.5-2 pc radius (Oka et al. 2011; Liu et al. 2012, 2013; Mills et al. 2013; Smith and Wardle 2014; Harada et al. 2015; Takekawa, Oka, and Tanaka 2017; Mills, Togi, and Kaufman 2017; Sandqvist et al. 2017). Using the mass profile of Genzel et al. (2003b) for Milky Way's NSC and the mass estimate of (Gillessen et al. 2017) for Sgr A*, the SMBH influence radius turns out to be $R_{SOI}^{GC} \simeq 0.4\,pc$, much smaller than the inner edge of the CNR.

Another implication is that the formation of compact, CNR-like rings is not expected in GNs lacking a NSC, since the stellar potential would be too shallow to tidally disrupt a molecular cloud. These findings suggest that the radius of a CNR-like ring in a nucleated GN could be used as an upper limit of the SMBH influence radius (and thus of the SMBH mass), in the hypotheses that the gaseous ring formed according to this mechanism.

Furthermore, $R_{SOI}^{GC} \simeq 0.4\,pc$ is also the outer edge of the CW disk according to Bartko et al. (but see also Yelda et al. 2014, who estimate the outer edge at 0.13 pc). The CW disk might have originated from the fragmentation of an eccentric disk of gas (Nayakshin, Cuadra, and Springel 2007; Bonnell and Rice 2008; Mapelli et al. 2008; Hobbs and Nayakshin 2009; Alig et al. 2011; Mapelli et al. 2012; Lucas et al. 2013). This picture is consistent with the scenario presented here, in which an eccentric gaseous disk is expected to form at $r \lesssim 2R_{SOI}$ if a gas cloud penetrates the SMBH sphere of influence.

These results indicate that it is difficult to form a CNR-like ring without depositing some gas close to the SMBH. This strengthens the idea that the hot molecular gas observed near Sgr A* might be connected to the formation of the CNR.

Interestingly, the CO brightness distribution in the nucleus of NGC 3665 shows a central gap, which coincides with the estimated R_{SOI} of the central SMBH (see Fig. 6 of Onishi et al. 2017). It is unclear whether the gap inside R_{SOI} is due to the dissociation of molecular gas or to the absence of gas in the inner region. Based on the results shown in this Chapter and in Chapter 3, a possible explanation for the deficit of gas inside R_{SOI} is the lack of molecular clouds with angular momentum low enough to be captured by the SMBH gravity and form a disk.

However, the lack of CO emission in the R_{SOI} region of NGC 3665 can be due also to changes of composition in the molecular gas. The simulations presented here do not take into account the evolution of the gas chemistry. In the next study I will include non-equilibrium chemistry, which will allow to follow the formation and destruction of H_2 and CO self-consistently throughout the simulations.

5.4.1 *Caveats*

In this study, I did not examine the impact of the initial conditions on the formation of circumnuclear gas, which was instead investigated in Chapter 3. Following the results of Chapter 3, we can safely conclude that the initial conditions will not affect the morphology of the gas inside and outside R_{SOI}, which instead is mainly determined by the shape of the potential. On the other hand, the initial conditions will determine if gas can actually reach R_{SOI} and thus form a disk structure close to the SMBH.

In the simulations, the density profile of the NSCs is modeled as in Milky Way's NSC, i.e. as broken-power law cusped profile (Genzel et al. 2003a). While this is a conservative choice, the density profile of extra-galactic NSCs might be different. Present-day observations are not able to resolve in detail the luminosity profile at the very center of NSCs, and in recent surveys the surface brightness profiles of NSCs were fitted with a cored King (1962) model (Georgiev and Böker 2014; Georgiev et al. 2016).

Even so, a SMBH embedded into a star cluster is expected to develop a stellar cusp in about a relaxation time, which can be below Hubble time for NSCs (Bahcall and Wolf 1976). Bahcall and Wolf (1977) predicted the cusp power-law index to be between 1.5 and 2 for a realistic multi-mass cluster. This is consistent with the values adopted in this work.

Moreover, since the mechanism described in this work arises from the shape of the potential rather than its overall depth (i.e. total mass of SMBH plus NSC), it is expected to hold also for mass regimes not probed by the simulations ($M_{tot} \gtrsim 10^7\,M_\odot$).

A missing ingredient in this study is the feedback from stars formed in the course of the simulation. The main results presented in Section 5.3.1 are based solely on the dynamics of gas, which could be in principle affected by supernovae, photoionization and outflows from protostars (Pelupessy and Portegies Zwart 2012; Dale, Ercolano, and Bonnell 2015). Nonetheless, the bulk of star formation occurs at 1 Myr, and in most simulations (i.e. fist two rows of Figure 5.4) the gas has already settled long before the first supernovae may explode. In addition, the first stars quickly decouple from their parent gas stream. Being spatially separated, their impact on the gas through stellar feedback would be limited. More importantly, the cloud is quickly com-

pressed by tidal forces into streams of dense gas. To alter the gas dynamics, the stellar feedback has to induce a velocity comparable to the gas orbital velocity in the GN potential, which exceeds $> 50\,\mathrm{km\,s^{-1}}$. I thus expect the impact of stellar feedback on the molecular gas to be limited.

On the other hand, a fraction of the molecular gas could be dissociated and ionized either by the stellar radiation or by feedback from the SMBH. Ionized gas is much more sensible to radiative forces and as such it might display significant deviations from the molecular gas dynamics. One example is the so-called minispiral, a complex of ionized gas filaments that resides in the cavity of the CNR in the GC. These aspects will be tackled in a forthcoming work, which will include a better treatment of the gas chemistry. In this work I focus only on the dynamics of molecular gas, which is also a better tracer of the underlying gravitational potential.

5.5 CONCLUSIONS

I have investigated the formation of circumnuclear disks/rings in GNs with properties different from those of the GC, by means of SPH simulations. I simulated the infall and disruption of a molecular gas cloud towards the central parsecs of a GN, composed of a NSC and a SMBH.

I find that the mass ratio between the SMBH and the NSC has a deep impact on the dynamics of circumnuclear gas. Specifically, circumnuclear gas exhibits different morphology whether it settles inside or outside the radius of influence R_{SOI} of the SMBH, which is determined by the mass ration between SMBH and the NSC.

An extended gaseous disk forms only within $2R_{SOI}$, where the gravity of the SMBH dominates over that of the NSC. Gas that falls within $2R_{SOI}$ winds up around the SMBH forming a flattened, eccentric disk. The disk is asymmetrical and has an eccentricity that increases with increasing semimajor axis. The disk undergoes circularization due to the eccentricity gradient, which makes neighboring streamlines intersect and shock.

In contrast, compact gaseous rings form only outside the influence radius of the SMBH. Gas that falls outside R_{SOI} is stretched into a nearly-radial streamer by the tidal potential of the NSC. The streamer follows a rosette-like orbit and undergoes circularization through self-interaction. Eventually, a clumpy, eccentric ring (or annulus) with a cavity forms at radii larger than R_{SOI}.

The different evolution of the gas inside and outside R_{SOI} can explain why the inner edge of the CNR in the GC is at large distance from Sgr A* sphere of influence $R_{SOI}^{GC} \simeq 0.4\,\mathrm{pc}$.

These findings indicate that the formation of compact rings of gas occurs only in the nuclear regions dominated by the gravity of the

NSC. An implication of this is that the inner radius of circumnuclear rings can be used to infer an upper limit to the SMBH sphere of influence.

In addition, I find that the stars formed in the infalling gas can dynamically decouple from the parent streamer and take a different evolution. This occurs when stars form in streamers still undergoing circularization. As a consequence, stars remain into highly eccentric orbits while the gas circularizes.

In contrast, stars which form from a gas disk do not decouple from the gas: they form an eccentric disk embedded in the gaseous one. This is remarkable agreement with the properties of the CW disk in the GC, whose outer edge does not extend past $R_{SOI}^{GC} \simeq 0.4\,pc$.

6

PLANETARY DYNAMICS IN THE GALACTIC CENTRE: LOOKING FOR THE ORIGIN OF CLOUD G2

6.1 INTRODUCTION

This Chapter investigates the dynamics of planets and protoplanets near the SMBH in the GC, in order to put constraints on the origin of cloud G2. In particular, I study the tidal capture of hypothetical planets and protoplanets orbiting stars in the CW disk and in the S-star cluster. I simulate hierarchical three-body systems composed of a SMBH, a star, and a planet. In my three-body runs, the orbit of the star around the SMBH is randomly sampled according to the properties of the CW disk. I also simulate the entire S-star cluster, adding a planet to each simulated S-star. I show that the orbits of planets tidally stripped from the S-stars can match the orbits of cloud G2.

In Section 6.2 I describe the methodology I employed for my simulations; I present my results in Section 6.3. In Section 6.4, I discuss the implications of my work. My conclusions are presented in Section 6.5. This Chapter is based on Trani et al. (2016a).

6.2 METHODS

6.2.1 *Mikkola's Algorithmic Regularization code*

Modelling the evolution of planets close to the SMBH is challenging, because of the extreme mass ratios involved. Thus, my simulations are run by means of a fully regularized N-body code that implements the Mikkola's algorithmic regularization (Mikkola and Tanikawa 1999a,b). This code is particularly suitable for studying the dynamical evolution of few-body systems in which strong gravitational encounters are very frequent and the mass ratio between the interacting objects is large. The MAR scheme removes the singularity of the two-body gravitational potential for $r \to 0$, by means of a transformation of the time coordinate (see Mikkola and Tanikawa 1999a for the details).

This implementation uses a leapfrog scheme in combination with the Bulirsh-Stoer extrapolation algorithm (Stoer and Bulirsch 1980) to increase the accuracy of the numerical results. The code integrates the equations of motion employing relative coordinates by means of the so called chain structure. This change of coordinates reduces round-

off errors significantly (Aarseth 2003). At present, this code is a sub-module of the direct N-body code HiGPUs-R which is still under development (Spera, in preparation; see Capuzzo-Dolcetta, Spera, and Punzo 2013 for the current non-regularized version of HiGPUs). Still, it can be used as a stand-alone tool to study the dynamical evolution of few-body systems with very high precision.

Tidal dissipation is not taken into account in the current version of the code. In fact, I expect the effect of tidal dissipation to be negligible in my simulations, since the timescale of orbital decay is $\approx$1 Gyr, much longer than the length of my simulations (10^3-10^4 yr).

6.2.2 *CW disk simulations*

Simulating the entire CW disk ($>$ 1000 stars) in the same run is prohibitive for MAR codes. Thus, I run simulations of a three-body hierarchical system composed of a SMBH, a star and a planet initially bound to the star. I set the SMBH, star and planet masses to $4.31 \times 10^6\,M_\odot$ (Gillessen et al. 2009a), $5\,M_\odot$, and $10\,M_{Jup}$, respectively, where M_{Jup} is the mass of Jupiter. The stellar orbit around the SMBH is modeled following the properties of the stars in the CW disk. The semi-major axis is drawn from a power-law distribution with index $\Gamma = 1.93$ (Do et al. 2013), in the range 0.03-0.06 pc, corresponding to the inner edge of the CW disk (planets orbiting CW stars on outer orbits are less likely affected by the SMBH tidal field). The star eccentricity is drawn from a Gaussian distribution centered at 0.3 with $\sigma = 0.1$. A planet will likely remain bound to the star if its distance from the star is less than Jacobi radius r_J of the star-planet system:

$$r_J = d\left(\frac{m}{3M_{SMBH}}\right)^{1/3}, \tag{6.1}$$

where M_{SMBH} is the SMBH mass, m is the total mass of the star-planet system and d is the distance between the star and the SMBH.

With these initial conditions I expect the Jacobi radius to be in the range of 20-90 AU . I assume that the planet orbit around the star is circular with radius in the uniform range 10-100 AU. Planets with a semi-major axis smaller than 10 AU will unlikely be captured by the SMBH, while planets with semi-major axis larger than 100 AU will be already unbound from the star. I set the planet orbit eccentricity to zero in order to avoid the parameter space to explode. On the other hand, I expect that planets on eccentric orbits escape even faster.

I consider different inclinations with respect to the star orbit: coplanar prograde orbits ($i = 0°$, set A), coplanar retrograde orbits ($i = 180°$, set B), inclined prograde orbits (uniformly distributed over $270° < i < 90°$, set C), and inclined retrograde orbits (uniformly distributed over $90° < i < 270°$, set D). The mean anomalies of star and planet are uniformly distributed between 0 and 2π. I run 10^4 realizations for

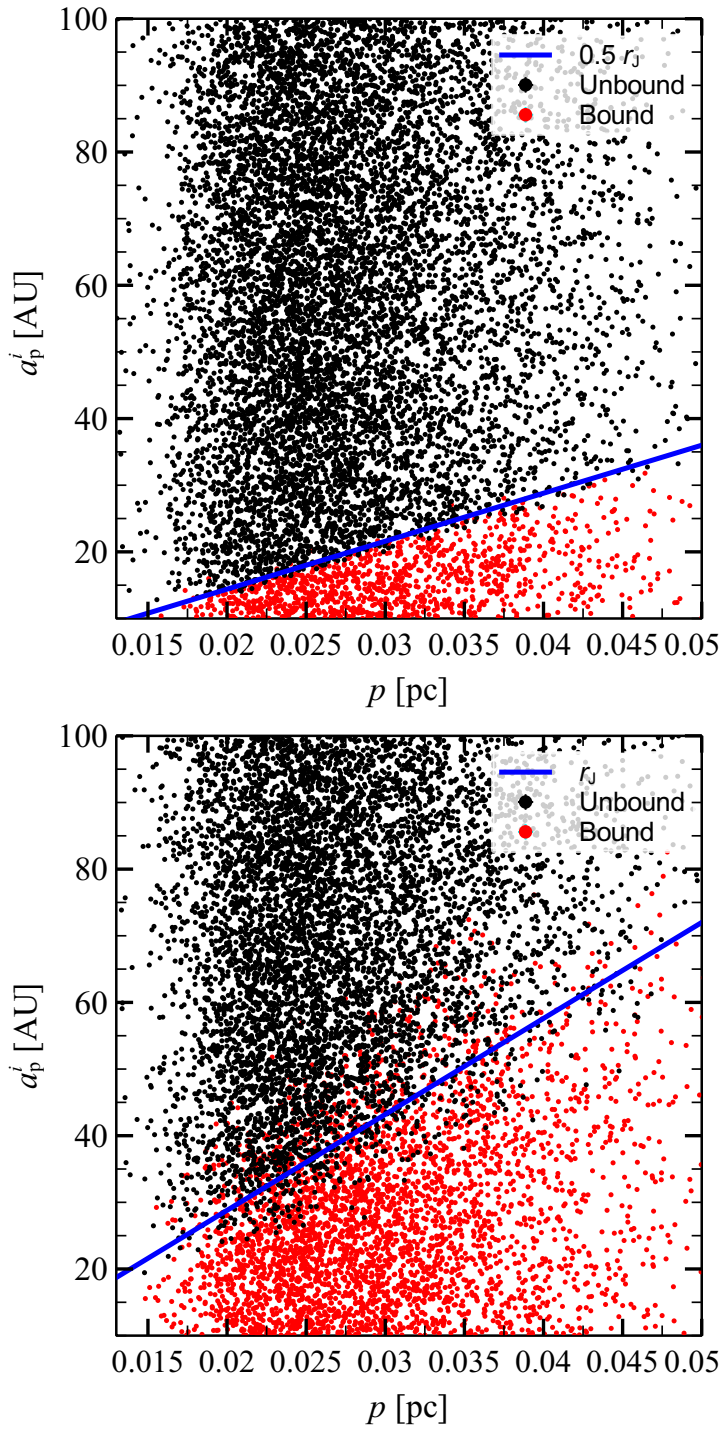

Figure 6.1: Initial semi-major axis of the planet versus pericenter distance of star orbit. Each dot represents a single realization of a three-body system of set A (coplanar prograde, top panel) and set B (coplanar retrograde, bottom panel). Red dots: realizations in which the planet remains bound to the star throughout the simulation. Black dots: realizations in which the planet becomes unbound with respect to the star. Blue solid line: Jacobi radius (Equation 6.1), multiplied by 0.5 in the bottom panel.

SET	PLANET ORBIT	N	N_{unb}
A	Coplanar, prograde	10^4	8903
B	Coplanar, retrograde	10^4	6488
C	Inclined, prograde	10^4	8817
D	Inclined, retrograde	10^4	7791

Table 6.1: Main properties of the simulations of planets in the CW disk. Column 1: set name; column 2: planet orbit spin with respect to stellar orbit; column 3: number of realizations; column 4: number of realizations in which the planet becomes unbound with respect to the parent star.

each set and stop the simulations at 10^4 yr. Table 6.1 shows a summary of the simulation sets presented in this paper.

6.2.3 *S-star simulations*

Unlike the CW disk, the S-star cluster is sufficiently small to be simulated in the same run with the MAR algorithm. I run simulations of the 27 innermost S-stars for which the orbital elements are known, using as initial condition the orbital parameters reported by Gillessen et al. (2009a). I assign to each star a planet of $10\,M_{Jup}$ in circular orbit. The planet semi-major axis ranges between 1 and 20 AU, distributed in 20 equally spaced bins. For each semi-major axis I run 1000 realizations randomizing the planet orbit orientation over the sphere, for a total of 20000 realizations. I stop the simulations at 1000 yr.

6.3 RESULTS

6.3.1 *Planets in the clockwise disk*

In 88-89% of the prograde runs (set A and C) the planet escapes from the star and starts orbiting the SMBH. The escape fraction in retrograde runs (set B and C) is lower: 65% and 78% of planets are tidally captured by the SMBH in set B and set D, respectively (see Table 6.1).

Figure 6.1 shows the initial semi-major axis of the planet a_p^i versus the pericenter distance p of the stellar orbit for set A (coplanar prograde, top panel) and set B (coplanar retrograde, bottom panel). The colors indicate whether the planet remains bound to its parent star throughout the simulations.

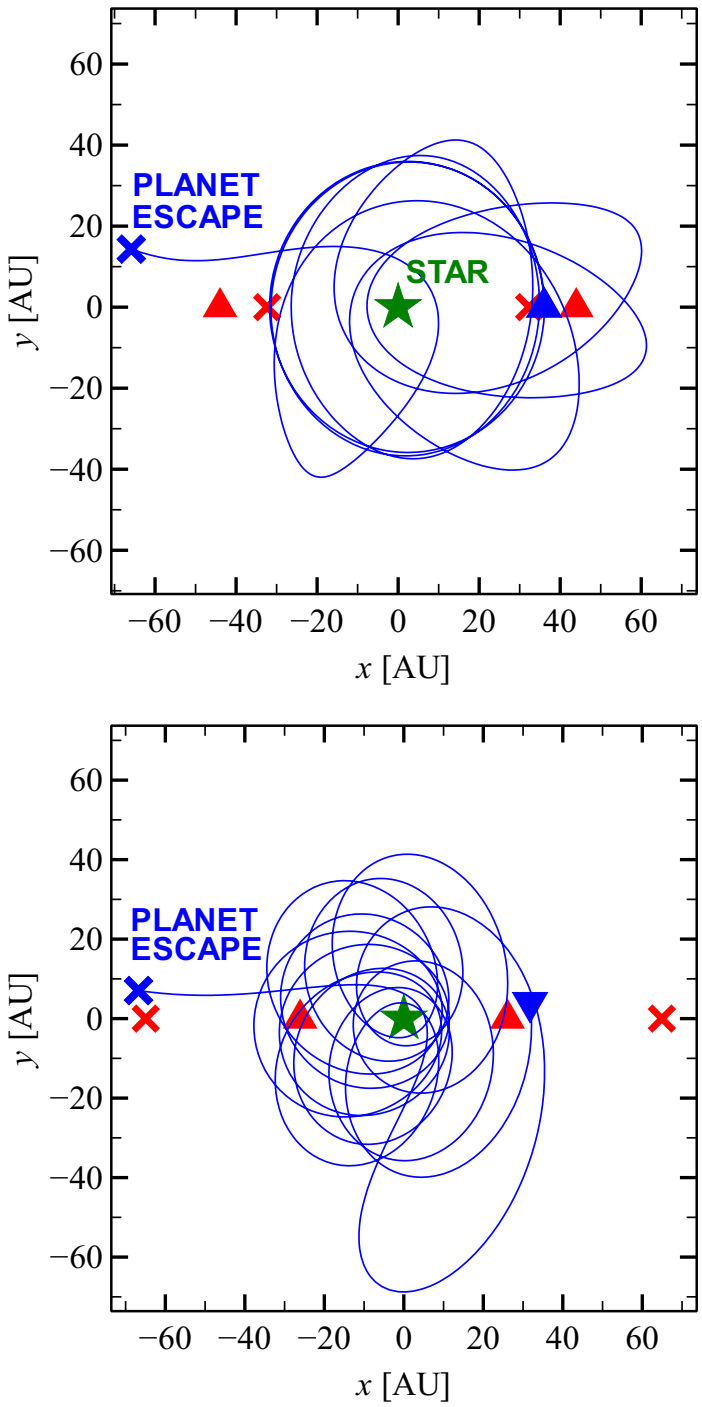

Figure 6.2: Planet trajectory in the reference frame that corotates with the star for a single simulation of set A (top panel) and set B (bottom panel). The negative x-axis points always towards the SMBH, while the star tangential velocity lies in along the positive y-axis. Blue solid line: planet trajectory. Blue triangle: initial planet position. Blue cross: planet position at the time the planet becomes unbound with respect to the star. Green star: star position. Red triangle: initial Jacobi radius of the system (Equation 6.1), multiplied by 0.5 in the top panel. Red cross: same as red triangle, but at the time the planet becomes unbound with respect to the star.

The unbound and bound regions in the $a_p^i - p$ plane are clearly distinct. The boundary between the two regions scales linearly with p, as expected from the Jacobi radius r_J linear dependence on the star-SMBH distance (equation 6.1).

In the case of set A (Figure 6.1, top panel) the boundary is $0.5\,r_J$. In the case of set B (Figure 6.1, bottom panel) the boundary is $\sim 1\ r_J$. The boundary is $\sim 0.5\ r_J$ and $\sim 0.9\ r_J$ for set C and D, respectively. Thus, the boundary radius is smaller for prograde orbits than for retrograde orbits. This difference is linked to the direction of the Coriolis force. Moreover, the boundary is less sharp in the case of retrograde orbits. This likely occurs because retrograde planets spend several periods at radius $\sim r_J$ without escaping, thanks to the stabilizing effect of the Coriolis force. In contrast, prograde planets escape immediately outside $0.5 r_J$. As a consequence, planets in retrograde orbits are more affected by perturbations from the tidal field, which is stronger at larger distances from the star (Hamilton and Burns 1991; Hamilton and Burns 1992).

Figure 6.2 shows the trajectory of a planet in a single simulation of set A (coplanar and prograde, top panel) and set B (coplanar and retrograde, bottom panel). The reference frame corotates with the star in its motion around the SMBH, so that the SMBH is always directed towards the negative $x-$axis. In the top panel, the planet orbit is initially within half of the Jacobi radius and the planet completes an orbit around the star before being captured by the SMBH. However, as the star moves towards its pericenter, the Jacobi radius of the system shrinks and the planet is captured by the tidal forces of the SMBH.

In the case of retrograde orbits (Figure 6.2, bottom panel), the planet trajectory can be much more convoluted. In this case, the planet orbit becomes unstable after the third pericenter passage of the parent star around the SMBH; the orbit of the planet becomes prograde before escaping from the Hill sphere of the star. Moreover, the Hill sphere at the initial time is smaller than that at the moment of planet escape, indicating that planet escape does not occur at pericenter passage. For more details about the temporary orbit of simulated planets see Section 6.4.2.

Figures 6.3 and 6.4 show the orbital properties of the planets after they are captured by the SMBH. In 95% of the runs of set A (Figure 6.3, top panel) the semi-major axis of the planet a_p (with respect to the SMBH) differs less than 7% from the semi-major axis of its parent star a_s.

The small difference between a_p and a_s is motivated by the change of the orbital energy of the planet being of the same order of magnitude as the binding energy of the star-planet system (E_{sp}). For these assumptions, $E_{sp} \approx 10^{43}\,erg$. This is much smaller than the binding energy between the star and the SMBH ($\approx 10^{49}$ erg s^{-1}), indicating that the recoil velocity acquired by the planet during the cap-

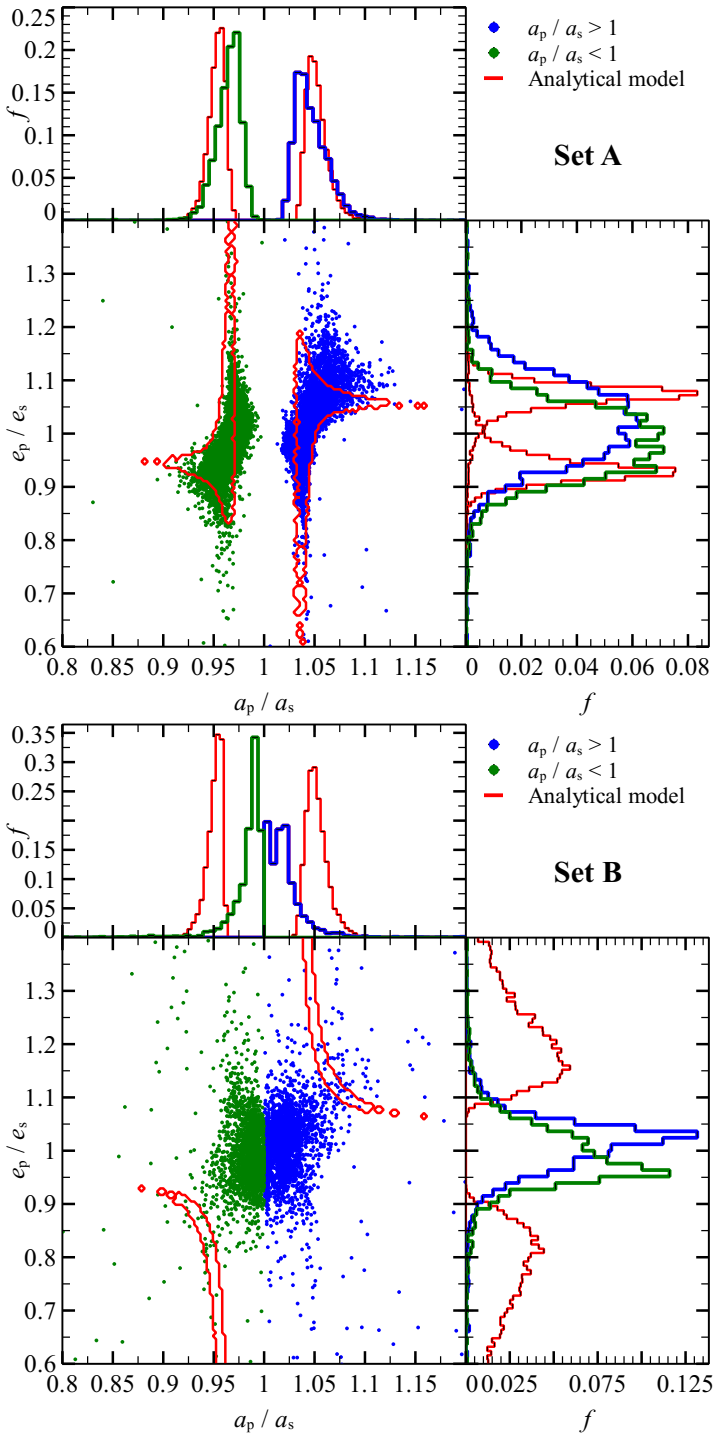

Figure 6.3: Semi-major axis of the planet orbit (around the SMBH) normalized to the semi-major axis of the star orbit a_p/a_s versus eccentricity of the planet orbit (around the SMBH) normalized to the eccentricity of the parent star orbit e_p/e_s. Blue dots indicate realizations in which the planet semi-major axis is larger than its parent star semi-major axis ($a_p/a_s > 1$); green dots indicate realizations in which the planet semi-major axis is smaller than its parent star semi-major axis ($a_p/a_s < 1$); red contours indicate predictions of the analytic model (Equations 6.2). Green histograms indicate the distributions of planets with $a_p/a_s < 1$, while blue histograms indicate the distributions of planets with $a_p/a_s > 1$. Top panel: set A (coplanar prograde runs). Bottom panel: set B (coplanar retrograde runs).

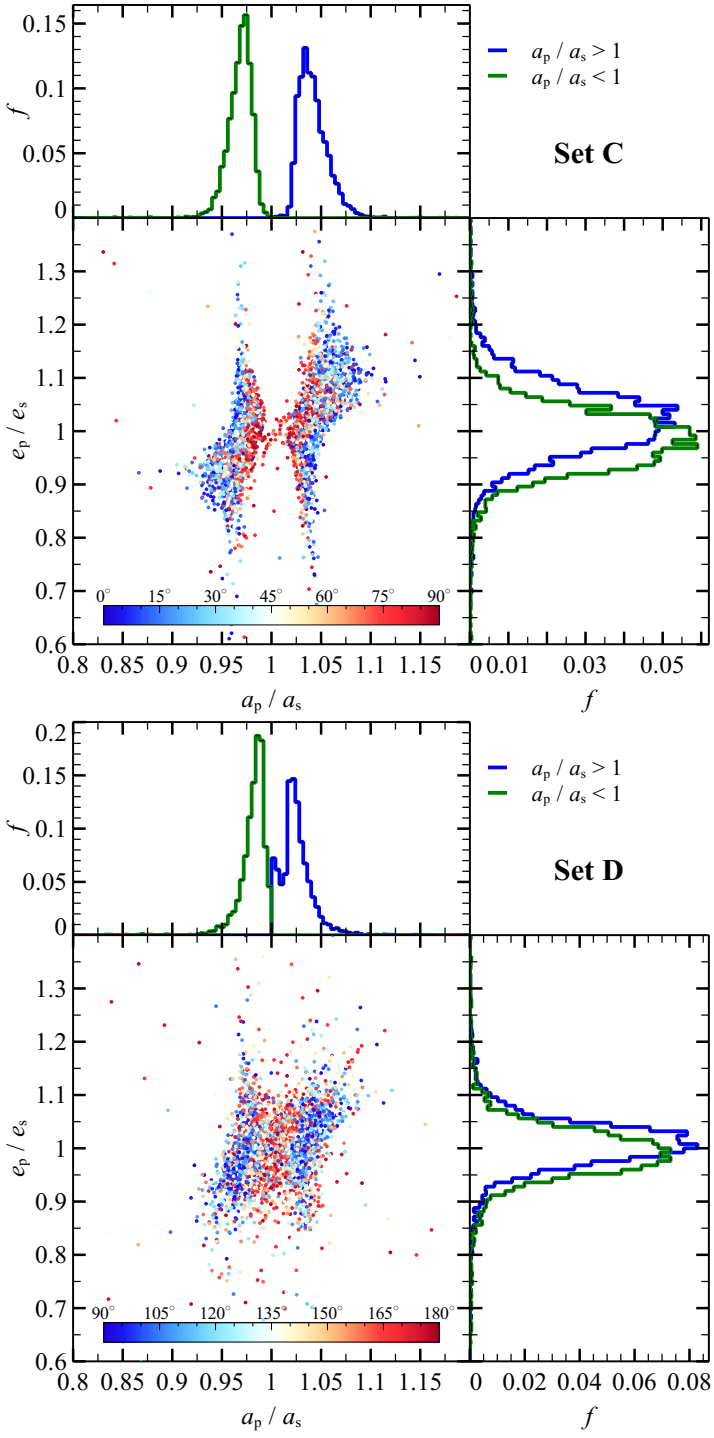

Figure 6.4: Same as Figure 6.3, but for the sets with inclined planetary orbits. The color map indicates the inclination of the planetary orbit with respect to the star orbit. $i = 0°, 90°$ and $180°$ correspond to prograde coplanar orbits, normal orbits and retrograde coplanar orbits, respectively. Top panel: set C (inclined prograde runs). Bottom panel: set D (inclined retrograde runs).

ture event is much smaller than its initial velocity with respect to the SMBH.

The gap in the semi-major axis distribution in the top panels of Figures 6.3 and 6.4 indicates that the semi-major axis of the escaped planet is never equal to the semi-major axis of the parent star. The gap becomes wider as the planet orbit eccentricity deviates from that of its parent star.

The eccentricity distribution depends on whether the planet has a smaller or larger semi-major axis than its parent star. In the case of smaller semi-major axis, the eccentricity distribution is centered at lower eccentricity relative to the parent star, while in the case of larger semi-major axis the eccentricity distribution is centered at higher eccentricity relative to the parent star. In 95% of the runs of set A the eccentricity of the planet orbit e_p differs less than 15% from the eccentricity of its parent star e_s.

In runs of set B (retrograde coplanar runs, see Figure 6.3, bottom panel), the distribution of semi-major axis of planets normalized to that of stars with respect to the SMBH (a_p/a_s) has no gaps. The spread in semi-major axis is lower than in set A, while the spread of eccentricities is higher. As in set A, tighter planet orbits tend to have higher eccentricity and *vice versa*.

Figure 6.4 shows the orbital properties of the planets for the runs of set C (inclined and prograde, top panel) and set D (inclined and retrograde, bottom panel). Inclined orbits follow the same trend as coplanar ones: runs of set C exhibit a gap in the a_p/a_s distribution, while runs of set D show no gap.

About 51% runs of set A and C (prograde runs) have $a_p < a_s$. In contrast, just 45% and 43% runs of set B and D (retrograde runs) have $a_p < a_s$, respectively. In the retrograde runs, the planets tend to end on orbits less bound than those of their parent star.

Figure 6.5 shows the ratio a_p/a_s between the planet semi-major axis and that of its parent star versus the orbital phase of the planet at the first pericenter passage of the star. I predict the orbital phase analytically using the initial conditions of each realization. From the top panel of Figure 6.5 it is apparent that the planet will likely have a semi-major axis smaller than that of its parent star ($a_p/a_s < 1$) in runs of set A if it is in between the SMBH and the star during the stellar pericenter passage ($\varphi_p \simeq 180°$). In contrast, the planet will likely have a semi-major axis larger than that of its parent star ($a_p/a_s > 1$) if the planet is on the opposite side of the orbit with respect to the SMBH ($\varphi_p \simeq 0°$). Figure 6.6 is a schematic representation of this result. The same trend is still present (but much less evident) in runs of set B (Figure 6.5, bottom panel).

I find that the planet may undergo a close encounter with the star during its orbit around the SMBH. This occurs because the planet remains on a orbit similar to that of its parent star, so that it may

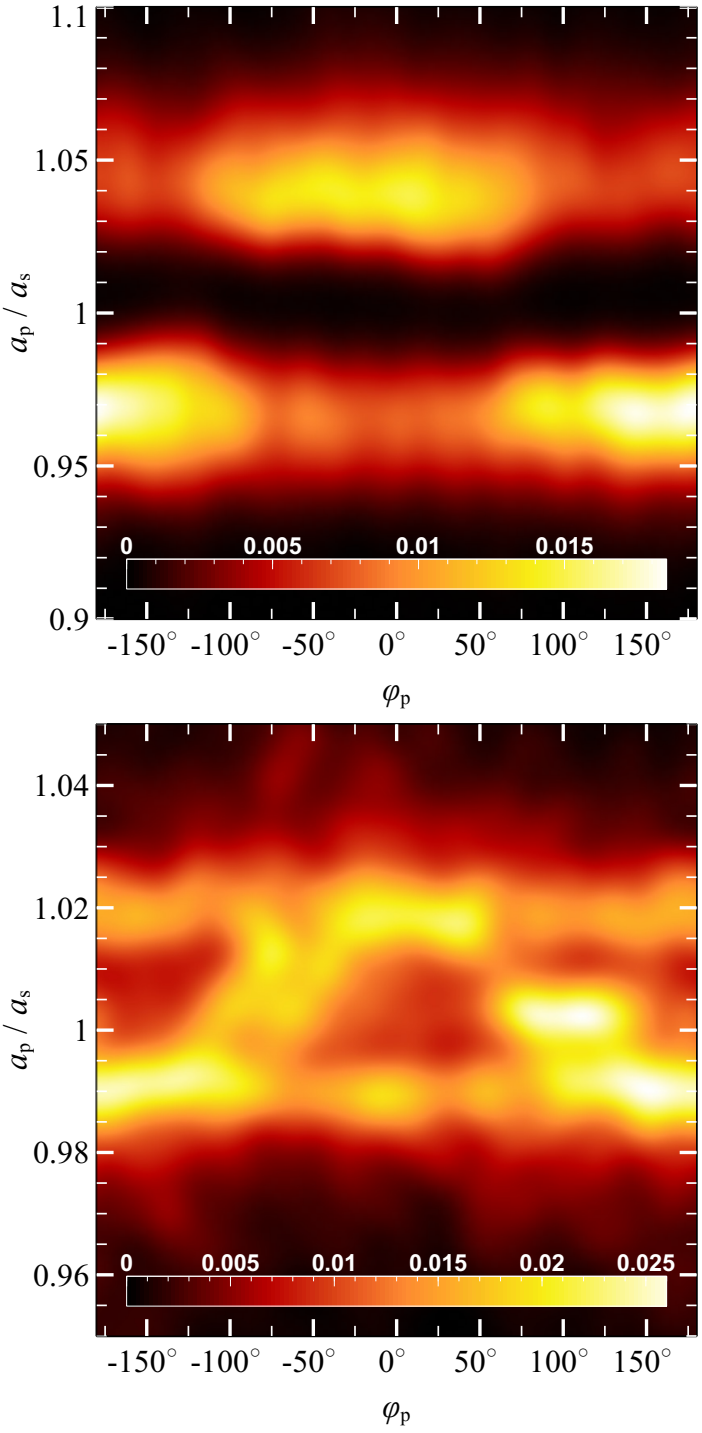

Figure 6.5: Probability density map of the ratio of the planet semi-major axis a_p to that of the star a_s versus the planet orbital phase around the star at the star first pericenter passage. $\varphi_p = 180°$ indicates that the planet is in between the SMBH and the star, while $\varphi_p = 0°$ indicates that the planet is in opposition with respect to the SMBH. Top panel: set A (coplanar prograde runs). Bottom panel: set B (coplanar retrograde runs).

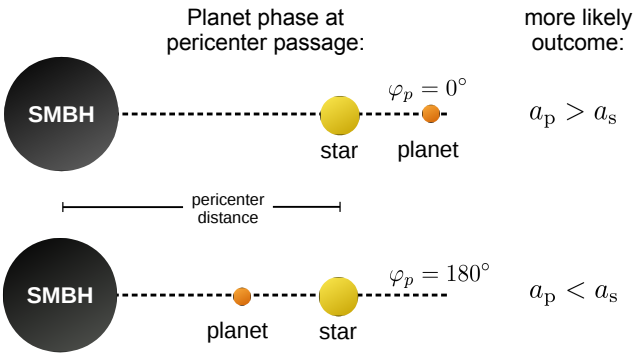

Figure 6.6: Schematic representation of two extreme orbital phases of the planet at the star pericenter passage, along with the more likely outcomes if the planet gets stripped from its parent star. a_p: planet semi-major axis with respect to the SMBH after it becomes unbound, a_s: parent star semi-major axis, φ: planet orbital phase at the star pericenter passage.

encounter again the star after one synodic period. However, since the difference between the orbital periods of the star and the planet is negligible, the synodic period is $\gtrsim$ 5000 yr. On this timescale, perturbations from nearby stars might become non-negligible before the planet undergo the encounter with its parent star.

6.3.2 *Planets in S-stars cluster*

Figure 6.7 shows the fraction of captured and ejected planets versus the initial semi-major axis of planet orbits for all S-stars realizations. As expected, the fraction of unbound planets increases with the initial semi-major axis. 57% of the planets in my simulations gets captured by the SMBH. In total 0.18% of the planets get ejected from the system. The fraction of ejected planets decreases for larger initial semi-major axis. This is expected: the larger the semi-major axis, the smaller the binding energy of the planet-star system that can be released as recoil velocity during the encounter with the SMBH.

Figure 6.8 shows the trajectory of a planet around S19 star, in the rotating reference frame that corotates with the star. The star orbit lies in the x-y plane, and the negative x-axis is always directed towards the SMBH. The planet orbit has an initial radius of 10 AU and it is inclined by 20° with respect to the star orbit. The planet orbit becomes immediately eccentric ($e \simeq 0.8$) due to the strong tidal forces and gets an inclination by 45° and a semi-major axis of 8 AU. The orbit remains stable around the star for several periods, until the planet is kicked into a looser orbit with $i \simeq 100°$, $a \simeq 20$ AU and $e \simeq 0.3$. After 260 yr,

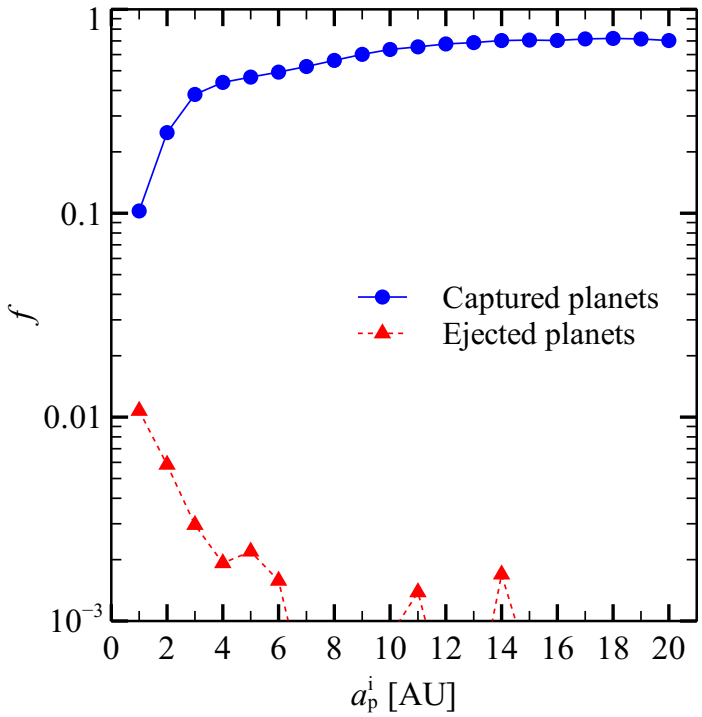

Figure 6.7: Fraction of captured and ejected planets as function of initial semi-major axis of planet orbit for all S-stars realizations. Blue solid line: fraction of unbound planets. Red dashed line: fraction of planets ejected from the system. Planets whose initial semi-major axis is larger than the Jacobi radius of the star at the initial conditions are not included in this Figure.

the planet escapes along the negative x-axis and gets captured by the SMBH.

The morphology of planet orbits varies greatly from simulation to simulation. Flips of planet orbit may occur, with the planet spending time on several temporarily-stable orbits around the star before escaping. In Section 6.4.3 I compare the orbital parameters of the captured planets with the ones of the G1 and G2 cloud.

6.4 DISCUSSION

6.4.1 *Orbital properties of unbound planets*

As shown in Figures 6.3 and 6.4, planets remain on orbits similar to those of their parent star after being captured by the SMBH. This implies that the velocity kick induced by the SMBH is at least one order of magnitude less than the star orbital velocity. Furthermore, there is a gap in the distribution of the semi-major axes of captured planets in the prograde case.

Figure 6.5 (showing the semi-axis ratio a_p/a_s versus the orbital phase of the planet) suggests that planets escaping from L1 (inner

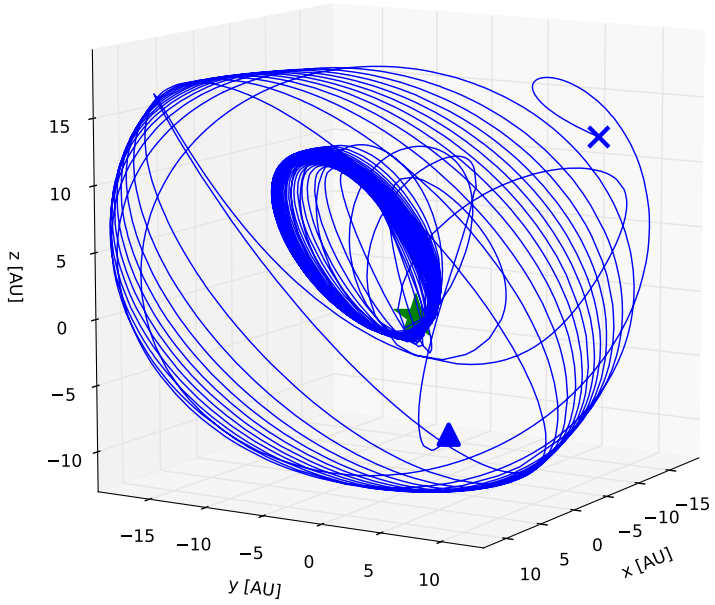

Figure 6.8: Planet trajectory around the star S19 of the S-star cluster, in the reference frame that corotates with the star. The initial semi-major axis of the planet is 10 AU. Blue triangle: initial planet position. Blue cross: planet position at the time the planet becomes unbound with respect to the star (540 yr). Green star: star position. The SMBH is located along the negative x-axis, while the star tangential velocity is directed along the positive y-axis.

Lagrangian point) end on tighter orbits, while planets escaping from L2 (outer Lagrangian point) end on looser orbits.

Based on these considerations, the change in specific angular momentum and energy of the planet can be estimated in the framework of the restricted three-body problem. I develop a simple analytic model based on three assumptions: (i) the planet becomes unbound during the star pericenter passage, (ii) the planet escapes the Hill sphere of the star from either the outer or the inner Lagrangian point, (iii) the planet velocity with respect to the rotating frame of reference at the moment of escape equals its orbital velocity v_p. With these assumptions I can compute the difference of the specific energy and angular momentum between the planet and the star orbit, ΔE and ΔL, respectively:

$$\begin{aligned} \Delta E &= -\frac{G\,M_{SMBH}}{p}\frac{r_J}{p-r_J} - v_s^2\frac{r_J}{p}\left(1-\frac{1}{2}\frac{r_J}{p}\right) \\ \Delta L &= -r_J\,v_s - p\,v_p + r_J\,v_p, \end{aligned} \tag{6.2}$$

where G is the gravitational constant, M_{SMBH} is the SMBH mass, p is the pericenter distance of the star orbit, r_J is the Jacobi radius at pericenter (equation 6.1), v_s is the star velocity at pericenter, and v_p is the orbital velocity of the planet. The sign of r_J and v_p is positive if the planet escapes from the inner Lagrangian point, negative if the

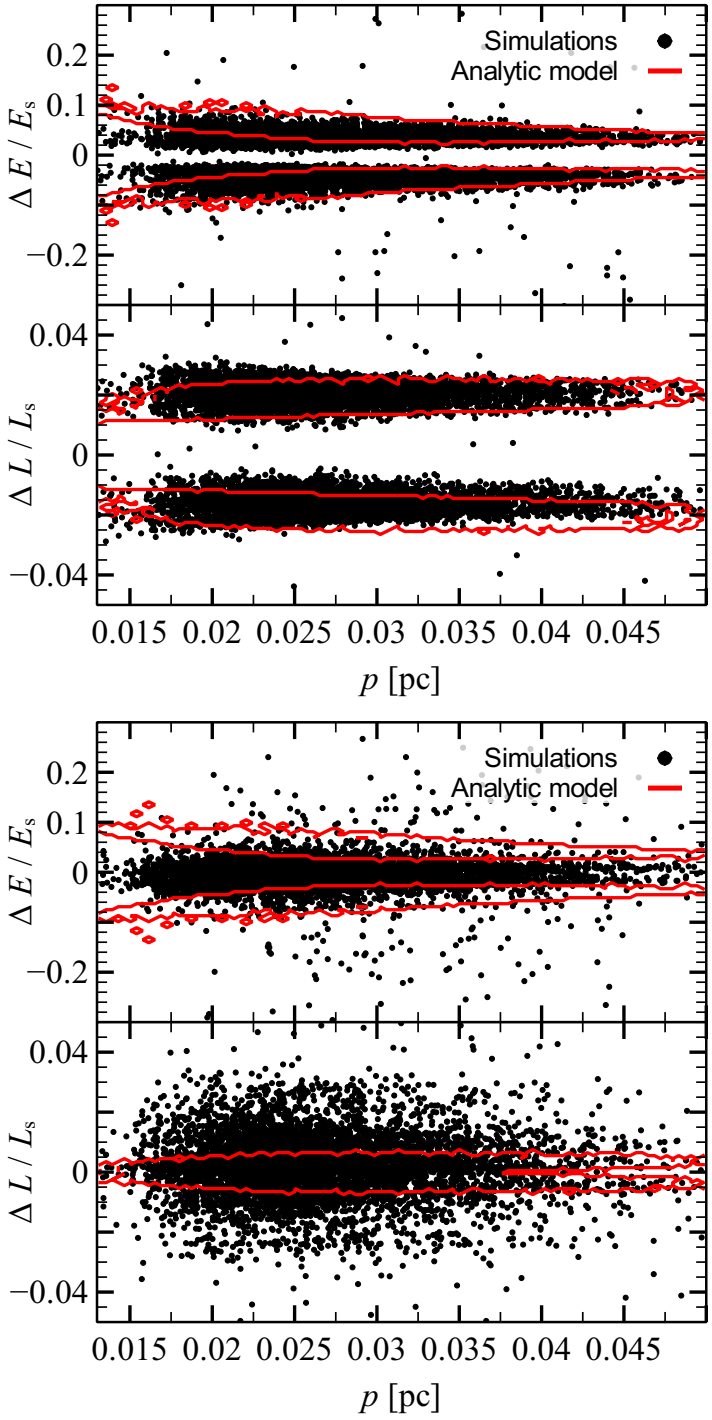

Figure 6.9: Top-half (bottom-half) panels: energy (angular momentum) difference between planet and star orbits around the SMBH as a function of the pericenter distance of the stellar orbit, normalized to the star energy (angular momentum). Black dots: results of the simulations. Red contours: predictions of the analytic model (Equations 6.2). Top panel: set A (coplanar prograde runs). Bottom panel: set B (coplanar retrograde runs).

planet escapes from the outer Lagrangian point, and v_p changes sign for retrograde orbits.

Figure 6.9 shows the variation of energy (ΔE) and angular momentum (ΔL) predicted from the analytic model compared to the simulations. In the case of prograde orbits (top panel, set A), the simple analytic model reproduces very well the bimodal energy distribution. The analytic model overestimates ΔE with decreasing pericenter distance, because the planet may escape before reaching the pericenter, if the pericenter is very small. In contrast, the analytic model does not match the variation of energy and angular momentum in the simulations with retrograde orbits (bottom panel of Figure 6.9, set B).

Inserting the values drawn from the initial conditions of my simulations into equation 6.1 and 6.2 I can evaluate the orbital parameters of the planet new orbit around the SMBH. Figure 6.3 shows the predicted a_p/a_s and e_p/e_s along with the results of the simulations.

The predicted semi-major axis distribution matches the simulations in the case of prograde orbits (set A, Figure 6.3, top panel), reproducing the gap in the semi-major axis distribution.

However, the analytic model also predicts a bimodality in the eccentricity distribution, which is not present in the simulations. In particular, the analytic model predicts that tighter orbits have mostly lower eccentricity and looser orbits have mostly higher eccentricity, while in the simulations I find mixed outcomes.

This happens because the planet can escape before the star reaches its pericenter, thus invalidating assumption (i) of the analytic model. Moreover, 85% of the unbound planets begin the simulation outside $0.5r_J$ so that they may become immediately unbound and consequently violate all the assumptions of the analytic model.

The analytic model fails to predict the distribution of both semi-major axis and eccentricity in the case of retrograde orbits (set B, Figure 6.3, bottom panel). This occurs because the escape mechanism for retrograde orbits is different from that of prograde orbits. Just a minor fraction of retrograde planets escape from one of the Lagrangian points (e.g. Figure 6.5). Moreover, planets in retrograde orbits can survive several star pericenter passages before being kicked into an unstable orbit, and the planet escape may occur anywhere along the star orbit (see Figure 6.2, bottom panel).

My results are consistent with the findings of Suetsugu and Ohtsuki (2013), who studied the orbital properties of temporary captured planetesimals by a planet in circular heliocentric orbit. Suetsugu and Ohtsuki (2013) highlight that captures of planetesimals into prograde orbits about the planet (i.e., through L1 or L2 Lagrangian points) take place for a certain range of semi-major axes, leading to a gap in semi-major axis distribution, whereas captures into retrograde orbits do not produce a significant gap.

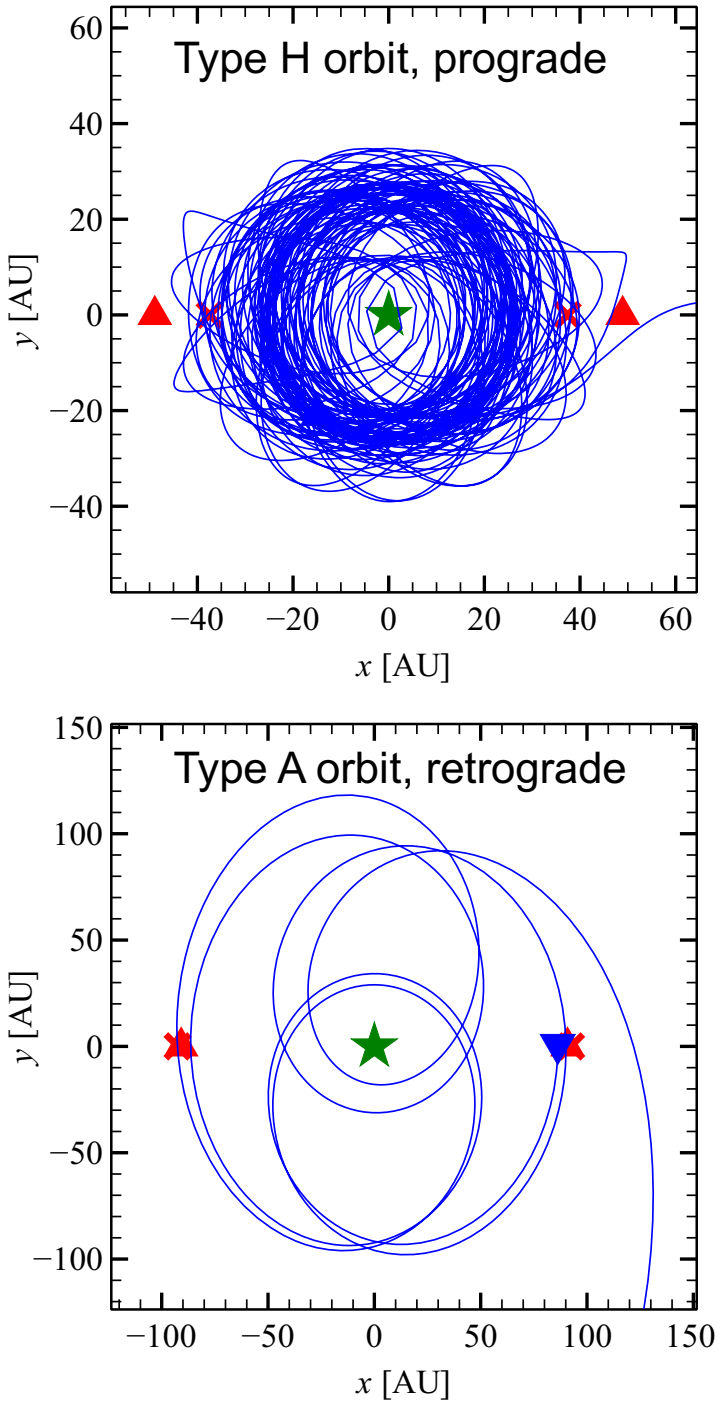

Figure 6.10: Same as Figure 6.2, but for two different realizations. Top panel: simulation from set A (coplanar prograde) that I classify as Type H (Suetsugu, Ohtsuki, and Tanigawa 2011). Bottom panel: simulation from set B (coplanar retrograde) that I classify as Type A (Suetsugu, Ohtsuki, and Tanigawa 2011).

6.4.2 *Classification of planet orbits*

Temporary planet orbits around the star (before tidal capture by the SMBH) can be classified according to Suetsugu, Ohtsuki, and Tanigawa (2011), who studied the orbital properties of temporary captured planetesimals by a planet in circular heliocentric orbit. They distinguish four types of orbits, three for retrograde orbits and one for prograde orbits, and find that the orbit type depends on the eccentricity and energy of the planetesimal initial orbit around the Sun.

I find that most prograde orbits of set A are of type H (Hill sphere-shaped, top panel of Figure 6.10), which is typical of low-energy orbits that remain confined inside the Hill sphere, with escapes mainly occurring through the Lagrangian points. On the other hand, most retrograde orbits of set B are of type A (apple-shaped, bottom panel of Figure 6.10). Planets on type A orbits can orbit past the Hill sphere of the star without escaping. Escapes occur mainly in the SMBH-star direction but not strictly through the Lagrangian points.

I do not find any evidence of type R and E orbits in our simulations. These orbit types were found by Suetsugu, Ohtsuki, and Tanigawa (2011) in the case of high velocity-dispersion between the planet and the planetesimal. The dispersion-dominated velocity regime is excluded by construction in our case, since the planet is initially bound to the star.

I note that many examined orbits are irregular and do not resemble any of aforementioned orbit types. This is due to the eccentricity of the star orbit that makes the tidal field experienced by the planet not stationary, unlike in the zero-eccentricity study of Suetsugu, Ohtsuki, and Tanigawa (2011). This leads to an additional perturbation that can modify the shape of the planet orbit, and may cause earlier escape than in the zero-eccentricity case.

6.4.3 *Comparison with G2 and G1 cloud orbits*

Figure 6.11 shows the probability density map of finding an unbound planet in the semi-major axis – eccentricity plane for the CW disk simulations. No planet can match the orbits of the G1 or G2 cloud. In particular, none of the simulated planets can achieve a highly eccentric orbit. In fact, the closest pericenter passage of an unbound planet in our simulations is 1750 AU, a factor of ~9 larger than the pericenter passage of the G1 cloud.

Since unbound planets remain on orbits similar to those of their parent star, I expect that they will experience scattering with the stars in the CW disk. Angular momentum diffusion and scattering in the CW disk may bring low-mass objects on nearly radial orbits (Murray-Clay and Loeb 2012). N-body simulations that include the entire CW

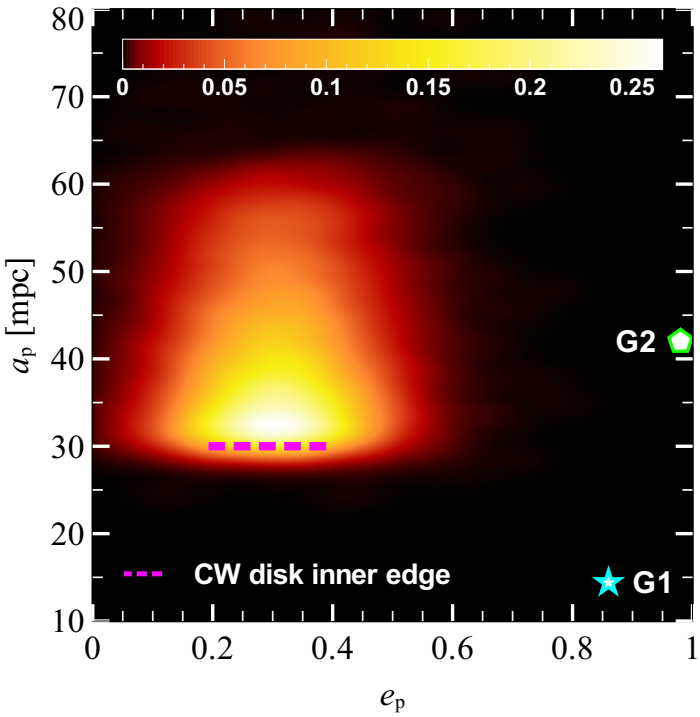

Figure 6.11: Probability density map of semi-major axis and eccentricity of captured planets in the CW disk simulations. Green pentagon: G2 cloud. Cyan star: G1 cloud. Magenta dashed line: inner edge of the CW disk. All simulated sets were used.

disk are required to study this effect and will be presented in a forthcoming study.

Figure 6.12 is the same as Figure 6.11 but for captured planets in the S-stars simulations. Most planets escaped from the S-stars are on highly eccentric orbits and are compatible with the G1 and G2 cloud. In particular, I find that captured planets have a probability of 2% and 70% to have semi-major axis and eccentricity within 1σ of the observations for G2 and G1.

I also study the inclination of the orbits of captured planets. Figure 6.13 shows the probability density map of finding an unbound planet in the pericenter distance – inclination plane for the S-star simulations. Since captured planets retain approximately the same inclination as their parent star, each blob corresponds to one or more S-stars.

None of the simulated planets has exactly the same inclination as G2 and G1 orbits. Although planets escaped from S29 lie very close to the position of G2 in the $p - i$ plane, further analysis reveals that longitude of the ascending node Ω mismatches by $\sim 75°$; therefore the orbit of G2 and the one of the planets escaped from S29 do not lie on the same plane.However, the orbital properties of several S-stars are still unconstrained (Gillessen et al. 2009a). Many S-stars fainter than $m_H > 19$ are not even detected. Identifying more S-stars and de-

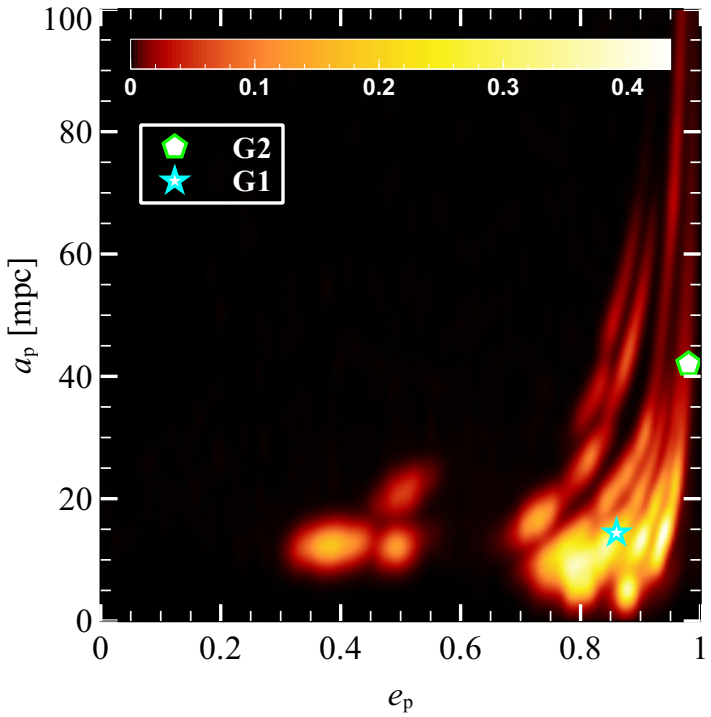

Figure 6.12: Probability density map of semi-major axis and eccentricity of the captured planets in the S-stars simulations. Green pentagon: G2 cloud. Cyan star: G1 cloud.

riving their orbital properties (especially their inclinations) will give important clues on this scenario.

Moreover, explaining G1 and G2 with this scenario requires that planets can exist around S-stars. One of the most popular scenarios to explain the formation of the S-stars, the so-called binary breakup scenario (Perets et al. 2009) predicts that the S-stars were captured by the SMBH via the Hills mechanism, during encounters with binary stars. A proto-planetary disk might be disrupted during the binary encounter with the SMBH. Alternatively, the planet might have been formed around the S-star before it was captured by the SMBH. Ginsburg, Loeb, and Wegner (2012) showed that some planets will likely remain bound to their star during a three-body encounter, if their semi-major axis is $a_p^i \gtrsim 0.5\,\mathrm{AU}$, since planets with $a_p^i \lesssim 0.5\,\mathrm{AU}$ will be more likely ejected from the system. However, the closest the planet to the S-star, the more difficult is for the SMBH to capture it. All these issues deserve further study.

Finally, it is important to note that the simulations were done for a star-planet system, but these results hold also for a star-star system. In other words, a low-mass star initially bound to an S-star might have been captured by the SMBH into a new orbit, matching the eccentricity and semi-major axis of G1 and G2.

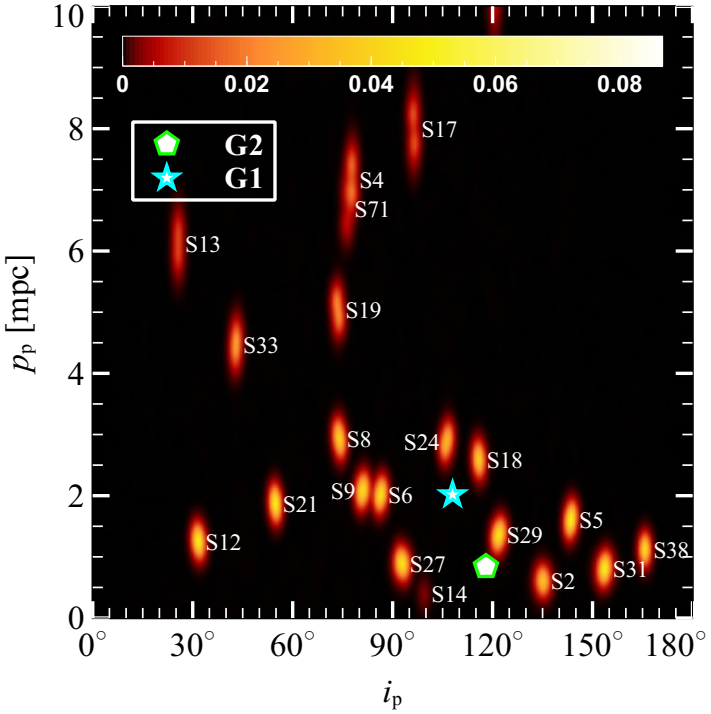

Figure 6.13: Probability density map of pericenter distance and inclination of captured planets in the S-stars simulations. Green pentagon: G2 cloud. Cyan star: G1 cloud. Each blob corresponds to the planets escaped by a single S-star, labeled on the map.

6.5 CONCLUSIONS

I investigated the dynamics of planets orbiting the young stars in the inner edge of the CW disk and in the S-star cluster by means of regularized N-body simulations. I simulated 4×10^4 hierarchical systems consisting of the SMBH, a star and its planet lying in the CW disk. I also ran 2×10^4 N-body realizations of the 27 innermost S-stars, assigning a planet to each S-star.

The planet may escape its parent star and be tidally captured by the SMBH, depending on the properties of the orbit of the star and the planet. Planets on retrograde (prograde) orbits are captured if their orbit lies outside r_J ($0.5r_J$), where r_J is the Jacobi radius.

I study the orbital properties of starless planets around the SMBH and find that planets remain on orbits similar to the ones of their parent star. In particular, I find that in 95% of the runs the semi-major axis and eccentricity of the planet orbit differ less than 6% and 13% from those of the parent star, respectively.

In case of prograde coplanar orbits, the semi-major axis of starless planets can be approximately predicted using a simple analytic model. I show that the escape mechanism of the planet from the Hill sphere of the parent star determines the semi-major axis of the planet: if the planet escapes from the inner Lagrangian point (i.e. the one lo-

cated towards the SMBH) it will end on a tighter orbit; in contrast, if the planet escapes from the outer Lagrange point it will end on a looser orbit. Furthermore, I find that looser orbits tend to have higher eccentricity with respect to the parent star orbit, while tighter orbits tend to have lower eccentricity.

In the case of planets in the CW disk, I find that the closest passage near the SMBH achieved by a starless planet is at 1750 AU, a factor ~9 larger than the pericenter distance of the G2 cloud orbit. I speculate that perturbations from other stars in the CW disk may bring planets into nearly radial orbits. In forthcoming studies I will investigate the effect of angular momentum transport and scatterings on the dynamics of planets in the CW disk.

In contrast, the semi-major axis and eccentricity of planets escaping from the S-stars can match those of G1 and G2. The main issue is that the orbital planes of known S-stars do not match those of G1 and G2. Therefore, future detection of S-stars with approximately the same orbital plane as G1 and G2 are essential to support this scenario. I note that the simulations were run for star-planet systems, but these predictions apply to any low-mass companions of the CW disk stars and of the S-stars. Thus, this scenario also predicts that G1 and G2 might be low-mass stars that were previously bound to S-stars.

7 CONCLUSIONS

This Thesis has examined several present-day issues related to the GC and other GNs, which concern the dynamics of different astronomical objects – stars, molecular clouds and planets – in the extreme environment of GNs. In order to shed light on these problems, I have employed various numerical and analytic tools, which allowed me to model the broad range of physics undergoing in these exceptional environment.

In Chapter 3 I propose that the CNR formed through the infall and tidal disruption of a molecular cloud in the gravitational potential of the GC, and I investigate this scenario by means of SPH simulations. I find that the tidal disruption of a single molecular cloud can produce several rings and disks in orbit around the SMBH, whose precise geometry depends on the initial orbit of the cloud. The disruption of a molecular cloud with sufficiently low angular momentum leads to the formation of two distinct structures: an outer gaseous ring, whose properties match the CNR, and an inner disk which can be interpreted as the progenitor of the CW disk in the GC. In case of clouds with higher angular momentum, only an outer ring forms with no inner disk. In addition, I show that rings and disks formed in the disruption of a single cloud can be significantly misaligned because of the cloud extent, which makes different parts of the cloud have different impact parameter with respect to the SMBH. I argue that the formation of the CW disk and that of the CNR in our Galaxy might both be associated with the disruption of a single molecular cloud. This work has already offered crucial insights to interpret new data from the Nobeyama 45m radio telescope (Takekawa, Oka, and Tanaka 2017).

Chapter 4 aimed to unravel some of the mysteries about the origin of the young stars in the GC. I investigated the dynamical perturbations induced by the CNR on the CW disk and explored the processes which affect the evolution of a nearly-Keplerian stellar disk orbiting a SMBH. To this end, I combined direct N-body simulations of a stellar disk with SPH simulations of an infalling molecular cloud by means of the AMUSE software. The CNR was formed from the tidal disruption of a molecular cloud as described in Chapter 3. The stellar disk had properties similar to the CW disk and was formed self consistently by the infall and collapse of a disrupted molecular cloud. In this way, I obtained a self-consistent treatment of gas for the formation of the CNR and high accuracy to follow the evolution of the stars in the SMBH potential. I find that the CNR is inefficient in altering the stel-

lar orbits of the CW disk on a timescale comparable with their age. Therefore, the CNR can not be invoked to explain the young stars which do not lie in the CW disk. On the other hand, I show that gas in the inner cavity of the CNR can significantly affect the disk coherence. Specifically, I highlight two key physical processes which may disrupt the outer part of the stellar disk: precession induced by gas in the inner cavity and two-body relaxation among disk stars. This result suggests that a gaseous ring might have resided inside the inner cavity of the CNR in the past.

In Chapter 5 I investigate the formation of circumnuclear gas in GNs with properties different from the GC. I simulate the infall and disruption of a molecular cloud in the tidal potential of a GN, composed of a SMBH and a NSC. I find that the dynamics of gas changes dramatically depending on the mass ratio between the SMBH and NSC. Specifically, the morphology of the circumnuclear gas depends on whether gas is captured inside the influence radius of the SMBH R_{SOI} or not. Gas captured inside R_{SOI} is flattened into an eccentric disk, which may extend only up to $2R_{SOI}$. In contrast, gas captured in the tidal potential of the NSC gets stretched into a radial streamer, which undergoes circularization via self-interaction. Eventually, the streamers form a CNR-like structure outside R_{SOI}. This result implies that the formation of a CNR-like structure is a signature of the presence of a NSC. At the same time it suggests that the inner edge of molecular rings can give an upper limit on the SMBH influence radius. Furthermore, I show that stars formed from circumnuclear gas can decouple dynamically from the parent gas and follow an evolution different from that of the gas, since stars are not affected by shocks and viscous forces. This leads to the formation of semi-circularized ring of gas and several eccentric stellar streamers.

In Chapter 6 I investigated the origin of cloud G2 by studying the tidal capture of planets orbiting stars close to Sgr A*. I have run high-accuracy few-body simulations of hierarchical SMBH-star-planet systems. The stars were modeled as belonging to either the CW disk and the S-star clusters. In addition, I developed an analytic model to predict the orbital properties of planets after they get captured by the SMBH. I find that planets escaping from stars in the CW disk tend to remain in the stellar disk, so that their orbit is only mildly eccentric and does not match the G2 orbit. In contrast, I find that planets escaped from the S-stars can match the semimajor axis and eccentricity of the G2 cloud, but not its orbital inclination. Nonetheless, only a few S-stars are currently known and more will be detected in the future. The identification of more S-stars will prove crucial to confirm this scenario.

7.1 OUTLOOK

My work opens a number of intriguing perspectives for future developments. One crucial step will be inclusion of non-equilibrium chemistry in the SPH simulations. This will ensure two advantages. First, it guarantees that gas cooling is modeled using the detailed atomic and molecular cooling functions, which do not depend only on temperature and density but also on the species abundance. This latter evolves self-consistently within the simulations, taking also into account cosmic-ray ionization rate, which can be non-negligible in GN environments (Goto et al. 2013). Second, it enables to study the composition of gas, focusing on the molecular gas tracers such as HCO^+, CO, H_3^+. In this way, the simulations will be directly comparable with present and forthcoming observations. This will be the core project of my forthcoming JSPS fellowship.

In addition, the simulations presented in Chapter 5 can be exploited to improve the models used to infer the dynamical mass of SMBH from high resolution interferometry. While the effect of warps and outflows in circumnuclear gas has been recently investigated by Yoon (2017), further study is required to constrain the effects of non-circular motions due to disk eccentricity and irregular spatial distribution.

In this Thesis, all SMBHs were considered to be quiescent, i.e. I neglected any form of AGN feedback. Although this is certainly the case for the current state of the GC, it is not necessarily true in general. The addition of AGN feedback prescription to the simulations would allow to investigate a broad range of phenomena in GNs.

Furthermore, new approaches could be pursued to explore the origin of cloud G2. Simulations in Chapter 6 showed that starless planets could orbit in the CW disk along with the massive stars. A three-body encounter involving two disk stars and a planet could eject the latter from the disk and bring it on an orbit close to the SMBH. Given its numerical complexity, this scenario has not yet been investigated. However, given the intrinsic Keplerian nature of the problem, it is possible to approach it by borrowing numerical techniques from planetary dynamics. In this way I will be able to study the effect of angular momentum transport and even three-body scatterings on the dynamics of planets embedded in the CW disk.

A

EARLY EVOLUTION OF YOUNG MASSIVE STAR CLUSTERS: THE INTERPLAY BETWEEN DYNAMICAL HEATING AND STELLAR MASS LOSS

Young dense star star clusters (SCs) are self-gravitating systems composed of young stars that formed from the same giant molecular cloud and are approximately coeval. Young dense SC cores may reach densities higher than $10^3\ M_\odot pc^{-3}$, much like globular clusters, but have smaller sizes. Young dense SCs have virial radius $r_{vir} \sim 1\,pc$, while globular clusters have $r_{vir} \sim 10\,pc$ (Portegies Zwart, McMillan, and Gieles 2010). Such self-gravitating systems evolve through two-body relaxation, i.e., the exchange of energy between stars due to long-range two-body interactions. The two-body relaxation timescale (t_{relax}) is the time needed for the system to lose memory of its initial velocities. As $t_{relax} \propto r_{vir}^{3/2} M^{1/2}$ (where M is the total mass of the cluster), young dense SCs have $t_{relax} \lesssim 100$ Myr, much less than globular clusters, which have $t_{relax} \gtrsim 1$ Gyr.

Thus, young dense SCs are exceptional laboratories to study the dynamics of star clusters, for three reasons: (i) they evolve much faster than globular cluster; (ii) they are objects of recent formation, and may be observed at different stages of evolution, unlike the much older globular clusters; (iii) gas dynamics and stellar evolution may still play a relevant role in the dynamical evolution, unlike globular clusters, which are gas-poor, evolved systems. Stellar evolution may affect the dynamical evolution of young dense SCs mainly through stellar winds and supernovae. Both phenomena remove mass from the cluster, making the potential well shallower. Moreover, compact remnants may sink to the cluster core and affect the evolution of the whole SC via three-body encounters.

In this Appendix I investigate how metal-dependent stellar evolution affects the dynamical evolution of young dense SCs. In particular, I compare the effects of stellar evolution for different structural parameters of the cluster (total mass, virial radius, concentration, metallicity). For this purpose, I run a set of direct-N body simulations that incorporated the self-consistent treatment of stellar evolution. I identified three regimes of evolution which depend on the metallicity and the dynamical age of young dense SCs. This allows to explain how the interplay between stellar evolution and dynamics shapes the observable properties of the young dense SCs in the Local Group.

A.1 INTRODUCTION

Dense SCs are collisional systems: their two-body relaxation timescale is shorter than their lifetime. This causes the evaporation of stars from the core, removing kinetic energy. Since a self-gravitating system has a negative heat capacity, the velocity dispersion of the core increases as it contracts. More stars escape from the core, which loses even more kinetic energy. This runaway process is called gravothermal instability and leads the core to collapse (e.g. Spitzer 1987; Aarseth 2003; Binney and Tremaine 2008).

Only an energy source in the core can halt the collapse and quench the instability. This energy source can be represented by three-body encounters, i.e. close encounters between a binary and a single star. During such encounters, part of the internal energy of the binary may be redistributed as kinetic energy between the single star and the centre of mass of the binary. In this way, the binary hardens (i.e. its binding energy increases) and the kinetic energy of the system increases (Heggie 1975). By this process, called binary hardening, few binaries in the core can provide the kinetic energy needed to restore the virial equilibrium and reverse the core collapse. If there are no primordial binaries in the core, binary formation is triggered by the high stellar density of the core during the collapse. In the post-collapse phase, the energy generated by three-body encounters in the core is driven outwards by two-body relaxation and the SC expands. This expansion causes the half-mass radius to increase according to $r_{hm} \propto t^{2/3}$ (Elson, Hut, and Inagaki 1987).

Mass loss by stellar evolution can deeply affect the evolution of a SC before and after core collapse (Angeletti and Giannone 1977, 1980; Applegate 1986; Chernoff and Weinberg 1990; Portegies Zwart and McMillan 2007; Vesperini, McMillan, and Portegies Zwart 2009; Lamers, Baumgardt, and Gieles 2010; Gieles 2013). Moreover, supernovae (SNe) occur in the first 50 Myr since the birth of a SC.

Metallicity (Z) also plays a relevant role, since it determines the efficiency of stellar winds (Leitherer, Robert, and Drissen 1992; Maeder 1992; Pols et al. 1998; Portinari, Chiosi, and Bressan 1998; Kudritzki 2002). High-metallicity stars lose more mass by stellar winds than low-metallicity stars (Vink, de Koter, and Lamers 2001; Vink and de Koter 2005). Since it drives the mass loss rate of a star, metallicity indirectly affects the outcome of a SN explosion.

Schulman, Glebbeek, and Sills (2012) performed N-body simulations of intermediate-mass young SCs with a wide spectrum of metallicities, and found the size of SCs to be metallicity dependent. Metal-rich SCs expand more rapidly than metal-poor SCs in the first 20 Myr, while the trend reverses thereafter. Similarly, Downing (2012) simulated globular clusters with different metallicity using Monte Carlo methods. He found that the half-mass radius of metal-poor SCs is

smaller at early times than that of metal-rich SCs, but then grows larger within a relaxation timescale, in agreement with Schulman, Glebbeek, and Sills (2012).

Mapelli and Bressan (2013) ran N-body simulations of intermediate-mass young SCs with different metallicity, and found that the half-mass radius of metal-poor SCs grows larger than that of metal-rich SCs, while the core radius of metal-poor SCs expands less than that of metal-rich SCs after core collapse. They interpreted this result as an effect of the interplay between mass loss by stellar winds and dynamical heating, the expansion of the core being driven mostly by mass loss in metal-rich SCs and by three-body encounters in metal-poor SCs.

On the other hand, Sippel et al. (2012) investigated the effect of metallicity on massive $N = 10^5$ SCs using direct N-body simulations with stellar and binary evolution (Hurley, Pols, and Tout (2000) and Hurley, Tout, and Pols (2002)). They found no structural differences between SCs at different metallicities.

Our aim is to check the relative importance of binary hardening and metallicity-dependent stellar evolution in determining the structural properties of SCs. In particular, I will expand and generalize the results presented in Mapelli and Bressan (2013), by considering a different SC mass range, different central densities and concentrations.

In Section A.2, I describe the methodology that I employed for my simulations; in Section A.3 I present my results, with particular attention for the evolution of core and half-mass radius, and for the core radius oscillations. In Section A.4, I discuss the implications of my work and I compare it with analytic models. Our conclusions are presented in Section A.6.

A.2 METHOD

The simulations were run with the starlab software environment (Portegies Zwart and Verbunt 1996; Portegies Zwart et al. 2001), which uses a fourth-order Hermite integrator to compute the dynamics of stars and binaries. Single star and binary evolution are implemented in the SeBa routine (Portegies Zwart and Verbunt 1996). Our version of starlab includes new recipes for stellar evolution, as described in Mapelli et al. (2013). In particular, it includes the metallicity-dependence of stellar radius, temperature and luminosity, by implementing the polynomial fitting formulae of Hurley, Pols, and Tout (2000). It also includes updated recipes for mass loss by stellar winds of main sequence stars, by using the prescription of Vink, de Koter, and Lamers (2001).

Mapelli et al. (2013) also added an approximate treatment for luminous blue variable (LBV) and Wolf-Rayet (WR) stars. In this version of starlab, helium giants coming from stars with $m_{zams} > 25\,M_\odot$ are

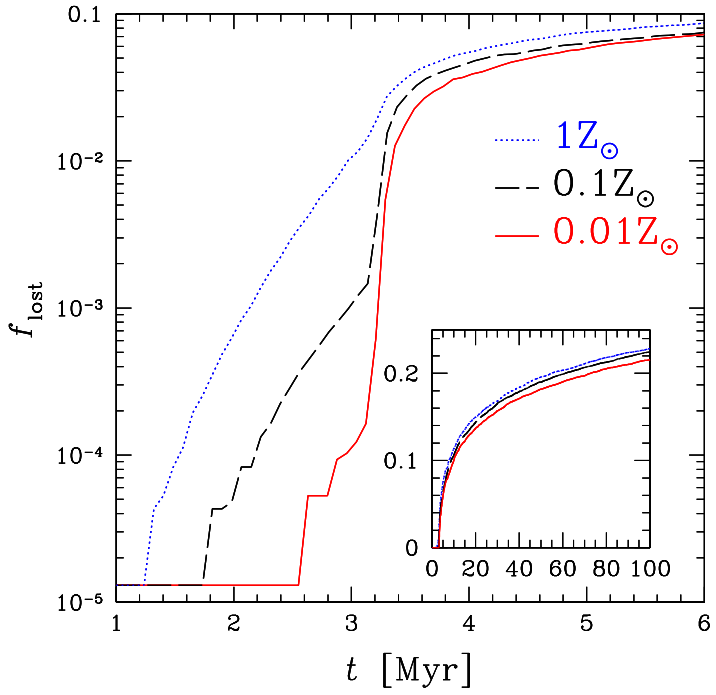

Figure A.1: Cumulative mass loss by stellar winds and SNe normalized to the initial mass of the SC as a function of time for three different metallicities. Solid red line: $Z = 0.01\,Z_\odot$; dashed black line: $Z = 0.1\,Z_\odot$; dotted blue line: $Z = 1\,Z_\odot$. Each line is the median value of 10 simulated SCs for different metallicity.

labelled as WR stars and they undergo mass loss-rate by stellar winds given by the formula: $\dot{m} = 10^{-13}\,(L/L_\odot)^{1.5}\,(Z/Z_\odot)^{0.86}\,M_\odot\,yr^{-1}$, where $L_\odot$ is the solar luminosity (Mapelli et al. 2013; Belczynski et al. 2010; Vink and de Koter 2005; Hamann and Koesterke 1998).

In the code, post-main-sequence stars with luminosity $L > 6 \times 10^5\,L_\odot$ and radius $R > 10^5\,(L/L_\odot)^{-0.5}\,R_\odot$, where $R_\odot$ is the solar radius, are labelled as LBV stars (Humphreys and Davidson 1994). Their mass-loss rate is calculated as $\dot{m} = f_{LBV} \times 10^{-4}\,yr^{-1}$, where $f_{LBV} = 1.5$ is an arbitrary constant chosen to reproduce the most massive known stellar BHs (Belczynski et al. 2010).

Stellar winds of asymptotic giant branch stars are modelled as in the original version of starlab and do not include any metal-dependent recipes. I assume that the mass lost by stellar winds and SNe is ejected from the SC, and it is thus removed from the simulation. This assumption is realistic for SN ejecta and also for the winds of massive stars, which are expected to move fast (> 2000 km s^{-1} for the O stars, e.g. Muijres et al. 2012; > 1000 km s^{-1} for the WR stars, e.g. Vink and de Koter 2005; Martins et al. 2008b) with respect to the central escape velocity of the simulated SCs ($\sim$12 km s^{-1} for SCs of set A and B, and $\sim$6 km s^{-1} for SCs of set B). Stellar winds by AGB stars have much smaller velocities ($10-20$ km s^{-1}, Loup et al. 1993; González Delgado

et al. 2003; Nanni et al. 2013; Schulman, Glebbeek, and Sills 2012), but still sufficiently high to escape from my simulated SCs. Furthermore, AGB stars do not play an important role for the results presented in this paper, as the winds from AGB stars become important at $\gtrsim 50$ Myr.

The formation of stellar remnants is implemented as described in Mapelli et al. 2013. In particular, black hole (BH) masses for various metallicities follow the distribution described in Fig. 1 of Mapelli and Bressan (2013; see also Fryer 1999; Fryer and Kalogera 2001; Belczynski et al. 2010; Fryer et al. 2012), If the final mass m_{fin} of the progenitor star (i.e. the mass before the collapse) is > 40 $M_\odot$, I assume that the SN fails and that the star collapses quietly to a BH. The requirement that $m_{fin} > 40$ $M_\odot$ implies that only stars with ZAMS mass $\geqslant 80$ and $\geqslant 100$ $M_\odot$ can undergo a failed SN at $Z = 0.01$ and 0.1 $Z_\odot$, respectively. If $m_{fin} > 40$ $M_\odot$, the mass of the BH is derived as $m_{BH} = m_{CO} + f_{coll}\,(m_{He} + m_H)$, where m_{CO} is the final mass of the Carbon Oxygen (CO) content of the progenitor, while m_{He} and m_H are the residual mass of Helium (He) and of Hydrogen (H), respectively. f_{coll} is the fraction of He and H mass that collapses to the BH in the failed SN scenario. I assume $f_{coll} = 2/3$ to match the maximum values of m_{BH} at $Z = 0.01$ $Z_\odot$ derived by Belczynski et al. 2010. In this scenario, BHs with mass up to ~80 $M_\odot$ (~40 $M_\odot$) can form if the metallicity of the progenitor is $Z \sim 0.01$ $Z_\odot$ (Z~0.1 $Z_\odot$). BHs that form from quiet collapse are assumed to receive no natal kick (Fryer et al. 2012). For BHs that form from a SN explosion, the natal kicks were drawn from the same distribution as neutron stars but scaled with the ratio of the mass (see Mapelli et al. 2013 for details).

A.2.1 *Initial conditions and simulation grid*

The SCs are initialised as a multi-mass, isotropic King (1966) model composed of $N = 50000$ stars and no initial binaries. Neglecting the primordial binaries increases the importance of formation and hardening of binaries by three-body encounters during core collapse, without altering the behaviour of core and half-mass radius significantly, as shown by Mapelli and Bressan (2013). It also diminishes the statistical noise of the simulations, allowing to determine more easily the moment of core collapse (Heggie, Trenti, and Hut 2006). I adopt two values for the dimensionless potentials: $W_0 = 5$ and $W_0 = 9$, which correspond to an initial concentration of $c = 1.031$ and $c = 2.120$, respectively. Two different virial radii r_{vir} were chosen for the models with $W_0 = 5$: $r_{vir} = 1$ pc (set A) and $r_{vir} = 5$ pc (set B). The SCs with $W_0 = 9$ were modelled with $r_{vir} = 1$ pc only (set C). The stars follow a Kroupa (2001) IMF with $m_{max} = 150\,M_\odot$ and $m_{min} = 0.1\,M_\odot$. The values of the initial relaxation timescale are listed in Table A.1, along with the main initial conditions. These initial conditions resemble the

SET	N	M [10^4 $M_\odot$]	r_{vir} [pc]	W_0	ρ_c [$M_\odot$ pc^{-3}]	t_{rh} [Myr]	t_{rc} [Myr]
A	50K	3.25	1	5	2×10^4	36	29
B	50K	3.25	5	5	2×10^2	394	308
C	50K	3.25	1	9	10^7	44	$\lesssim 1$

Table A.1: Initial conditions. N: number of centres of mass; M: SC average mass; W_0: dimensionless central potential of the King (1966) model; ρ_c: core mass density; t_{rh}: relaxation timescale at half-mass radius in Myr; t_{rc}: relaxation timescale at core radius in Myr;

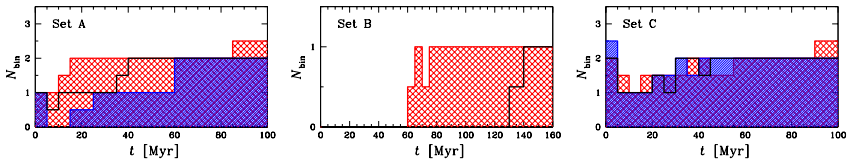

Figure A.2: Number of hard binaries in my simulations as a function of time for the three considered metallicities: $Z = 1\,Z_\odot$ (hatched blue histogram), $Z = 0.1\,Z_\odot$ (black empty histogram) and $Z = 0.01\,Z_\odot$ (cross-hatched red histogram). Since my simulations do not have primordial binaries, all the binaries are formed dynamically. Left-hand panel: SCs with initial $r_{vir} = 1$ pc and $W_0 = 5$ (set A). Middle panel: SCs with initial $r_{vir} = 5$ pc and $W_0 = 5$ (set B). Right-hand panel: SCs with initial $r_{vir} = 1$ pc and $W_0 = 9$ (set C). Each histogram is the median value of 10 realizations.

properties of observed young massive SCs (see e.g. Portegies Zwart, McMillan, and Gieles 2010).

Each model was run for three metallicities: $Z = 1, 0.1, 0.01\,Z_\odot$. For these initial conditions, SCs with different metallicity experience different mass loss by stellar evolution, as shown in Fig. A.1. Regardless of the metallicity, most of the mass loss by stellar evolution occurs in the first $\simeq 10$ Myr, so I expect that stellar mass loss will drive the dynamics only in the early evolution of the SCs. In the following, I will define $t_{se} \simeq 6$ Myr the lifetime of the massive stars ($> 30\ M_\odot$).

I have run each simulation for at least 100 Myr. I ran 10 realisations for each set of initial conditions, changing only the random numbers used to compute each realisation. I checked that there are no significant differences in the median values of core and half-mass radius if I consider either five or ten realizations. Thus, ten realizations per metallicity are sufficient to filter out most stochastic fluctuations. No external tidal field was set for the simulations. In this way I focus on the intrinsic properties of the simulated SCs.

A.3 RESULTS

A.3.1 *Evolution of core and half-mass radius*

In this section I discuss the structural evolution of the simulated SCs. All the quantities discussed in this section are median quantities computed from the ten realisation for each metallicity. To check if binary hardening is driving the reverse of core collapse I follow the binding energy of the binaries in the simulations. Since the simulations have no primordial binaries, the total binary binding energy at a given time corresponds to the kinetic energy injected into the SC. I also checked the number of binaries formed during the simulations. Fig. A.2 shows the number of binaries as a function of time for set A, set B and set C. No more than three hard binaries are present on average at a single time, indicating that most of the binary binding energy is retained in few hard binaries. The number of binaries formed during the simulations depends on the considered initial conditions (set A, B and C), and on the metallicity.

Set A

SCs of set A collapse at the same time, regardless of the metallicity. At $t_{cc} \simeq 3$ Myr, the collapse is halted, the core bounces and begins to expand. Metallicity affects only the post-collapse phase: the core bounce is stronger at higher metallicity (Fig. A.3, left-hand panel). This difference is maximum at 10 Myr, when the mass loss from the most massive stars is over, and the core radius of $Z = 1\,Z_\odot$ SCs has grown 60 per cent larger than that of $Z = 0.01\,Z_\odot$ SCs. I also find that, in the long run, the core radius of metal-poor SCs becomes larger, on average, than the core radius of $Z = 1\,Z_\odot$ SCs.

The half-mass radius of metal-poor SCs expands more than that of metal-rich ones (Fig. A.3, middle panel). At 100 Myr, the half-mass radius of $Z = 0.01\,Z_\odot$ SCs is 14 per cent larger than the half-mass radius of $Z = 1\,Z_\odot$ SCs. The reasons for the expansion of the halo will be discussed in Section A.4.

The right-hand panel of Fig. A.3 shows the evolution of the binary binding energy. The first peak in the binary binding energy coincides with the core bounce, but disappears immediately after for SCs with $Z = 1\,Z_\odot$ and $Z = 0.1\,Z_\odot$. Only in the case with $Z = 0.01\,Z_\odot$ the hardening goes on right after the bounce at 3 Myr. In general, the hardening of binaries starts later at higher metallicity. In SCs with $Z = 1\,Z_\odot$, binary hardening begins at 20–50 Myr, depending on the simulation. In SCs with $Z = 0.1\,Z_\odot$, the binary hardening occurs even earlier, at 10–25 Myr. The left-hand panel of Fig. A.2 shows that only two hard binaries form on average during each simulation of set A. Binaries are formed earlier in metal-poor SCs, as a consequence of the earlier binary hardening.

Set B

The left-hand panel of Fig. A.4 shows the evolution of the core radius of the SCs of set B. During the first 3 Myr there is a weak decrease in the core radius. The decrease of core radius is the beginning of a long and slow phase of core collapse, interrupted by the first SN explosions at 3 Myr. The impulsive mass loss at 3 Myr causes an expansion of both core and half-mass radius. The initial expansion of the core is over at ≈ 7 Myr. Then, the core begins to collapse, faster at lower metallicity. In the simulations with $Z = 1\,Z_\odot$ the core radius remains approximately constant, and only three SCs out of ten show a decrease in core radius after 120–130 Myr. Six of the SCs with $Z = 0.1\,Z_\odot$ show a core bounce at ≈160 Myr, while three experience an early core collapse at 100–120 Myr. In SCs with $Z = 0.01\,Z_\odot$ the collapse begins immediately after the initial expansion, but the time when core collapse stops varies from SC to SC, and goes from 50 Myr to 140 Myr.

At 3 Myr the half-mass radius evolves in the opposite way with respect to SCs of set A: the half-mass radius of metal-rich SCs expands more than that of the metal-poor SCs, at least during the first 60 Myr (Fig. A.4, middle panel). The half-mass radius of metal-rich SCs at ≈35 Myr is 5 per cent larger than that of metal-poor SCs.

At 60–70 Myr the half-mass radius of SCs with $Z = 0.01\,Z_\odot$ begins to expand faster than that of metal-rich SCs. This coincides with the beginning of binary hardening in SCs with $Z = 0.01\,Z_\odot$. The half-mass radius of SCs with $Z = 0.01\,Z_\odot$ at 160 Myr has grown 4 per cent larger than the half-mass radius of metal-rich SCs. With respect to the SCs of set A, the difference in half-mass radius among SCs of different metallicity remains < 10 per cent throughout the simulations.

Binary hardening occurs earlier at low metallicity (Fig. A.4, right-hand panel). Binary hardening is absent in the SCs with $Z = 1\,Z_\odot$, since they are the only SCs not experiencing core collapse in the time spanned by the simulations. In fact, no hard binaries are formed in $Z = 1\,Z_\odot$ SCs, and only one is formed (on average) in SCs with $Z \leqslant 0.1\,Z_\odot$ (Fig. A.2, middle panel).

Set C

The high ($W_0 = 9$) initial concentration of SCs of set C implies that the core of the SCs of set C is already collapsed at the beginning of the simulations. During the simulations, the core radius never reaches values as small as the initial one. Since the core is already collapsed, strong three-body encounters immediately occur and cause the core to rapidly expand (Fig. A.5, left-hand panel). The right-hand panel of Fig. A.5 shows a peak of binary binding energy at 3 Myr, which is five orders of magnitude higher than the one in the less concentrated SCs of set A.

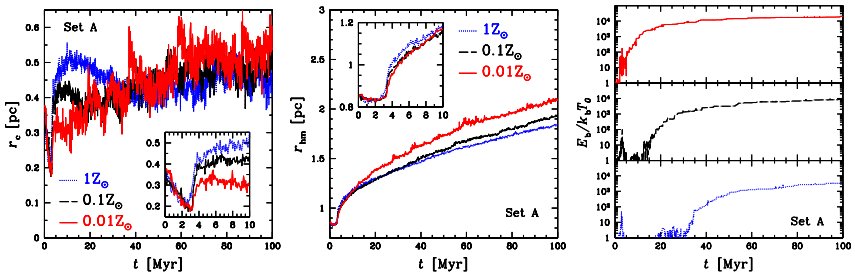

Figure A.3: Core (left-hand panel) and half-mass (middle panel) radius as a function of time for the three considered metallicities. In the insets: zoom of the first 10 Myr. Right-hand panel: total internal energy of the binary content of the SCs as a function of time, normalised to the initial $k_b T_0 = \frac{1}{3}\langle K\rangle|_{t=0}$, where $\langle K\rangle$ is the average kinetic energy of a star. Solid red line: $Z = 0.01\,Z_\odot$; dashed black line: $Z = 0.1\,Z_\odot$; dotted blue line: $Z = 1\,Z_\odot$. Each line is the median value of 10 simulated SCs with initial $r_{vir} = 1\,pc$ and $W_0 = 5$ (set A).

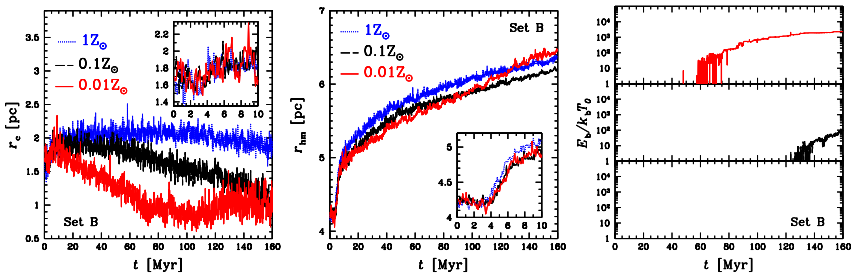

Figure A.4: Same as Fig. A.3, but for simulations with $r_{vir} = 5\,pc$ and $W_0 = 5$ (set B).

At ≈5 Myr the core radius of SCs with $Z = 1, 0.1\,Z_\odot$ has expanded 30 per cent more than that of $Z = 0.01\,Z_\odot$ SCs. This difference is half as much as in the SCs of set A. Afterwards, the expansion slows down due to the diminished stellar mass loss rate. However, the core density in metal-poor SCs is still high enough to make binary hardening go on. As in SCs of set A, I find that the core of metal-poor SCs expands faster than the core of metal-rich SCs, in the long run.

I notice no further binary hardening after the initial expansion of the core in metal-rich SCs, at least until the core collapses again. The second collapse and the hardening of binaries varies from SC to SC, but it generally begins earlier at lower metallicity. The hardening of binaries begins around 20 Myr for the SCs with $Z = 1\,Z_\odot$ and at 10–15 Myr for the SCs with $Z = 0.1\,Z_\odot$ and $0.01\,Z_\odot$. This behaviour is similar to the one observed in the SCs of set A, and indicates that stellar mass loss has sustained the initial expansion. Right-hand panel of Fig. A.2 shows that two hard binaries are formed on average in each simulation. There are no significant differences in the number of binaries between SCs of different metallicity.

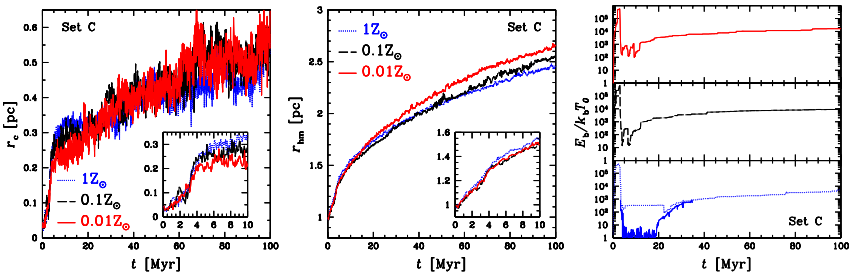

Figure A.5: Same as Fig. A.3, but for simulations with $r_{vir} = 1$ pc and $W_0 = 9$ (set C). The solid cyan line in the bottom right panel is the binding energy of the binaries in the core of the SCs with $Z = 1\,Z_\odot$. The plateau of the binary binding energy in $Z = 1\,Z_\odot$ SCs from 5 Myr to 30 Myr is due to an hard binary escaping from the core.

The middle panel of Fig. A.5, shows the evolution of the half-mass radius. I find that at 100 Myr, the half-mass radius of $Z = 0.01\,Z_\odot$ SCs is larger by 8 per cent than the one of $Z = 1\,Z_\odot$ SCs. The difference is less pronounced than in less concentrated SCs of set A, in agreement with the results of Schulman, Glebbeek, and Sills (2012). Moreover, I notice that at 100 Myr the half-mass radius of the SCs with $W_0 = 9$ is larger by 30 per cent than the half-mass radius of the SCs with $W_0 = 5$.

A.3.2 *Core radius oscillations*

In the post-collapse phase, the core can still be subject to the gravothermal instability which has driven the collapse phase. In this case, the re-expansion of the core is quickly halted and the gravothermal catastrophe is restored. Then the core undergoes repeated contractions and re-expansions, which are called gravothermal oscillations.

Gravothermal oscillations were first discovered by Bettwieser and Sugimoto (1984) by following the post-collapse phase of SCs using a gas model. The oscillations were later found also in Fokker-Plank calculations (Cohn, Hut, and Wise 1989) and N-body simulations (Makino 1996). These oscillations are called gravothermal, since gravothermal instability is thought to drive both expansion and contraction phases (Makino and Sugimoto 1987; Heggie, Inagaki, and McMillan 1994; Makino 1996; McMillan and Engle 1996; Breen and Heggie 2012b,a). While the collapse phase is always driven by the gravothermal instability, it is debated whether and under which conditions the expansion phase has a gravothermal nature.

Most of my simulated SCs show core radius oscillations. These are not present in the core radius profile shown in Figs A.3, A.4 and A.5 since the oscillations cancel out when summing and averaging multiple SCs.

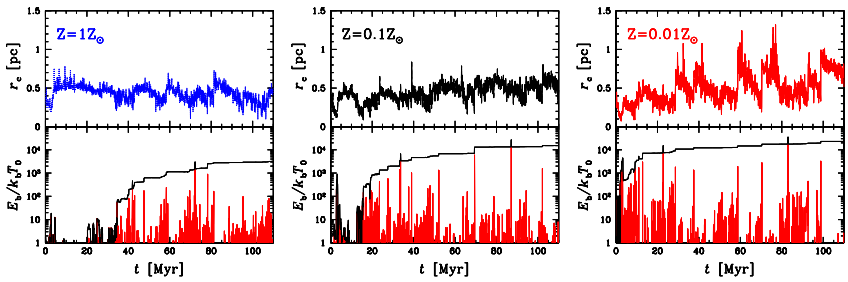

Figure A.6: Top panels: core radius as a function of time for three selected clusters from Set A. Bottom panels: total internal energy of the binary content of the SCs as a function of time, normalized to the initial $k_b T_0 = \frac{1}{3}\langle K\rangle|_{t=0}$, where $\langle K\rangle$ is the average kinetic energy of a star. Black line: cumulative binary binding energy. Ochre line: increment in binary binding energy. Each line is obtained from single simulations with $r_{vir} = 1\,pc$ and $W_0 = 5$ (set A). Left-hand panel: $Z = 1\,Z_\odot$. Middle panel: $Z = 0.1\,Z_\odot$. Right-hand panel: $Z = 0.01\,Z_\odot$.

In Fig. A.6, I show the evolution of core radius and binary binding energy for three individual simulations of set A. While the first core collapse occurs at 3 Myr for every realisation, the subsequent oscillations are stochastic and vary from SC to SC. After the first bounce at 3 Myr, the core collapse goes on and it is halted by a series of further core bounces. The resulting profile of the core radius versus time has a saw-tooth appearance.

The oscillations are metallicity dependent: number and amplitude of oscillations increase at lower metallicity. From the lower panels of Fig. A.6, it is evident that every increase of core radius matches always the increments in the binary binding energy. This indicates that while the first bounce is mostly supported by mass loss by SNe and stellar winds, further bounces are supported only by binary hardening. The randomness of the oscillations is a consequence of the stochastic nature of three-body encounters.

The simulations of Fig. A.6 represent the typical oscillations for the simulations of set A at the given metallicity. Individual simulations of set C present the same behaviour. This is not the case for the simulations of set B, because some of them do not undergo a core collapse phase. In the case of set B, mild oscillations occur in one SC with $Z = 0.1\,Z_\odot$ and in most of the SC with $Z = 0.01\,Z_\odot$.

A.4 DISCUSSION

A.4.1 *Interplay between dynamics and stellar evolution*

The expansion of the half-mass radius is the consequence of a heating mechanism being active in the core. This mechanism can be either binary hardening, or mass loss by stellar evolution. However, these two

processes are metallicity dependent: stellar winds are inefficient at lower metallicity and do not contribute to reverse the core collapse. Thus, the core density increases more dramatically, and this enhances close encounters and thus binary hardening. A higher metallicity leads to stronger stellar-mass loss, which partially reverses core collapse, without strong binary hardening. Thus, I expect the half-mass radius of SCs with different metallicity to behave differently according to the dominant process that heats the SCs. If binary hardening is the dominant process, I expect the half-mass radius of metal-poor SCs to grow faster than that of metal-rich ones, because three-body encounters transfer more energy into the halo. In contrast, if stellar mass loss is the dominant process, metal-rich SCs are expected to expand more with respect to metal-poor SCs, because stellar winds make the potential well shallower.

In both set A and set C, the half-mass radius of metal-poor SCs becomes larger than that of metal-rich ones, even if the size difference is more pronounced in set A than in set C. This indicates that binary hardening is responsible for the expansion of the SCs of both sets A and C. In contrast, metal-poor SCs of set B have a slightly smaller half-mass radius than that of metal-rich SCs until 80 Myr. After that time, the half-mass radius of SCs with $Z = 0.01\,Z_\odot$ begins to expand faster than that of metal-rich SCs. This means that, until the 80 Myr, the main heating mechanism of the SCs is stellar mass loss, but then binary hardening begins to be dominant in SCs with $Z = 0.01\,Z_\odot$.

The different evolution of the three simulated sets can be explained by considering how fast is the core collapse (expressed in terms of the core collapse timescale t_{cc}) with respect to the lifetime of massive stars $t_{se} \sim 6$ Myr.

Set A

SCs of set A have a half-mass relaxation timescale of $t_{rh} \simeq 30\,\mathrm{Myr}$. If I assume $t_{cc} \simeq 0.15$–$0.20\ t_{rh}$ (Portegies Zwart and McMillan 2002; Gürkan, Freitag, and Rasio 2004; see also Fujii and Portegies Zwart 2014 and Section A.4.3) the core collapse proceeds simultaneously with the stellar mass loss ($t_{cc} \sim t_{se}$) in SCs of set A. In this situation, the interplay between the two processes is complicated.

Core collapse reaches its maximum at 3 Myr. While the first hard binaries begin to form, the first SNe remove mass from the SC and drive the expansion of the core. The expansion of the core is stronger in metal-rich SCs, because of the higher mass loss from the massive stars. The expansion also quenches three-body encounters. Only in the case with $Z = 0.01\,Z_\odot$ the core does not expand enough to quench the hardening, which instead goes on after the bounce.

The importance of stellar mass loss during the core bounce is confirmed by a set of test simulations without stellar evolution (see Sec-

tion A.5). Though some hard binary form in the core collapse, the core bounce is mainly due to the mass loss by the SN explosions.

Fig. A.3 shows that the binary binding energy at high metallicity ($Z \geqslant 0.1\,Z_\odot$) goes almost to zero during the expansion of the core. The main reason is that the binaries formed during the core collapse are unbound by the first SN explosions. In fact, the most massive stars are members of the first hard binaries, so that they are the first to undergo SN explosion. This is confirmed by the left-hand panel of Fig. A.2 which shows that one hard binary is formed during the first 5 Myr, but then is disrupted in high metallicity ($Z \geqslant 0.1\,Z_\odot$) SCs.

As stellar mass loss becomes less intense, the core begins to recollapse. The recollapse is faster in metal-poor SCs than in metal-rich SCs, for two reasons: (i) the core of metal-poor SCs has become more dense and massive than that of metal-rich ones; (ii) metal-poor SCs have a higher maximum remnant mass, and core collapse in SCs with a mass spectrum tends to proceed on the dynamical friction timescale of the most massive stars, which shortens as the mass of the stars increases (Fujii and Portegies Zwart 2014).

The reversal of the second core collapse can not be sustained by stellar mass loss, and eventually binary hardening is triggered. Because the second core collapse occurs faster in metal-poor SCs, binary hardening begins earlier (Fig. A.3). For this reason (and also for the higher frequency and strength of three-body encounters), more kinetic energy is extracted from binaries in metal-poor SCs than in metal-rich SCs. As soon as this kinetic energy is carried outwards by two-body relaxation, the rest of the SC expands and the half-mass radius increases accordingly. This results in a faster expansion of the half-mass radius in metal-poor SCs with respect to metal-rich ones. The stronger heating causes also the core radius of metal-poor SCs to become larger than the core radius of $Z = 1\,Z_\odot$ SCs. Overall, set A confirms the trend found by Mapelli and Bressan (2013), who simulate ten times less massive SCs.

Set B

SCs of set B have a larger virial radius, which results in a longer half-mass relaxation timescale $t_{rh} \simeq 308$ Myr. Thus, the core collapses when the most massive stars have already died for a long time ($t_{cc} \gg t_{se}$). In this regime, stellar evolution and dynamics are decoupled, and the evolution of the SCs is characterized by an early stage dominated by stellar mass loss, followed by a late stage dominated by binary hardening. The stage dominated by stellar mass loss lasts longer for metal-rich SCs.

After 60–70 Myr the half-mass radius of SCs with $Z = 0.01\,Z_\odot$ begins to expand faster than that of metal-rich SCs. I argue that this faster expansion is driven by the additional heating due to binary

hardening. In fact, only $Z = 0.01\,Z_\odot$ SCs undergo significant heating by binary hardening before 100 Myr (Fig. A.4).

The differences in half-mass radius between SCs of different metallicity remain very small (< 10 per cent) throughout the simulations. This can be due to the differences in stellar mass loss (Fig. A.1) being too small to produce significant differences in the SC expansion. However, I can not exclude that size differences due to binary hardening may become significant at > 160 Myr, the time at which I stop the simulations.

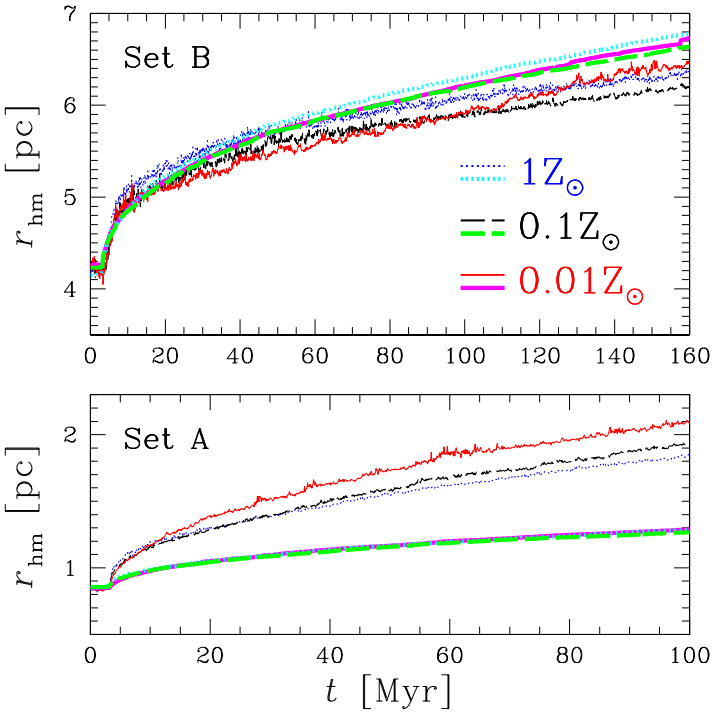

Figure A.7: Half-mass radius as a function of time. The solid red thin line, the dashed black thin line and the dotted blue thin line are the median value of the half-mass radius obtained from the simulations with $Z = 0.01\,Z_\odot$, $Z = 0.1\,Z_\odot$ and $Z = 1\,Z_\odot$, respectively. The solid magenta thick line, the dashed green thick line and the dotted cyan thick line are computed using a semi-analytic prescription (see Section A.4.1) with $Z = 0.01\,Z_\odot$, $Z = 0.1\,Z_\odot$ and $Z = 1\,Z_\odot$, respectively. The lines representing the semi-analytic prescription are smoother than the lines of the N-body simulations. In the bottom panel, the lines of the semi-analytic prescription overlap. Top panel: SCs with initial $r_{vir} = 5$ pc and $W_0 = 5$ (set B). Bottom panel: SCs with initial $r_{vir} = 1$ pc and $W_0 = 5$ (set A).

In the case of the simulations of set B, the stellar mass loss is the source of energy initially driving the expansion of the SCs. To check this, I compare the time evolution of the half-mass radius in the simulations with that of an analytic model (Fig. A.7). In this model, I assume that the half-mass radius changes according to the expansion

of the SC due to mass loss. Then, mass is ejected in a time shorter than the dynamical time, the half-mass radius r_{hm} is related to the total mass M of the SC by the formula (see e.g. Hills 1980):

$$\frac{r_{hm}(t)}{r_{hm}(0)} = \frac{M(t)/M(0)}{2M(t)/M(0) - 1} \tag{A.1}$$

For $M(t)$, $M(0)$ and $r_{hm}(0)$ I use the values obtained from the simulations. In particular, for $M(t)$ I use the total bound mass of the SCs, to take into account the escapers due to SN kicks.

This impulsive approximation is valid for the first SNe, but begins to overestimate the half-mass radius expansion at later times, when the mass loss rate slows down. Nonetheless, Fig. A.7 fairly reproduces the evolution of the half-mass radius for set B in the first ~60 Myr. This semi-analytic prescription fails to reproduce the evolution of the half-mass radius for set A, because the expansion is mostly due to binary hardening.

Set C

SCs of set C have the same size and mass as SCs of set A, but are much more concentrated. They have a core relaxation timescale shorter than 1 Myr, which means that the core is already collapsed at the beginning of the simulations ($t_{cc} \ll t_{se}$). The initial core density of these SCs is high enough to make binary hardening the dominant process involved in the reversal of the core collapse.

As in the SCs of set A, the energy generated by three-body encounters is higher in metal-poor SCs. As a result, metal-poor SCs expand more than metal-rich SCs. However, the size differences between SCs of different metallicity are smaller with respect to the set A (8 per cent, compared to 14 per cent). I argue that stellar mass loss contributes to the expansion to a lesser extent with respect to SCs of set A. Stellar mass loss is less important than dynamics and the differences arising from different metallicities are less evident. In fact, SCs of set C expand more than SCs of set A, and this is due to the stronger heating by binary hardening.

A.4.2 *Core oscillations: gravothermal or not?*

I investigated whether or not the oscillations found in the simulations of set A are gravothermal. While the contracting phase of the oscillations is always driven by the gravothermal instability, the expanding phase may not. According to McMillan and Engle (1996), the evidence of gravothermal behaviour is a prolonged expansion of the core, during which there is no binary heating. This would mean that the energy required to expand the core is flowing from outside the core, rather than being generated by three-body encounters in the core.

I do not find any significant prolonged expansion of the core without binary activity. I argue that most of the expansion phases of the oscillations are not gravothermal, but are driven only by binary hardening. Another clue of the non-gravothermal behaviour of the oscillations is that many core bounces are very rapid. This is mostly evident in the SCs with $Z = 0.01\,Z_\odot$ (Fig. A.6, lower panel), in which the increase in core radius is very discontinuous. Gravothermal oscillations should exhibit a much longer expansion phase, which proceeds on the relaxation timescale of the core (Bettwieser and Sugimoto 1984). Furthermore, after that the rapid expansion occurs, the core immediately begins to lose kinetic energy, i.e. the collapse driven by gravothermal instability is immediately restored. If an energy flux was established from the inner halo to the core, the core would not lose kinetic energy so quickly and the transition between expansion and contraction phase would be more gradual. The increase of oscillations at lower metallicity confirms that these oscillations are related to strong three-body encounters, rather than to an inverse temperature gradient.

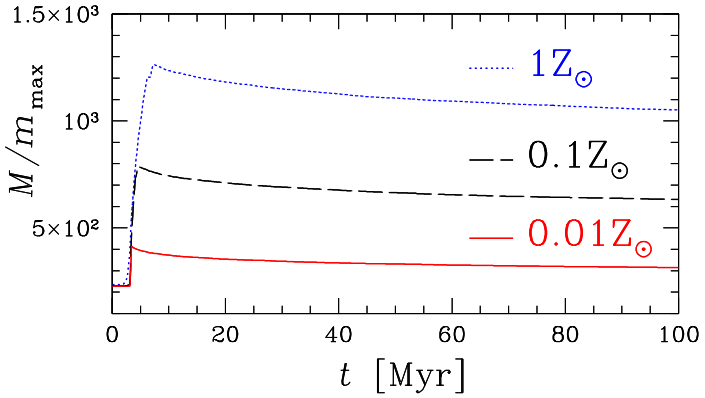

Figure A.8: Ratio of total mass of the SC M and the maximum stellar mass m_{max} as a function of time for my simulated SCs. Solid red line: $Z = 0.01\,Z_\odot$; dashed black line: $Z = 0.1\,Z_\odot$; dotted blue line: $Z = 1\,Z_\odot$.

This result is consistent with the criterion of Breen and Heggie (2012a) for gravothermal oscillations in multi-mass systems. They argued that gravothermal oscillations should occur for SCs in which $N_{eff} = M/m_{max} \gtrsim 10^4$. As shown in Fig. A.8, N_{eff} is always well below this limit, especially for the metal-poor SCs.

In particular, the expanding phase of the oscillations in SCs with $Z = 0.01\,Z_\odot$ are very rapid and dramatic. They correspond to a sudden increase of binary binding energy due to a single, strong three-body encounter occurred in the core. These three-body encounters are associated with the ejection of a binary or of a massive star.

A.4.3 *Core collapse time*

The SCs of set A have a relaxation timescale of $t_{rh} \simeq 36\,\mathrm{Myr}$. If I assume $t_{cc} \simeq 0.2 t_{rh}$ (Portegies Zwart and McMillan 2002), I expect the core collapse to take place at $t_{cc} \simeq 7\,\mathrm{Myr}$. However, I find that the core collapse occurs much earlier, at $t_{cc} \simeq 3\,\mathrm{Myr}$. In particular, the SCs of set A undergo core collapse at the same time as the SCs simulated by Mapelli and Bressan (2013), which have $N = 5000$ and a half-mass relaxation time of $t_{rh} \simeq 12\,\mathrm{Myr}$.

The most likely explanation is provided by Fujii and Portegies Zwart (2014). They find that the core collapse time scales as $t_{cc}/t_{rc} \propto (m_{max}/\langle m \rangle)^{-1}$, where $\langle m \rangle$ is the mean stellar mass and m_{max} the upper mass limit of the IMF. This relation starts to deviate at a larger values of $m_{max}/\langle m \rangle$ for models with low N (see Fig. 6 of Fujii and Portegies Zwart 2014). In particular, Fujii and Portegies Zwart (2014) find that this scaling breaks for $N_{eff} = M/m_{max} \lesssim 100$, below which the system starts to behave chaotically.

While the SCs of set A and those in Mapelli and Bressan (2013) have the same ratio $m_{max}/\langle m \rangle \simeq 230$, the former have $N_{eff} \simeq 216$ while the latter have $N_{eff} \simeq 23$. This means that the ratio t_{cc}/t_{rc} is different for each SC model. In fact, the left-hand panel of Fig. 6 in Fujii and Portegies Zwart (2014) shows that the ratio t_{cc}/t_{rc} of the two models with $m_{max}/\langle m \rangle \simeq 258$, $N = 2k$ and $N = 32k$ differs roughly by a factor of $1/3$. Since the t_{rh} of the SCs of set A is 3 times the t_{rh} of the SCs in Mapelli and Bressan (2013), the factor $1/3$ cancels the differences in the relaxation timescale and leads to the same t_{cc} for both simulations.

A.5 RUNS WITHOUT STELLAR MASS LOSS

I simulated two additional sets (of 10 SCs each) with the same initial conditions as set A and B, but without stellar evolution. I switched off stellar winds and SN explosions, so that stars do not lose mass throughout simulations. The simulations without stellar evolution are the extreme case in which dynamical heating is the only process driving the expansion of the SCs. I plot the evolution of core and half-mass radius of these simulations in Fig. A.9, in comparison with that of the runs with stellar evolution.

The left-hand panel of Fig. A.9 confirms that stellar mass loss does not influence the core collapse time. Comparing the core radii, it is apparent that the initial expansion of the core is caused only by stellar evolution. Also the expansion of the half-mass radius is strongly influenced by stellar evolution. The increase in half-mass radius at 3 Myr is stronger in SCs with stellar evolution, since it is mainly due to the first SN explosions. However, at late times, the half-mass radius in the simulations without stellar evolution increases much faster than

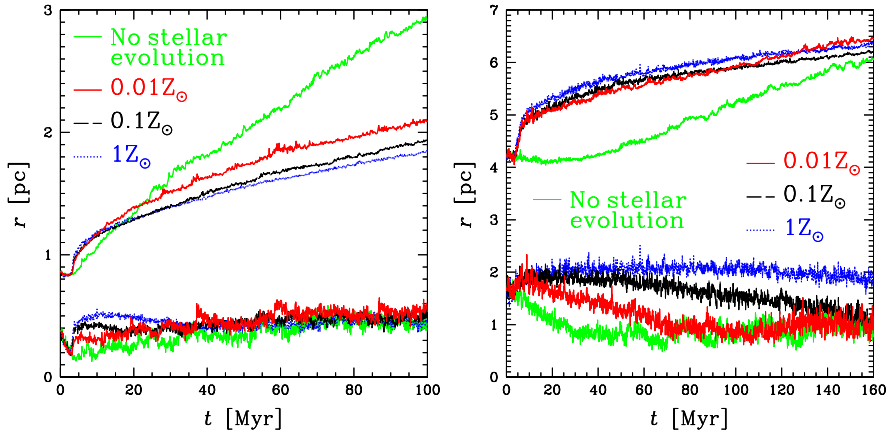

Figure A.9: Core (bottom lines) and half-mass (top lines) radius as a function of time for the three considered metallicities, and for simulations without stellar evolution. Solid red line: $Z = 0.01\,Z_\odot$; dashed black line: $Z = 0.1\,Z_\odot$; dotted blue line: $Z = 1\,Z_\odot$. Solid green line: no stellar evolution. Left-hand panel: SCs with $r_{vir} = 1\,pc$ and $W_0 = 5$ (set A); right-hand panel: SCs with $r_{vir} = 5\,pc$ and $W_0 = 5$ (Set B). Each line is the median value of 10 simulated SCs.

that of SCs with stellar evolution, due to the enhanced dynamical heating.

In the right-hand panel of Fig. A.9 it is evident that the weak core collapse in the first 3 Myr of SCs with of set B is the beginning of a longer core collapse. In the simulations with stellar evolution, this collapse is interrupted by the sudden ejection of mass by the first SNe. From the comparison of the half-mass radius, it is also clear that the increase of the half-mass radius after 3 Myr is only due to the stellar evolution.

A.6 CONCLUSIONS

I ran direct N-body simulations to investigate the impact of stellar evolution and dynamics on the structural properties of SCs. Three sets of initial conditions were used to vary the core relaxation timescale t_{rc} of the SCs and thus the importance of dynamics. I expect that the efficiency of stellar evolution with respect to dynamical heating depends on the ratio between the core collapse timescale t_{cc} and the lifetime of massive stars t_{se}. I consider three cases: $t_{cc} \sim t_{se}$, $t_{cc} \gg t_{se}$, $t_{cc} \ll t_{se}$.

Metallicity plays an important role: metal-rich SCs lose more mass than metal-poor SCs because of stellar winds and SNe. I find that the main effect of stellar mass loss is to delay the hardening of binaries, and this delay is more severe for higher metallicity.

I found size differences in SCs with different metallicity. The differences are more significant in the simulations with $t_{cc} \sim t_{se}$ (set A), for which I find that at $t = 100\,\mathrm{Myr}$ metal-poor SCs have a 14 per cent larger half-mass radius than metal-rich SCs. Similar size differences were found in the simulations with $t_{cc} \ll t_{se}$ (set C). Simulations with $t_{cc} \gg t_{se}$ (set B) do not show significant size differences between SCs of different metallicity.

This result can be explained as follows.

- In the SCs of set A ($t_{cc} \sim t_{se}$), stellar mass loss contributes to the reversal of core collapse, and this contribution becomes more important at higher metallicity. As a result, the hardening of binaries begins later for metal-rich SCs, even if the core collapse occurs at the same time regardless of the metallicity. The expansion of the core after collapse (i.e. the core bounce) is larger for high metallicity.

  Thus, the core of metal-poor SCs remains much denser, and the hardening of binaries begins earlier at low metallicity. Moreover, the hardening of binaries is enhanced by the more massive remnants of metal-poor SCs. Due to the enhanced heating, the half-mass radius of metal-poor SCs expands faster and, by the end of the simulation, it is 14 per cent larger than the half-mass radius of metal-rich SCs

  The SCs of set A exhibit the same behaviour as the less massive SCs simulated by Mapelli and Bressan (2013), except for the core radius oscillations. In particular, the size differences between SCs with different metallicity are consistent with the results of Mapelli and Bressan (2013) and Schulman, Glebbeek, and Sills (2012).

- For SCs of set B ($t_{cc} \gg t_{se}$), the delay of binary hardening is a consequence of the delayed core collapse. During the first $\sim 60\,\mathrm{Myr}$, the evolution of the SCs is ruled by stellar evolution. During this time, the SCs experience an expansion of the core, which lasts longer for higher metallicity. Stellar mass loss also drives the expansion of the half-mass radius. Before the core collapse of the metal-poor SCs, the half-mass radius of metal-rich SCs is 5 per cent larger than that that of metal-poor SCs.

  Once metal-poor SCs experience core collapse, the injection of energy by three-body encounters begins in their core. As a consequence, metal-poor SCs begin to expand more than metal-rich ones, and the half-mass radius of metal-poor SCs becomes larger than the half-mass radius of metal-rich SCs. However, on average, the differences in half-mass radius between SCs with different metallicity remain < 10 per cent, throughout the simulations.

- For SCs of set C ($t_{cc} \ll t_{se}$), the core of the SCs is already collapsed at the beginning of the simulations. The initial core density of these SCs is so high that binary hardening is the dominant process involved in the reversal of the core collapse. Since stellar mass loss is less important than dynamics, the differences arising from different metallicities are less evident. After the reversal of core collapse, the evolution of the simulated SCs with $W_0 = 9$ is qualitatively similar to the evolution of SCs with $W_0 = 5$, but the size differences between SCs with different metallicity are smaller.

Finally, I found core radius oscillations in the simulated SCs with $r_{vir} = 1\,pc$ and in some of the SCs with $r_{vir} = 5\,pc$. These oscillations grow in number and amplitude as metallicity decreases. I investigated whether the expansion phase of these oscillations was driven by gravothermal instability or by strong three-body interactions occurring in the core. I concluded that most of the oscillations are not gravothermal, but they are associated with the ejection of massive stars and binaries from the core.

In summary, I confirm that the interplay between metallicity-dependent stellar evolution and dynamical heating is a crucial ingredient to understand the evolution of young SCs. In forthcoming studies, I will investigate how the physics of gas evaporation and the presence of strong tidal fields can affect this scenario.

B

NUMERICAL METHODS

In this Chapter I describe the numerical methods employed in this Thesis. Section B.1 presents the fundamentals of the AMUSE framework, which was used in Chapter 4. Section B.2 describes the regularized code used to run the simulations in Chapter 6.

B.1 THE AMUSE FRAMEWORK

AMUSE is python framework that interfaces numerical solvers provided by the astrophysical community, which are referred as community codes. Each community code is tailored for a specific astrophysical domain, e.g. direct N-body codes for collisional dynamics, SPH or grid-based codes for hydrodynamic problems and tree codes for collisionless dynamics.

All the community codes are set up and run via an AMUSE user script written in PYTHON. The communication between the PYTHON layer and the community codes is handled via MPI message channels. However, all the complexity of the MPI interface is hidden from the user script layer.

Figure B.1 shows a scheme of the AMUSE design. An AMUSE application consists of a user script, an interface layer and the community code, which can be written in any programming language. The end user only has to write the PYTHON user script, wherein the initial data, the community codes and parameters are specified.

One of the greatest strength of AMUSE is its built-in parallelism. Each code "lives" in its own independent MPI instance, thus avoiding name space conflicts. This makes possible to run multiple parallel instances of codes which were not originally designed for parallelism. Moreover, every code shares the same interface for the setup of parameters and initial conditions, which makes extremely easy to change and test different numerical methods for the same physical application.

Besides the ability to run parallel instances of different codes in a single user script, AMUSE has the ability to couple the them in order to simulate complex physical systems with multiple components. For example, a direct N-body and a SPH solver can be used to simulate an embedded star cluster composed of gas and stars. The AMUSE user script for this application runs in parallel the SPH code to evolve the gas particles and the direct N-body code to evolve the stellar dynamics. Gravitational coupling between gas and stellar particles is provided by the BRIDGE scheme, described in the next section.

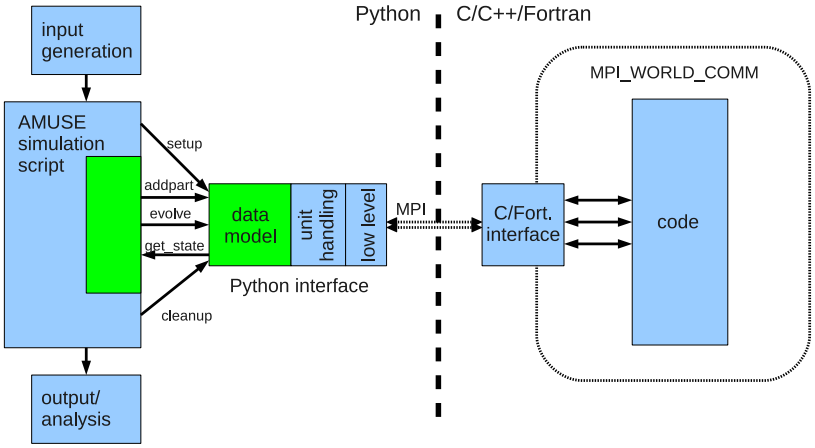

Figure B.1: Design of the AMUSE interface. This diagram represents the way in which a community code is accessed from the AMUSE framework. The code has a thin layer of interface functions in its native language which communicate through an MPI message channel with the PYTHON host process. On the PYTHON side the user script ("AMUSE simulation script") only accesses generic calls ("setup," "evolve" etc.) to a high level interface. This high level interface calls the low level interface functions, hiding details about units and the code implementation. From Fig. 1 of Pelupessy et al. (2013).

Many other kind of coupling are possible. One-way coupling can be used in case a sub-system is affected by another one, but the reverse effect is negligible, for example in case of stellar evolution in a star cluster simulation. While stellar dynamics is affected by mass loss via stellar winds and supernovae, stellar evolution is largely unaffected by dynamics.

Hierarchical or nested coupling is also possible when several independent subsystems are embedded into a larger one, as for planetary systems around stars in a stellar cluster. A code can deal with the stellar dynamics, ignoring the planets contribution to the gravitational potential, while multiple planetary evolution codes can be run independently on the every star hosting a planet. Perturbation from other stars in the star cluster can be added easily at the user script layer via BRIDGE.

This approach would not be appropriate during close stellar encounters, where the planet-planet interactions become non-negligible. In this cases, AMUSE allows for dynamic coupling during run-time: codes can be stopped and started according to condition specified in the user script. For example, during a close encounter between stars two hosting planets, the two planetary codes "attached" to the stars can be stopped and the whole subsystem can be integrated using a

few-body code on the fly, without any user intervention (e.g. see Cai et al. 2017).

B.1.1 *The* BRIDGE *scheme*

The classical BRIDGE scheme was originally developed by Fujii et al. (2007) to simulate a star cluster orbiting a parent galaxy, modeled with "live" particles. Given the large number of particles constituting the galaxy model, it becomes prohibitively expensive to simulate the whole system with direct N-body methods (whose computational cost scales as N^2). Moreover, the level of accuracy required to integrate a collisionless system such a galaxy can be fulfilled by computationally cheaper methods like tree force evaluation method (whose computational cost scales as $N \log N$).

To speed up the calculations, in Fujii et al. (2007) the cluster is integrated using accurate direct summation of the gravitational forces among all stars. Interactions among the stars in the galaxy, and between galactic and cluster stars, are computed using a fast tree-based integrator.

This is implemented as an extension of the mixed-variable symplectic scheme, which was first introduced by Wisdom and Holman (1991) and Kinoshita, Yoshida, and Nakai (1991) for the long-term interaction of planetary systems and it is still used nowadays by several planetary evolution codes (e.g. MERCURY Chambers 1999, GENGA Grimm and Stadel 2014).

In the BRIDGE implementation of Fujii et al. (2007), the Hamiltonian of the entire system is divided into two parts:

$$H = H_A + H_B, \tag{B.1}$$

where H_A is the potential energy of the gravitational interactions between galaxy particles and the star cluster (W_{g-c}):

$$H_A = W_{g-c}, \tag{B.2}$$

and H_B is the sum of the total kinetic energy of all particles ($K_g + K_c$) and the potential energy of the star cluster particles (W_c) and the galaxy (W_g)

$$H_B = K_g + W_g + K_c + W_c \equiv H_g + H_c \tag{B.3}$$

The time evolution of any quantity f under this Hamiltonian can then be written approximately (because we have truncated the formal solution to just the second-order terms) as:

$$f'(t + \Delta t) \approx e^{\frac{1}{2}\Delta t \mathcal{A}} e^{\Delta t \mathcal{B}} e^{\frac{1}{2}\Delta t \mathcal{A}} f(t), \tag{B.4}$$

where the operators $\mathcal{A}$ and $\mathcal{B}$ are defined by $\mathcal{A}f = \{f, H_A\}$, $\mathcal{B}f = \{f, H_B\}$, and $\{.,.\}$ is a Poisson bracket. The evolution operator $e^{\Delta t \mathcal{B}}$ splits into

two independent parts because H_B consists of two parts without cross terms. This leads to familiar second-order Leapfrog algorithm.

Within AMUSE, BRIDGE is extended to work between particles associated to any community code embedded into AMUSE. The mutual interaction between codes occurs in kick-drift-kick leapfrog scheme with a fixed timestep Δt , which is set in the user script. Suppose we want to gravitationally couple two distinct codes, say CODE A and CODE B. Each code has its own set of particles, whose mutual gravitational interaction is evolved individually with their respective integrator. At each BRIDGE timestep Δt, CODE B particles evolve due to the gravity of CODE A particles in the following way:

1. At time t_0, the gravitational acceleration from CODE A particles on CODE B particles $a_0^{A\to B}$ is computed using any user-defined algorithm (e.g. direct computation or tree algorithm).
2. Particles of CODE B are given a velocity kick due to the acceleration $a_0^{A\to B}$ for half a timestep.
3. Positions and velocities of CODE B particles are evolved from timestep t_0 to $t_0 + \Delta t$ using CODE B integrator.
4. At time $t_0 + \Delta t$, the acceleration from CODE A particles on CODE B particles $a_1^{A\to B}$ is recomputed.
5. Particles of CODE B are given a second velocity kick due to the acceleration $a_1^{A\to B}$ for half a timestep.

The previous steps can be repeated with the two codes switched, so that in the end CODE A and CODE B are mutually coupled. The scheme is summarized in Figure B.2.

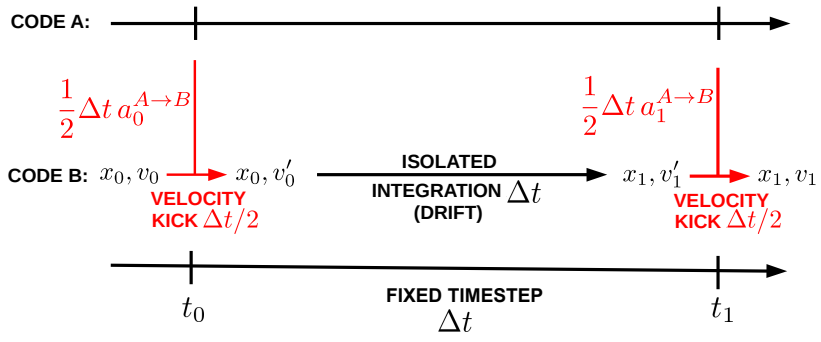

Figure B.2: Sketch of the BRIDGE scheme. For simplicity, only the interaction from CODE A to CODE B is showed.

B.2 FEW-BODY REGULARIZED CODE

The code used in Chapter 6 is code for few-body integration which can achieve energy and angular momentum conservation down to machine precision. It based on the following techniques: regularization of the equations of motion (Section B.2.1), chain coordinates to reduce round-off errors (Section B.2.2) and Bulirsch–Stoer extrapolation (Section B.2.3).

B.2.1 *Regularization*

One well known issue of integrating compact self-gravitating systems is simply that the Newtonian gravitational force scales as r^{-2}, with r being the particle separation. This means that for two particles, $r \to 0$ and $a \to \infty$. In this case, to mantain the same accuracy, the integration timestep has to decrease, possibly leading to the halt of the integration.

One possible solution is to remove the singularity of the force in $r = 0$ by adding a so-called softening in the expression of the Newtonian force:

$$\mathbf{F}(r) = -\frac{GmM}{r^2 + \epsilon^2}\hat{r} \tag{B.5}$$

This method is not optimal for collisional systems, as it *de facto* prevents particles to interact at distances shorter than ϵ.

Another approach to transform the Hamiltonian into an equivalent form in which the equations of motions do not display a singularity in $r = 0$. This method is called regularization and it consists essentially of a transformation of space and/or time variables. The regularized equation of motions for the coplanar three-body problem were introduced by Levi-Civita (1920) and later generalized to three dimensions by Kustaanheimo and Stiefel (1965). The Kustaanheimo and Stiefel (1965) regularization has been widely applied to regularize the integration of binaries in direct N-body simulations.

The regularization for few-body problem was first introduced by Mikkola and Tanikawa (1999b). Mikkola and Tanikawa (1999a) first noted that the Hamiltonian for the two-body problem

$$H = \frac{1}{2}\mathbf{p}^2 - m/r \tag{B.6}$$

(with $G = 1$) could be extended in phase space to the equivalent logarithmic form:

$$H = \frac{1}{2}\log(\mathbf{p}^2 + P_t) + \log(mr) \tag{B.7}$$

where $\mathbf{p}$ is the momentum vector conjugate to the position vector $\mathbf{r}$, $r = |\mathbf{r}|$, and P_t is the momentum of t, treated as a coordinate in the extended phase space.

In fact, any Hamiltonian of the form

$$\Lambda = \log(T + P_t) - \log(U) \tag{B.8}$$

(where $T(\mathbf{p})$ is the kinetic energy and $U(\mathbf{q}, t)$ the negative potential energy) leads to the same equations of motion of the Hamiltonian $H = T - U$. The equations of motion derivable from Λ are:

$$\frac{d\mathbf{p}}{ds} = -\frac{d\Lambda}{d\mathbf{q}} = \frac{dU}{d\mathbf{q}}\frac{1}{U} \tag{B.9}$$

$$\frac{dP_t}{ds} = -\frac{d\Lambda}{dt} = \frac{dU}{dt}\frac{1}{U} \tag{B.10}$$

$$\frac{d\mathbf{q}}{ds} = \frac{d\Lambda}{d\mathbf{p}} = \frac{dT}{d\mathbf{p}}\frac{1}{T + P_t} \tag{B.11}$$

$$\frac{dt}{ds} = \frac{d\Lambda}{dP_t} = \frac{1}{T + P_t} \tag{B.12}$$

where s is the new independent variable, related to the time t by Equation B.12. Since Λ does not explicitly depend on s, P_t can be chosen to be $P_t = -T + U$. Using the previous expression and Equation B.12, it is possible to recover the familiar equations of motions:

$$\begin{aligned} \frac{d\mathbf{p}}{dt} &= \frac{dU}{d\mathbf{q}} \\ \frac{dP_t}{dt} &= \frac{dU}{dt} \\ \frac{d\mathbf{q}}{dt} &= \frac{dT}{d\mathbf{p}} \end{aligned} \tag{B.13}$$

Analogously, equations of motions can be derived from Equation B.6.

$$\frac{d\mathbf{p}}{ds} = -\frac{\mathbf{r}}{r^2} \tag{B.14}$$

$$\frac{d\mathbf{r}}{ds} = \frac{\mathbf{p}}{\mathbf{p}^2/2 + P_t} \tag{B.15}$$

$$\frac{dt}{ds} = \frac{1}{\mathbf{p}^2/2 + P_t} \tag{B.16}$$

and Equation B.10 is not needed since there is no time-dependent potential. The expression for s can be derived from Equation B.12:

$$s = \int^t (\mathbf{p}/2 - m/r)\, dt \tag{B.17}$$

This set of equations is manifestly symplectic and can be integrated with a Leapfrog method.

$$\mathbf{r}_{1/2} = \mathbf{r}_0 + \frac{h}{2}\frac{\mathbf{p}_0}{\mathbf{p}_0^2/2 + P_t} \tag{B.18}$$

$$t_{1/2} = t_0 + \frac{h}{2}\frac{1}{\mathbf{p}_0^2/2 + P_t} \tag{B.19}$$

$$\mathbf{p} = \mathbf{r}_1 - h\frac{\mathbf{r}_{1/2}}{r_{1/2}^2} \tag{B.20}$$

$$\mathbf{r}_1 = \mathbf{r}_{1/2} + \frac{h}{2}\frac{\mathbf{p}_1}{\mathbf{p}_1^2/2 + P_t} \tag{B.21}$$

$$t_1 = t_{1/2} + \frac{h}{2}\frac{1}{\mathbf{p}_1^2/2 + P_t} \tag{B.22}$$

where h is the timestep in s.

This algorithm produces exact conservation of energy and angular momentum, regardless of h. This can be easily shown by noting that $\mathbf{r}_1 \times \mathbf{p}_1 = \mathbf{r}_0 \times \mathbf{p}_1$ and $\mathbf{e}_1 = \mathbf{p}_1 \times (\mathbf{r}_1 \times \mathbf{p}_1)/m - \mathbf{r}_1/r_1 = \mathbf{p}_0 \times (\mathbf{r}_0 \times \mathbf{p}_0)/m - \mathbf{r}_0/r_0 = \mathbf{e}_0$. On the other hand, this algorithm introduces an error on time (i.e. phase), since Equation B.22 only approximates Equation B.12. It can be shown that the time error is $O(h^3)$.

Note that this regularization does not remove the singularity in $r = 0$, for which $|p| \to \infty$. However, as long as r is not numerically evaluated at 0, the algorithm will produce exact results for all the orbital parameters except pericenter time. The advantage of this regularization is that is achieved without any coordinate ($\mathbf{r}$) transformation, unlike Kustaanheimo and Stiefel (1965) regularization. Furthermore, while the above equations are valid for the two-body problem, they can be quickly generalized to the N-body problem. In addition, this method can be extended to include time-dependent and even velocity-dependent forces (see Mikkola and Merritt 2006).

B.2.2 *Chain coordinates*

Another issue in the integration of closely-approaching particle are round-off errors. These can quickly arise if the interparticle separation is very small compared to the distance from the center-of-mass. This can happen easily in case of close binaries far from the center of a star cluster.

A solution is provided by the so-called chain algorithm, first introduced by Mikkola and Aarseth (1993) to regularize the few-body problem using a chain of Kustaanheimo and Stiefel (1965) regularized pairs. The method works as follows.

A chain of interparticle vectors is formed so that all particles included in the chain. The first segment of the chain is chosen to be the shortest interparticle distance in the system. The next segment is included so that it connects the particle closest to one of the ends of the current chain. This process is repeated until all particles are included.

As the system evolve, care is taken to update the chain so that any chained vector is always shorter than adjacent non-chained vectors.

It is possible to transform the old coordinates $\mathbf{r} = (\mathbf{r}_1, \mathbf{r}_2, ..., \mathbf{r}_N)$, $\mathbf{p} = (\mathbf{p}_1, \mathbf{p}_2, ..., \mathbf{p}_N)$ into new "chain" coordinates $\mathbf{R} = (\mathbf{R}_1, \mathbf{R}_2, ..., \mathbf{R}_{N-1})$, $\mathbf{P} = (\mathbf{P}_1, \mathbf{P}_2, ..., \mathbf{P}_{N-1})$ so that $\mathbf{P}_k = \mathbf{p}_{k+1} - \mathbf{p}_k$ and $\mathbf{R}_k = \mathbf{r}_{k+1} - \mathbf{r}_k$, with $k = 1, 2, ..., N$ and N is the number of particles along the chain. The corresponding generating function S takes the form:

$$S = \sum_{k=1}^{N-1} \mathbf{P}_k (\mathbf{r}_{k+1} - \mathbf{r}_k) \tag{B.23}$$

From the new Hamiltonian $H = T(\mathbf{P}) + U(\mathbf{R})$ it is then possible to derive the equations of motions analog to Equations B.14–B.16 and build a Leapfrog based on chain interparticle coordinates.

B.2.3 *Bulirsch–Stoer extrapolation*

A simple Leapfrog integration might not be accurate enough for some application. The Leapfrog integration error δ over a fixed time interval with timestep h can be expanded as $\delta = A_2 h^2 + A_4 h^4 + A_6 h^4 + ...$ Therefore, the results from the Leapfrog are then suitable to be improved with the Bulirsch-Stoer extrapolation.

The idea behind Bulirsch–Stoer extrapolation is to consider the results of a numerical integration as being an analytic function of the stepsize h. The solution of a given time interval s is computed for smaller and smaller substeps h and then it is extrapolated to zero h. Figure B.3 outlines the extrapolation method.

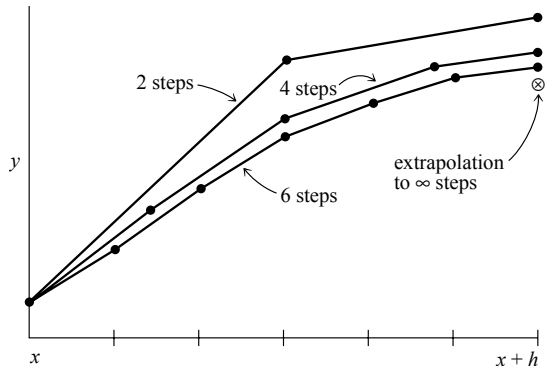

Figure B.3: Outline of the Bulirsch-Stoer extrapolation method. A stepsize interval h is spanned by different sequences of finer and finer substeps. Their results are extrapolated to an answer that is supposed to correspond to infinitely fine substeps. From *Numerical Recipes 3rd Edition: The Art of Scientific Computing*.

The number of timestep subdivisions to compute before the final extrapolation depends on the target accuracy, and it set to a maximum of 16. The solution is extrapolated using rational functions.

Rational function fits are superior to polynomials because of their ability to model functions with poles and their better convergence properties.

BIBLIOGRAPHY

Aarseth, S. J. (2003). "Gravitational N-Body Simulations". In: p. 430.

Agarwal, M. and M. Milosavljević (2011). "Nuclear Star Clusters from Clustered Star Formation". In: *ApJ* 729, 35, p. 35. DOI: 10.1088/0004-637X/729/1/35. arXiv: 1008.2986.

Agertz, O. et al. (2007). "Fundamental differences between SPH and grid methods". In: *MNRAS* 380, pp. 963–978. DOI: 10.1111/j.1365-2966.2007.12183.x. eprint: astro-ph/0610051.

Aharon, D. and H. B. Perets (2015). "Formation and Evolution of Nuclear Star Clusters with In Situ Star Formation: Nuclear Cores and Age Segregation". In: *ApJ* 799, 185, p. 185. DOI: 10.1088/0004-637X/799/2/185. arXiv: 1409.5121.

Alig, C. et al. (2011). "Simulations of direct collisions of gas clouds with the central black hole". In: *MNRAS* 412, pp. 469–486. DOI: 10.1111/j.1365-2966.2010.17915.x. arXiv: 0908.1100 [astro-ph.GA].

Alig, C. et al. (2013). "Numerical Simulations of the Possible Origin of the Two Sub-parsec Scale and Counterrotating Stellar Disks around SgrA*". In: *ApJ* 771, 119, p. 119. DOI: 10.1088/0004-637X/771/2/119. arXiv: 1305.2953.

Allen, D. A., A. R. Hyland, and D. J. Hillier (1990). "The source of luminosity at the Galactic Centre". In: *MNRAS* 244, pp. 706–713.

Andersen, D. R. et al. (2008). "Caught in Formation: The Nuclear-Cluster-to-Be in NGC 2139". In: *ApJ* 688, 990-999, pp. 990–999. DOI: 10.1086/592342. arXiv: 0808.1321.

Angeletti, L. and P. Giannone (1977). "Dynamical evolution of clusters with stellar mass loss". In: *A&A* 58, pp. 363–372.

Angeletti, L. and P. Giannone (1980). "Dynamical evolution of cluster models with a continuous stellar mass loss". In: *A&A* 85, pp. 113–118.

Antonini, F. (2013). "Origin and Growth of Nuclear Star Clusters around Massive Black Holes". In: *ApJ* 763, 62, p. 62. DOI: 10.1088/0004-637X/763/1/62. arXiv: 1207.6589.

Antonini, F., E. Barausse, and J. Silk (2015). "The Coevolution of Nuclear Star Clusters, Massive Black Holes, and Their Host Galaxies". In: *ApJ* 812, 72, p. 72. DOI: 10.1088/0004-637X/812/1/72. arXiv: 1506.02050.

Antonini, F. et al. (2012). "Dissipationless Formation and Evolution of the Milky Way Nuclear Star Cluster". In: *ApJ* 750, 111, p. 111. DOI: 10.1088/0004-637X/750/2/111. arXiv: 1110.5937.

Ao, Y. et al. (2013). "The thermal state of molecular clouds in the Galactic center: evidence for non-photon-driven heating". In: *A&A*

550, A135, A135. DOI: 10.1051/0004-6361/201220096. arXiv: 1211.7142.

Applegate, J. H. (1986). "Dynamical effects of stellar evolution in globular clusters". In: *ApJ* 301, pp. 132–144. DOI: 10.1086/163881.

Arca-Sedda, M. and R. Capuzzo-Dolcetta (2014). "The globular cluster migratory origin of nuclear star clusters". In: *MNRAS* 444, pp. 3738–3755. DOI: 10.1093/mnras/stu1683. arXiv: 1405.7593.

Arca-Sedda, M., R. Capuzzo-Dolcetta, and M. Spera (2016). "The dearth of nuclear star clusters in bright galaxies". In: *MNRAS* 456, pp. 2457–2466. DOI: 10.1093/mnras/stv2835. arXiv: 1510.01137.

Baganoff, F. K. et al. (2003). "Chandra X-Ray Spectroscopic Imaging of Sagittarius A* and the Central Parsec of the Galaxy". In: *The Astrophysical Journal* 591.2, p. 891. URL: http://stacks.iop.org/0004-637X/591/i=2/a=891.

Bahcall, J. N. and R. A. Wolf (1976). "Star distribution around a massive black hole in a globular cluster". In: *ApJ* 209, pp. 214–232. DOI: 10.1086/154711.

Bahcall, J. N. and R. A. Wolf (1977). "The star distribution around a massive black hole in a globular cluster. II Unequal star masses". In: *ApJ* 216, pp. 883–907. DOI: 10.1086/155534.

Balcells, M., A. W. Graham, and R. F. Peletier (2007). "Galactic Bulges from Hubble Space Telescope NICMOS Observations: Central Galaxian Objects, and Nuclear Profile Slopes". In: *ApJ* 665, pp. 1084–1103. DOI: 10.1086/519752. eprint: astro-ph/0404379.

Balick, B. and R. L. Brown (1974). "Intense sub-arcsecond structure in the galactic center". In: *ApJ* 194, pp. 265–270. DOI: 10.1086/153242.

Ballone, A. et al. (2013). "Hydrodynamical Simulations of a Compact Source Scenario for the Galactic Center Cloud G2". In: *ApJ* 776, 13, p. 13. DOI: 10.1088/0004-637X/776/1/13. arXiv: 1305.7238.

Barth, A. J. et al. (2016a). "Measurement of the Black Hole Mass in NGC 1332 from ALMA Observations at 0.044 arcsecond Resolution". In: *ApJ* 822, L28, p. L28. DOI: 10.3847/2041-8205/822/2/L28. arXiv: 1605.01346.

Barth, A. J. et al. (2016b). "Toward Precision Black Hole Masses with ALMA: NGC 1332 as a Case Study in Molecular Disk Dynamics". In: *ApJ* 823, 51, p. 51. DOI: 10.3847/0004-637X/823/1/51. arXiv: 1603.04523.

Bartko, H. et al. (2009). "Evidence for Warped Disks of Young Stars in the Galactic Center". In: *ApJ* 697, pp. 1741–1763. DOI: 10.1088/0004-637X/697/2/1741. arXiv: 0811.3903.

Bartko, H. et al. (2010). "An Extremely Top-Heavy Initial Mass Function in the Galactic Center Stellar Disks". In: *ApJ* 708, pp. 834–840. DOI: 10.1088/0004-637X/708/1/834. arXiv: 0908.2177.

Bate, M. R., I. A. Bonnell, and N. M. Price (1995). "Modelling accretion in protobinary systems". In: *MNRAS* 277, pp. 362–376. DOI: 10.1093/mnras/277.2.362. eprint: astro-ph/9510149.

Becklin, E. E., I. Gatley, and M. W. Werner (1982). "Far-infrared observations of Sagittarius A - The luminosity and dust density in the central parsec of the Galaxy". In: *ApJ* 258, pp. 135–142. DOI: 10.1086/160060.

Becklin, E. E. and G. Neugebauer (1968). "Infrared Observations of the Galactic Center". In: *ApJ* 151, p. 145. DOI: 10.1086/149425.

Bekki, K. (2007). "The Formation of Stellar Galactic Nuclei through Dissipative Gas Dynamics". In: *PASA* 24, pp. 77–94. DOI: 10.1071/AS07008.

Bekki, K. and A. W. Graham (2010). "On the Transition from Nuclear-cluster- to Black-hole-dominated Galaxy Cores". In: *ApJ* 714, pp. L313–L317. DOI: 10.1088/2041-8205/714/2/L313. arXiv: 1004.3627.

Bekki, K. et al. (2004). "Cluster Cannibalism and Scaling Relations of Galactic Stellar Nuclei". In: *ApJ* 610, pp. L13–L16. DOI: 10.1086/423130. eprint: astro-ph/0406442.

Belczynski, K. et al. (2010). "On the Maximum Mass of Stellar Black Holes". In: *ApJ* 714, pp. 1217–1226. DOI: 10.1088/0004-637X/714/2/1217. arXiv: 0904.2784 [astro-ph.SR].

Beloborodov, A. M. et al. (2006). "Clockwise Stellar Disk and the Dark Mass in the Galactic Center". In: *ApJ* 648, pp. 405–410. DOI: 10.1086/504279. eprint: astro-ph/0601273.

Bernardi, M. et al. (2007). "Selection Bias in the M_L-σ and M_L-L Correlations and Its Consequences". In: *ApJ* 660, pp. 267–275. DOI: 10.1086/512719. eprint: astro-ph/0609300.

Bettwieser, E. and D. Sugimoto (1984). "Post-collapse evolution and gravothermal oscillation of globular clusters". In: *MNRAS* 208, pp. 493–509. DOI: 10.1093/mnras/208.3.493.

Biernacki, P., R. Teyssier, and A. Bleuler (2017). "On the dynamics of supermassive black holes in gas-rich, star-forming galaxies: the case for nuclear star cluster co-evolution". In: *MNRAS* 469, pp. 295–313. DOI: 10.1093/mnras/stx845. arXiv: 1701.05190.

Binney, J. and S. Tremaine (2008). "Galactic Dynamics: Second Edition". In:

Blum, R. D., D. L. Depoy, and K. Sellgren (1995). "A comparison of near-infrared spectra of the galactic center compact He I emission-line sources and early-type mass-losing stars". In: *ApJ* 441, pp. 603–616. DOI: 10.1086/175386.

Blum, R. D., K. Sellgren, and D. L. Depoy (1995). "Discovery of a possible Wolf-Rayet star at the galactic center". In: *ApJ* 440, pp. L17–L20. DOI: 10.1086/187750.

Blum, R. D. et al. (2003). "Really Cool Stars and the Star Formation History at the Galactic Center". In: *ApJ* 597, pp. 323–346. DOI: 10.1086/378380. eprint: astro-ph/0307291.

Boehle, A. et al. (2016). "An Improved Distance and Mass Estimate for Sgr A* from a Multistar Orbit Analysis". In: *ApJ* 830, 17, p. 17. DOI: 10.3847/0004-637X/830/1/17. arXiv: 1607.05726.

Böker, T. et al. (2002). "A Hubble Space Telescope Census of Nuclear Star Clusters in Late-Type Spiral Galaxies. I. Observations and Image Analysis". In: *AJ* 123, pp. 1389–1410. DOI: 10.1086/339025. eprint: astro-ph/0112086.

Böker, T. et al. (2004). "A Hubble Space Telescope Census of Nuclear Star Clusters in Late-Type Spiral Galaxies. II. Cluster Sizes and Structural Parameter Correlations". In: *AJ* 127, pp. 105–118. DOI: 10.1086/380231. eprint: astro-ph/0309761.

Boley, A. C. (2009). "The Two Modes of Gas Giant Planet Formation". In: *ApJ* 695, pp. L53–L57. DOI: 10.1088/0004-637X/695/1/L53. arXiv: 0902.3999 [astro-ph.EP].

Boley, A. C. et al. (2010). "Clumps in the outer disk by disk instability: Why they are initially gas giants and the legacy of disruption". In: *Icarus* 207, pp. 509–516. DOI: 10.1016/j.icarus.2010.01.015. arXiv: 0909.4543 [astro-ph.EP].

Bonnell, I. A. and W. K. M. Rice (2008). "Star Formation Around Supermassive Black Holes". In: *Science* 321, p. 1060. DOI: 10.1126/science.1160653. arXiv: 0810.2723.

Breen, P. G. and D. C. Heggie (2012a). "Gravothermal oscillations in multicomponent models of star clusters". In: *MNRAS* 425, pp. 2493–2500. DOI: 10.1111/j.1365-2966.2012.21688.x. arXiv: 1207.2672.

Breen, P. G. and D. C. Heggie (2012b). "Gravothermal oscillations in two-component models of star clusters". In: *MNRAS* 420, pp. 309–319. DOI: 10.1111/j.1365-2966.2011.20036.x. arXiv: 1110.5198.

Brooks, A. and C. Christensen (2016). "Bulge Formation via Mergers in Cosmological Simulations". In: *Galactic Bulges* 418, p. 317. DOI: 10.1007/978-3-319-19378-6_12. arXiv: 1511.04095.

Burkert, A. et al. (2012). "Physics of the Galactic Center Cloud G2, on Its Way toward the Supermassive Black Hole". In: *ApJ* 750, 58, p. 58. DOI: 10.1088/0004-637X/750/1/58. arXiv: 1201.1414.

Cai, M. X. et al. (2017). "Stability of multiplanetary systems in star clusters". In: *MNRAS* 470, pp. 4337–4353. DOI: 10.1093/mnras/stx1464. arXiv: 1706.03789 [astro-ph.EP].

Calderón, D. et al. (2016). "Clump formation through colliding stellar winds in the Galactic Centre". In: *MNRAS* 455, pp. 4388–4398. DOI: 10.1093/mnras/stv2644. arXiv: 1507.07012.

Cappellari, M. et al. (2002). "The Counterrotating Core and the Black Hole Mass of IC 1459". In: *ApJ* 578, pp. 787–805. DOI: 10.1086/342653. eprint: astro-ph/0202155.

Capuzzo-Dolcetta, R. (1993). "The Evolution of the Globular Cluster System in a Triaxial Galaxy: Can a Galactic Nucleus Form by

Globular Cluster Capture?" In: *ApJ* 415, p. 616. DOI: 10.1086/173189. eprint: astro-ph/9301006.

Capuzzo-Dolcetta, R. and P. Miocchi (2008a). "Merging of Globular Clusters in Inner Galactic Regions. II. Nuclear Star Cluster Formation". In: *ApJ* 681, 1136-1147, pp. 1136–1147. DOI: 10.1086/588017. arXiv: 0801.1072.

Capuzzo-Dolcetta, R. and P. Miocchi (2008b). "Self-consistent simulations of nuclear cluster formation through globular cluster orbital decay and merging". In: *MNRAS* 388, pp. L69–L73. DOI: 10.1111/j.1745-3933.2008.00501.x. arXiv: 0804.4421.

Capuzzo-Dolcetta, R., M. Spera, and D. Punzo (2013). "A fully parallel, high precision, N-body code running on hybrid computing platforms". In: *Journal of Computational Physics* 236, pp. 580–593. DOI: 10.1016/j.jcp.2012.11.013. arXiv: 1207.2367 [astro-ph.IM].

Carmona-Loaiza, J. M. et al. (2014). "Overlapping inflow events as catalysts for supermassive black hole growth". In: *MNRAS* 438, pp. 1698–1713. DOI: 10.1093/mnras/stt2316. arXiv: 1312.2595 [astro-ph.GA].

Carollo, C. M., M. Stiavelli, and J. Mack (1998). "Spiral Galaxies with WFPC2. II. The Nuclear Properties of 40 Objects". In: *AJ* 116, pp. 68–84. DOI: 10.1086/300407. eprint: astro-ph/9804007.

Carson, D. J. et al. (2015). "The Structure of Nuclear Star Clusters in Nearby Late-type Spiral Galaxies from Hubble Space Telescope Wide Field Camera 3 Imaging". In: *AJ* 149, 170, p. 170. DOI: 10.1088/0004-6256/149/5/170. arXiv: 1501.05586.

Chambers, J. E. (1999). "A hybrid symplectic integrator that permits close encounters between massive bodies". In: *MNRAS* 304, pp. 793–799. DOI: 10.1046/j.1365-8711.1999.02379.x.

Chang, P. (2009). "The effectiveness of the Kozai mechanism in the Galactic Centre". In: *MNRAS* 393, pp. 224–228. DOI: 10.1111/j.1365-2966.2008.14202.x. arXiv: 0811.0829.

Chatzopoulos, S. et al. (2015). "The old nuclear star cluster in the Milky Way: dynamics, mass, statistical parallax, and black hole mass". In: *MNRAS* 447, pp. 948–968. DOI: 10.1093/mnras/stu2452. arXiv: 1403.5266.

Chernoff, D. F. and M. D. Weinberg (1990). "Evolution of globular clusters in the Galaxy". In: *ApJ* 351, pp. 121–156. DOI: 10.1086/168451.

Christopher, M. H. et al. (2005). "HCN and HCO^+ Observations of the Galactic Circumnuclear Disk". In: *ApJ* 622, pp. 346–365. DOI: 10.1086/427911. eprint: astro-ph/0502532.

Clénet, Y. et al. (2005). "A dual emission mechanism in <ASTROBJ>Sgr A*/L'</ASTROBJ>?" In: *A&A* 439, pp. L9–L13. DOI: 10.1051/0004-6361:200500146. eprint: astro-ph/0507088.

Cohn, H., P. Hut, and M. Wise (1989). "Gravothermal oscillations after core collapse in globular cluster evolution". In: *ApJ* 342, pp. 814–822. DOI: 10.1086/167638.

Collin, S. and J.-P. Zahn (1999). "Star formation and evolution in accretion disks around massive black holes." In: *A&A* 344, pp. 433–449.

Collin, S. and J.-P. Zahn (2008). "Star formation in accretion discs: from the Galactic center to active galactic nuclei". In: *A&A* 477, pp. 419–435. DOI: 10.1051/0004-6361:20078191. arXiv: 0709.3772.

Côté, P. et al. (2006). "The ACS Virgo Cluster Survey. VIII. The Nuclei of Early-Type Galaxies". In: *ApJS* 165, pp. 57–94. DOI: 10.1086/504042. eprint: astro-ph/0603252.

Cullen, L. and W. Dehnen (2010). "Inviscid smoothed particle hydrodynamics". In: *MNRAS* 408, pp. 669–683. DOI: 10.1111/j.1365-2966.2010.17158.x. arXiv: 1006.1524 [astro-ph.IM].

D'Alessio, P., N. Calvet, and L. Hartmann (2001). "Accretion Disks around Young Objects. III. Grain Growth". In: *ApJ* 553, pp. 321–334. DOI: 10.1086/320655. eprint: astro-ph/0101443.

Dale, J. E., B. Ercolano, and I. A. Bonnell (2015). "Early evolution of embedded clusters". In: *MNRAS* 451, pp. 987–1003. DOI: 10.1093/mnras/stv913. arXiv: 1504.05896.

Davis, T. A. (2014). "A figure of merit for black hole mass measurements with molecular gas". In: *MNRAS* 443, pp. 911–918. DOI: 10.1093/mnras/stu1163. arXiv: 1406.2555.

Davis, T. A. et al. (2013). "A black-hole mass measurement from molecular gas kinematics in NGC4526". In: *Nature* 494, pp. 328–330. DOI: 10.1038/nature11819. arXiv: 1301.7184 [astro-ph.CO].

Davis, T. A. et al. (2017). "WISDOM Project – II. Molecular gas measurement of the supermassive black hole mass in NGC 4697". In: *MNRAS* 468, pp. 4675–4690. DOI: 10.1093/mnras/stw3217. arXiv: 1703.05248.

De Colle, F. et al. (2014). "A Stellar Wind Origin for the G2 Cloud: Three-dimensional Numerical Simulations". In: *ApJ* 789, L33, p. L33. DOI: 10.1088/2041-8205/789/2/L33. arXiv: 1406.1188.

Deguchi, S. et al. (2004). "SiO Maser Survey of IRAS Sources in the Inner Galactic Disk". In: *PASJ* 56, pp. 765–802. DOI: 10.1093/pasj/56.5.765. eprint: astro-ph/0407419.

Do, T. et al. (2013). "Stellar Populations in the Central 0.5 pc of the Galaxy. I. A New Method for Constructing Luminosity Functions and Surface-density Profiles". In: *ApJ* 764, 154, p. 154. DOI: 10.1088/0004-637X/764/2/154. arXiv: 1301.0539 [astro-ph.SR].

Do, T. et al. (2014). "Prospects for Measuring Supermassive Black Hole Masses with Future Extremely Large Telescopes". In: *AJ* 147, 93, p. 93. DOI: 10.1088/0004-6256/147/4/93. arXiv: 1401.7988.

Do, T. et al. (2015). "Discovery of Low-metallicity Stars in the Central Parsec of the Milky Way". In: *ApJ* 809, 143, p. 143. DOI: 10.1088/0004-637X/809/2/143. arXiv: 1506.07891.

Downing, J. M. B. (2012). "Is there a size difference between red and blue globular clusters?" In: *MNRAS* 425, pp. 2234–2243. DOI: 10.1111/j.1365-2966.2012.21680.x. arXiv: 1204.5363.

Dressler, A. and D. O. Richstone (1988). "Stellar dynamics in the nuclei of M31 and M32 - Evidence for massive black holes?" In: *ApJ* 324, pp. 701–713. DOI: 10.1086/165930.

Dubinski, J., R. Narayan, and T. G. Phillips (1995). "Turbulence in Molecular Clouds". In: *ApJ* 448, p. 226. DOI: 10.1086/175954. eprint: astro-ph/9501032.

Eckart, A. et al. (1993). "Near-infrared 0.15 arcsec resolution imaging of the Galactic center". In: *ApJ* 407, pp. L77–L80. DOI: 10.1086/186810.

Eckart, A. et al. (1995). "High angular resolution spectroscopic and polarimetric imaging of the galactic center in the near-infrared". In: *ApJ* 445, pp. L23–L26. DOI: 10.1086/187880.

Eisenhauer, F. et al. (2005). "SINFONI in the Galactic Center: Young Stars and Infrared Flares in the Central Light-Month". In: *ApJ* 628, pp. 246–259. DOI: 10.1086/430667. eprint: astro-ph/0502129.

Elson, R., P. Hut, and S. Inagaki (1987). "Dynamical evolution of globular clusters". In: *ARA&A* 25, pp. 565–601. DOI: 10.1146/annurev.aa.25.090187.003025.

Emsellem, E. and G. van de Ven (2008). "Formation of Central Massive Objects via Tidal Compression". In: *ApJ* 674, 653-659, pp. 653–659. DOI: 10.1086/524720. arXiv: 0710.3161.

Erwin, P. and D. A. Gadotti (2012). "Do Nuclear Star Clusters and Supermassive Black Holes Follow the Same Host-Galaxy Correlations?" In: *Advances in Astronomy* 2012, 946368, p. 946368. DOI: 10.1155/2012/946368. arXiv: 1112.2740 [astro-ph.CO].

Espada, D. et al. (2017). "Disentangling the Circumnuclear Environs of Centaurus A: III. An Inner Molecular Ring, Nuclear Shocks and the CO to warm H2 interface". In: *ArXiv e-prints*. arXiv: 1706.05762.

Etxaluze, M. et al. (2011). "The Galactic Center in the Far-infrared". In: *AJ* 142, 134, p. 134. DOI: 10.1088/0004-6256/142/4/134. arXiv: 1108.0313.

Falcke, Heino et al. (1998). "The Simultaneous Spectrum of Sagittarius A* from 20 Centimeters to 1 Millimeter and the Nature of the Millimeter Excess". In: *The Astrophysical Journal* 499.2, p. 731. URL: http://stacks.iop.org/0004-637X/499/i=2/a=731.

Federrath, C. et al. (2010). "Modeling Collapse and Accretion in Turbulent Gas Clouds: Implementation and Comparison of Sink Particles in AMR and SPH". In: *ApJ* 713, pp. 269–290. DOI: 10.1088/0004-637X/713/1/269. arXiv: 1001.4456 [astro-ph.SR].

Feldmeier-Krause, A. et al. (2015). "KMOS view of the Galactic centre. I. Young stars are centrally concentrated". In: *A&A* 584, A2, A2. DOI: 10.1051/0004-6361/201526336. arXiv: 1509.04707.

Feldmeier-Krause, A. et al. (2017). "KMOS view of the Galactic Centre - II. Metallicity distribution of late-type stars". In: *MNRAS* 464, pp. 194–209. DOI: 10.1093/mnras/stw2339. arXiv: 1610.01623.

Feldmeier, A. et al. (2014). "Large scale kinematics and dynamical modelling of the Milky Way nuclear star cluster". In: *A&A* 570, A2, A2. DOI: 10.1051/0004-6361/201423777. arXiv: 1406.2849.

Ferrarese, L., H. C. Ford, and W. Jaffe (1996). "Evidence for a Massive Black Hole in the Active Galaxy NGC 4261 from Hubble Space Telescope Images and Spectra". In: *ApJ* 470, p. 444. DOI: 10.1086/177876.

Ferrarese, L. and H. Ford (2005). "Supermassive Black Holes in Galactic Nuclei: Past, Present and Future Research". In: *Space Sci. Rev.* 116, pp. 523–624. DOI: 10.1007/s11214-005-3947-6. eprint: astro-ph/0411247.

Ferrarese, L. et al. (2006). "A Fundamental Relation between Compact Stellar Nuclei, Supermassive Black Holes, and Their Host Galaxies". In: *ApJ* 644, pp. L21–L24. DOI: 10.1086/505388. eprint: astro-ph/0603840.

Fisher, D. B. and N. Drory (2016). "An Observational Guide to Identifying Pseudobulges and Classical Bulges in Disc Galaxies". In: *Galactic Bulges* 418, p. 41. DOI: 10.1007/978-3-319-19378-6_3. arXiv: 1512.02230.

Fritz, T. K. et al. (2016). "The Nuclear Cluster of the Milky Way: Total Mass and Luminosity". In: *ApJ* 821, 44, p. 44. DOI: 10.3847/0004-637X/821/1/44.

Fryer, C. L. (1999). "Mass Limits For Black Hole Formation". In: *ApJ* 522, pp. 413–418. DOI: 10.1086/307647. eprint: astro-ph/9902315.

Fryer, C. L. and V. Kalogera (2001). "Theoretical Black Hole Mass Distributions". In: *ApJ* 554, pp. 548–560. DOI: 10.1086/321359. eprint: astro-ph/9911312.

Fryer, C. L. et al. (2012). "Compact Remnant Mass Function: Dependence on the Explosion Mechanism and Metallicity". In: *ApJ* 749, 91, p. 91. DOI: 10.1088/0004-637X/749/1/91. arXiv: 1110.1726 [astro-ph.SR].

Fujii, M. S. and S. Portegies Zwart (2014). "The moment of core collapse in star clusters with a mass function". In: *MNRAS* 439, pp. 1003–1014. DOI: 10.1093/mnras/stu015. arXiv: 1304.1550.

Fujii, M. et al. (2007). "BRIDGE: A Direct-Tree Hybrid N-Body Algorithm for Fully Self-Consistent Simulations of Star Clusters and Their Parent Galaxies". In: *PASJ* 59, pp. 1095–1106. DOI: 10.1093/pasj/59.6.1095. arXiv: 0706.2059.

Gaburov, E., S. Harfst, and S. Portegies Zwart (2009). "SAPPORO: A way to turn your graphics cards into a GRAPE-6". In: *NewA*

14, pp. 630–637. DOI: 10.1016/j.newast.2009.03.002. arXiv: 0902.4463 [astro-ph.IM].

Gallego-Cano, E. et al. (2017). "The distribution of old stars around the Milky Way's central black hole I: Star counts". In: *ArXiv e-prints*. arXiv: 1701.03816.

Gammie, C. F. (2001). "Nonlinear Outcome of Gravitational Instability in Cooling, Gaseous Disks". In: *ApJ* 553, pp. 174–183. DOI: 10.1086/320631. eprint: astro-ph/0101501.

García-Burillo, S. et al. (2016). "ALMA Resolves the Torus of NGC 1068: Continuum and Molecular Line Emission". In: *ApJ* 823, L12, p. L12. DOI: 10.3847/2041-8205/823/1/L12. arXiv: 1604.00205.

Gebhardt, K. et al. (2003). "Axisymmetric Dynamical Models of the Central Regions of Galaxies". In: *ApJ* 583, pp. 92–115. DOI: 10.1086/345081. eprint: astro-ph/0209483.

Genzel, R. et al. (1996). "The Dark Mass Concentration in the Central Parsec of the Milky Way". In: *ApJ* 472, p. 153. DOI: 10.1086/178051.

Genzel, R. et al. (2003a). "The Stellar Cusp around the Supermassive Black Hole in the Galactic Center". In: *ApJ* 594, pp. 812–832. DOI: 10.1086/377127. eprint: astro-ph/0305423.

Genzel, R. et al. (2003b). "The Stellar Cusp around the Supermassive Black Hole in the Galactic Center". In: *ApJ* 594, pp. 812–832. DOI: 10.1086/377127. eprint: astro-ph/0305423.

Genzel, Reinhard, Frank Eisenhauer, and Stefan Gillessen (2010). "The Galactic Center massive black hole and nuclear star cluster". In: *Rev. Mod. Phys.* 82 (4), pp. 3121–3195. DOI: 10.1103/RevModPhys.82.3121. URL: https://link.aps.org/doi/10.1103/RevModPhys.82.3121.

Georgiev, I. Y. and T. Böker (2014). "Nuclear star clusters in 228 spiral galaxies in the HST/WFPC2 archive: catalogue and comparison to other stellar systems". In: *MNRAS* 441, pp. 3570–3590. DOI: 10.1093/mnras/stu797. arXiv: 1404.5956.

Georgiev, I. Y. et al. (2009). "Globular cluster systems in nearby dwarf galaxies - II. Nuclear star clusters and their relation to massive Galactic globular clusters". In: *MNRAS* 396, pp. 1075–1085. DOI: 10.1111/j.1365-2966.2009.14776.x. arXiv: 0903.2857.

Georgiev, I. Y. et al. (2016). "Masses and scaling relations for nuclear star clusters, and their co-existence with central black holes". In: *MNRAS* 457, pp. 2122–2138. DOI: 10.1093/mnras/stw093. arXiv: 1601.02613.

Ghez, A. M. et al. (1998). "High Proper-Motion Stars in the Vicinity of Sagittarius A*: Evidence for a Supermassive Black Hole at the Center of Our Galaxy". In: *ApJ* 509, pp. 678–686. DOI: 10.1086/306528. eprint: astro-ph/9807210.

Ghez, A. M. et al. (2000). "The accelerations of stars orbiting the Milky Way's central black hole". In: *Nature* 407, pp. 349–351. DOI: 10.1038/35030032. eprint: astro-ph/0009339.

Ghez, A. M. et al. (2003). "The First Measurement of Spectral Lines in a Short-Period Star Bound to the Galaxy's Central Black Hole: A Paradox of Youth". In: *ApJ* 586, pp. L127–L131. DOI: 10.1086/374804. eprint: astro-ph/0302299.

Ghez, A. M. et al. (2005). "The First Laser Guide Star Adaptive Optics Observations of the Galactic Center: Sgr A*'s Infrared Color and the Extended Red Emission in its Vicinity". In: *ApJ* 635, pp. 1087–1094. DOI: 10.1086/497576. eprint: astro-ph/0508664.

Gieles, M. (2013). "Mass Loss of Stars in Star Clusters: an Energy Source for Dynamical Evolution". In: *370 Years of Astronomy in Utrecht*. Ed. by G. Pugliese, A. de Koter, and M. Wijburg. Vol. 470. Astronomical Society of the Pacific Conference Series, p. 339. arXiv: 1209.2071 [astro-ph.SR].

Gillessen, S. et al. (2009a). "Monitoring Stellar Orbits Around the Massive Black Hole in the Galactic Center". In: *ApJ* 692, pp. 1075–1109. DOI: 10.1088/0004-637X/692/2/1075. arXiv: 0810.4674.

Gillessen, S. et al. (2009b). "The Orbit of the Star S2 Around SGR A* from Very Large Telescope and Keck Data". In: *ApJ* 707, pp. L114–L117. DOI: 10.1088/0004-637X/707/2/L114. arXiv: 0910.3069.

Gillessen, S. et al. (2012). "A gas cloud on its way towards the supermassive black hole at the Galactic Centre". In: *Nature* 481, pp. 51–54. DOI: 10.1038/nature10652. arXiv: 1112.3264 [astro-ph.GA].

Gillessen, S. et al. (2013a). "New Observations of the Gas Cloud G2 in the Galactic Center". In: *ApJ* 763, 78, p. 78. DOI: 10.1088/0004-637X/763/2/78. arXiv: 1209.2272.

Gillessen, S. et al. (2013b). "Pericenter Passage of the Gas Cloud G2 in the Galactic Center". In: *ApJ* 774, 44, p. 44. DOI: 10.1088/0004-637X/774/1/44. arXiv: 1306.1374.

Gillessen, S. et al. (2017). "An Update on Monitoring Stellar Orbits in the Galactic Center". In: *ApJ* 837, 30, p. 30. DOI: 10.3847/1538-4357/aa5c41. arXiv: 1611.09144.

Ginsburg, I., A. Loeb, and G. A. Wegner (2012). "Hypervelocity planets and transits around hypervelocity stars". In: *MNRAS* 423, pp. 948–954. DOI: 10.1111/j.1365-2966.2012.20930.x. arXiv: 1201.1446.

Gnedin, O. Y., J. P. Ostriker, and S. Tremaine (2014). "Co-evolution of Galactic Nuclei and Globular Cluster Systems". In: *ApJ* 785, 71, p. 71. DOI: 10.1088/0004-637X/785/1/71. arXiv: 1308.0021.

Goicoechea, J. R. et al. (2013). "Herschel* Far-infrared Spectroscopy of the Galactic Center. Hot Molecular Gas: Shocks versus Radiation near Sgr A". In: *ApJ* 769, L13, p. L13. DOI: 10.1088/2041-8205/769/1/L13. arXiv: 1305.1119.

González Delgado, D. et al. (2003). ""Thermal" SiO radio line emission towards M-type AGB stars: A probe of circumstellar dust formation and dynamics". In: *A&A* 411, pp. 123–147. DOI: 10.1051/0004-6361:20031068. eprint: astro-ph/0302179.

Goodman, J. (2003). "Self-gravity and quasi-stellar object discs". In: *MNRAS* 339, pp. 937–948. DOI: 10.1046/j.1365-8711.2003.06241.x. eprint: astro-ph/0201001.

Goto, M. et al. (2013). "H3+ Spectroscopy and the Ionization Rate of Molecular Hydrogen in the Central Few Parsecs of the Galaxy". In: *Journal of Physical Chemistry A* 117, pp. 9919–9930. DOI: 10.1021/jp400017s. arXiv: 1305.3915.

Graham, A. W. (2008). "Populating the Galaxy Velocity Dispersion - Supermassive Black Hole Mass Diagram: A Catalogue of (M_{bh}, σ) Values". In: *PASA* 25, pp. 167–175. DOI: 10.1071/AS08013. arXiv: 0807.2549.

Graham, A. W. (2012). "Extending the M_{bh}-σ diagram with dense nuclear star clusters". In: *MNRAS* 422, pp. 1586–1591. DOI: 10.1111/j.1365-2966.2012.20734.x. arXiv: 1202.4056.

Graham, A. W. (2016). "Galaxy Bulges and Their Massive Black Holes: A Review". In: *Galactic Bulges* 418, p. 263. DOI: 10.1007/978-3-319-19378-6_11. arXiv: 1501.02937.

Graham, A. W. and N. Scott (2013). "The M_{BH}-$L_{spheroid}$ Relation at High and Low Masses, the Quadratic Growth of Black Holes, and Intermediate-mass Black Hole Candidates". In: *ApJ* 764, 151, p. 151. DOI: 10.1088/0004-637X/764/2/151. arXiv: 1211.3199.

Graham, A. W. and N. Scott (2015). "The (Black Hole)-bulge Mass Scaling Relation at Low Masses". In: *ApJ* 798, 54, p. 54. DOI: 10.1088/0004-637X/798/1/54. arXiv: 1412.3091.

Graham, A. W. and L. R. Spitler (2009). "Quantifying the coexistence of massive black holes and dense nuclear star clusters". In: *MNRAS* 397, pp. 2148–2162. DOI: 10.1111/j.1365-2966.2009.15118.x. arXiv: 0907.5250.

Greenhill, L. J., J. M. Moran, and J. R. Herrnstein (1997). "The Distribution of H_2O Maser Emission in the Nucleus of NGC 4945". In: *ApJ* 481, pp. L23–L26. DOI: 10.1086/310643. eprint: astro-ph/9702220.

Grimm, S. L. and J. G. Stadel (2014). "The GENGA Code: Gravitational Encounters in N-body Simulations with GPU Acceleration". In: *ApJ* 796, 23, p. 23. DOI: 10.1088/0004-637X/796/1/23. arXiv: 1404.2324 [astro-ph.EP].

Gualandris, A., M. Mapelli, and H. B. Perets (2012). "Eccentric disc instability in stellar discs formed from inspiralling gas clouds in the Galactic Centre". In: *MNRAS* 427, pp. 1793–1799. DOI: 10.1111/j.1365-2966.2012.22133.x. arXiv: 1209.3021.

Guillard, N., E. Emsellem, and F. Renaud (2016). "New insights on the formation of nuclear star clusters". In: *MNRAS* 461, pp. 3620–3629. DOI: 10.1093/mnras/stw1570. arXiv: 1606.09537.

Guillochon, J. et al. (2014). "Possible Origin of the G2 Cloud from the Tidal Disruption of a Known Giant Star by Sgr A*". In: *ApJ* 786, L12, p. L12. DOI: 10.1088/2041-8205/786/2/L12. arXiv: 1401.2990 [astro-ph.HE].

Gullieuszik, M. et al. (2014). "Probing the nuclear star cluster of galaxies with extremely large telescopes". In: *A&A* 568, A89, A89. DOI: 10.1051/0004-6361/201424279. arXiv: 1406.7818.

Gürkan, M. A., M. Freitag, and F. A. Rasio (2004). "Formation of Massive Black Holes in Dense Star Clusters. I. Mass Segregation and Core Collapse". In: *ApJ* 604, pp. 632–652. DOI: 10.1086/381968. eprint: astro-ph/0308449.

Haas, J. and L. Šubr (2016). "Rich Kozai-Lidov Dynamics in an Initially Thin and Eccentric Stellar Disk around a Supermassive Black Hole". In: *ApJ* 822, 25, p. 25. DOI: 10.3847/0004-637X/822/1/25. arXiv: 1602.05582.

Haas, J., L. Šubr, and P. Kroupa (2011). "The coupling of a young stellar disc with the molecular torus in the Galactic Centre". In: *MNRAS* 412, pp. 1905–1912. DOI: 10.1111/j.1365-2966.2010.18025.x. arXiv: 1011.3815.

Haas, J., L. Šubr, and D. Vokrouhlický (2011). "Secular theory of the orbital evolution of the young stellar disc in the Galactic Centre". In: *MNRAS* 416, pp. 1023–1032. DOI: 10.1111/j.1365-2966.2011.19100.x. arXiv: 1105.4608.

Hamann, W.-R. and L. Koesterke (1998). "Spectrum formation in clumped stellar winds: consequences for the analyses of Wolf-Rayet spectra". In: *A&A* 335, pp. 1003–1008.

Hamilton, D. P. and J. A. Burns (1992). "Orbital stability zones about asteroids. II - The destabilizing effects of eccentric orbits and of solar radiation". In: *Icarus* 96, pp. 43–64. DOI: 10.1016/0019-1035(92)90005-R.

Hamilton, Douglas P. and Joseph A. Burns (1991). "Orbital stability zones about asteroids". In: *Icarus* 92.1, pp. 118–131. DOI: 10.1016/0019-1035(91)90039-v. URL: http://dx.doi.org/10.1016/0019-1035(91)90039-V.

Harada, N. et al. (2015). "Chemical features in the circumnuclear disk of the Galactic center". In: *Astronomy & Astrophysics* 584, A102. DOI: 10.1051/0004-6361/201526994. URL: https://doi.org/10.1051/0004-6361/201526994.

Harfst, S. et al. (2007). "Performance analysis of direct N-body algorithms on special-purpose supercomputers". In: *NewA* 12, pp. 357–377. DOI: 10.1016/j.newast.2006.11.003. eprint: astro-ph/0608125.

Hartmann, M. et al. (2011). "Constraining the role of star cluster mergers in nuclear cluster formation: simulations confront integral-field data". In: *MNRAS* 418, pp. 2697–2714. DOI: 10.1111/j.1365-2966.2011.19659.x. arXiv: 1103.5464.

Hayfield, T. et al. (2011). "The properties of pre-stellar discs in isolated and multiple pre-stellar systems". In: *MNRAS* 417, pp. 1839–1852. DOI: 10.1111/j.1365-2966.2011.19371.x. arXiv: 1003.2594 [astro-ph.EP].

Heggie, D. C. (1975). "Binary evolution in stellar dynamics". In: *MNRAS* 173, pp. 729–787. DOI: 10.1093/mnras/173.3.729.

Heggie, D. C., S. Inagaki, and S. L. W. McMillan (1994). "Gravothermal Expansion in an N-Body System". In: *MNRAS* 271, p. 706. DOI: 10.1093/mnras/271.3.706. eprint: astro-ph/9308046.

Heggie, D. C., M. Trenti, and P. Hut (2006). "Star clusters with primordial binaries - I. Dynamical evolution of isolated models". In: *MNRAS*. eprint: astro-ph/0602408.

Hernquist, L. (1990). "An analytical model for spherical galaxies and bulges". In: *ApJ* 356, pp. 359–364. DOI: 10.1086/168845.

Hills, J. G. (1980). "The effect of mass loss on the dynamical evolution of a stellar system - Analytic approximations". In: *ApJ* 235, pp. 986–991. DOI: 10.1086/157703.

Ho, L. C. et al. (2002). "An Efficient Strategy to Select Targets for Gas-dynamical Measurements of Black Hole Masses Using the Hubble Space Telescope". In: *PASP* 114, pp. 137–143. DOI: 10.1086/338546. eprint: astro-ph/0110671.

Hobbs, A. and S. Nayakshin (2009). "Simulations of the formation of stellar discs in the Galactic Centre via cloud-cloud collisions". In: *MNRAS* 394, pp. 191–206. DOI: 10.1111/j.1365-2966.2008.14359.x. arXiv: 0809.3752.

Humphreys, R. M. and K. Davidson (1994). "The luminous blue variables: Astrophysical geysers". In: *PASP* 106, pp. 1025–1051. DOI: 10.1086/133478.

Hurley, J. R., O. R. Pols, and C. A. Tout (2000). "Comprehensive analytic formulae for stellar evolution as a function of mass and metallicity". In: *MNRAS* 315, pp. 543–569. DOI: 10.1046/j.1365-8711.2000.03426.x. eprint: astro-ph/0001295.

Hurley, J. R., C. A. Tout, and O. R. Pols (2002). "Evolution of binary stars and the effect of tides on binary populations". In: *MNRAS* 329, pp. 897–928. DOI: 10.1046/j.1365-8711.2002.05038.x. eprint: astro-ph/0201220.

Jackson, J. M. et al. (1993). "Neutral gas in the central 2 parsecs of the Galaxy". In: *ApJ* 402, pp. 173–184. DOI: 10.1086/172120.

Jiang, N. et al. (2013). "UM 625 Revisited: Multiwavelength Study of a Seyfert 1 Galaxy with a Low-mass Black Hole". In: *ApJ* 770, 3, p. 3. DOI: 10.1088/0004-637X/770/1/3. arXiv: 1304.5807.

Jiang, Y.-F. et al. (2011). "The Host Galaxies of Low-mass Black Holes". In: *ApJ* 742, 68, p. 68. DOI: 10.1088/0004-637X/742/2/68. arXiv: 1107.4105 [astro-ph.CO].

Kaufmann, T., C. Wheeler, and J. S. Bullock (2007). "On the morphologies, gas fractions, and star formation rates of small galaxies". In: *MNRAS* 382, pp. 1187–1195. DOI: 10.1111/j.1365-2966.2007.12436.x. arXiv: 0706.0210.

King, I. R. (1966). "The structure of star clusters. III. Some simple dynamical models". In: *AJ* 71, p. 64. DOI: 10.1086/109857.

King, I. (1962). "The structure of star clusters. I. an empirical density law". In: *AJ* 67, p. 471. DOI: 10.1086/108756.

Kinoshita, H., H. Yoshida, and H. Nakai (1991). "Symplectic integrators and their application to dynamical astronomy". In: *Celestial Mechanics and Dynamical Astronomy* 50, pp. 59–71.

Kolykhalov, P. I. and R. A. Syunyaev (1980). "The Outer Parts of the Accretion Disks around Supermassive Black Holes in Galaxy Nuclei and Quasars". In: *Soviet Astronomy Letters* 6, pp. 357–361.

Kormendy, J. (1985). "Families of ellipsoidal stellar systems and the formation of dwarf elliptical galaxies". In: *ApJ* 295, pp. 73–79. DOI: 10.1086/163350.

Kormendy, J. (1988). "Evidence for a supermassive black hole in the nucleus of M31". In: *ApJ* 325, pp. 128–141. DOI: 10.1086/165988.

Kormendy, J. (2016). "Elliptical Galaxies and Bulges of Disc Galaxies: Summary of Progress and Outstanding Issues". In: *Galactic Bulges* 418, p. 431. DOI: 10.1007/978-3-319-19378-6_16. arXiv: 1504.03330.

Kormendy, J., R. Bender, and M. E. Cornell (2011). "Supermassive black holes do not correlate with galaxy disks or pseudobulges". In: *Nature* 469, pp. 374–376. DOI: 10.1038/nature09694. arXiv: 1101.3781.

Kormendy, J. and L. C. Ho (2013). "Coevolution (Or Not) of Supermassive Black Holes and Host Galaxies". In: *ARA&A* 51, pp. 511–653. DOI: 10.1146/annurev-astro-082708-101811. arXiv: 1304.7762.

Kormendy, J. and D. Richstone (1995). "Inward Bound—The Search For Supermassive Black Holes In Galactic Nuclei". In: *ARA&A* 33, p. 581. DOI: 10.1146/annurev.aa.33.090195.003053.

Kormendy, J. et al. (2009). "Structure and Formation of Elliptical and Spheroidal Galaxies". In: *ApJS* 182, pp. 216–309. DOI: 10.1088/0067-0049/182/1/216. arXiv: 0810.1681.

Kornei, K. A. and N. McCrady (2009). "A Young Super Star Cluster in the Nuclear Region of NGC 253". In: *ApJ* 697, pp. 1180–1186. DOI: 10.1088/0004-637X/697/2/1180. arXiv: 0902.4027 [astro-ph.SR].

Kozai, Y. (1962). "Secular perturbations of asteroids with high inclination and eccentricity". In: *AJ* 67, p. 591. DOI: 10.1086/108790.

Krabbe, A. et al. (1991). "A cluster of He I emission-line stars in the Galactic center". In: *ApJ* 382, pp. L19–L22. DOI: 10.1086/186204.

Krabbe, A. et al. (1995). "The Nuclear Cluster of the Milky Way: Star Formation and Velocity Dispersion in the Central 0.5 Parsec". In: *ApJ* 447, p. L95. DOI: 10.1086/309579.

Kroupa, P. (2001). "On the variation of the initial mass function". In: *MNRAS* 322, pp. 231–246. DOI: 10.1046/j.1365-8711.2001.04022.x. eprint: astro-ph/0009005.

Kudritzki, R. P. (2002). "Line-driven Winds, Ionizing Fluxes, and Ultraviolet Spectra of Hot Stars at Extremely Low Metallicity. I. Very Massive O Stars". In: *ApJ* 577, pp. 389–408. DOI: 10.1086/342178. eprint: astro-ph/0205210.

Kuo, C. Y. et al. (2011). "The Megamaser Cosmology Project. III. Accurate Masses of Seven Supermassive Black Holes in Active Galaxies with Circumnuclear Megamaser Disks". In: *ApJ* 727, 20, p. 20. DOI: 10.1088/0004-637X/727/1/20. arXiv: 1008.2146.

Kustaanheimo, P. and E. Stiefel (1965). In: *J. Reine Angew. Math.* 218, p. 204. DOI: 10.1515/crll.1965.218.204.

Lamers, H. J. G. L. M., H. Baumgardt, and M. Gieles (2010). "Mass-loss rates and the mass evolution of star clusters". In: *MNRAS* 409, pp. 305–328. DOI: 10.1111/j.1365-2966.2010.17309.x. arXiv: 1007.1078.

Larson, R. B. (1981). "Turbulence and star formation in molecular clouds". In: *MNRAS* 194, pp. 809–826. DOI: 10.1093/mnras/194.4.809.

Lauer, T. R. et al. (1995). "The Centers of Early-Type Galaxies with HST.I.An Observational Survey". In: *AJ* 110, p. 2622. DOI: 10.1086/117719.

Launhardt, R., R. Zylka, and P. G. Mezger (2002). "The nuclear bulge of the Galaxy. III. Large-scale physical characteristics of stars and interstellar matter". In: *A&A* 384, pp. 112–139. DOI: 10.1051/0004-6361:20020017. eprint: astro-ph/0201294.

Leigh, N., T. Böker, and C. Knigge (2012). "Nuclear star clusters and the stellar spheroids of their host galaxies". In: *MNRAS* 424, pp. 2130–2138. DOI: 10.1111/j.1365-2966.2012.21365.x. arXiv: 1205.5033.

Leitherer, C., C. Robert, and L. Drissen (1992). "Deposition of mass, momentum, and energy by massive stars into the interstellar medium". In: *ApJ* 401, pp. 596–617. DOI: 10.1086/172089.

Levi-Civita, T.E. (1920). In: *Acta Math.* 42, p. 99. DOI: 10.1515/crll.1965.218.204.

Levin, Y. and A. M. Beloborodov (2003). "Stellar Disk in the Galactic Center: A Remnant of a Dense Accretion Disk?" In: *ApJ* 590, pp. L33–L36. DOI: 10.1086/376675. eprint: astro-ph/0303436.

Li, Y., Z. Haiman, and M.-M. Mac Low (2007). "Correlations between Central Massive Objects and Their Host Galaxies: From Bulgeless

Spirals to Ellipticals". In: *ApJ* 663, pp. 61–70. DOI: 10.1086/518398. eprint: astro-ph/0607444.

Lidov, M. L. (1962). "The evolution of orbits of artificial satellites of planets under the action of gravitational perturbations of external bodies". In: *Planet. Space Sci.* 9, pp. 719–759. DOI: 10.1016/0032-0633(62)90129-0.

Lindqvist, M. et al. (1992). "OH/IR stars close to the Galactic Centre. I - Observational data". In: *A&AS* 92, pp. 43–62.

Liu, Hauyu Baobab et al. (2012). "MILKY WAY SUPERMASSIVE BLACK HOLE: DYNAMICAL FEEDING FROM THE CIRCUMNUCLEAR ENVIRONMENT". In: *The Astrophysical Journal* 756.2, p. 195. DOI: 10.1088/0004-637x/756/2/195. URL: https://doi.org/10.1088/0004-637x/756/2/195.

Liu, Hauyu Baobab et al. (2013). "INTERSTELLAR MEDIUM PROCESSING IN THE INNER 20 pc IN GALACTIC CENTER". In: *The Astrophysical Journal* 770.1, p. 44. DOI: 10.1088/0004-637x/770/1/44. URL: https://doi.org/10.1088/0004-637x/770/1/44.

Lo, K. Y. (2005). "Mega-Masers and Galaxies". In: *ARA&A* 43, pp. 625–676. DOI: 10.1146/annurev.astro.41.011802.094927.

Löckmann, U. and H. Baumgardt (2009). "On the number of young stellar discs in the Galactic Centre". In: *MNRAS* 394, pp. 1841–1846. DOI: 10.1111/j.1365-2966.2009.14466.x. arXiv: 0901.1660.

Löckmann, U., H. Baumgardt, and P. Kroupa (2009). "Influence of a stellar cusp on the dynamics of young stellar discs and the origin of the S-stars in the Galactic Centre". In: *MNRAS* 398, pp. 429–437. DOI: 10.1111/j.1365-2966.2009.15157.x. arXiv: 0906.0574.

López-Gonzaga, N. et al. (2014). "Revealing the large nuclear dust structures in NGC 1068 with MIDI/VLTI". In: *A&A* 565, A71, A71. DOI: 10.1051/0004-6361/201323002. arXiv: 1401.3248.

Lotz, J. M., B. W. Miller, and H. C. Ferguson (2004). "The Colors of Dwarf Elliptical Galaxy Globular Cluster Systems, Nuclei, and Stellar Halos". In: *ApJ* 613, pp. 262–278. DOI: 10.1086/422871. eprint: astro-ph/0406002.

Lotz, J. M. et al. (2001). "Dynamical Friction in DE Globular Cluster Systems". In: *ApJ* 552, pp. 572–581. DOI: 10.1086/320545. eprint: astro-ph/0102079.

Loup, C. et al. (1993). "CO and HCN observations of circumstellar envelopes. A catalogue - Mass loss rates and distributions". In: *A&AS* 99, pp. 291–377.

Lu, J. R. et al. (2009). "A Disk of Young Stars at the Galactic Center as Determined by Individual Stellar Orbits". In: *ApJ* 690, pp. 1463–1487. DOI: 10.1088/0004-637X/690/2/1463. arXiv: 0808.3818.

Lu, J. R. et al. (2013). "Stellar Populations in the Central 0.5 pc of the Galaxy. II. The Initial Mass Function". In: *ApJ* 764, 155, p. 155. DOI: 10.1088/0004-637X/764/2/155. arXiv: 1301.0540 [astro-ph.SR].

Lucas, W. E. et al. (2013). "Misaligned streamers around a Galactic Centre black hole from a single cloud's infall". In: *MNRAS* 433, pp. 353–365. DOI: 10.1093/mnras/stt727. arXiv: 1305.0012.

Macchetto, F. et al. (1997). "The Supermassive Black Hole of M87 and the Kinematics of Its Associated Gaseous Disk". In: *ApJ* 489, pp. 579–600. DOI: 10.1086/304823. eprint: astro-ph/9706252.

Madigan, A.-M., Y. Levin, and C. Hopman (2009). "A New Secular Instability of Eccentric Stellar Disks around Supermassive Black Holes, with Application to the Galactic Center". In: *ApJ* 697, pp. L44–L48. DOI: 10.1088/0004-637X/697/1/L44. arXiv: 0812.3395.

Madigan, A.-M., M. McCourt, and R. M. O'Leary (2017). "Using gas clouds to probe the accretion flow around Sgr A*: G2's delayed pericentre passage". In: *MNRAS* 465, pp. 2310–2316. DOI: 10.1093/mnras/stw2815. arXiv: 1602.02760 [astro-ph.HE].

Maeder, A. (1992). "Stellar yields as a function of initial metallicity and mass limit for black hole formation". In: *A&A* 264, pp. 105–120.

Magorrian, J. et al. (1998). "The Demography of Massive Dark Objects in Galaxy Centers". In: *AJ* 115, pp. 2285–2305. DOI: 10.1086/300353. eprint: astro-ph/9708072.

Makino, J. (1996). "Postcollapse Evolution of Globular Clusters". In: *ApJ* 471, p. 796. DOI: 10.1086/178007. eprint: astro-ph/9608160.

Makino, J. and D. Sugimoto (1987). "Effect of suprathermal particles on gravothermal oscillation". In: *PASJ* 39, pp. 589–603.

Maoz, E. (1998). "Dynamical Constraints on Alternatives to Supermassive Black Holes in Galactic Nuclei". In: *ApJ* 494, pp. L181–L184. DOI: 10.1086/311194. eprint: astro-ph/9710309.

Mapelli, M. and A. Bressan (2013). "Impact of metallicity on the evolution of young star clusters". In: *MNRAS* 430, pp. 3120–3127. DOI: 10.1093/mnras/stt119. arXiv: 1301.4227.

Mapelli, M. and A. Gualandris (2016). "Star Formation and Dynamics in the Galactic Centre". In: Lecture Notes in Physics, Berlin Springer Verlag 905. Ed. by F. Haardt et al., p. 205. DOI: 10.1007/978-3-319-19416-5_6. arXiv: 1505.05473.

Mapelli, M., A. Gualandris, and T. Hayfield (2013). "Perturbations induced by a molecular cloud on the young stellar disc in the Galactic Centre". In: *MNRAS* 436, pp. 3809–3819. DOI: 10.1093/mnras/stt1858. arXiv: 1310.0024.

Mapelli, M. and E. Ripamonti (2015). "Signatures of Planets and Protoplanets in the Galactic Center: A Clue to Understanding the G2 Cloud?" In: *ApJ* 806, 197, p. 197. DOI: 10.1088/0004-637X/806/2/197. arXiv: 1504.04624.

Mapelli, M. and A. A. Trani (2016). "Modelling the formation of the circumnuclear ring in the Galactic centre". In: *A&A* 585, A161, A161. DOI: 10.1051/0004-6361/201527195. arXiv: 1510.05259.

Mapelli, M. et al. (2008). "In situ formation of the massive stars around SgrA*". In: *ArXiv e-prints*. arXiv: 0805.0185.

Mapelli, M. et al. (2012). "In Situ Formation of SgrA* Stars Via Disk Fragmentation: Parent Cloud Properties and Thermodynamics". In: *ApJ* 749, 168, p. 168. DOI: 10.1088/0004-637X/749/2/168. arXiv: 1202.0555.

Mapelli, M. et al. (2013). "Dynamics of stellar black holes in young star clusters with different metallicities - I. Implications for X-ray binaries". In: *MNRAS* 429, pp. 2298–2314. DOI: 10.1093/mnras/sts500. arXiv: 1211.6441 [astro-ph.HE].

Marrone, D. P. et al. (2008). "An X-Ray, Infrared, and Submillimeter Flare of Sagittarius A*". In: *The Astrophysical Journal* 682.1, p. 373. URL: http://stacks.iop.org/0004-637X/682/i=1/a=373.

Marrone, Daniel P. et al. (2006). "Interferometric Measurements of Variable 340 GHz Linear Polarization in Sagittarius A*". In: *The Astrophysical Journal* 640.1, p. 308. URL: http://stacks.iop.org/0004-637X/640/i=1/a=308.

Martins, F. et al. (2008a). "On the Nature of the Fast-Moving Star S2 in the Galactic Center". In: *ApJ* 672, L119, p. L119. DOI: 10.1086/526768. arXiv: 0711.3344.

Martins, F. et al. (2008b). "The most massive stars in the Arches cluster". In: *A&A* 478, pp. 219–233. DOI: 10.1051/0004-6361:20078469. arXiv: 0711.0657.

Mason, R. E. et al. (2015). "The Nuclear Near-Infrared Spectral Properties of Nearby Galaxies". In: *ApJS* 217, 13, p. 13. DOI: 10.1088/0067-0049/217/1/13. arXiv: 1503.01836.

Mathur, S. et al. (2012). "Supermassive Black Holes, Pseudobulges, and the Narrow-line Seyfert 1 Galaxies". In: *ApJ* 754, 146, p. 146. DOI: 10.1088/0004-637X/754/2/146. arXiv: 1102.0537.

McConnell, N. J. and C.-P. Ma (2013). "Revisiting the Scaling Relations of Black Hole Masses and Host Galaxy Properties". In: *ApJ* 764, 184, p. 184. DOI: 10.1088/0004-637X/764/2/184. arXiv: 1211.2816.

McConnell, N. J. et al. (2011). "Two ten-billion-solar-mass black holes at the centres of giant elliptical galaxies". In: *Nature* 480, pp. 215–218. DOI: 10.1038/nature10636. arXiv: 1112.1078 [astro-ph.CO].

McCourt, M. and A.-M. Madigan (2016). "Going with the flow: using gas clouds to probe the accretion flow feeding Sgr A*". In: *MNRAS* 455, pp. 2187–2199. DOI: 10.1093/mnras/stv2232. arXiv: 1503.04801 [astro-ph.HE].

McGinn, M. T. et al. (1989). "Stellar kinematics in the Galactic center". In: *ApJ* 338, pp. 824–840. DOI: 10.1086/167239.

McMillan, S. L. W. and K. A. Engle (1996). "Are Gravothermal Oscillations Gravothermal?" In: *Dynamical Evolution of Star Clusters: Confrontation of Theory and Observations*. Ed. by P. Hut and J. Makino. Vol. 174. IAU Symposium, p. 379.

Merritt, D. et al. (2011). "Stellar dynamics of extreme-mass-ratio inspirals". In: *Phys. Rev. D* 84.4, 044024, p. 044024. DOI: 10.1103/PhysRevD.84.044024. arXiv: 1102.3180 [astro-ph.CO].

Meyer, F. and E. Meyer-Hofmeister (2012). "A nova origin of the gas cloud at the Galactic center?" In: *A&A* 546, L2, p. L2. DOI: 10.1051/0004-6361/201220145. arXiv: 1208.6514 [astro-ph.SR].

Mezger, P. G. et al. (1999). "The nuclear bulge of the Galaxy. II. The K band luminosity function of the central 30 PC". In: *A&A* 348, pp. 457–465.

Mikkola, S. and S. J. Aarseth (1993). "An implementation of N-body chain regularization". In: *Celestial Mechanics and Dynamical Astronomy* 57, pp. 439–459. DOI: 10.1007/BF00695714.

Mikkola, S. and D. Merritt (2006). "Algorithmic regularization with velocity-dependent forces". In: *MNRAS* 372, pp. 219–223. DOI: 10.1111/j.1365-2966.2006.10854.x. eprint: astro-ph/0605054.

Mikkola, S. and K. Tanikawa (1999a). "Algorithmic regularization of the few-body problem". In: *MNRAS* 310, pp. 745–749. DOI: 10.1046/j.1365-8711.1999.02982.x.

Mikkola, S. and K. Tanikawa (1999b). "Explicit Symplectic Algorithms For Time-Transformed Hamiltonians". In: *Celestial Mechanics and Dynamical Astronomy* 74, pp. 287–295. DOI: 10.1023/A:1008368322547.

Mills, E. A. C., A. Togi, and M. Kaufman (2017). "Hot Molecular Gas in the Circumnuclear Disk". In: *ArXiv e-prints*. arXiv: 1701.04826.

Mills, E. A. C. et al. (2013). "THE EXCITATION OF HCN AND HCO^+ IN THE GALACTIC CENTER CIRCUMNUCLEAR DISK". In: *The Astrophysical Journal* 779.1, p. 47. DOI: 10.1088/0004-637x/779/1/47. URL: https://doi.org/10.1088/0004-637x/779/1/47.

Milosavljević, M. (2004). "On the Origin of Nuclear Star Clusters in Late-Type Spiral Galaxies". In: *ApJ* 605, pp. L13–L16. DOI: 10.1086/420696. eprint: astro-ph/0310574.

Miralda-Escudé, J. (2012). "A Star Disrupted by a Stellar Black Hole as the Origin of the Cloud Falling toward the Galactic Center". In: *ApJ* 756, 86, p. 86. DOI: 10.1088/0004-637X/756/1/86. arXiv: 1202.5496.

Miyazaki, Atsushi, Takahiro Tsutsumi, and Masato Tsuboi (2004). "Intraday Variation of Sagittarius A* at Short Millimeter Wavelengths". In: *The Astrophysical Journal Letters* 611.2, p. L97. URL: http://stacks.iop.org/1538-4357/611/i=2/a=L97.

Miyoshi, M. et al. (1995). "Evidence for a black hole from high rotation velocities in a sub-parsec region of NGC4258". In: *Nature* 373, pp. 127–129. DOI: 10.1038/373127a0.

Monaco, L. et al. (2009). "The young stellar population at the center of NGC 205". In: *A&A* 502, pp. L9–L12. DOI: 10.1051/0004-6361/200912412. arXiv: 0907.0029.

Monaghan, J. J. (1992). "Smoothed particle hydrodynamics". In: *ARA&A* 30, pp. 543–574. DOI: 10.1146/annurev.astro.30.1.543.

Monaghan, J. J. (1997). "SPH and Riemann Solvers". In: *Journal of Computational Physics* 136, pp. 298–307. DOI: 10.1006/jcph.1997.5732.

Montero-Castaño, M., R. M. Herrnstein, and P. T. P. Ho (2009). "Gas Infall Toward Sgr A* from the Clumpy Circumnuclear Disk". In: *ApJ* 695, pp. 1477–1494. DOI: 10.1088/0004-637X/695/2/1477. arXiv: 0903.0886 [astro-ph.GA].

Moran, J. M., L. J. Greenhill, and J. R. Herrnstein (1999). "Observational Evidence for Massive Black Holes in the Centers of Active Galaxies". In: *Journal of Astrophysics and Astronomy* 20, p. 165. DOI: 10.1007/BF02702350. eprint: astro-ph/0002085.

Morris, J. P. and J. J. Monaghan (1997). "A Switch to Reduce SPH Viscosity". In: *Journal of Computational Physics* 136, pp. 41–50. DOI: 10.1006/jcph.1997.5690.

Muijres, L. et al. (2012). "Mass-loss predictions for evolved very metal-poor massive stars". In: *A&A* 546, A42, A42. DOI: 10.1051/0004-6361/201118666. arXiv: 1209.5934 [astro-ph.SR].

Müller Sánchez, F. et al. (2009). "Molecular Gas Streamers Feeding and Obscuring the Active Nucleus of NGC 1068". In: *ApJ* 691, pp. 749–759. DOI: 10.1088/0004-637X/691/1/749. arXiv: 0809.4943.

Murray-Clay, R. A. and A. Loeb (2012). "Disruption of a proto-planetary disc by the black hole at the milky way centre". In: *Nature Communications* 3, 1049, p. 1049. DOI: 10.1038/ncomms2044. arXiv: 1112.4822.

Nanni, A. et al. (2013). "Evolution of thermally pulsing asymptotic giant branch stars - II. Dust production at varying metallicity". In: *MNRAS* 434, pp. 2390–2417. DOI: 10.1093/mnras/stt1175. arXiv: 1306.6183 [astro-ph.SR].

Nayakshin, S. and J. Cuadra (2005). "A self-gravitating accretion disk in Sgr A* a few million years ago: Is Sgr A* a failed quasar?" In: *A&A* 437, pp. 437–445. DOI: 10.1051/0004-6361:20042052. eprint: astro-ph/0409541.

Nayakshin, S., J. Cuadra, and V. Springel (2007). "Simulations of star formation in a gaseous disc around Sgr A* - a failed active galactic nucleus". In: *MNRAS* 379, pp. 21–33. DOI: 10.1111/j.1365-2966.2007.11938.x. eprint: astro-ph/0701141.

Nayakshin, S., M. I. Wilkinson, and A. King (2009). "Competitive feedback in galaxy formation". In: *MNRAS* 398, pp. L54–L57. DOI: 10.1111/j.1745-3933.2009.00709.x. arXiv: 0907.1002.

Neumayer, N. and C. J. Walcher (2012). "Are Nuclear Star Clusters the Precursors of Massive Black Holes?" In: *Advances in Astronomy* 2012, 709038, p. 709038. DOI: 10.1155/2012/709038. arXiv: 1201.4950.

Neumayer, N. et al. (2007). "The Central Parsecs of Centaurus A: High-excitation Gas, a Molecular Disk, and the Mass of the Black

Hole". In: *ApJ* 671, pp. 1329–1344. DOI: 10.1086/523039. arXiv: 0709.1877.

Nguyen, D. D. et al. (2014). "Extended Structure and Fate of the Nucleus in Henize 2-10". In: *ApJ* 794, 34, p. 34. DOI: 10.1088/0004-637X/794/1/34. arXiv: 1408.4446.

Nguyen, D. D. et al. (2017). "Improved Dynamical Constraints on the Mass of the Central Black Hole in NGC 404". In: *ApJ* 836, 237, p. 237. DOI: 10.3847/1538-4357/aa5cb4. arXiv: 1610.09385.

Oka, Tomoharu et al. (2011). "A NEW LOOK AT THE GALACTIC CIRCUMNUCLEAR DISK". In: *The Astrophysical Journal* 732.2, p. 120. DOI: 10.1088/0004-637x/732/2/120. URL: https://doi.org/10.1088/0004-637x/732/2/120.

Onishi, K. et al. (2015). "A Measurement of the Black Hole Mass in NGC 1097 Using ALMA". In: *ApJ* 806, 39, p. 39. DOI: 10.1088/0004-637X/806/1/39. arXiv: 1506.05917.

Onishi, K. et al. (2017). "WISDOM project - I. Black hole mass measurement using molecular gas kinematics in NGC 3665". In: *MNRAS* 468, pp. 4663–4674. DOI: 10.1093/mnras/stx631. arXiv: 1703.05247.

Oort, J. H. (1974). "The Galactic Centre (review: Summary and Concluding Remarks)". In: IAU Symposium 60. Ed. by F. J. Kerr and S. C. Simonson, p. 539.

Paudel, S., T. Lisker, and H. Kuntschner (2011). "Nuclei of early-type dwarf galaxies: insights from stellar populations". In: *MNRAS* 413, pp. 1764–1776. DOI: 10.1111/j.1365-2966.2011.18256.x. arXiv: 1012.4092.

Paumard, T. et al. (2006a). "The Two Young Star Disks in the Central Parsec of the Galaxy: Properties, Dynamics, and Formation". In: *ApJ* 643, pp. 1011–1035. DOI: 10.1086/503273. eprint: astro-ph/0601268.

Paumard, T. et al. (2006b). "The Two Young Star Disks in the Central Parsec of the Galaxy: Properties, Dynamics, and Formation". In: *ApJ* 643, pp. 1011–1035. DOI: 10.1086/503273. eprint: astro-ph/0601268.

Pelupessy, F. I. and S. Portegies Zwart (2012). "The evolution of embedded star clusters". In: *MNRAS* 420, pp. 1503–1517. DOI: 10.1111/j.1365-2966.2011.20137.x. arXiv: 1111.0992 [astro-ph.SR].

Pelupessy, F. I. et al. (2013). "The Astrophysical Multipurpose Software Environment". In: *A&A* 557, A84, A84. DOI: 10.1051/0004-6361/201321252. arXiv: 1307.3016 [astro-ph.IM].

Perets, H. B. and A. Mastrobuono-Battisti (2014). "Age and Mass Segregation of Multiple Stellar Populations in Galactic Nuclei and their Observational Signatures". In: *ApJ* 784, L44, p. L44. DOI: 10.1088/2041-8205/784/2/L44. arXiv: 1401.1824.

Perets, H. B. et al. (2009). "Dynamical Evolution of the Young Stars in the Galactic Center: N-body Simulations of the S-Stars". In: *ApJ*

702, pp. 884–889. DOI: 10.1088/0004-637X/702/2/884. arXiv: 0903.2912 [astro-ph.GA].

Pflamm-Altenburg, J. and P. Kroupa (2009). "Recurrent gas accretion by massive star clusters, multiple stellar populations and mass thresholds for spheroidal stellar systems". In: *MNRAS* 397, pp. 488–494. DOI: 10.1111/j.1365-2966.2009.14954.x. arXiv: 0904.4476.

Pfuhl, O. et al. (2011). "The Star Formation History of the Milky Way's Nuclear Star Cluster". In: *ApJ* 741, 108, p. 108. DOI: 10.1088/0004-637X/741/2/108. arXiv: 1110.1633.

Pfuhl, O. et al. (2014). "Massive Binaries in the Vicinity of Sgr A*". In: *ApJ* 782, 101, p. 101. DOI: 10.1088/0004-637X/782/2/101. arXiv: 1307.7996.

Pfuhl, O. et al. (2015). "The Galactic Center Cloud G2 and its Gas Streamer". In: *ApJ* 798, 111, p. 111. DOI: 10.1088/0004-637X/798/2/111. arXiv: 1407.4354.

Phifer, K. et al. (2013). "Keck Observations of the Galactic Center Source G2: Gas Cloud or Star?" In: *ApJ* 773, L13, p. L13. DOI: 10.1088/2041-8205/773/1/L13. arXiv: 1304.5280.

Philipp, S. et al. (1999). "The nuclear bulge. I. K band observations of the central 30 PC". In: *A&A* 348, pp. 768–782.

Plewa, P. M. et al. (2017). "The Post-pericenter Evolution of the Galactic Center Source G2". In: *ApJ* 840, 50, p. 50. DOI: 10.3847/1538-4357/aa6e00. arXiv: 1704.05351.

Poliachenko, V. L. and I. G. Shukhman (1977). "Evaluation of the maximum anisotropy of the stellar velocity distribution in galaxies". In: *Soviet Astronomy Letters* 3, pp. 134–136.

Pols, O. R. et al. (1998). "Stellar evolution models for Z = 0.0001 to 0.03". In: *MNRAS* 298, pp. 525–536. DOI: 10.1046/j.1365-8711.1998.01658.x.

Portegies Zwart, S. F. and S. L. W. McMillan (2002). "The Runaway Growth of Intermediate-Mass Black Holes in Dense Star Clusters". In: *ApJ* 576, pp. 899–907. DOI: 10.1086/341798. eprint: astro-ph/0201055.

Portegies Zwart, S. F. and S. L. W. McMillan (2007). "Simulating Young Star-Clusters with Primordial Binaries". In: *Massive Stars in Interactive Binaries*. Ed. by N. St.-Louis and A. F. J. Moffat. Vol. 367. Astronomical Society of the Pacific Conference Series, p. 597.

Portegies Zwart, S. F., S. L. W. McMillan, and M. Gieles (2010). "Young Massive Star Clusters". In: *ARA&A* 48, pp. 431–493. DOI: 10.1146/annurev-astro-081309-130834. arXiv: 1002.1961.

Portegies Zwart, S. F. and F. Verbunt (1996). "Population synthesis of high-mass binaries." In: *A&A* 309, pp. 179–196.

Portegies Zwart, S. F. et al. (2001). "Star cluster ecology - IV. Dissection of an open star cluster: photometry". In: *MNRAS* 321, pp. 199–

226. DOI: 10.1046/j.1365-8711.2001.03976.x. eprint: astro-ph/0005248.

Portegies Zwart, S. et al. (2009). "A multiphysics and multiscale software environment for modeling astrophysical systems". In: *NewA* 14, pp. 369–378. DOI: 10.1016/j.newast.2008.10.006. arXiv: 0807.1996.

Portegies Zwart, S. et al. (2013). "Multi-physics simulations using a hierarchical interchangeable software interface". In: *Computer Physics Communications* 183, pp. 456–468. DOI: 10.1016/j.cpc.2012.09.024. arXiv: 1204.5522 [astro-ph.IM].

Portinari, L., C. Chiosi, and A. Bressan (1998). "Galactic chemical enrichment with new metallicity dependent stellar yields". In: *A&A* 334, pp. 505–539. eprint: astro-ph/9711337.

Press, William H. et al. (2007). *Numerical Recipes 3rd Edition: The Art of Scientific Computing*. 3rd ed. New York, NY, USA: Cambridge University Press. ISBN: 0521880688, 9780521880688.

Prodan, S., F. Antonini, and H. B. Perets (2015). "Secular Evolution of Binaries near Massive Black Holes: Formation of Compact Binaries, Merger/Collision Products and G2-like Objects". In: *ApJ* 799, 118, p. 118. DOI: 10.1088/0004-637X/799/2/118. arXiv: 1405.6029.

Read, J. I., T. Hayfield, and O. Agertz (2010). "Resolving mixing in smoothed particle hydrodynamics". In: *MNRAS* 405, pp. 1513–1530. DOI: 10.1111/j.1365-2966.2010.16577.x. arXiv: 0906.0774.

Reines, A. E., J. E. Greene, and M. Geha (2013). "Dwarf Galaxies with Optical Signatures of Active Massive Black Holes". In: *ApJ* 775, 116, p. 116. DOI: 10.1088/0004-637X/775/2/116. arXiv: 1308.0328.

Requena-Torres, M. A. et al. (2012). "GREAT confirms transient nature of the circum-nuclear disk". In: *A&A* 542, L21, p. L21. DOI: 10.1051/0004-6361/201219068. arXiv: 1203.6687.

Rieke, G. H., M. J. Rieke, and A. E. Paul (1989). "Origin of the excitation of the galactic center". In: *ApJ* 336, pp. 752–761. DOI: 10.1086/167047.

Rossa, J. et al. (2006). "Hubble Space Telescope STIS Spectra of Nuclear Star Clusters in Spiral Galaxies: Dependence of Age and Mass on Hubble Type". In: *AJ* 132, pp. 1074–1099. DOI: 10.1086/505968. eprint: astro-ph/0604140.

Rusli, S. P. et al. (2013). "The Influence of Dark Matter Halos on Dynamical Estimates of Black Hole Mass: 10 New Measurements for High-σ Early-type Galaxies". In: *AJ* 146, 45, p. 45. DOI: 10.1088/0004-6256/146/3/45. arXiv: 1306.1124.

Sanders, R. H. (1998). "The circumnuclear material in the Galactic Centre - A clue to the accretion process". In: *MNRAS* 294, p. 35.

DOI: 10.1046/j.1365-8711.1998.01127.x. eprint: astro-ph/9708272.

Sanders, R. H. and T. Lowinger (1972). "The Distribution of Mass in the Galactic Nucleus". In: *AJ* 77, p. 292. DOI: 10.1086/111281.

Sandqvist, A. et al. (2017). "Odin observations of ammonia in the Sgr A +50 km s^{-1} cloud and circumnuclear disk". In: *A&A* 599, A135, A135. DOI: 10.1051/0004-6361/201629954. arXiv: 1701.02536.

Sarzi, M. et al. (2001). "Supermassive Black Holes in Bulges". In: *ApJ* 550, pp. 65–74. DOI: 10.1086/319724. eprint: astro-ph/0010240.

Sarzi, M. et al. (2005). "The Stellar Populations in the Central Parsecs of Galactic Bulges". In: *ApJ* 628, pp. 169–186. DOI: 10.1086/428637. eprint: astro-ph/0410220.

Savorgnan, G. A. D. et al. (2016). "Supermassive Black Holes and Their Host Spheroids. II. The Red and Blue Sequence in the M_{BH}-$M_{*,sph}$ Diagram". In: *ApJ* 817, 21, p. 21. DOI: 10.3847/0004-637X/817/1/21. arXiv: 1511.07437.

Schartmann, M. et al. (2012). "Simulations of the Origin and Fate of the Galactic Center Cloud G2". In: *ApJ* 755, 155, p. 155. DOI: 10.1088/0004-637X/755/2/155. arXiv: 1203.6356.

Schödel, R., D. Merritt, and A. Eckart (2009). "The nuclear star cluster of the Milky Way: proper motions and mass". In: *A&A* 502, pp. 91–111. DOI: 10.1051/0004-6361/200810922. arXiv: 0902.3892.

Schödel, R. et al. (2002). "A star in a 15.2-year orbit around the supermassive black hole at the centre of the Milky Way". In: *Nature* 419, pp. 694–696. DOI: 10.1038/nature01121. eprint: astro-ph/0210426.

Schödel, R. et al. (2003). "Stellar Dynamics in the Central Arcsecond of Our Galaxy". In: *ApJ* 596, pp. 1015–1034. DOI: 10.1086/378122. eprint: astro-ph/0306214.

Schödel, R. et al. (2007). "The structure of the nuclear stellar cluster of the Milky Way". In: *A&A* 469, pp. 125–146. DOI: 10.1051/0004-6361:20065089. eprint: astro-ph/0703178.

Schödel, R. et al. (2014). "Surface brightness profile of the Milky Way's nuclear star cluster". In: *A&A* 566, A47, A47. DOI: 10.1051/0004-6361/201423481. arXiv: 1403.6657.

Schödel, R. et al. (2017). "The distribution of stars around the Milky Way's central black hole II: Diffuse light from sub-giants and dwarfs". In: *ArXiv e-prints*. arXiv: 1701.03817.

Schulman, R. D., E. Glebbeek, and A. Sills (2012). "The effect of stellar metallicity on the sizes of star clusters". In: *MNRAS* 420, pp. 651–657. DOI: 10.1111/j.1365-2966.2011.20079.x. arXiv: 1110.5878 [astro-ph.GA].

Scott, N. and A. W. Graham (2013). "Updated Mass Scaling Relations for Nuclear Star Clusters and a Comparison to Supermas-

sive Black Holes". In: *ApJ* 763, 76, p. 76. DOI: 10.1088/0004-637X/763/2/76. arXiv: 1205.5338 [astro-ph.CO].

Scott, N., A. W. Graham, and J. Schombert (2013). "The Supermassive Black Hole Mass-Spheroid Stellar Mass Relation for Sérsic and Core-Sérsic Galaxies". In: *ApJ* 768, 76, p. 76. DOI: 10.1088/0004-637X/768/1/76. arXiv: 1303.5490.

Serabyn, E. and J. H. Lacy (1985). "Forbidden NE II observations of the galactic center - Evidence for a massive block hole". In: *ApJ* 293, pp. 445–458. DOI: 10.1086/163250.

Serabyn, E. et al. (1986). "CO 1 - 0 and CS 2 - 1 observations of the neutral disk around the galactic center". In: *A&A* 169, pp. 85–94.

Seth, A. C. et al. (2006). "Clues to Nuclear Star Cluster Formation from Edge-on Spirals". In: *AJ* 132, pp. 2539–2555. DOI: 10.1086/508994. eprint: astro-ph/0609302.

Seth, A. C. et al. (2008a). "The Rotating Nuclear Star Cluster in NGC 4244". In: *ApJ* 687, 997-1003, pp. 997–1003. DOI: 10.1086/591935. arXiv: 0807.3044.

Seth, A. C. et al. (2010). "The NGC 404 Nucleus: Star Cluster and Possible Intermediate-mass Black Hole". In: *ApJ* 714, pp. 713–731. DOI: 10.1088/0004-637X/714/1/713. arXiv: 1003.0680.

Seth, A. et al. (2008b). "The Coincidence of Nuclear Star Clusters and Active Galactic Nuclei". In: *ApJ* 678, 116-130, pp. 116–130. DOI: 10.1086/528955. arXiv: 0801.0439.

Shahzamanian, B. et al. (2016). "Polarized near-infrared light of the Dusty S-cluster Object (DSO/G2) at the Galactic center". In: *A&A* 593, A131, A131. DOI: 10.1051/0004-6361/201628994. arXiv: 1607.04568.

Shankar, F., M. Bernardi, and R. K. Sheth (2017). "Selection bias in dynamically measured supermassive black hole samples: dynamical masses and dependence on Sérsic index". In: *MNRAS* 466, pp. 4029–4039. DOI: 10.1093/mnras/stw3368. arXiv: 1701.01732.

Shankar, F. et al. (2016). "Selection bias in dynamically measured supermassive black hole samples: its consequences and the quest for the most fundamental relation". In: *MNRAS* 460, pp. 3119–3142. DOI: 10.1093/mnras/stw678. arXiv: 1603.01276.

Shcherbakov, R. V. (2014). "The Properties and Fate of the Galactic Center G2 Cloud". In: *ApJ* 783, 31, p. 31. DOI: 10.1088/0004-637X/783/1/31. arXiv: 1309.2282 [astro-ph.HE].

Shlosman, I. and M. C. Begelman (1987). "Self-gravitating accretion disks in active galactic nuclei". In: *Nature* 329, pp. 810–812. DOI: 10.1038/329810a0.

Shlosman, I., J. Frank, and M. C. Begelman (1989). "Bars within bars - A mechanism for fuelling active galactic nuclei". In: *Nature* 338, pp. 45–47. DOI: 10.1038/338045a0.

Siegel, M. H. et al. (2007). "The ACS Survey of Galactic Globular Clusters: M54 and Young Populations in the Sagittarius Dwarf

Spheroidal Galaxy". In: *ApJ* 667, pp. L57–L60. DOI: 10.1086/522003. arXiv: 0708.0027.

Sigurdsson, S. and M. J. Rees (1997). "Capture of stellar mass compact objects by massive black holes in galactic cusps". In: *MNRAS* 284, pp. 318–326. DOI: 10.1093/mnras/284.2.318. eprint: astro-ph/9608093.

Sippel, A. C. et al. (2012). "N-body models of globular clusters: metallicities, half-light radii and mass-to-light ratios". In: *MNRAS* 427, pp. 167–179. DOI: 10.1111/j.1365-2966.2012.21969.x. arXiv: 1208.4851.

Smith, I. L. and M. Wardle (2014). "An analysis of HCN observations of the Circumnuclear Disc at the Galactic Centre". In: *MNRAS* 437, pp. 3159–3171. DOI: 10.1093/mnras/stt2092. arXiv: 1310.8429.

Spitzer, L. (1987). "Dynamical evolution of globular clusters". In:

Stewart, G. R. and S. Ida (2000). "Velocity Evolution of Planetesimals: Unified Analytical Formulas and Comparisons with N-Body Simulations". In: *Icarus* 143, pp. 28–44. DOI: 10.1006/icar.1999.6242.

Stoer, J. and R. Bulirsch (1980). "Introduction to Numerical Analysis". In: ed. by Springer-Verlag.

Storey, J. W. V. and D. A. Allen (1983). "The galactic nucleus". In: *MNRAS* 204, pp. 1153–1161. DOI: 10.1093/mnras/204.4.1153.

Suetsugu, R. and K. Ohtsuki (2013). "Temporary capture of planetesimals by a giant planet and implication for the origin of irregular satellites". In: *MNRAS* 431, pp. 1709–1718. DOI: 10.1093/mnras/stt290.

Suetsugu, R., K. Ohtsuki, and T. Tanigawa (2011). "Temporary Capture of Planetesimals by a Planet from Their Heliocentric Orbits". In: *AJ* 142, 200, p. 200. DOI: 10.1088/0004-6256/142/6/200.

Takekawa, S., T. Oka, and K. Tanaka (2017). "Physical Contact between the +20 km s^{-1} Cloud and the Galactic Circumnuclear Disk". In: *ApJ* 834, 121, p. 121. DOI: 10.3847/1538-4357/834/2/121. arXiv: 1612.03591.

Toomre, A. (1964). "On the gravitational stability of a disk of stars". In: *ApJ* 139, pp. 1217–1238. DOI: 10.1086/147861.

Trani, A. A., M. Mapelli, and A. Bressan (2014). "The impact of metallicity-dependent mass-loss versus dynamical heating on the early evolution of star clusters". In: *MNRAS* 445, pp. 1967–1976. DOI: 10.1093/mnras/stu1898. arXiv: 1409.3006.

Trani, A. A. et al. (2016a). "Dynamics of Tidally Captured Planets in the Galactic Center". In: *ApJ* 831, 61, p. 61. DOI: 10.3847/0004-637X/831/1/61.

Trani, A. A. et al. (2016b). "The Influence of Dense Gas Rings on the Dynamics of a Stellar Disk in the Galactic Center". In: *ApJ* 818, 29, p. 29. DOI: 10.3847/0004-637X/818/1/29. arXiv: 1512.02682.

Trani, A. A. et al. (2017). "Circumnuclear rings and disks as indicators of supermassive black hole presence". In:

Treffers, R. R. et al. (1976). "The 1.4-2.7 micron spectrum of the point source at the galactic center". In: *ApJ* 209, pp. L115–L118. DOI: 10.1086/182280.

Tremaine, S. D., J. P. Ostriker, and L. Spitzer Jr. (1975). "The formation of the nuclei of galaxies. I - M31". In: *ApJ* 196, pp. 407–411. DOI: 10.1086/153422.

Tremaine, S. et al. (2002). "The Slope of the Black Hole Mass versus Velocity Dispersion Correlation". In: *ApJ* 574, pp. 740–753. DOI: 10.1086/341002. eprint: astro-ph/0203468.

Trippe, S. et al. (2008). "Kinematics of the old stellar population at the Galactic centre". In: *A&A* 492, pp. 419–439. DOI: 10.1051/0004-6361:200810191. arXiv: 0810.1040.

Tsatsi, A. et al. (2017). "On the rotation of nuclear star clusters formed by cluster inspirals". In: *MNRAS* 464, pp. 3720–3727. DOI: 10.1093/mnras/stw2593. arXiv: 1610.01162.

Turner, M. L. et al. (2012). "The ACS Fornax Cluster Survey. VI. The Nuclei of Early-type Galaxies in the Fornax Cluster". In: *ApJS* 203, 5, p. 5. DOI: 10.1088/0067-0049/203/1/5. arXiv: 1208.0338.

Ulubay-Siddiki, A., H. Bartko, and O. Gerhard (2013). "On the possibility of a warped disc origin of the inclined stellar discs at the Galactic Centre". In: *MNRAS* 428, pp. 1986–2000. DOI: 10.1093/mnras/sts167. arXiv: 1210.4750.

Ulubay-Siddiki, A., O. Gerhard, and M. Arnaboldi (2009). "Self-gravitating warped discs around supermassive black holes". In: *MNRAS* 398, pp. 535–547. DOI: 10.1111/j.1365-2966.2009.15089.x. arXiv: 0909.5333.

Valencia-S., M. et al. (2015). "Monitoring the Dusty S-cluster Object (DSO/G2) on its Orbit toward the Galactic Center Black Hole". In: *ApJ* 800, 125, p. 125. DOI: 10.1088/0004-637X/800/2/125. arXiv: 1410.8731.

Valluri, M. et al. (2005). "The Low End of the Supermassive Black Hole Mass Function: Constraining the Mass of a Nuclear Black Hole in NGC 205 via Stellar Kinematics". In: *ApJ* 628, pp. 137–152. DOI: 10.1086/430752. eprint: astro-ph/0502493.

Vesperini, E., S. L. W. McMillan, and S. Portegies Zwart (2009). "Effects of Primordial Mass Segregation on the Dynamical Evolution of Star Clusters". In: *ApJ* 698, pp. 615–622. DOI: 10.1088/0004-637X/698/1/615. arXiv: 0904.3934 [astro-ph.GA].

Vink, J. S. and A. de Koter (2005). "On the metallicity dependence of Wolf-Rayet winds". In: *A&A* 442, pp. 587–596. DOI: 10.1051/0004-6361:20052862. eprint: astro-ph/0507352.

Vink, J. S., A. de Koter, and H. J. G. L. M. Lamers (2001). "Mass-loss predictions for O and B stars as a function of metallicity". In:

A&A 369, pp. 574–588. DOI: 10.1051/0004-6361:20010127. eprint: astro-ph/0101509.

Vollmer, B. and W. J. Duschl (2001). "The stability of the Circumnuclear Disk clouds in the Galactic Centre". In: *A&A* 377, pp. 1016–1022. DOI: 10.1051/0004-6361:20011082. eprint: astro-ph/0108354.

Wadsley, J. W., B. W. Keller, and T. R. Quinn (2017). "Gasoline2: A Modern SPH Code". In: *ArXiv e-prints*. arXiv: 1707.03824 [astro-ph.IM].

Wadsley, J. W., J. Stadel, and T. Quinn (2004). "Gasoline: a flexible, parallel implementation of TreeSPH". In: *NewA* 9, pp. 137–158. DOI: 10.1016/j.newast.2003.08.004. eprint: astro-ph/0303521.

Walcher, C. J. et al. (2006). "Stellar Populations in the Nuclei of Late-Type Spiral Galaxies". In: *ApJ* 649, pp. 692–708. DOI: 10.1086/505166. eprint: astro-ph/0604138.

Walsh, J. L. et al. (2013). "The M87 Black Hole Mass from Gas-dynamical Models of Space Telescope Imaging Spectrograph Observations". In: *ApJ* 770, 86, p. 86. DOI: 10.1088/0004-637X/770/2/86. arXiv: 1304.7273.

Wardle, M. and F. Yusef-Zadeh (2008). "On the Formation of Compact Stellar Disks around Sagittarius A*". In: *ApJ* 683, L37, p. L37. DOI: 10.1086/591471. arXiv: 0805.3274.

Wehner, E. H. and W. E. Harris (2006). "From Supermassive Black Holes to Dwarf Elliptical Nuclei: A Mass Continuum". In: *ApJ* 644, pp. L17–L20. DOI: 10.1086/505387. eprint: astro-ph/0603801.

Wisdom, J. and M. Holman (1991). "Symplectic maps for the n-body problem". In: *AJ* 102, pp. 1528–1538. DOI: 10.1086/115978.

Witzel, G. et al. (2014). "Detection of Galactic Center Source G2 at 3.8 μm during Periapse Passage". In: *ApJ* 796, L8, p. L8. DOI: 10.1088/2041-8205/796/1/L8. arXiv: 1410.1884 [astro-ph.HE].

Wright, M. C. H. et al. (2001). "Molecular Tracers of the Central 12 Parsecs of the Galactic Center". In: *ApJ* 551, pp. 254–268. DOI: 10.1086/320089. eprint: astro-ph/0011331.

Xu, Ya-Di et al. (2006). "Thermal X-Ray Iron Line Emission from the Galactic Center Black Hole Sagittarius A*". In: *The Astrophysical Journal* 640.1, p. 319. URL: http://stacks.iop.org/0004-637X/640/i=1/a=319.

Yelda, S. et al. (2014). "Properties of the Remnant Clockwise Disk of Young Stars in the Galactic Center". In: *ApJ* 783, 131, p. 131. DOI: 10.1088/0004-637X/783/2/131. arXiv: 1401.7354 [astro-ph.GA].

Yoon, I. (2017). "Black hole mass measurement using molecular gas kinematics: what ALMA can do". In: *MNRAS* 466, pp. 1987–2005. DOI: 10.1093/mnras/stw3171. arXiv: 1701.05683.

Yusef-Zadeh, F., H. Bushouse, and M. Wardle (2012). "Hubble Space Telescope Observations of the Stellar Distribution near Sgr A*". In: *ApJ* 744, 24, p. 24. DOI: 10.1088/0004-637X/744/1/24. arXiv: 1109.2175.

Yusef-Zadeh, F. et al. (2006a). "A Multiwavelength Study of Sgr A*: The Role of Near-IR Flares in Production of X-Ray, Soft gamma-Ray, and Submillimeter Emission". In: *The Astrophysical Journal* 644.1, p. 198. URL: http://stacks.iop.org/0004-637X/644/i=1/a=198.

Yusef-Zadeh, F. et al. (2006b). "Flaring Activity of Sagittarius A* at 43 and 22 GHz: Evidence for Expanding Hot Plasma". In: *The Astrophysical Journal* 650.1, p. 189. URL: http://stacks.iop.org/0004-637X/650/i=1/a=189.

Yusef-Zadeh, F. et al. (2008). "Massive Star Formation in the Molecular Ring Orbiting the Black Hole at the Galactic Center". In: *ApJ* 683, L147, p. L147. DOI: 10.1086/591731. arXiv: 0807.1745.

Yusef-Zadeh, F. et al. (2013). "ALMA Observations of the Galactic Center: SiO Outflows and High-mass Star Formation near Sgr A*". In: *ApJ* 767, L32, p. L32. DOI: 10.1088/2041-8205/767/2/L32. arXiv: 1303.3403.

Yusef-Zadeh, F. et al. (2015a). "Radio Continuum Observations of the Galactic Center: Photoevaporative Proplyd-like Objects Near Sgr A*". In: *ApJ* 801, L26, p. L26. DOI: 10.1088/2041-8205/801/2/L26. arXiv: 1502.03109.

Yusef-Zadeh, F. et al. (2015b). "Signatures of Young Star Formation Activity within Two Parsecs of Sgr A*". In: *ApJ* 808, 97, p. 97. DOI: 10.1088/0004-637X/808/1/97. arXiv: 1505.05177.

Yusef-Zadeh, F. et al. (2017). "ALMA and VLA Observations: Evidence for Ongoing Low-mass Star Formation near Sgr A*". In: *MNRAS* 467, pp. 922–927. DOI: 10.1093/mnras/stx142. arXiv: 1701.05939.

Zajaček, M. et al. (2017). "Nature of the Galactic centre NIR-excess sources. I. What can we learn from the continuum observations of the DSO/G2 source?" In: *ArXiv e-prints*. arXiv: 1704.03699.

Zasov, A. V. and A. M. Cherepashchuk (2013). "Supermassive black holes and central star clusters: Connection with the host galaxy kinematics and color". In: *Astronomy Reports* 57, pp. 797–810. DOI: 10.1134/S1063772913110085. arXiv: 1312.4255.

Zubovas, K. (2015). "AGN activity and nuclear starbursts: Sgr A* activity shapes the Central Molecular Zone". In: *MNRAS* 451, pp. 3627–3642. DOI: 10.1093/mnras/stv1173. arXiv: 1505.05464.

de Francesco, G., A. Capetti, and A. Marconi (2008). "Measuring supermassive black holes with gas kinematics. II. The LINERs <ASTROBJ>IC 989</ASTROBJ>, <ASTROBJ>NGC 5077</ASTROBJ>, and <ASTROBJ>NGC 6500</ASTROBJ>". In: *A&A* 479, pp. 355–363. DOI: 10.1051/0004-6361:20078570. arXiv: 0801.0064.

den Brok, M. et al. (2014). "The HST/ACS Coma Cluster Survey - X. Nuclear star clusters in low-mass early-type galaxies: scaling relations". In: *MNRAS* 445, pp. 2385–2403. DOI: 10.1093/mnras/stu1906. arXiv: 1409.4766.

Šubr, L. ., J. Schovancová, and P. Kroupa (2009). "The warped young stellar disc in the Galactic centre". In: *A&A* 496, pp. 695–699. DOI: 10.1051/0004-6361:200811075.

Šubr, L. and J. Haas (2012). "Dynamical evolution of the young stellar disc in the Galactic centre". In: Journal of Physics Conference Series 372, 012018, p. 012018. DOI: 10.1088/1742-6596/372/1/012018.

Šubr, L. and J. Haas (2014). "Two-body Relaxation Driven Evolution of the Young Stellar Disk in the Galactic Center". In: *ApJ* 786, 121, p. 121. DOI: 10.1088/0004-637X/786/2/121. arXiv: 1404.0380.

van den Bosch, R. C. E. et al. (2012). "An over-massive black hole in the compact lenticular galaxy NGC 1277". In: *Nature* 491, pp. 729–731. DOI: 10.1038/nature11592. arXiv: 1211.6429 [astro-ph.CO].

van den Bosch, R. C. E. et al. (2015). "Hunting for Supermassive Black Holes in Nearby Galaxies With the Hobby-Eberly Telescope". In: *ApJS* 218, 10, p. 10. DOI: 10.1088/0067-0049/218/1/10. arXiv: 1502.00632.

van den Bosch, R. C. E. et al. (2016). "Toward Precision Supermassive Black Hole Masses Using Megamaser Disks". In: *ApJ* 819, 11, p. 11. DOI: 10.3847/0004-637X/819/1/11. arXiv: 1601.00645.

van der Marel, R. P. and F. C. van den Bosch (1998). "Evidence for a 3 X 10ˆ8 M_$M_\odot$ Black Hole in NGC 7052 from Hubble Space Telescope Observations of the Nuclear Gas Disk". In: *AJ* 116, pp. 2220–2236. DOI: 10.1086/300593. eprint: astro-ph/9804194.